AN EXPERIMENTAL INVESTIGATION OF VIBRATION SUPPRESSION IN LARGE SPACE STRUCTURES USING POSITIVE POSITION FEEDBACK

Thesis by

James L. Fanson

In Partial Fulfillment of the Requirements

for the Degree of

Doctor of Philosophy

California Institute of Technology

Pasadena, California

1987

Submitted November 24, 1986

ACKNOWLEDGEMENTS

I would like to express my deep appreciation to Professor Thomas Caughey for his encouragement throughout this work. His powerful insight into physical problems has led to the elegant technique of Positive Position Feedback on which this work is based, as well as to solutions to many technical aspects of the laboratory implementations. He has made himself available for discussions on any subject at any time.

My thanks go to Professor W. D. Iwan for allowing me the opportunity to be a Teaching Assistant for his dynamics class.

I would also like to thank my many friends at the Jet Propulsion Laboratory: Dr. Jay-Chung Chen for his support of the work and for volunteering abstracts to conferences, Dr. Donald Edberg for many helpful discussions on laboratory technique, Mr. John Garba for his support, Dr. Donald Rapp (the human battering ram) for helping to make the funding for this work a reality, Mr. Ben Wada for free computer time, Dr. Robert Norton for MINIPLOT and for being nursemaid to the VAX, Mr. Ralph Chen for laboratory time, and Mr. Bill Layman and the *Galileo* project.

Finally, I would like to express my deepest appreciation to my wife Dr. Helene Schember, whose steadfast love and support have made all of this possible.

This research was funded by grants from the Jet Propulsion Laboratory Director's Discretionary Fund (JPL 780-00272-0-3540), and the NASA Graduate Student Researchers Program (NGT-05-002-801). I also received support from Caltech in the form of Fellowships, Teaching and Research Assistantships, and from the NASA Office of Aeronautics and Space Technology.

ABSTRACT

A new technique for vibration suppression in Large Space Structures is demonstrated in laboratory experiments on a thin cantilever beam, resulting in substantially reduced dynamic response. This technique, called *Positive Position Feedback*, makes use of generalized displacement measurements to accomplish vibration suppression.

The concept of a piezoelectric *active-member* is developed in relation to controlling space-truss type structures. The active-member functions dually as a structural member and a control actuator. Piezoelectric ceramic material is adhered to a thin cantilever beam and simulates the use of an active-member. This *space-realizable* control scheme makes use of strain measurements, a preferred measurement quantity for vibration suppression, and internal control forces which completely decouple the rigid-body motion from the elastic motion.

A simple necessary and sufficient condition for stability with Positive Position Feedback is presented. This condition is non-dynamic and is in general easily satisfied. As a result, Positive Position Feedback is demonstrated to have superior robust stability properties. It is also demonstrated that with Positive Position Feedback, all control and observation spillover is stabilizing. Five experiments are described in which the first six modes of vibration of the cantilever beam are controlled.

TABLE OF CONTENTS

LIST OF FIGURES

LIST OF TABLES

ACRONYMS

ACCESS	Assembly Concept for Construction of Erectable Space Structures
COFS	Control of Flexible Structures
DOFB	Direct Output Feedback
DVFB	Direct Velocity Feedback
EASE	Experimental Assembly of Structures in EVA
EVA	Extra-Vehicular Activity
FEM	Finite Element Method
FFT	Fast Fourier Transform
IMSC	Independent Modal Space Control
ISI	Integrated Systems Incorporated
JPL	Jet Propulsion Laboratory
LAC	Low Authority Control
LAS	Lyapunov Asymptotically Stable
LSS	Large Space Structures
LQ	Linear Quadratic
LQG	Linear Quadratic Gaussian
MESS	Model Error Sensitivity Suppression
MIMO	Multi-Input-Multi-Output
MIT	Massachusetts Institute of Technology
MMC	Modern Modal Control
MSC	MacNeal-Schwendler Corporation
NASA	National Aeronautics and Space Administration
PDE	Partial Differential Equation
PPF	Positive Position Feedback
PZT	Lead Zirconate Titanate
QUASAT	Quasar Satellite
SAFE	Solar Array Flight Experiment
SDOF	Single Degree-of-Freedom
SISO	Single-Input-Single-Output
STI	Synergistic Technology Incorporated

NOMENCLATURE

A	quantity defined in Eq. (4.3.10b); constant in Eq. (4.6.8)
$A(s)$	transfer matrix used for root contour Eq. (5.3.3a)
a	numerator of plant transfer function in vicinity of i^{th} mode
a_1	$= f_a W_a E_a d_{31}(t_a + t_b)$
a_2	$= \frac{1}{2} f_s\, g_{31}\, t_s(t_s + t_b) E_b$
B	filter damping matrix; matrix partition defined in Eq. (4.5.14); constant in Eq. (4.6.8)
$B(s)$	beam transfer matrix
B_α	$\alpha = 1, 2$; matrix partitions defined Eq. (4.5.15)
b	additive real scalar constant of plant transfer function in vicinity of the i^{th} mode
C	gain matrix; matrix of modal coupling coefficients; vector of sensor coupling coefficients in Figure (5.1)
C_{PZT}	capacitance of sensor
C_α	$\alpha = 1, 2$; capacitor values for PPF filter
c	viscous damping coefficient
$c_{\rm cr}$	critical viscous damping coefficient
C_i	curvature coefficient defined in Eq. (4.3.6)
D	structure damping matrix; location of neutral axis defined in Figure (4.2); vector of actuator coupling coefficients in Figure (5.1)
D_f	filter damping matrix
D_j	$= \phi_j'(x_2) - \phi_j'(x_1)$
d_{31}	piezoelectric transverse charge coefficient
E	Young's modulus; matrix defined in Eq. (4.5.8)
$E_{1,2,3}$	Young's modulus of material in Sections 1, 2, 3 of beam cross section
E_a	Young's modulus of actuator material
E_b	Young's modulus of aluminum beam
E_f	applied electric field
$E^{1/2}$	$= \sqrt{a_1 a_2}\, G^{1/2} C$
$F(t)$	arbitrary excitation force
F_a	axial force on beam cross section
f_a	actuator calibration factor

f_s	sensor calibration factor
G	gain matrix
g	scalar gain
g_{31}	piezoelectric transverse voltage coefficient
I	geometric moment of inertia of beam section
iff	if and only if
$\mathcal{I}$	Hamiltonian Action
$J_i(s)$	plant transfer function in vicinity of i^{th} mode
j	the imaginary unit $(= \sqrt{-1})$
K	structure stiffness matrix
$K(s)$	control compensator transfer matrix
k	stiffness in Eq. (4.6.1)
k_α	$\alpha = 1, 2$; PPF filter transfer functions in Eq. (5.3.1)
L	length of beam; matrix defined in Eq. (4.5.4)
m	mass in Eq. (4.6.1)
$m(x)$	mass/unit length of composite beam
M	structure mass matrix; applied bending moment
N	matrix defined in Eq. (4.5.4)
N_f	number of filters
N_m	number of structural modes
P	amplitude of sinusoidal excitation in Eq. (4.6.4)
$P(s)$	plant transfer function
P_k	k^{th} principal minor of N
$P_n(s)$	band limited plant transfer function retaining n modes
R	radius of curvature defined in Figure (4.2); shunt resistance
R_α	$\alpha = 1, 2$; resistor value for PPF filter
S	sensor and actuator coupling matrix
s	Laplace Transform variable $(= j\omega)$
T	kinetic energy
$T(s)$	PPF filter transfer function; loop transfer function
t_1	thickness of Section 1 of beam cross section; initial time of admissible motion in Hamilton's Principal derivation
t_2	thickness of Section 2 of beam cross section; final time of admissible motion in Hamilton's Principal derivation

t_3	thickness of Section 3 of beam cross section
t_a	thickness of actuator ceramic
t_b	thickness of aluminum beam
t_e	distance ceramics extend past edge of beam
t_s	thickness of sensor ceramic
$\mathbf{u}$	filter state vector
V	elastic potential energy; Lyapunov Function
V_a	applied voltage; actuator voltage
V_{PZT}	voltage produced by ceramic material
V_s	sensor voltage
W	work done by applied follower moment
W_1	width of actuator ceramic in Figure (4.1)
W_2	width of sensor ceramic in Figure (4.1)
W_3	width of aluminum beam in Figure (4.1)
W_a	width of actuator ceramic
W_b	width of aluminum beam
W_s	width of sensor ceramic
x	coordinate axis of Figures (4.1) (4.2); displacement coordinate of SDOF oscillator
x_1	location of edge of actuator nearest the root — Station 1
x_2	location of edge of actuator nearest the free end — Station 2
y	coordinate axis of Figures (4.1) (4.2); physical beam deflection
$\mathbf{y}$	displacement vector in global coordinates
z	coordinate axis which forms right-handed system in Figure (4.2)
γ	fixed value for filter gain in root contour
δ	variation of quantity in Hamilton's Principal derivation
δ_{ij}	Kronecker Delta
$\varepsilon_1(y)$	strain in Section 1 of beam cross section
$\varepsilon_2(y)$	strain in Section 2 of beam cross section
$\varepsilon_3(y)$	strain in Section 3 of beam cross section
ε_a	uniform axial strain across beam section
$\varepsilon_b(y)$	bending strain across beam section
ε_E	piezoelectric free strain
ς	damping ratio $(= \mathrm{c}/\mathrm{c_{cr}})$

ζ_i	damping ratio of i^{th} mode
ζ_f	filter damping ratio
ζ_p	prescribed closed loop damping ratio
$\boldsymbol{\eta}$	vector of filter coordinates
η	filter coordinate
λ	eigenvalue of matrix $\Omega - a_1 a_2 C^T G C$
$\boldsymbol{\xi}$	vector of modal coordinates
ξ	modal coordinate
$\xi_i(t)$	modal coordinate of i^{th} mode
σ	uniaxial stress
σ_s	stress on sensor ceramic
σ_x	stress along x axis
ϕ_i	mode shape of i^{th} mode
$\boldsymbol{\psi}$	transformed vector of filter coordinates
Ω	modal frequency matrix
Ω_f	filter frequency matrix
ω	circular frequency, modal frequency
ω_d	damped frequency $= \omega\sqrt{1-\zeta^2}$
ω_f	filter frequency
ω_{pi}	frequency of i^{th} mode
ω_{zi}	frequency of i^{th} zero

Chapter 1

INTRODUCTION

With the ever increasing capabilities of constructing large complex structures in space come new engineering challenges. Because of the cost of placing material in orbit,* spacecraft are necessarily designed to be as low-mass as possible. Traditionally, the most demanding physical environment on spacecraft has been the launch loading associated with achieving orbit. This has generally meant a tradeoff between making the spacecraft as low-mass as possible while ensuring sufficient strength, which usually involves ensuring sufficient structural stiffness. For the next generation of spacecraft that will be constructed or erected in space, the launch environment becomes almost irrelevant. Consequently, stiffness is not critical to the survival of the structure and requirements on stiffness can be greatly relaxed. Large Space Structures (LSS), or Large Flexible Structures as they are sometimes called, are vehicles and platforms designed specifically for the zero-gravity environment of space. These flexible spacecraft, and the means to control them, are the subject of this research.

1.1 Motivation for Active Control of Large Space Structures

Most of the applications for large space structures involve *very* stringent performance requirements which cannot be met by a structure that is flimsy and flexible. Consider, for example, the wrap-rib mesh deployable antenna. Reflectors ranging in size from 20 to 100 meters in diameter are presently in preliminary design at the Caltech Jet Propulsion Laboratory [1]. The pointing accuracy for the QUASAT application of this antenna is one minute of arc of

* The cost of launch services using the Space Shuttle Space Transportation System currently exceeds $2,000/lb.

the intended direction, and the surface of the antenna must stay within one millimeter of the intended configuration. This pointing and surface shape accuracy must be maintained in spite of thermal distortions due to solar radiation, and the vibrations induced from attitude maneuvers. Such a structure will have vibratory modes which are low frequency and may have low damping ratios. The 55 meter reflector has a vibratory mode at 0.18 Hz. If the damping ratio of this mode is as low as 0.1 percent, the settling time of the antenna will approach one hour. The performance requirements and the low frequency, low inherent damping characteristics of the wrap-rib antenna are typical of what may be expected for LSS of the future. Because passive damping techniques are ineffective at these low frequencies, the need for active control of LSS is indicated.

1.2 The Large Space Structure Control Problem

The wrap-rib antenna is a good example of a Large Space Structure because it illustrates the three basic objectives of LSS control. First, an antenna is useless if it does not point at the correct target. The first objective of a control system is therefore one of pointing, or attitude control. Second, a reflector will not function as an antenna if its surface is not parabolic. If the structure is vibrating, the surface geometry will be changing with time and will not generally be correct. Thus, the second objective of a control system is vibration suppression: either minimizing the amplitude of vibration, or damping out the vibration as quickly as possible, or both. Finally, after the vibration has stopped, if the nominal surface is not parabolic, it must be deformed back into the correct shape. The third objective then is shape control. While mission specific reqirements will vary, the three objectives of attitude control, vibration suppression, and shape

control are representative of the functions any LSS control system may be called on to perform.

The first objective, attitude control, is not new to the spacecraft control community. Nearly all spacecraft flown in the past 25 years have had such a control system. However, the second and third objectives, which stem from the elastic behavior of the structure, are relatively new. While current spacecraft such as *Galileo* and *Hubble Space Telescope* have some flexible dynamics, the current approach is to achieve attitude control in spite of the elastic modes. As the frequency of the elastic dynamics gets lower, it begins to overlap with the bandwidth of the attitude controller. When it is not possible to ignore the flexible dynamics, or when the flexible nature of the structure becomes the subject of the control, then the problem is one of LSS control.

1.3 Some Difficulties in the Control of Flexible Structures

The Large Space Structure control problem is inherently difficult for a variety of reasons. To begin with, LSS are distributed parameter systems. The best mathematical model for distributed parameter systems is the Partial Differential Equation (PDE). However, most engineering systems are so complicated that it is most difficult, if not impossible, to find a suitable PDE to accurately describe a particular system together with its boundary conditions. Even if a PDE could be found, there is no guarantee that it will be amenable to analysis [2,3]. The engineer is compelled, therefore, to work with a discretized model, usually via the Finite Element Method (FEM).

The PDE model is characterized by an infinite number of degrees of freedom and an infinite frequency spectrum. An equivalent discretized model would also

require an infinite number of degrees of freedom.* Since it is intractable to work with discrete models of infinite size, a finite dimensional or truncated model is substituted. One consequence of using a truncated model is that some dynamics of the system will *always* remain completely unmodelled. In practical terms, this means that the actual structure will always have vibrational modes that are not contained in the mathematical model. In addition, LSS are likely to manifest very densely spaced, lightly-damped modes which cause stability complications involving the control system rolloff. To accurately model the dynamical characteristics of LSS up to frquencies of practical interest, finite dimensional models of relatively high order are required. Current spacecraft such as *Galileo* require models on the order of 10,000 degrees of freedom** [4]. It is not unreasonable to expect that FEM models of LSS may reach hundreds of thousands of degrees of freedom. While structural dynamics applications can accommodate models of this size, state variable control applications generally begin to exceed computational capability with plant models of about two hundred states [5]. A great deal of current research addresses how to reduce a high order structural model to a lower order plant model for control applications [6,7]. Most control design methodologies make use of two different size models: a low order model for control system synthesis, and a high order "truth model" for stability and performance tests.

In practice, FEM structural models always require verification and fine-tuning. Normally, this verification is done by means of ground tests on either the actual flight hardware, or a structural equivalent. Since most of the concern for

---

* For an entertaining discourse on the infinite modes assumption, see Hughes [12].

** This number refers to the stiffness degrees of freedom. Typically, the mass matrix contains fewer terms.

the structure has been in the launch loads area, most ground tests are performed in a *launch* or *stowed* configuration. For LSS the configuration of interest is the *deployed* state. Since LSS are designed for the zero-g environment of space, they cannot support their own weight, and hence, ground testing will be a very tricky business. It is doubtful that full-scale testing will be possible at all for the very largest structures. As a result, ground test strategies may have to resort to component testing with subsequent analytical coupling, or perhaps to scale model testing. While it is possible to do some amount of verification in this manner, a model based on ground tests may have questionable accuracy. It is inevitable that some system identification tests will have to be performed on-orbit, in zero gravity and in hard vacuum. To further complicate matters, the structural characteristics of LSS are likely to change with time as a result of outgassing, cold welding of joints, depletion of consumables, mass redistribution, growth of the structure as in the case of an evolving space station, etc. In summary, the model of the structure used for the control system design will have considerable uncertainty, due to both parametric uncertainty and truncation. Any control scheme for LSS will have to maintain stability and performance in the face of uncertainty,* and be able to accommodate the need for on-orbit system identification testing.

One might expect that the best way to control distributed parameter systems is with "distributed control," i.e., spatially distributed actuators and sensors. It would then be possible, for example, to apply a control force proportional to a mode shape. However, truly distributed sensors and actuators are

* This is the definition of robustness.

not currently feasible; discrete sensors and actuators must be used. Furthermore, practical limitations necessitate that only a finite number of such devices will be available to implement any control scheme. This implies that the final control compensator must be of relatively low order in terms of input and output states, certainly lower than the size of the truncated plant model. A consequence of using discrete sensors on a distributed parameter system is that the sensor measurements will always be contaminated by modes which are not being controlled, and which may not even be modelled. This is the Observation Spillover phenomenon [8]. Efforts have been made to eliminate this effect by means of spatial modal filters [9] and comb filters [28], but in practice observation spillover will always be present to some extent. Similarly, as a consequence of using discrete actuators, the control system will always excite modes that are not being controlled: the Control Spillover phenomenon [8,10]. This effect is more difficult to manage. As will be discussed in the next section, if both control and observation spillover are present, a nominally stable system can go unstable. There are other problems associated with actuators: they have finite bandwidths. This means that actuator dynamics has to be taken into account in the control design process, or it may destabilize modes in the region of the actuator natural frequency [11]. Because the modes of LSS will become dense at higher frequencies, there will always be a mode nearby these frequencies.

Finally, once a control system is designed, it must be implemented in real-time by means of an on-board computer. Because computing power is limited, the control algorithm to be used must not be too computationally intensive, or unacceptable destabilizing time delays may be introduced. For these and other reasons, the LSS control problem is an especially challenging one.

1.4 Previous Work—Theory

Developing solutions to the LSS control problem has occupied a sizable portion of the aerospace research community for the past 15 years. The subject is broad and interdisciplinary, drawing on control and estimation theory, optimization, structural dynamics, structures, and large-scale computing among others. While a comprehensive survey will not be attempted here, it is of interest to highlight some of the developments of LSS control techniques. A more complete background can be found in several excellent survey articles [3,13-16].

1.4.1 State-Space Methods

Serious interest in the LSS control problem developed at a time when Modern Control Theory, comprising stochastic optimal control and estimation theory, was replacing Classical Control as the dominant control paradigm. One of the major accomplishments of the state-space methods, culminating in the Linear Quadratic Gaussian (LQG) unified design procedure, was the ability to straightforwardly synthesize a compensator for a multivariable system while optimizing the closed loop performance in some specific sense [17]. Since LSS control is a multivariable problem, most techniques have been formulated in state-space form. The structure, or plant, is modelled as a linear time-invariant first-order differential equation. The plant model can be written in terms of physical coordinates, in which case the problem is one of Direct Output Feedback (DOFB), or it can be written in terms of modal states, in which case the problem is one of modal control. Modal control lends itself more readily to reduced order models, since only the important modes need be retained. Exactly how the retained modes should be chosen is a topic of current research [6,7].

The formulation of the DOFB method can be found in [18–22]. Balas [18] investigates the spillover phenomenon in relation to DOFB. He uses an example of a simply supported beam to demonstrate how spillover can cause instability. Direct Velocity Feedback (DVFB) is examined in [19,20,23]. These references show that DVFB used in conjunction with compatible, collocated actuators and rate sensors produces a closed loop system which is unconditionally stable as long as rigid body modes are ignorable. A popular technique for achieving desired closed loop performance in DOFB is pole placement. This method attempts to prescribe the closed loop pole locations subject to observability and controllability constraints. The pole placement technique is described in [24,25]. Pole placement can also be used in modal control [26].

Many different modal control schemes have been proposed. They can be divided into two types. The first type is called Modern Modal Control (MMC) by Balas, or Coupled Controls by Meirovitch. It involves a reduced order plant model in modal coordinates together with some type of modal state estimator, which synthesizes coordinates that cannot be measured directly. The second type is somewhat less conventional and is called Independent Modal Space Control (IMSC).

Much research has been done on MMC. The formulation of the problem can be found in [8,21,22,27,28]. The primary variations in the technique involve how the performance criteria are specified and how the estimator is designed. The most common method for specifying performance is in terms of a quadratic cost functional that penalizes various portions of the state and control vectors by appropriate weighting matrices. The synthesis of the controller then usually involves solving either the deterministic LQ optimal control and estimation

problem, or the stochastic LQG problem. The construction of the state vectors and weighting matrices allows considerable design freedom for reducing effects such as spillover. It is common practice to partition the state vector into controlled and residual modes and then attempt to design the control system in such a way that it does not destabilize the residual dynamics. It is then hoped that the controller will maintain stability and performance when it is implemented on the full order system. Balas again uses the simply supported beam example to demonstrate spillover induced instability [8]. He proposes the use of a prefilter consisting of phase-locked loops tuned to the controlled modes to reduce observation spillover. He also proposes having a very large number of sensors to approximate a distributed sensor. This is essentially equivalent to Meirovitch's modal filter. Model Error Sensitivity Suppression (MESS) attempts to reduce spillover by including in the performance index a weight on the control spillover terms [29]. This leads to a control which is "orthogonal" to the residual modes. By the well-known duality relationships, the same technique reduces observation spillover through the observer. Skelton and Likins [30] propose an adaptive technique using an orthogonal filter to estimate the "model error vector" and hence improve the convergence properties of the state estimator. Premont [31] proposes a nonlinear technique where the magnitude of the control force is reduced when the energy of the controlled modes decays below a certain level.

The second modal control method, IMSC, is developed in [9,16,32–34]. This technique constructs the control force vector in modal space from the *uncoupled* modal equations and then transforms back to physical space via the modal matrix. Since the control vector is constructed in such a way that all the modes

are uncoupled, it is orthogonal to the space spanned by the residual modes. The drawback is that the number of actuators must equal the order of the system.

Other more specialized control theories have been developed. Aubrun [35] uses root perturbation techniques to formulate Low-Authority Control (LAC). Schaechter [36] defines a control law that includes feedback of only those state variables that are physically near a particular actuator, i.e., local control.

The problem of spillover has plagued LSS control techniques from the beginning. With the exception of DVFB using compatible, collocated actuators and rate sensors, no state-space method has been developed that is completely immune from its destabilizing effects. DVFB requires true rate sensing in order to be implemented and suffers from the destabilizing effects of finite actuator dynamics. The problems of actuator dynamics have been largely ignored by the LSS control comunity. It is shown by Goh and Caughey [11] that finite actuator dynamics can render a nominally stable system unstable. This adds yet another destabilizing effect which must be overcome.

We propose a technique called Positive Position Feedback (PPF), which does have immunity from spillover induced instability, and which does not require rate sensing. The method was originally proposed to overcome the instabilities associated with finite actuator dynamics [2,11]. This research investigates the feasibility of implementing PPF as a vibration suppression technique for LSS.

1.4.2 The Return of the Frequency Domain

One of the basic difficulties in using standard state-space LQG methods on LSS is that robustness is not guaranteed [37,42]. This is because it is impossible to implement full-state feedback on LSS, even with an observer. Optimal control

techniques provide an *optimal* control for a given model but optimality is not necessarily a good measure of robustness. LQG can frequently result in controllers which are too complex for practical implementation. In fact, there is no guarantee that the compensator itself will be stable [38]. It has been shown that standard LQG implementation on LSS problems can have vanishing robustness [39,40].

In the late 1970's new methods for dealing with plant uncertainty were developed. Ironically, this involved a return to the frequency domain. Components in the control system are modelled as linear time-invariant systems with transfer function matrices. The input-output properties of these matrices are characterized by singular values [41].

In recent years an attempt has been made to patch the LQG method by incorporating frequency dependent constraints [45,46]. These techniques formulate the truncated plant model as frequency dependent unstructured uncertainty, and make use of the robustness results in terms of singular values [41]. One method introduces frequency dependence in the weighting matrices of the cost functional [43,44]. The weighting penalizes high frequency control activity where the plant uncertainty is greatest. While these methods look promising, there have as yet been relatively few applications to LSS.

Finally, there is an interesting theory based on positivity of operators. The method is described in [47–50]. In this technique, the plant and compensator are manipulated in such a way that they each appear "passive." Stability is then assured.

1.5 Previous Work — Experiment

Experiments play an important role in turning LSS control theories into usable technologies. The ultimate laboratory for LSS control tests is the zero-gravity environment of orbit. The National Aeronautics and Space Administration (NASA) is organizing a test program that will incorporate both ground and flight tests using the Space Shuttle. It will be several years, however, before flights commence. At present, ground based laboratory experiments are the only means of validating LSS control technologies. Since the present work is primarily aimed at vibration suppression, experiments on shape control and slewing will not be reviewed. References [51–60] present a good sampling of LSS control experiments. As can be seen from the references, the results of these experiments have appeared in the literature relatively recently. A summary follows:

- Bailey and Hubbard [51]: a beam experiment implementing nonlinear feedback tailored to the specific test structure.
- Aubrun [52]: beam and plate experiments implementing LAC.
- Dehghanyar et al. [53]: a beam experiment implementing suboptimal pulse control.
- Meirovitch and Baruh [54]: a beam experiment implementing IMSC using on-off control.
- Schäfer and Holzach [55] and Hanagud et al. [58]: beam experiments implementing DVFB with collocated sensors and actuators.
- Schaechter and Eldred [56]: a beam experiment implementing MMC. Instability induced by model error is demonstrated.
- Hallauer and Skidmore [57]: a grid experiment implementing IMSC using tuned filters to extract modal coordinates. A controller-induced instability occurred.
- Brennan [59]: a beam experiment implementing LAC.
- Simonian et al. [60]: a truss experiment implementing Positivity methods.

The beam structures in [51–56,58,59], and the truss [60] are simple structures in the sense that the frequencies of the lower modes are widely spaced. LSS will certainly have densely spaced modes, and hence this aspect of the LSS control problem is not yet adequately addressed. The grid in [51] is designed to have a dozen modes between 0.6 and 10 Hz, and it is noteworthy that the only experiment with dense modes exhibited an anomalous instability. In practice, it is difficult to achieve dense modes in a simple structure. The price paid for increased modal density is increased cost of the test specimen and increased complexity in the laboratory.

1.5.1 Space-Realizable Control

Unfortunately, many of the experimental implementations mentioned in the previous section suffer from the problem of not being "space-realizable." This means that, for one reason or another, the method of sensing or actuation used in the experiment cannot be used in space. The issue of space-realizability has been largely neglected in the LSS control community until very recently. For example, the actuators used in Dehghanyar et al. [53] are gas jets. Gas jets expend consumable propellant, which is not cheaply or easily replenished in space. Certainly, actuators for vibration suppression will have to be electrically powered since electricity is the only readily available source of energy in space. Aubrun [52] makes use of proof-mass dampers, which are linear analogs of control-moment-gyros. Neither of these types of actuators will work quasi-statically, and hence *cannot* be used for shape control. Furthermore, proof-mass dampers lose their effectiveness at low frequency. To regain effectiveness the

reaction mass must be made very large. Bailey and Hubbard [51] use a space-realizable actuator and sensor, but the sensor is an accelerometer. Accelerometers do not work well at low-g levels. In order to obtain high signal-to-noise ratio measurements for low-amplitude low-frequency vibration, the accelerometers may have to be massive. In addition, acceleration is an inertial quantity and hence automatically couples the rigid body modes to the measurements of elastic motion. This may be undesirable in some circumstances.

The implementations in [54–57] suffer from a more serious problem: they are "sky-hook" experiments. Sky-hook experiments involve actuators or sensors that are attached to a rigid frame, which is adjacent to but separate from the test structure. Since no sky-hooks exist in space, these implementations are clearly not space-realizable.

This leaves experiments [58,59,60] and perhaps [51] as examples of space-realizable approaches. Simonian et al. [60] use an electromagnetic voice-coil type actuator in series with the diagonal members of the truss structure. This type of actuator produces a force by means of electromagnetic field interactions between a magnet and a wire coil. When current is fed to the device, a force is produced. The unfortunate converse of this is that when no current is present, no force is available. This means that if a failure were to occur in an actuator implemented as in [60], a structural member of a truss would effectively disappear. This could have disastrous consequences for the structure. In short, the design is not failure-tolerant. In addition, electromagnetic actuators have finite actuator dynamics and require substantial power supplies.

Interestingly, the remaining cases [51,58,59] and the current research have one thing in common: they make use of piezoelectric materials. It appears that

the potential for the use of piezoelectric materials in the control of Large Space Structures was realized independently and simultaneously in at least three locations: *MIT/Draper Lab.*, *Georgia Institute of Technology*, and *Caltech/JPL.* Bailey and Hubbard [51] use piezoelectric polymer film. Hanagud et al. [58] and the present work use piezoelectric ceramics. Crawley and de Luis [61,62] have investigated incorporating piezoelectric ceramics into new types of composites. This work all appears to have been motivated by the use of piezoelectric materials for shape control of optics, and by the work of Forward and Swigart [63,64]. Forward used piezoelectric ceramics to implement DVFB to damp out the bending modes of a cylindrical mast. While this structure was stiff and therefore not of the LSS type, the methodology is applicable.

1.6 Proposed Vibration Suppression Technology for LSS

We propose the concept of an active-member, or smart-member, which is a control actuator that functions dually as a structural element. In this sense it is not an add-on device such as a gas jet or proof-mass damper, but is actually part of the structure itself. The active-member concept was originally alluded to by Canavin [22], and later by Caughey et al. [65], and Chen [66]. We propose that piezoelectric ceramic active-members be used to replace elements of truss-type structures. We further propose a sensing scheme based on strain measurements. Strain is intimately related to the elastic deformation of a structure, and is therefore a natural quantity to measure for use in a vibration suppression control system. Collocated strain sensors and piezoelectric actuators can then be used to implement Positive Position Feedback. The approach outlined above is demonstrated on a thin, flexible cantilever beam. The details of the approach are left to the sequel.

Chapter 2

APPROACH

This research investigates a unified approach to the Vibration Suppression control objective for LSS. The approach encompasses both a control strategy and a space-realizable sensing and actuation method. The control strategy, Positive Position Feedback, achieves vibration suppression using strain measurements only. It is shown that strain is a preferred measurement quantity. The Positive Position Feedback technique will be described in detail. The vibration suppression is effected by means of internal force producing devices that can be electrically powered and operated quasi-statically and are therefore space-realizable. The hardware aspects of implementing this approach on real LSS are discussed. These considerations will motivate the design of the experiment in Chapter 3.

2.1 Hardware Aspects

The following sections suggest how the present approach to vibration suppression might be implemented on real LSS. The importance of *internal* sensing and actuation is stressed. Examples of proposed LSS are used to motivate the concept of a piezoelectric active-member. These considerations are taken into account in the design of the experiment in Chapter 3, which attempts to capture as many of the important aspects of LSS implementability as possible in a simplified two-dimensional uniform beam.

2.1.1 Vibration Suppression Control Objective

The three basic objectives of LSS control are: 1) attitude control, 2) vibration suppression, and 3) shape control. The current research is concerned with

the second objective. While a control subsystem for any given spacecraft may have to perform all three of the above functions, it is not generally necessary that all functions be implemented by the same compensator. It may be desirable that vibration suppression be accomplished by a control system which is separate and autonomous from the attitude control system. For a broad class of structures, the attitude control specifications relate solely to the rigid-body modes of the structure. Rigid-body modes can be actuated only by "external" force producing devices such as gas jets or control-moment-gyros. We have seen that such devices are not well suited for low frequency vibration suppression and *cannot* be used for shape control. This suggests that the following natural distinction can be drawn between attitude control on the one hand, and vibration suppression and shape control on the other: Attitude control relates to the rigid-body modes of the structure and can be effected only by *external* force producing devices, while vibration suppression and shape control relate to the flexible-body modes and can be effected by *internal* force producing devices. This point of view simply recognizes that vibration and shape are elastic phenomena, whereas attitude generally is not.

It follows from this distinction that measurements used to implement vibration suppression should be closely related to the *elastic* motion. The quantity most intimately related to elastic motion is strain. Strain, which is easily measured even at low frequency, is a generalized displacement; however, most vibration suppression techniques require rate or velocity information in some form. Rate information can be obtained in one of four ways: 1) by direct measurement by a rate sensor, 2) by differentiating displacement measurements, 3) by integrating acceleration measurements, and 4) through synthesis by means

of filters or an observer. The first three methods have some drawbacks. Velocity is relatively difficult to measure directly, and velocity transducers tend to be heavy. Differentiating displacements is not a good technique because differentiation amplifies noise. Integrating acceleration is feasible as long as the accelerations can be measured accurately, but since acceleration is an inertial quantity, obtaining velocity by integration results in an inertial velocity, which can be contaminated by rigid-body modes.

Filters also have some complicating factors. Displacement measurements passed through filters produce velocity information over a fairly narrow passband. This can create difficulties outside the passband, where the unwanted phase shift of the filter can cause closed loop instability. In practice, the filters are usually tuned to the frequencies of the structural modes in order to synthesize modal velocities. Examples of this method can be found in Forward [64], and Hanagud et al. [58]. Observers form the basis of Modern Control methods for LSS, which have already been discussed in Chapter 1.

Positive Position Feedback (PPF) makes use of tuned filters; however, the synthesis of velocity is not an explicit part of the theory. Rather, global asymptotic stability is achieved based on the form of the compensator alone. PPF will be discussed in more detail in Section (2.2). The important aspect of PPF in the present context is that it does not require rate information and hence, strain, a desirable measurement quantity for vibration suppression, can be used directly.

Internal force producing devices such as piezoelectric actuators have two important advantages. First, they can be electrically powered and can operate quasi-statically and are therefore space-realizable. Second, if only internal forces are applied to a structure, the rigid-body modes cannot be excited. This

decoupling is advantageous because it means that the vibration suppression system *cannot* upset the pointing orientation of the spacecraft. Thus, if strain measurements and internal forces are used, the elastic motion is *completely* decoupled from the rigid-body modes. This is the approach taken in the current work.

2.1.2 Generic Truss-Type Large Space Structures

A large class of proposed LSS are built from three-dimensional space-truss beams, structures that are of particular interest to this work. An example of such a structure is the Space Station depicted in Figure (2.1). The Space Station is composed of relatively rigid life-support modules and flexible space-truss beams which support solar power arrays, radiators, etc. There have been two LSS related experiments conducted on Space Shuttle missions 61-B and 41-D in support of Space Station development. On mission 61-B, astronauts constructed two truss-type structures while in orbit: the ten bay ACCESS truss and the EASE pyramid truss. Figure (2.2) shows astronaut Lt. Col. Sherwood Spring holding the assembled 45 foot ACCESS structure, and Figure (2.3) shows the EASE truss being assembled. On mission 41-D the 105 foot long SAFE flexible solar power system was deployed. The support structure for SAFE was a deployable astro-mast truss.

These large space-truss beams are the type of structure which we propose to control by means of active-members. The active-member concept is detailed in the next section.

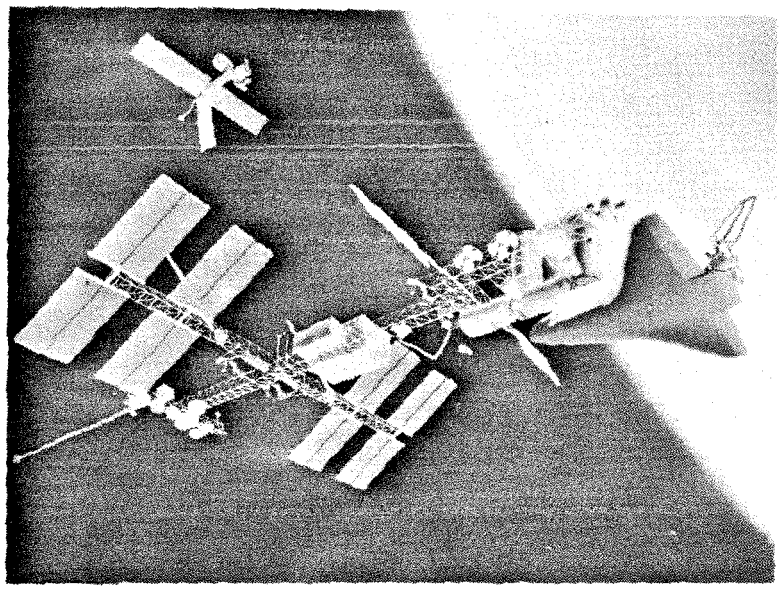

Figure 2.1 Space Station concept.

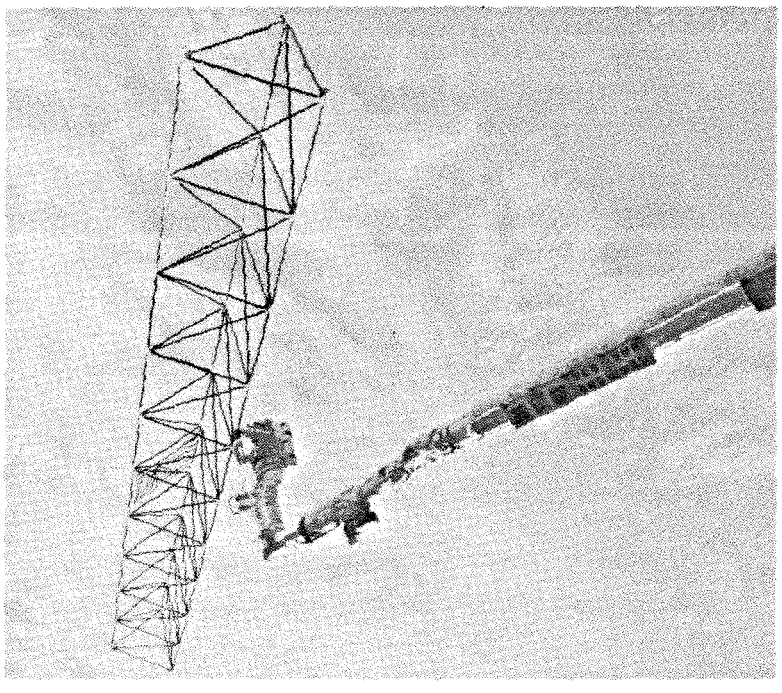

Figure 2.2 ACCESS truss constructed on Space Shuttle mission 61-B.

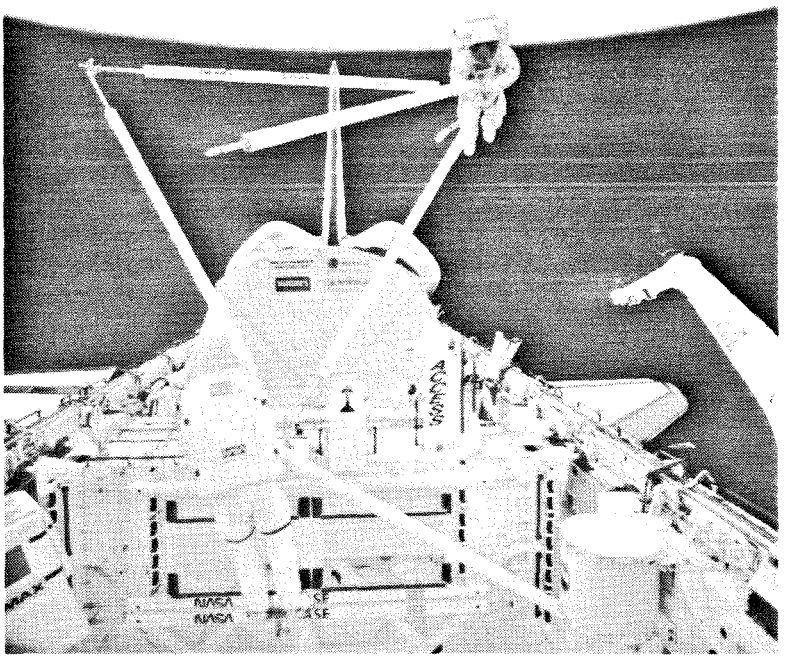

Figure 2.3 EASE truss constructed on Space Shuttle mission 61-B.

2.3 Piezoelectric "Active-Member" Concept

An active-member is a control actuator that functions dually as a structural element. While other types of control actuators such as gas jets or control-moment-gyros are add-on devices, the active-member is an integral part of the structure. Canavin [22] originally suggested the idea of making structural elements out of collocated actuators and rate sensors that could then implement DVFB. The idea was expressed in general terms and the implementation was not specific. We propose the collocated strain sensor/piezoelectric actuator active-member.

Piezoelectric materials are inherent electro-mechanical transducers. Actuators made of piezoelectric materials can be powered electrically and can typically be operated at frequecies ranging from static (DC) to several kilohertz. This

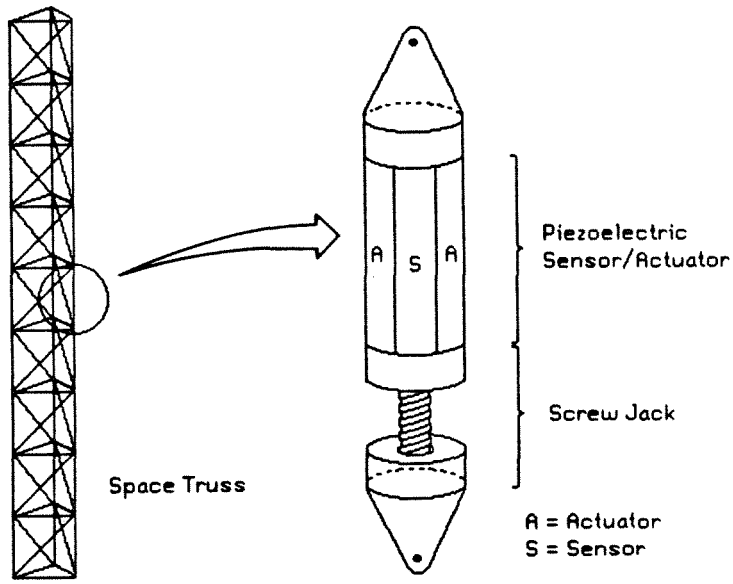

Figure 2.4 Active Member Concept for LSS.

essentially removes the actuator dynamics from consideration because the controller bandwidth will be far below the resonant frequencies of the actuator. One drawback of piezoelectric materials is that they cannot produce the large displacements necessary to implement shape control. However, actuators such as screw jacks can be added to the active-member in series with the piezoelectric component to provide this capability. The type of active-member that might be used on a space-truss beam of a LSS is depicted in Figure (2.4).

Active longerons in a space-truss beam (as depicted in Figure (2.4)) can induce bending loads on the structure and can be used to damp out bending vibration. Active diagonals can be used to damp out torsional vibration. The experiment described in Chapter 3 is designed to simulate active longerons on a beam. Bending strain is measured and the actuators apply bending moments.

The active-member can also be used as an exciter for on-orbit system identification testing. Since they induce internal forces, the active-members can be tuned to excite modal responses as in a conventional sine dwell modal test.

2.2 Positive Position Feedback

The control strategy that is implemented in this work is called Positive Position Feedback (PPF). PPF was originally proposed for LSS vibration suppression by Caughey and Goh [2,11]. The technique was conceived in relation to the problem of finite actuator dynamics. It is shown in [2] that by appropriate arrangement PPF causes the actuator dynamics to synchronize with tuning filters, removing the actuator dynamics from the analysis. Piezoelectric actuators have sufficiently high natural frequencies that we can ignore their dynamics completely in the present case. The basic theory and the major results of PPF will be reviewed in the following sections. A more detailed analysis can be found in [2]. A new result, discussed in Section (2.2.3), is that the multi-mode synthesis procedure proposed in [2] can result in reduced closed loop performance if the system poles and zeros nearly cancel. An approach for recovering performance is proposed.

2.2.1 Scalar Case

The underlying features of Positive Position Feedback are best demonstrated by considering the scalar case. The system consists of two scalar equations, one describing the structure, and one describing the compensator:

$$\text{structure:} \qquad \ddot{\xi} + 2\,\varsigma\,\omega\,\dot{\xi} + \omega^2\,\xi = g\,\omega^2\,\eta, \tag{2.2.1a}$$

$$\text{compensator:} \qquad \ddot{\eta} + 2\,\varsigma_f\,\omega_f\,\dot{\eta} + \omega_f^2\,\eta = \omega_f^2\,\xi, \tag{2.2.1b}$$

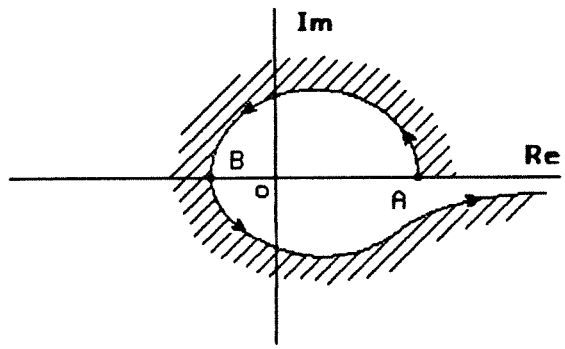

Figure 2.5 Nyquist plot of scalar PPF.
Hatched area is enclosed by curve.

where g is the scalar gain > 0, ξ is the modal coordinate, η is the filter coordinate, ω and ω_f are the structural and filter frequencies, respectively, and ζ and ζ_f are the structural and filter damping ratios, respectively. The compensator is composed of a second-order filter with the same form as the modal equation of (2.2.1a), but with much higher damping ratio. The positive position terminology in the name PPF is derived from the fact that the position coordinate of (2.2.1a) is positively fed to the filter, and the position coordinate of (2.2.1b) is positively fed back to the structure. A Nyquist stability analysis of this system of equations results in the Nyquist curve shown in Figure (2.5). The necessary and sufficient condition for stability is:

$$\text{stability iff:} \qquad 0 < g < 1. \tag{2.2.2}$$

In terms of the figure, stability is ensured as long as the Nyquist curve does not enclose the origin. This implies that point A must lie to the right of the origin and point B to the left. Point B always lies to the left of the origin if point A is to the right and $g > 0$. Thus, the stability condition relates to the

point A, which is the point of the locus corresponding to zero frequency. We will see that a static, i.e., non-dynamic, stability criterion is characteristic of PPF. A more complete picture of the behavior of system (2.2.1) can be gained from a root locus plot that traces the movement of the closed loop eigenvalues (or poles) as a function of gain. Three cases are possible, depending on whether the damped frequency of the filter is greater than, equal to, or less than the damped frequency of the structure. The three types of root locus plot* are illustrated in Figures (2.6a,b,c). The stability boundary is the same in each case, but the movement of the closed loop poles depends on the filter parameters. Thus, the closed loop performance is a function of filter parameters and gain, whereas stability depends on gain only. This allows the filter parameters to be chosen to give maximum performance without affecting the stability margins.

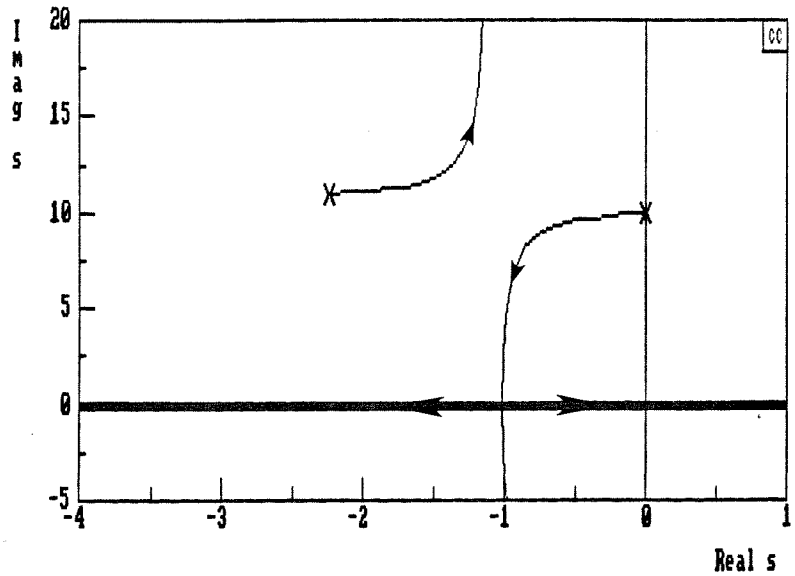

Figure 2.6a Root Locus for scalar PPF.
Case 1: $\omega_f\sqrt{1-\zeta_f^2} > \omega\sqrt{1-\zeta^2}$.

* These plots were generated by the computer program CC, a PC based program written at Caltech by P. M. Thompson.

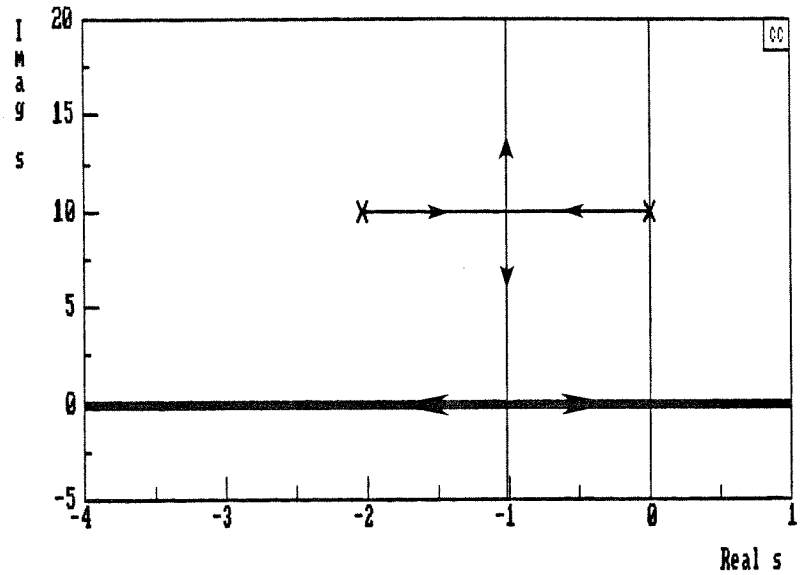

Figure 2.6b Root Locus for scalar PPF.
Case 2: $\omega_f\sqrt{1-\zeta_f^2} = \omega\sqrt{1-\zeta^2}$.

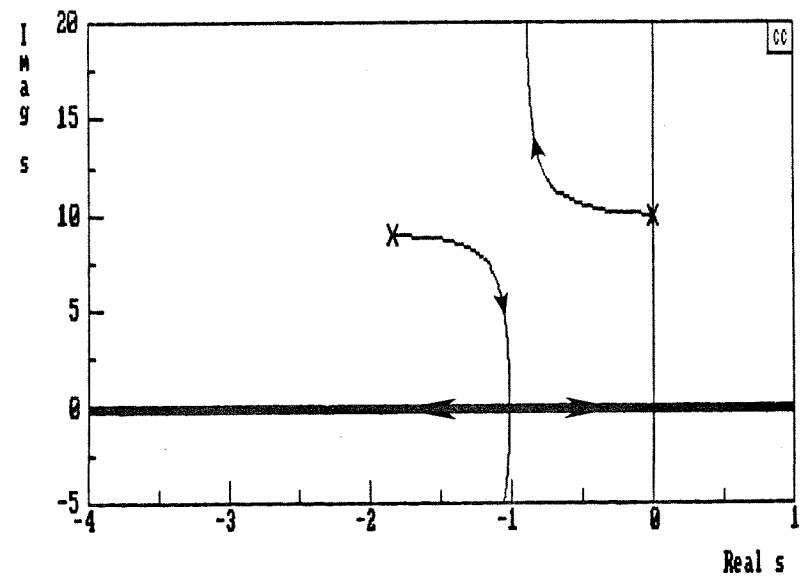

Figure 2.6c Root Locus for scalar PPF.
Case 3: $\omega_f\sqrt{1-\zeta_f^2} < \omega\sqrt{1-\zeta^2}$.

2.2.2 Multivariable Case

The equations describing a structure with more than one mode and a compensator with more than one filter are:

$$M\ddot{\mathbf{y}} + D\dot{\mathbf{y}} + K\mathbf{y} = S^T C\,\mathbf{u}, \tag{2.2.3a}$$

$$\ddot{\mathbf{u}} + B\dot{\mathbf{u}} + \Omega_f\,\mathbf{u} = \Omega_f\,S\,\mathbf{y}, \tag{2.2.3b}$$

where $\mathbf{y}$ is the structure's displacement vector in global coordinates, and $\mathbf{u}$ is the corresponding vector for the compensator filters. The matrix S is the rectangular coupling matrix, which contains ones and zeros depending on whether a sensor/actuator pair is located at the corresponding physical location on the structure. M, D, and K are the structural mass, damping, and stiffness matrices, respectively. B and Ω_f are the compensator damping and frequency matrices, respectively. C is the gain matrix. Equations (2.2.3) require that the sensors and the actuators be both collocated *and* compatible. Compatible sensors and actuators are those that couple into the structural equations by the same matrix S. If the sensors and actuators are not compatible, then two different rectangular matrices would appear in (2.2.3). The stability condition for the above system is:

$$\text{stability iff:} \qquad K - S^T C\,S > 0, \tag{2.2.4}$$

where the notation > 0 means that the matrix is positive definite. The proof of this result is similar to the proof for the modal form of PPF, which appears in Section (4.3). The stability condition of (2.2.4) is simple and elegant, and again, is a non-dynamic condition. The compensator in PPF perturbs the structure's stiffness matrix toward singularity. Since rigid-body modes are normally present

for LSS structural models, the matrix K may be singular to begin with, but that is only a minor complication. If K is singular due to rigid-body modes, condition (2.2.4) can be cast into modal form and the rigid-body modes can be removed by appropriate partitioning. The stability condition for PPF is generally easy to satisfy. Since the sensors and actuators are collocated, the stiffness matrix tends to be perturbed in block fashion, and as long as the local, or "element," stiffness is nonzero, the global stability criterion will be satisfied.

2.2.3 Synthesis for the Multivariable Case

Caughey and Goh [2] suggest a synthesis procedure for the multimode case based on the assumption that the filters can be tuned to individual modes that remain uncoupled to first order. This is true for *sufficiently small* gain. The results of the scalar analysis can then be used to obtain optimum performance on a mode-by-mode basis. If it is desired to give a certain mode a prescribed damping ratio ζ_p, the formulas for the filter frequency and damping ratio that give good robust performance are:

$$\zeta_f = \left[\frac{(1.02\,\zeta_p^2)^2}{(1.02\,\zeta_p^2)^2 + 0.16} \right]^{1/2}, \tag{2.2.5a}$$

$$\omega_f = \frac{\omega}{1.02\sqrt{1-\zeta_f^2}}. \tag{2.2.5b}$$

Figure (2.7a) shows an example where the prescribed damping ratio is 0.05 and the modal frequency is 10 rad/sec. The optimal performance occurs for a gain of 0.0256, and the stability margin occurs at a gain of 1.0. Figures (2.7b,c) show the effect of an additional structural mode. As the transmission zero (indicated by a circle) occurs closer to the pole of the controlled mode,

the closed loop performance deteriorates. The decrease in performance can be large if the pole and zero nearly cancel. We shall see in Chapter 4 that the test structure in the present experiment exhibits this close pole-zero geometry. In addition, the stability boundary is reduced from 1.0 in Figure (2.7a) to 0.09 in Figure (2.7c). In order to keep the modes uncoupled, the filter damping ratios cannot be very large. This implies that the achievable closed loop performance is strictly bounded, and the PPF control becomes a low authority control. Low authority control may provide sufficient performance in some cases but not in all. A method of recovering the closed loop performance is needed.

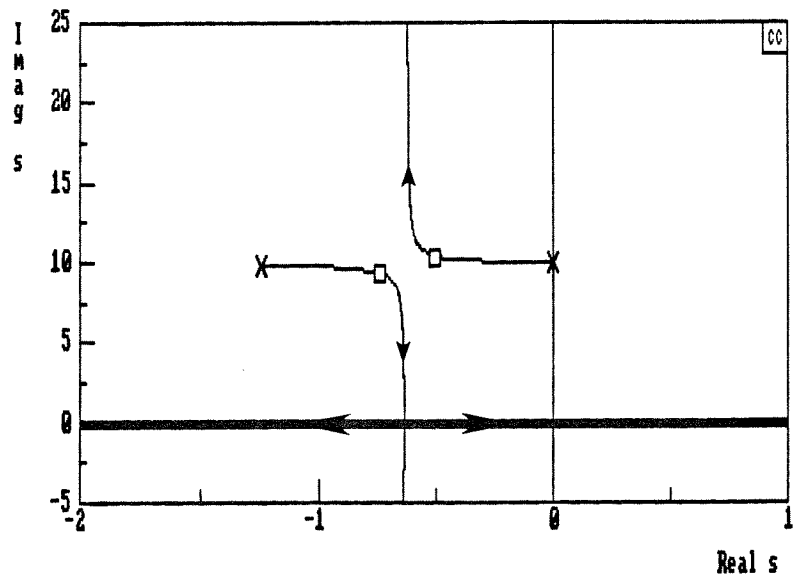

Figure 2.7a Uncoupled PPF synthesis with one mode present. Boxes indicate closed loop pole locations at design gain of 0.0256.

2.2.4 Performance Recovery for Close Pole-Zero Pairs

Closed loop performance in the presence of close pole-zero pairs can be recovered by increasing the frequency of the filter. Figure (2.8a) shows the effect of increasing the filter frequency from 9.88 to 11 rad/sec. The pole locations are

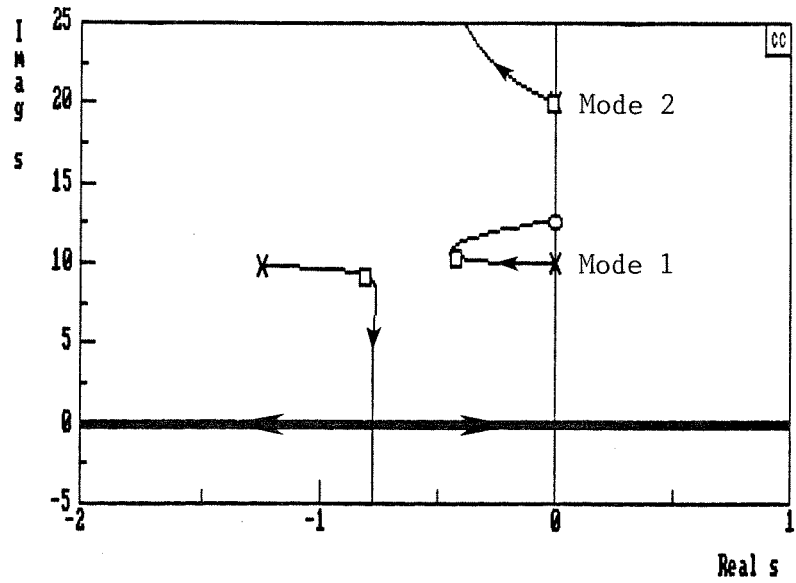

Figure 2.7b Uncoupled PPF synthesis with two modes present. Circle indicates transmission zero location.

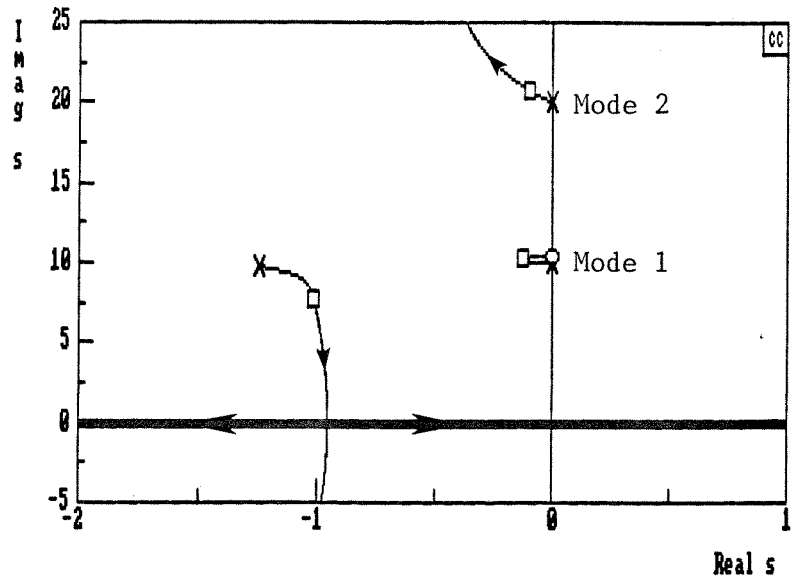

Figure 2.7c Uncoupled PPF synthesis with two modes present where the pole and zero nearly cancel.

brought back nearly to their original positions and at a lower gain. However, the pole locations are sensitive to the structural mode frequency. A small increase in the frequency of the first mode would result in the reduced performance of Figure (2.7c). If the filter frequency is increased further, as shown in Figure (2.8b), the nature of the root locus changes. Instead of the filter's pole moving to the real axis, it now approaches the intervening transmission zero. In this case, the two poles coalesce with the same negative real part and nearly equal frequencies. The pole positions are less sensitive to changes in the structural frequencies but are very sensitive to loop gain. Reduced sensitivity to both parameters is achieved by increasing the filter frequency still further as shown in Figure (2.8c), but the increased robustness comes at a cost of somewhat increased gain. This approach to performance recovery will be implemented in the design of the PPF compensator for the beam experiment described in the next chapter.

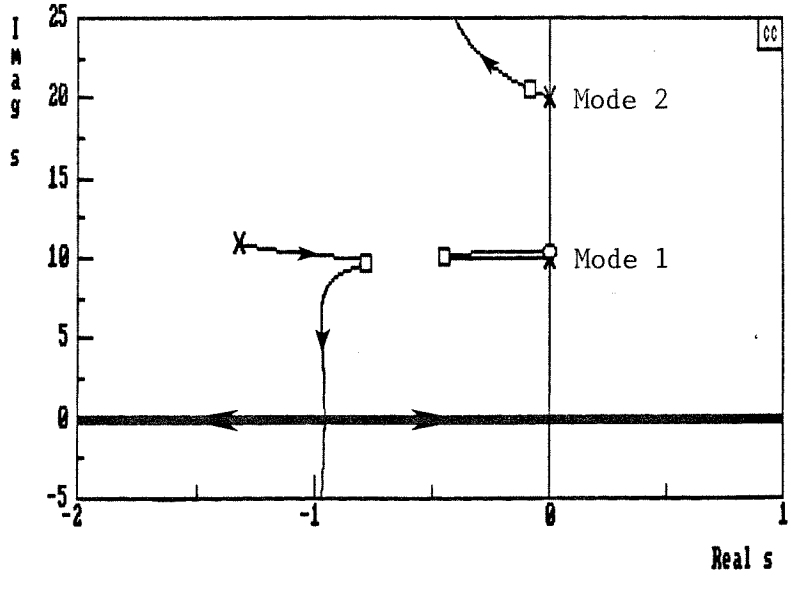

Figure 2.8a Performance Recovery.
$\omega_f = 11$, $\varsigma_f = 0.12$, gain $= 0.013$.

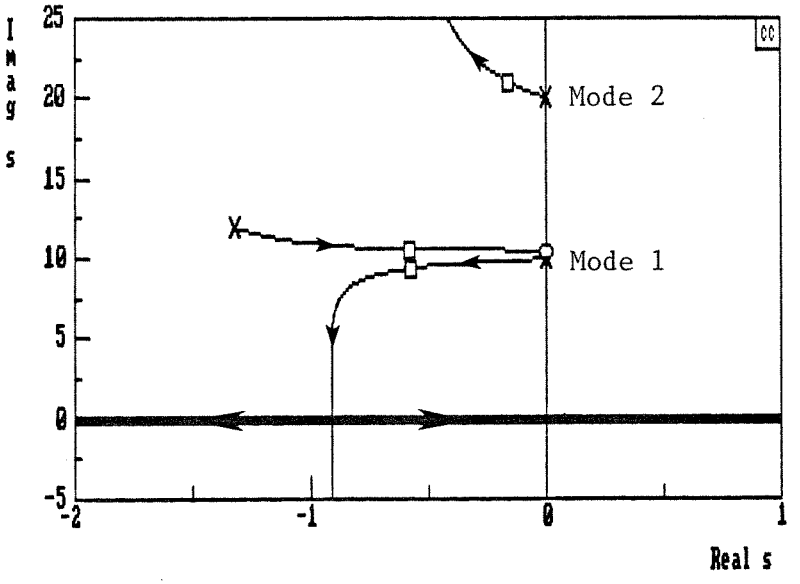

Figure 2.8b Performance Recovery.
$\omega_f = 12$, $\varsigma_f = 0.11$, gain $= 0.022$.

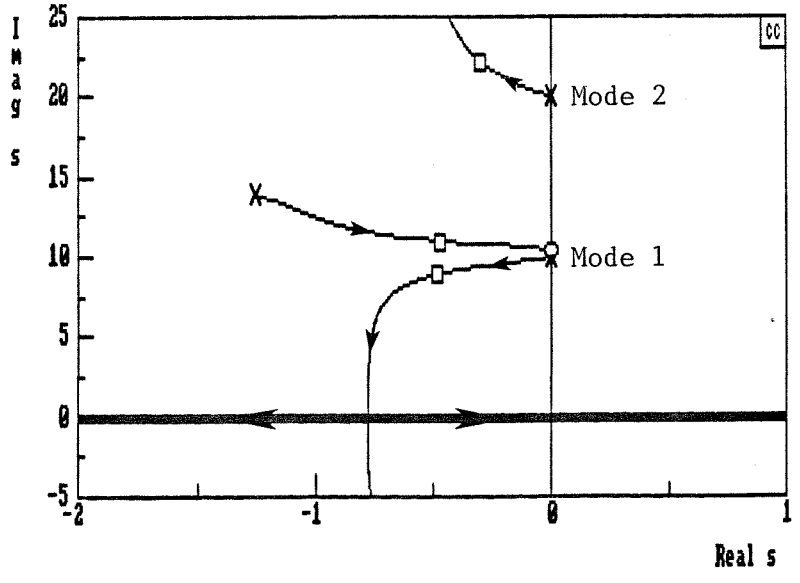

Figure 2.8c Performance Recovery.
$\omega_f = 14$, $\varsigma_f = 0.09$, gain $= 0.036$.

2.2.5 Stable Spillover

Another important feature of Positive Position Feedback is that all the spillover into uncontrolled or unmodelled modes is stabilizing. A proof of this is contained in [2]. Rather than reproduce the proof here, we demonstrate the effect in the following figure. A filter is located in the vicinity of mode number two. It is seen that the spillover into modes one and three causes them to move into the left half-plane, which is stabilizing.

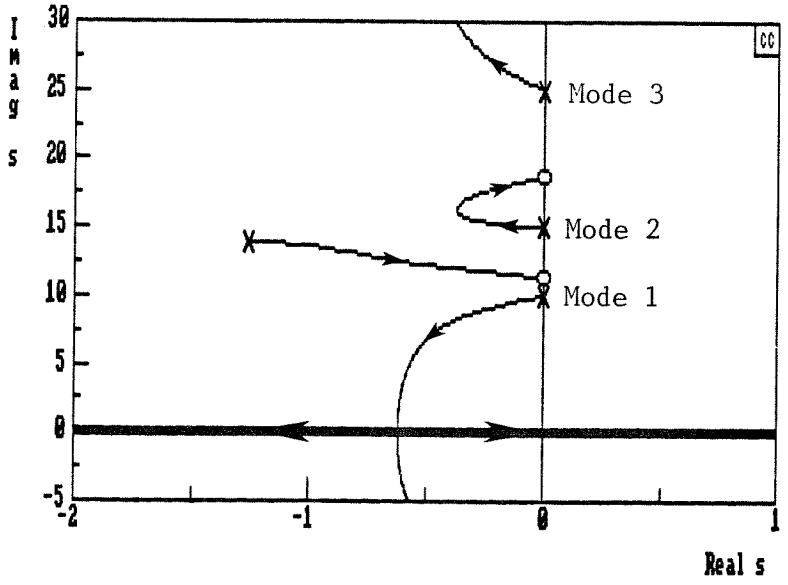

Figure 2.9 Stable spillover into uncontrolled modes.

Chapter 3

DESIGN OF THE EXPERIMENT

The experimental implementation of the approach outlined in Chapter 2 is described in the following sections. The test structure, a thin cantilever beam, exhibits many of the important characteristics of Large Space Structures (LSS). A space-realizable actuation and sensing scheme consisting of piezoelectric ceramic actuators and sensors attached to the test beam is used to simulate active-member longerons on a space-truss beam structure. The test structure, test fixture, and data acquisition/command generation system are described in detail, along with an analog circuit realization for the Positive Position Feedback (PPF) filters that constitute the control system compensator.

3.1 Test Structure

The test structure we have chosen is a uniform thin cantilever beam. The beam was made thin (20 mils) in order to achieve some of the characteristics that make LSS difficult to control. Specifically, the structure has low inherent out-of-plane stiffness due to its small section moment of inertia. It has low mass per unit length compared to lumped-mass type sensors such as accelerometers. The first bending mode frequency was designed to be fairly low at five Hertz. Finally, the structure was designed to have low modal damping. Low modal damping was obtained by eliminating sources of friction and nonlinearity, which can introduce unwanted dissipation. The cantilever boundary condition was chosen because it is simple to implement and introduces relatively little friction. Aerodynamic drag is the largest remaining source of additional dissipation, but its effect is small. Two important aspects of LSS that are not simulated by the cantilever

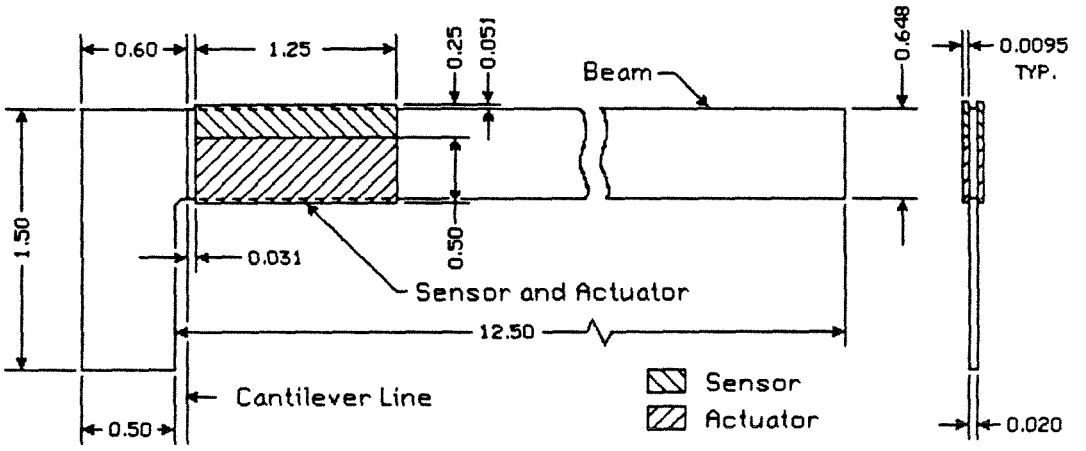

Figure 3.1 Detail of test structure showing location of first sensor/actuator pair. Drawing not to scale. All dimensions in inches.

beam are high modal density, modal coupling, and three dimensionality. These characteristics require a more complicated structure, a frame or a planar truss, for example. The higher modes of a cantilever beam are more closely spaced, and therefore some approximation of dense modes can be reached at the higher frequencies. It was decided that the first feasibility tests of PPF should be made on a structure which is simple, yet representative of LSS.

The test structure is shown schematically in Figure (3.1). The hatched areas are the first sensor/actuator pair near the root of the beam. Two configurations of piezobeam* were used for control experiments. The beam used in the single-input-single-output (SISO) experiment incorporated one sensor/actuator pair at the root, while the beam used in the multi-input-multi-output (MIMO) experiment incorporated two pairs at two different locations. The location of

* We shall refer to the composite structure consisting of the aluminum beam and the piezoelectric ceramic material as the *piezobeam*.

the second pair is discussed in Chapter 5. The mechanics of the sensors and actuators is discussed in detail in Section (3.2).

The test beam is made of 2024 aluminum sheet with a cantilevered length of approximately 12.5 inches and a uniform thickness of 20 mils. The fundamental natural frequency is approximately 5 Hz. The width of the beam was made large enough to restrict the motion to bending in one axis with no low frequency torsional modes. The test structure is therefore a uniform two-dimensional representation of a three-dimensional space-truss beam. The cross section of the beam is very thin; the addition of the piezoelectric ceramic sheet material increases the section bending stiffness by an order of magnitude, which means that the section properties of the *composite* piezobeam are highly discontinuous. A normal modes analysis was therefore performed numerically by means of the STAP and MSC/NASTRAN finite element programs,* both of which gave identical results. The calculated natural frequencies for both the SISO and MIMO piezobeam structures are compared with the measured frequencies in Table (3.1.1). The NASTRAN input file for the SISO piezobeam is given in Appendix A, and plots of the first eight mode shapes are shown in Appendix B.

3.2 Piezoelectric Actuators and Sensors

Piezoelectric material was selected for use as both sensors and actuators for a variety of reasons. One of the major motivations is that sensors and actuators so constructed are not electro-mechanical *devices* in the usual sense because they have no moving parts; the piezoelectric material itself is the electro-mechanical transducer. This is significant, for in the space environment moving

* MSC/NASTRAN is a widely used finite element program marketed by the MacNeal-Schwendler Corporation (MSC). STAP is a PC based finite element program written by R. L. Norton.

Table 3.1.1 NASTRAN and Measured Frequencies (Hz.)

Mode Number	SISO Piezobeam		MIMO Piezobeam	
	Predicted f	Measured f	Predicted f	Measured f
1	5.02	5.03	5.63	5.64
2	31.0	30.6	29.2	29.0
3	85.0	83.1	75.5	74.2
4	162	156	153	148
5	256	245	250	235
6	365	350	359	345
7	496	484	513	499
8	658	653	674	644

parts are avoided whenever possible. Secondly, the piezoelectric actuator is powered electrically and can be operated from zero frequency (static) to very high frequencies. This avoids the problem of finite actuator dynamics which can lead to instability. Thirdly, the piezoelectric sensor requires no power and, when operated as a strain gauge, provides high voltage output and therefore high signal-to-noise ratio measurements. Fourthly, the piezoelectric ceramic material has a Young's modulus nearly equal to aluminum. Thus, if a power failure were to occur, the actuators and sensors would revert to passive structural members with no degradation to the open loop spacecraft structure. Lastly, the material is lightweight and lends itself readily to the concept of a dual structural element/actuator.

Figure (3.2) shows a section of piezoelectric thin sheet viewed edge-on. The upper and lower surfaces are the electrodes. Part (a) of the figure describes the actuator piezoelectric. If an electric field E_f is applied across the piezoelectric in line with the poling direction, as indicated by the arrow, the piezoelectric

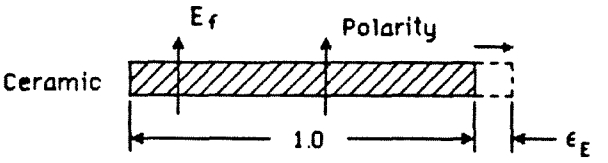

(a.) Actuator piezoelectric.

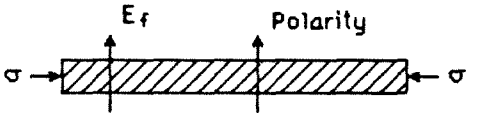

(b.) Sensor piezoelectric.

Figure 3.2 Electro-mechanical action of the actuator and sensor piezoelectrics.

lengthens by an amount ε_E. If the field is opposite to the poling direction, the piezoelectric shrinks. The equation relating the strain to the applied field is [67]:

$$\varepsilon_E = d_{31}\, E_f, \tag{3.2.1}$$

where d_{31} is called the piezoelectric strain constant, or the transverse charge coefficient, and is a material property of the piezoelectric. High d_{31} values are desirable for material that is to be used as an actuator.

Part (b) of Figure (3.2) describes the sensor piezoelectric. If a stress σ is applied to the material, an electric field is generated. The equation relating the applied stress to the resulting electric field is [67]:

$$E_f = -g_{31}\, \sigma, \tag{3.2.2}$$

where g_{31} is called the piezoelectric voltage constant, or transverse voltage coefficient, which is also a material property. High g_{31} values are desirable for

material which is to be used as a sensor. The subscript 31 refers to the particular geometry of the piezoelectrics used. The 3 direction is parallel to the poling direction, while the 1 direction is transverse to the poling direction. Thus, the electric field occurs along axis 3, and the stress or strain along axis 1.

Piezoelectric material is available as a polymer film or a ceramic. Each form has its advantages and disadvantages. We chose to use the ceramics because the d_{31} constant is an order of magnitude higher than that of the polymer. This is important when they are used as actuators. If the polymer is used as an actuator, the applied voltage must be much higher, typically several hundred volts, to compensate for the reduced strain constant. We desired to keep the voltages below 15 volts so that off-the-shelf 741 operational amplifiers could be used in the control circuit. Additionally, the Young's modulus of the polymer is more than an order of magnitude less than for the ceramic, which makes the polymer less well suited to the active-member concept outlined in Chapter 2.

The piezoelectric ceramic material chosen is type G-1195 thin sheet Lead-Zirconate-Titanate (PZT) solid solution, manufactured by Piezo Electric Products Inc., of Metuchen, New Jersey. The nominal thickness of the sheet is 10 mils. The breakdown voltage of G-1195 is approximately 15 volts/mil, which allows 150 volts to be applied to the actuator. Since we are restricting the voltage to less than 15 volts, the ceramics are only being used to one tenth of their rated capacity.

Thin sheet piezoelectric ceramic material was adhered to the surface of the beam as shown in Figure (3.3). The sensor and actuator are made of identical material, the actuator being twice as wide as the sensor. In the figure, the two ceramics labeled "A" serve as the actuator, while the two ceramics labeled "S"

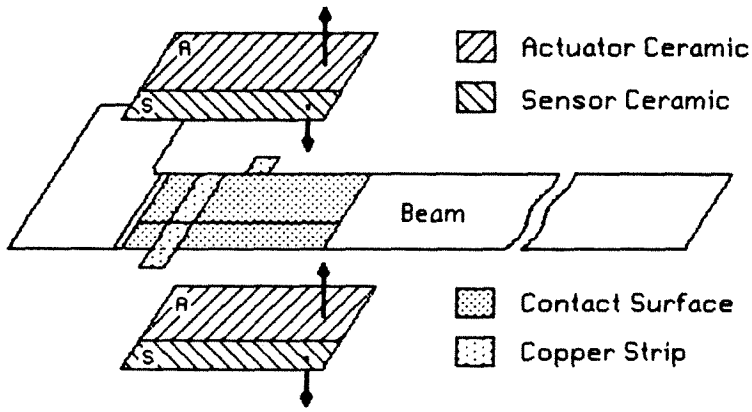

Figure 3.3 Layout of sensor and actuator ceramics. Arrows indicate poling direction.

serve as the sensor. In principle, the function of the two could be reversed. A cyanoacrylate adhesive was used to bond the ceramics to the aluminum beam. The surface in Figure (3.3) marked "contact surface" defines the area where adhesive contact is made. The procedure for bonding the ceramics is given in Appendix C and is derived from standard procedures used for mounting strain gauges. The method produced a bond which was stronger than the ceramic material.

The ceramics are attached symmetrically to both sides of the beam; this maintains the neutral axis of the composite beam at the midsection. The sensor ceramics are adhered adjacent to the actuator ceramics but are electrically isolated from them. In the experiment, the beam serves as the electrical "ground." In order to provide one side of each ceramic sheet with a good electrical contact to ground, two grooves were milled into the beam to a depth of 3 mils. In each groove, making contact between the beam and the back surface of the piezoelectric material, was laid a thin strip of copper sheet. This was done

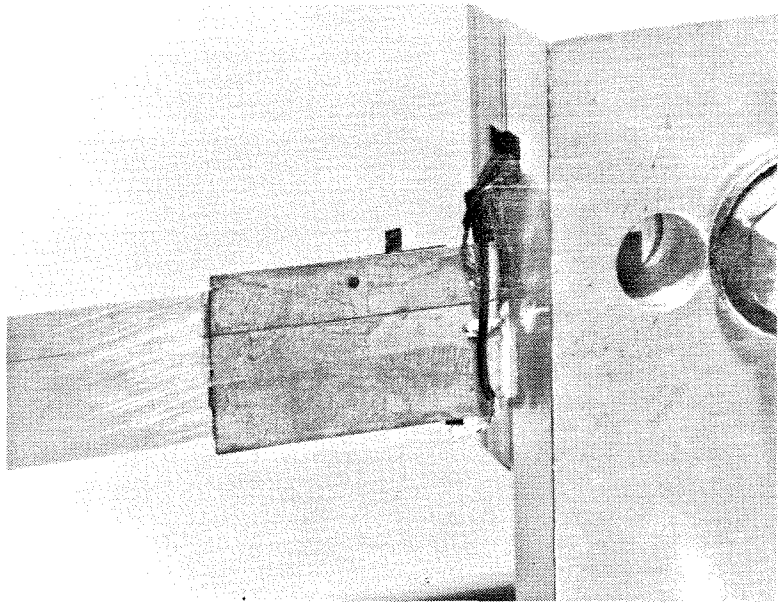

Figure 3.4 Sensor and actuator of the SISO piezobeam.

because the cyanoacrylate adhesive used to adhere the ceramics to the beam is non-conductive. The two surfaces of each ceramic sheet are plated by the manufacturer with a thin layer of nickel that serves as an electrode. Wire leads were soldered directly to the nickel electrodes using MIL-spec. flux and solder provided by the ceramic manufacturer. The sensor and actuator of the SISO piezobeam are shown in Figure (3.4).

Figure (3.3) also indicates the relative poling orientations of each ceramic sheet. Figure (3.5) shows a detail of the poling orientations and electrical boundary conditions of the actuator ceramics. The outer surfaces of the actuator ceramics are driven with the same applied voltage V_a; the inner surfaces, which are adhered to the beam, are maintained at ground. The poling orientations are such that the applied voltage causes one ceramic to expand, while the other contracts. This applies a bending moment to the beam in much the same way that an active longeron applies a bending moment to a space-truss.

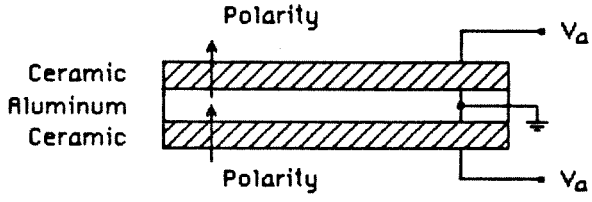

Figure 3.5 Actuator ceramic poling geometry and electrical boundary conditions.

The sensors are arranged in parallel fashion similar to the actuators as shown in Figure (3.3). When the beam bends, the stress applied to the sensor ceramics produces a voltage that is measured directly. For this beam, an output voltage on the order of one volt is typical. The stress applied to the sensor ceramics is related to the bending strain and hence, the sensor actually measures bending strain.

The derivation of the equations describing how the actuators and sensors couple into the beam equation of motion is deferred to Chapter 4.

3.3 Test Fixture

A test fixture was designed to allow the test structure to be excited by base excitation. In order to perform system identification tests and closed loop performance tests on several structural modes, it was necessary that the test fixture be able to excite the structure with a wide variety of disturbances, such as discrete sine sweeps, sine chirps, impulses, etc., over a wide frequency range (3 – 700 Hz).

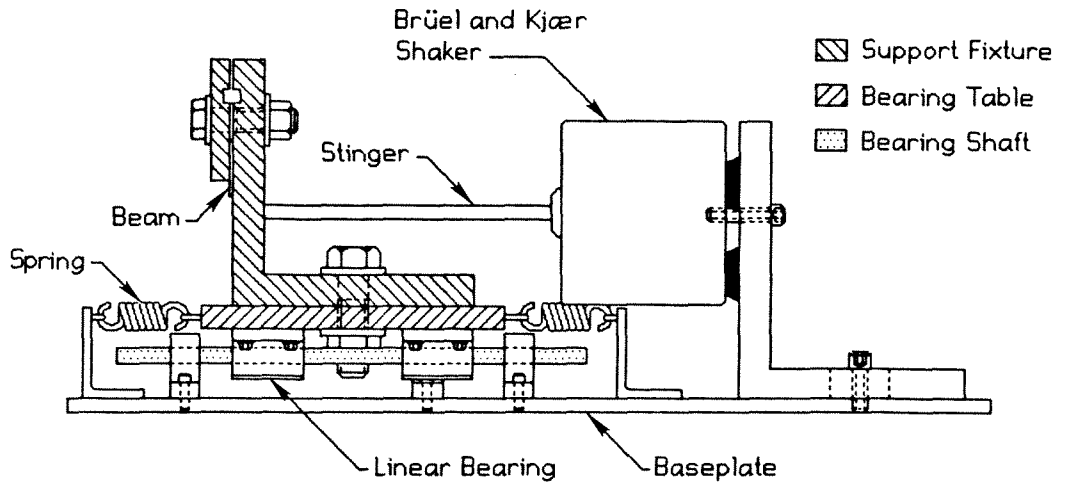

Figure 3.6 Test fixture.
Beam is cantilevered out of page.

The test fixture is shown schematically in Figure (3.6). The fixture consists of five basic parts: 1) a beam support fixture, 2) a linear bearing table, 3) a stinger, 4) a shaker, and 5) a shaker support flange. The beam support fixture consists of two parts that clamp the beam rigidly in a cantilevered configuration. The wiring associated with the sensors and actuators is routed through an access tunnel in the support fixture, which is bolted firmly to the linear bearing table. Detail drawings of the support fixture and the bearing table are given in Appendix D. The bearing table is supported by three Thomson Super Ball Bushing® pillow blocks. Two pillow blocks ride on one shaft and one on the second shaft. This three-point support minimizes binding due to misalignment. The bearing shafts are made of case-hardened ground steel and are supported on shaft support blocks that are mounted to a aluminum baseplate. The bearing table is connected to the shaker by means of a stinger, which is glued to the

bearing table and threaded into the shaker table. The stinger had to be re-designed twice to eliminate bending modes that interfered with the lower modes of the structure. The final design is a 1/2-inch brass tube with aluminum plugs in each end.

The shaker chosen is a 2.25 lb_f Brüel & Kjær type 4810 Mini-Shaker. It is a high quality shaker with a frequency range of DC to 18 kHz. The shaker specifications are given in Appendix D. Voltage signals from the data acqusition/command generation system are passed through a power amplifier, which in turn drives the shaker. The data acqusition system is described in the next section. The shaker is supported by the shaker support flange. The table of the shaker, the part of the shaker connected to the stinger, is supported by highly damped flexures which restrict the table motion to be rectilinear. The stiffness of the flexures combines with the mass of the beam support fixture/bearing table to create a test fixture vibratory mode at approximately 7 Hz. This was fairly close to the 5 Hz fundamental of the test beam, so springs were added to the bearing table to allow the fixture mode to be tuned to 10 Hz.

The baseplate rests on a steel plate, which in turn rests on a rubber cushion that serves to isolate the entire apparatus from building vibrations. Figure (3.7a,b) shows the test fixture and the SISO test beam.

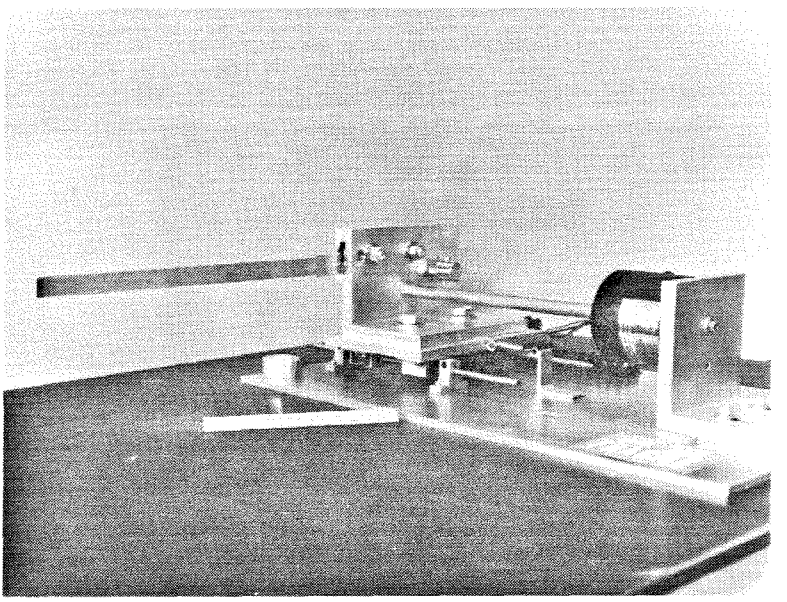

Figure 3.7a Test fixture and SISO piezobeam.
A six-inch rule stands in the foreground.

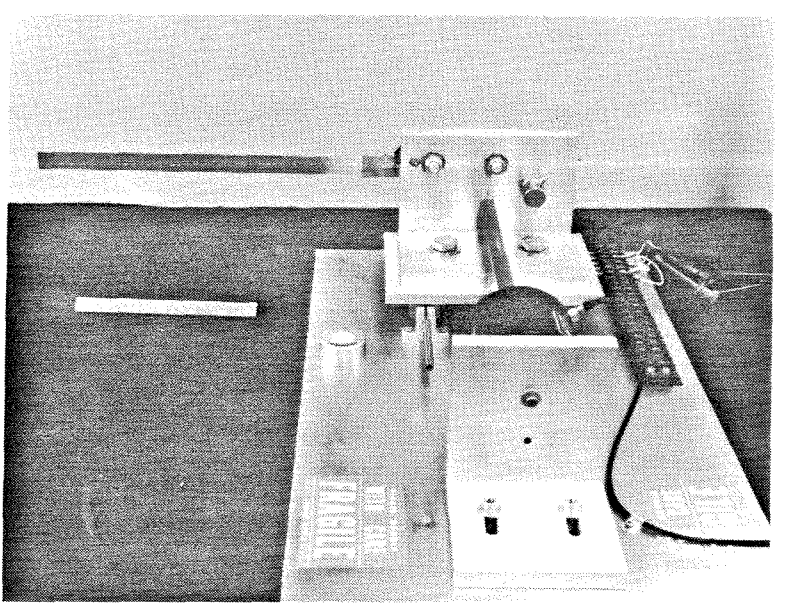

Figure 3.7b Test fixture and SISO piezobeam.

3.4 Data Acqusition/Command Generation System

A data acqusition/command generation system was used to excite the structure and to measure structural response. The analog control circuit was implemented separately. The data acqusition/command generation system used is the Synergistic Technology Incorporated (STI) VAMP system. The STI/VAMP system is designed for sophisticated high-speed multichannel structural dynamics testing. Specifically, the user is able to construct arbitrary time history voltage signals with which to drive the shakers and simultaneously excite the structure while measuring up to 64 channels of response data. The VAMP software can then be used for extensive post-processing. The particular VAMP system used in the current experiment consists of the following hardware:

- Digital Tape Drive,
- AA32 Amplifier/Filter System,
- 85 Mbyte Disk Drive,
- LSI 11/73 CPU,
- Dual Channel Digital to Analog System,
- STI Clocking System,
- 64 Channel 12 bit Analog to Digital System.

Generally, four channels of data were taken and one command channel was generated to drive the Mini-Shaker. Three types of tests were conducted: The first test is a *sine chirp*. In a sine chirp, the shaker is driven by a sinusoidal signal with the frequency of the sine wave swept continuously and rapidly from a lower frequency to a higher frequency. The response is then measured and a transfer function is computed. The second test is the SWIFT test. In a SWIFT test the structure is excited with a sinusoidal excitation at a fixed frequency, and the structure is allowed to reach a steady-state response. The Fourier coefficient of the transfer function corresponding to that frequency is then determined from an

average of the steady-state response. The excitation frequency is incremented and the process is repeated until 512 discrete frequencies are measured. The third type of test is the *free decay*. In a free decay test the structure is excited at a single frequency. After the structure has built up a steady response, the excitation is stopped abruptly and the free decay is measured. In this way the free decay of higher modes can be measured.

Chirp and SWIFT tests produce a transfer function between the output voltage of the sensor and the input voltage to the shaker amplifier. VAMP utilizes a post-processing program called FITTER, which curve-fits the measured complex transfer function and produces estimates of modal frequency and damping ratios. These frequency and damping ratios are used for open loop system identification and for closed loop performance measurements.

The VAMP software is based on the 1024 point Fast Fourier Transform (FFT). This size transform can result in limited frequency resolution baseband FFTs. In order to increase the frequency resolution without increasing the number of points in the FFT, Zoom FFTs are used. The Zoom FFT makes use of a larger time history record to produce a 1024 point FFT of increased resolution over a portion of the baseband frequency spectrum. The Zoom FFT was introduced by Brüel and Kjær, and is discussed in [68].

3.5 Positive Position Filter Realization

The Positive Position Feedback compensator is composed of filters with the following transfer function derived from the Laplace transform of Eq. (2.2.1b):

$$T(s) = \frac{\omega_f^2}{s^2 + 2\,\zeta_f\,\omega_f\,s + \omega_f^2}, \tag{3.5.1}$$

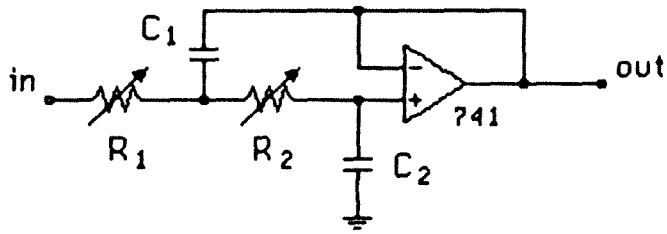

Figure 3.8 Positive Position Feedback filter realization.

where $s = j\omega$ is the Laplace transform variable, ω_f is the filter frequency, and ς_f is the filter damping ratio. It was desired to control the first six modes of the cantilever beam, which meant that the control system had to perform up to a frequency of 400 Hz. An analog control circuit was chosen for both simplicity and speed. A simple circuit realization which has as its transfer function Eq. (3.5.1) is shown in Figure (3.8) [69].

The filter frequency and damping ratio are related to the circuit component values by the following equations:

$$\omega_f = \sqrt{\frac{1}{R_1 R_2 C_1 C_2}}, \tag{3.5.2a}$$

$$\varsigma_f = \tfrac{1}{2}\omega_f (R_1 + R_2) C_2. \tag{3.5.2b}$$

The design procedure used to choose the component values is as follows:

Step 1: Choose resistor values $R_1 = R_2 = 50\text{k}$. This value of resistance is chosen to keep the capacitance values small.

Step 2: Calculate the capacitance C_2 from Eq. (3.5.2b).

Step 3: Calculate the capacitance C_1 from Eq. (3.5.2a).

This gives the nominal component values. Since actual capacitors are only available in discrete sizes, and since their values typically vary by $\pm$ 10%, the next steps fine-tune the design.

Step 4: From the measured capacitance values C_1 and C_2, calculate the resistor values R_1 and R_2 from the following quadratic which is derived from Eq. (3.5.2):

$$R_{1,2} = \frac{\zeta_f}{\omega_f C_2} \pm \sqrt{\left(\frac{\zeta_f}{\omega_f C_2}\right)^2 - \frac{1}{\omega_f^2 C_1 C_2}}. \qquad (3.5.3)$$

If the solution to Eq. (3.5.3) is complex, then one resistor is set to the value of the first term of Eq. (3.5.3). The second resistor value is determined from Eq. (3.5.2a), which results in the correct frequency for the filter. Usually, the resulting damping ratio is very close to the desired value.

Step 5: Test the filter by a VAMP chirp test and compare the FITTER curve-fit frequency and damping measurements with the desired values.

Step 6: Use Eq. (3.5.2) to estimate changes in R_1 and R_2 necessary to obtain the desired values.

In practice, this procedure resulted in filters with frequencies and damping ratios within one percent of the desired values.

Chapter 4

DERIVATION OF GOVERNING EQUATIONS

In this chapter, equations will be derived that describe how the actuators exert forces on the composite piezobeam, and how the elastic motion of the beam is measured by the sensor. The Partial Differential Equation of motion for the beam is derived. It is shown that the actuators couple into the modal equations through the difference in the slopes of the mode shapes at the ends of the actuator, and that the sensors couple through the curvature of the mode shape along the length of the sensor. The global stability properties of Positive Position Feedback in relation to the present experiment are presented in the form of a theorem in Section (4.5). Finally, the quantities that will be used in Chapter 5 as a measure of the performance of the vibration suppression system are discussed.

4.1 Mechanics Analysis of Composite Piezobeam

This section presents the derivation of the equations describing the mechanical behavior of the composite piezobeam. The equation relating the voltage applied to the actuator and the moment induced across the section of the piezobeam is derived, as well as the equation that relates the bending strain in the beam to the voltage produced on the sensor. As described in Chapter 3, the composite piezobeam is an aluminum beam with piezoelectric ceramic actuators and sensors bonded on either side.

4.1.1 Actuators

An electric field applied across a piezoelectric material causes a free strain* in accordance with the poled characteristics of the ceramic. For the type of ceramic used in this experiment, an electric field applied across the thickness of the ceramic induces a longitudinal free strain as shown in Figure (3.2a). The resulting free strain is given by

$$\varepsilon_E = d_{31} E_f = d_{31} \frac{V_a}{t_a}, \tag{4.1.1}$$

where V_a is the applied actuator voltage, and t_a is the thickness of the actuator ceramic. This relation maintains sign, i.e., if the applied electric field reverses sign, the free strain also reverses sign.

In the present configuration, the boundary conditions are not free-free because one surface of the ceramic is adhered to the beam. The stiffness of the beam resists the strain in the piezoelectric ceramic. The mechanics analysis approach to analyzing this configuration is analogous to that applied to a heated shaft held between rigid end constraints. The conceptual steps in the analysis are outlined below:

First, the electric field is applied across the ceramic, which is allowed to strain freely, say, in a positive sense. Second, a load is applied to the ceramic to strain it back to its original length; the ceramic is now under compression. Third, the compressed ceramic is adhered to the beam and the applied load is released. The ceramic will spring back to some fraction of its free strain and, in the process, strain the beam. The ceramic will then be under compression and

* Free strain implies that this strain is realized if the boundary conditions on the ceramic are free-free.

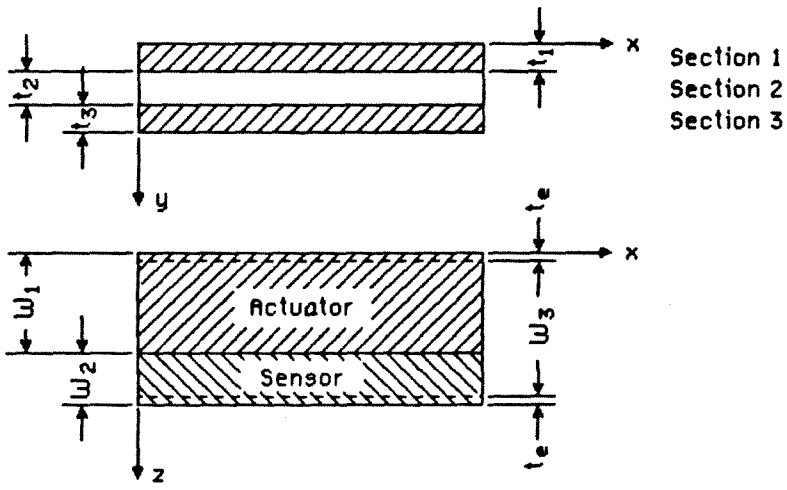

Figure 4.1 Arrangement of ceramics.

the beam under tension. Beam theory assumptions and small strain assumptions will be used throughout the analysis. The beam theory assumptions require that the strain across the section be linear plus a constant. We assume that the axial strain of the ceramics due to the applied voltage is constant. The resulting strain field on the composite structure is used to derive the axial force across the section, the location of the reference axis, and the induced bending moment across the section.

For this investigation, the actual geometry involves two actuator ceramics sandwiching the beam with their polarities arranged such that the same voltage applied to their outer surfaces causes one to strain positively and one to strain negatively — a push-pull arrangement, as shown in Figure (3.5). In addition, there are two narrower sensor ceramics sandwiching the beam, adjacent to the actuator ceramics. The arrangement is shown in Figures (3.3) and (4.1).

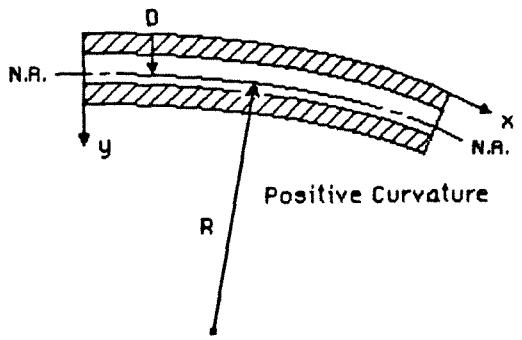

Figure 4.2 Composite deformation.

Deformation of Composite Beam

In general, a voltage applied to an actuator ceramic causes two effects: 1) a uniform axial strain is produced through the section of the beam, and 2) a bending moment is produced. If the bending strain is denoted by $\varepsilon_b(y)$ and the axial strain by ε_a, then, following the four conceptual steps discussed above, the axial strain field through the composite beam can be written as

$$\begin{aligned} \varepsilon_1(y) &= \varepsilon_a - \varepsilon_E + \varepsilon_b(y) && \text{(Section 1)}, \\ \varepsilon_2(y) &= \varepsilon_a + \varepsilon_b(y) && \text{(Section 2)}, \\ \varepsilon_3(y) &= \varepsilon_a + \varepsilon_E + \varepsilon_b(y) && \text{(Section 3)}. \end{aligned} \tag{4.1.2}$$

In accordance with standard beam theory, the bending strain can be written as

$$\varepsilon_b(y) = -\frac{(y - D)}{R}, \tag{4.1.3}$$

where R is the radius of curvature and D is the location of the reference axis, as shown in Figure (4.2).

Axial Force

The axial force F_a is obtained by integrating the stress across the section

$$F_a = \int_A \sigma_x \, dA = \int_A E \, \varepsilon_x \, dA. \tag{4.1.4}$$

The integral can be broken into three parts and written in terms of the strains of Eq. (4.1.2):

$$\begin{aligned} F_a = & \int_{\substack{\text{section}\\\text{one}}} E_1[\varepsilon_a - \varepsilon_E + \varepsilon_b(y)] \, dA + \int_{\substack{\text{section}\\\text{two}}} E_2[\varepsilon_a + \varepsilon_b(y)] \, dA \\ & + \int_{\substack{\text{section}\\\text{three}}} E_3[\varepsilon_a + \varepsilon_E + \varepsilon_b(y)] \, dA. \end{aligned} \tag{4.1.5}$$

The sensor part of the cross section, being passive, will only affect the axial strain, not the applied moment. Since the axial strain will turn out to be zero due to symmetry, the integrals are restricted to the width W_1. Evaluating each term separately we have

Section one:

$$\begin{aligned} \int_{\substack{\text{section}\\\text{one}}} E_1[\varepsilon_a - \varepsilon_E + \varepsilon_b(y)] \, dA &= \int_0^{t_1} \int_0^{W_1} E_1 \left[\varepsilon_a - \varepsilon_E - \frac{(y - D)}{R} \right] dz \, dy \\ &= W_1 \, E_1 \left[\left(\varepsilon_a - \varepsilon_E + \frac{D}{R} \right) t_1 - \frac{t_1^2}{2R} \right]. \end{aligned} \tag{4.1.6}$$

Section two:

$$\begin{aligned} \int_{\substack{\text{section}\\\text{two}}} E_2[\varepsilon_a + \varepsilon_b(y)] \, dA &= \int_{t_1}^{t_1 + t_2} \int_0^{W_1} E_2 \left[\varepsilon_a - \frac{(y - D)}{R} \right] dz \, dy \\ &= W_1 \, E_2 \left[\left(\varepsilon_a + \frac{D}{R} \right) t_2 - \frac{t_2^2}{2R} - \frac{t_1 t_2}{R} \right]. \end{aligned} \tag{4.1.7}$$

Section three:

$$\int_{\substack{\text{section}\\ \text{three}}} E_3[\varepsilon_a + \varepsilon_E + \varepsilon_b(y)]\, dA = \int_{t_1+t_2}^{t_1+t_2+t_3}\int_0^{W_1} E_3 \left[\varepsilon_a + \varepsilon_E - \frac{(y-D)}{R}\right] dz\, dy$$

$$= W_1 E_3 \left[\left(\varepsilon_a + \varepsilon_E + \frac{D}{R}\right) t_3 - \frac{t_3^2}{2R} - \frac{t_1 t_3}{R} - \frac{t_2 t_3}{R}\right]. \tag{4.1.8}$$

The axial force can be grouped into two components — a part due to axial strain, and a part due to pure bending strain, as follows:

$$\begin{aligned} F_a = & \underbrace{\left[W_1 E_1(\varepsilon_a - \varepsilon_E)t_1 + W_1 E_2 \varepsilon_a t_2 + W_1 E_3(\varepsilon_a + \varepsilon_E)t_3\right]}_{\text{due to axial strain}} \\ & + \underbrace{\left[W_1 E_1\left(\frac{Dt_1}{R} - \frac{t_1^2}{2R}\right) + W_1 E_2\left(\frac{Dt_2}{R} - \frac{t_1 t_2}{R} - \frac{t_2^2}{2R}\right)\right.}_{\text{due to bending strain}} \\ & \underbrace{\left. + W_1 E_3\left(\frac{Dt_3}{R} - \frac{t_3^2}{2R} - \frac{t_1 t_3}{R} - \frac{t_2 t_3}{R}\right)\right]}_{\text{due to bending strain}}. \end{aligned} \tag{4.1.9}$$

The reference axis is chosen such that the axial force due to pure bending is zero. Thus,

$$D = \frac{E_1\left(\frac{1}{2}t_1^2\right) + E_2\left(\frac{1}{2}t_2^2 + t_1 t_2\right) + E_3\left(\frac{1}{2}t_3^2 + t_1 t_3 + t_2 t_3\right)}{E_1 t_1 + E_2 t_2 + E_3 t_3}. \tag{4.1.10}$$

If axial inertia is ignored, then the remaining part of F_a must be zero also. This determines the axial strain ε_a as

$$\varepsilon_a = \left(\frac{E_1 t_1 - E_3 t_3}{E_1 t_1 + E_2 t_2 + E_3 t_3}\right) \varepsilon_E. \tag{4.1.11}$$

For the symmetrical geometry of the present arrangement of ceramics we have that: $t_1 = t_3 \equiv t_a$, and $E_1 = E_3 \equiv E_a$. With these substitutions Eqs. (4.1.10) and (4.1.11) reduce to

$$D = t_a + \tfrac{1}{2}t_2, \tag{4.1.12a}$$

$$\varepsilon_a = 0. \tag{4.1.12b}$$

Thus, there is no axial strain, and the neutral axis is unaltered at the midsection.

Induced Bending Moment

The induced bending moment M across the section is obtained by integrating the axial force across the section times its corresponding lever arm, which is the distance from the neutral axis

$$M = \int_A \sigma_x (y - D)\, dA = \int_A E\, \varepsilon_x (y - D)\, dA. \tag{4.1.13}$$

The bending strain $\varepsilon_b(y)$ is a consequence of the induced moment and is therefore not part of the moment integral. Furthermore, the axial strain ε_a is constant and will contribute no moment. Hence, the integral of Eq. (4.1.13) reduces to an integral over two sections given by

$$M = \int_{\substack{\text{section} \\ \text{one}}} E_1(-\varepsilon_E)(y - D)\, dA + \int_{\substack{\text{section} \\ \text{three}}} E_3(\varepsilon_E)(y - D)\, dA. \tag{4.1.14}$$

Evaluating each term separately, we have:

Section one:

$$\int_{\substack{\text{section}\\ \text{one}}} E_1(-\varepsilon_E)(y-D)\,dA = \int_0^{t_1}\int_0^{W_1} E_1(-\varepsilon_E)(y-D)\,dz\,dy$$
$$= -\varepsilon_E W_1 E_1\left(\frac{t_1^2}{2} - D t_1\right). \tag{4.1.15}$$

Section three:

$$\int_{\substack{\text{section}\\ \text{three}}} E_3(\varepsilon_E)(y-D)\,dA = \int_{t_1+t_2}^{t_1+t_2+t_3}\int_0^{W_1} E_3(-\varepsilon_E)(y-D)\,dz\,dy$$
$$= \varepsilon_E W_1 E_3\left(\frac{t_3^2}{2} + t_1 t_3 + t_2 t_3 - D t_3\right). \tag{4.1.16}$$

The induced moment across the section of the beam is then

$$M = \varepsilon_E W_1 \left[E_3\left(\tfrac{1}{2}t_3^2 + t_1 t_3 + t_2 t_3 - D t_3\right) - E_1\left(\tfrac{1}{2}t_1^2 - D t_1\right)\right]. \tag{4.1.17}$$

If we make the substitutions: $t_1 = t_3 \equiv t_a$, $E_1 = E_3 \equiv E_a$, $E_2 \equiv E_b$, $W_1 \equiv W_a$, and $t_2 \equiv t_b$, Eq. (4.1.17) becomes

$$M = W_a E_a \varepsilon_E t_a(t_a + t_b). \tag{4.1.18}$$

Substituting for ε_E from Eq. (4.1.1) gives

$$M = W_a E_a d_{31}(t_a + t_b) V_a. \tag{4.1.19}$$

Equation (4.1.19) indicates that the applied moment is proportional to the piezoelectric transverse charge coefficient d_{31} and the Young's modulus E_a of the

piezoelectric material. Both material properties are larger for the ceramics than for the polymers, making them superior *per volt* as actuators. Substituting the actual values for the variables from Appendix E we have

$$M = 1.02 \times 10^{-3} V_a \frac{\text{in} \cdot \text{lb}_\text{f}}{\text{volt}}. \tag{4.1.20}$$

A STAP finite element model of the SISO piezobeam was given a uniform applied moment over the length of the actuator, and the tip displacement was calculated. A comparison with the actual tip displacement, measured in the laboratory with a photonic sensor, suggests that the actual applied moment per volt is approximately seventy percent of that predicted by Eq. (4.1.19). This is not surprising in view of the simplifications inherent in the analysis, and is consistent with the overestimation assumption of constant strain through the actuator thickness.

4.1.2 Sensors

A stress applied to a piezoelectric material causes an electric field to be produced, as shown in Figure (3.2b), where the relation between stress and electric field is given by

$$E_f = \frac{V_s}{t_s} = -g_{31}\,\sigma, \tag{4.1.21}$$

where V_s is the voltage produced on the sensor and t_s is the thickness of the sensor ceramic. We assume that the sensor responds to the stress at the midplane of its thickness, and that the stress is constant along the length of the ceramic. When the beam is vibrating in a particular mode shape, however, the stress is not constant along the length of the sensor. This causes a complication in that

the sensor voltage produced on the electrode, which is common to the entire length of ceramic, is a function of the non-uniform stress field. This functional relationship is not known, causing the actual coupling of the sensor to higher modes to be somewhat difficult to calculate with sufficient accuracy for control synthesis.

Using the stated assumptions, we find that the stress produced at the sensor due to an applied pure moment, using the Young's Modulus of the aluminum beam, is

$$\sigma_s = -\frac{M(y-D)}{I}\bigg|_{\text{midsection}}, \tag{4.1.22}$$

where I is the moment of inertia of the composite cross section. The moment of inertia of the cross section is determined by means of an equivalent beam of varying width but uniform Young's modulus to be

$$\begin{aligned} I = {} & \tfrac{1}{12} W_b t_b^3 + \tfrac{1}{6} W_a \frac{E_a}{E_b} t_a^3 + \tfrac{1}{6} W_s \frac{E_s}{E_b} t_s^3 \\ & + 2 t_s W_a \frac{E_a}{E_b} \left(\frac{t_b + t_a}{2} \right)^2 + 2 t_s W_s \frac{E_s}{E_b} \left(\frac{t_b + t_s}{2} \right)^2 . \end{aligned} \tag{4.1.23}$$

If the applied moment is produced by the actuator, then, using Eqs. (4.1.20), (4.1.22), and (4.1.23), and substituting the values for width, thickness, and Young's modulus from Appendix E we have

$$\sigma_s = 4.579\, V_a \, \frac{\text{lb}_\text{f}}{\text{in}^2 \cdot \text{volt}}, \tag{4.1.24}$$

where σ_s is the midthickness stress at the sensor. Making use of Eqs. (4.1.21) and (4.1.24), and substituting for the transverse voltage coefficient, we can determine

the theoretical quasi-static ratio of applied actuator voltage to measured sensor voltage to be

$$\frac{V_a}{V_s} = 12. \tag{4.1.25}$$

The test structure was excited by a 5 volt sinusoidal signal on the actuators at 10 Hz, which is between the first and second modes, and the ratio of voltages was measured to be approximately 23. This value, along with the actuator calibration factor of 0.70 determined from the measurement of tip deflection, implies that the sensors produce only seventy-five percent of the voltage predicted. Again, this is not surprising in view of the simplifying assumptions.

4.2 Differential Equation of Motion

Since the composite piezobeam is a relatively simple structure, it can be modeled adequately by a simple Partial Differential Equation (PDE). The use of a PDE affords greater understanding of the physics of the problem than a Finite Element Method (FEM) approach. For this reason, the PDE will be used to model the coupling of the actuators and sensors into the modal equations of motion for the beam. The governing PDE is derived by the use of Hamilton's Principle and is based on the Bernoulli-Euler beam assumptions, which ignore shear deformation and rotary inertia.

A complete description of the problem requires actual values for the eigenfunctions or mode shapes of the composite beam. Since the PDE is not easily solved analytically to provide these functions, a FEM model is used in this part of the analysis.

4.2.1 Governing Partial Differential Equation

The applied moment from the actuators, which is derived in Section (4.1.1), rides along with the beam as it deflects. We call this type of moment a distributed *follower* moment. Figure (4.3) shows the coordinate system for deriving the equation of motion of the beam under a distributed follower moment. For the Hamilton's Principle derivation, all forms of energy must be accounted for:

$$\begin{aligned} \text{Elastic Potential Energy}: \quad & V = \frac{1}{2}\int_0^L E(x)I(x)\left(\frac{\partial^2 y}{\partial x^2}\right)^2 dx, \\ \text{Kinetic Energy}: \quad & T = \frac{1}{2}\int_0^L m(x)\left(\frac{\partial y}{\partial t}\right)^2 dx, \\ \text{Work done by Moment}: \quad & W = \int_0^L M(x)\left(\frac{\partial^2 y}{\partial x^2}\right) dx, \end{aligned} \tag{4.2.1}$$

where $m(x)$ is the mass/unit length of the composite structure. Notice that the work done by the follower moment involves the curvature of the beam, not a rotation.

The Hamiltonian "Action"* is given by

$$I = \int_{t_1}^{t_2} (T - V + W)\, dt. \tag{4.2.2}$$

Hamilton's Principle states that for an admissible motion, the variation of the action is zero

$$\delta I = 0. \tag{4.2.3}$$

* The Hamiltonian Action is an integral over time. In this analysis t_1 and t_2 represent two different times.

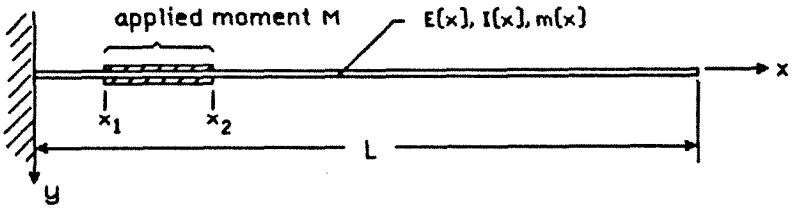

Figure 4.3 Beam with follower distributed moment.

Evaluating Eq. (4.2.3) we have

$$\delta I = \delta \left[\int_{t_1}^{t_2} \left\{ \frac{1}{2} \int_0^L m(x) \left(\frac{\partial y}{\partial t} \right)^2 dx - \frac{1}{2} \int_0^L E(x) I(x) \left(\frac{\partial^2 y}{\partial x^2} \right)^2 dx + \int_0^L M(x) \left(\frac{\partial^2 y}{\partial x^2} \right) dx \right\} dt \right] = 0. \tag{4.2.4}$$

Bringing the variation inside the integrals, and reversing the order of integration of the first term gives

$$\int_0^L \int_{t_1}^{t_2} m(x) \frac{\partial y}{\partial t} \delta \left(\frac{\partial y}{\partial t} \right) dt\, dx - \int_{t_1}^{t_2} \int_0^L E(x) I(x) \frac{\partial^2 y}{\partial x^2} \delta \left(\frac{\partial^2 y}{\partial x^2} \right) dx\, dt + \int_{t_1}^{t_2} \int_0^L M(x)\, \delta \left(\frac{\partial^2 y}{\partial x^2} \right) dx\, dt = 0. \tag{4.2.5}$$

Reversing differentiation and variation gives

$$\int_0^L \int_{t_1}^{t_2} m(x) \frac{\partial y}{\partial t} \frac{\partial}{\partial t} (\delta y)\, dt\, dx - \int_{t_1}^{t_2} \int_0^L E(x) I(x) \frac{\partial^2 y}{\partial x^2} \frac{\partial}{\partial x} \left(\delta \frac{\partial y}{\partial x} \right) dx\, dt + \int_{t_1}^{t_2} \int_0^L M(x) \frac{\partial}{\partial x} \left(\delta \frac{\partial y}{\partial x} \right) dx\, dt = 0. \tag{4.2.6}$$

Integrating by parts

$$\int_0^L \left\{ \underbrace{m(x)\frac{\partial y}{\partial t}\,\delta y\,\Big|_{t_1}^{t_2}}_{=0 \text{ by H.P.}} - \int_{t_1}^{t_2} \frac{\partial}{\partial t}\left(m(x)\frac{\partial y}{\partial t}\right)\delta y\,dt \right\} dx$$

$$- \int_{t_1}^{t_2} \left\{ \underbrace{E(x)I(x)\frac{\partial^2 y}{\partial x^2}\,\delta\left(\frac{\partial y}{\partial x}\right)\Big|_0^L}_{=0 \text{ by B.C.}} - \int_0^L \frac{\partial}{\partial x}\left(E(x)I(x)\,\frac{\partial^2 y}{\partial x^2}\right)\delta\left(\frac{\partial y}{\partial x}\right)dx \right\} dt$$

$$+ \int_{t_1}^{t_2} \left\{ \underbrace{M(x)\,\delta\left(\frac{\partial y}{\partial x}\right)\Big|_0^L}_{=0 \text{ by B.C.}} - \int_0^L \frac{\partial M(x)}{\partial x}\,\delta\left(\frac{\partial y}{\partial x}\right)dx \right\} dt = 0. \qquad (4.2.7)$$

The terms that are indicated by the underbrace notation H.P. are zero due to an axiom of Hamilton's Principle, which states that the variation of the path at the beginning and ending times is zero. The terms that are indicated by the underbrace notation B.C. are zero due to the natural or geometric boundary conditions, which are summarized at the end of this section. Integrating by parts again,

$$- \int_{t_1}^{t_2}\int_0^L m(x)\frac{\partial^2 y}{\partial t^2}\,\delta y\,dx\,dt + \int_{t_1}^{t_2} \underbrace{\frac{\partial}{\partial x}\left(E(x)I(x)\frac{\partial^2 y}{\partial x^2}\right)\delta y\,\Big|_0^L}_{=0 \text{ by B.C.}}\,dt$$

$$- \int_{t_1}^{t_2}\int_0^L \frac{\partial^2}{\partial x^2}\left(E(x)I(x)\frac{\partial^2 y}{\partial x^2}\right)\delta y\,dx\,dt - \int_{t_1}^{t_2} \underbrace{\frac{\partial M(x)}{\partial x}\,\delta y\,\Big|_0^L}_{=0 \text{ by B.C.}}\,dt$$

$$+ \int_{t_1}^{t_2}\int_0^L \frac{\partial^2 M(x)}{\partial x^2}\,\delta y\,dx\,dt = 0. \qquad (4.2.8)$$

Thus,

$$\int_{t_1}^{t_2}\int_0^L \left\{ -m(x)\frac{\partial^2 y}{\partial t^2} - \frac{\partial^2}{\partial x^2}\left(E(x)I(x)\frac{\partial^2 y}{\partial x^2}\right) + \frac{\partial^2 M(x)}{\partial x^2} \right\} \delta y\,dx\,dt = 0. \qquad (4.2.9)$$

Since the variation δy is arbitrary, the factor in braces must be zero. This gives the differential equation of motion as

$$m(x)\frac{\partial^2 y}{\partial t^2} + \frac{\partial^2}{\partial x^2}\left(E(x)I(x)\frac{\partial^2 y}{\partial x^2}\right) = \frac{\partial^2 M(x)}{\partial x^2}. \tag{4.2.10}$$

The following natural, geometric and axiomatic boundary conditions have been used in the analysis:

$$\begin{aligned}
&\text{at } t = t_1: \quad \delta y = 0; \\
&\text{at } t = t_2: \quad \delta y = 0; \\
&\text{at } x = 0: \quad \delta y = 0, \ \delta\left(\frac{\partial y}{\partial x}\right) = 0; \\
&\text{at } x = L: \quad \frac{\partial^2 y}{\partial x^2} = 0, \ \frac{\partial^3 y}{\partial x^3} = 0, \ M(x) = 0, \ \frac{\partial M(x)}{\partial x} = 0.
\end{aligned} \tag{4.2.11}$$

4.2.2 Modal Equations

This section presents the derivation of the modal participation factors for a beam acted upon by a follower distributed moment. As derived in Section (4.1.1), the piezoelectric actuators exert a follower distributed moment on the beam such that the bending moment induced across the beam section is constant everywhere along the length of the actuator, with magnitude given by

$$M = f_a W_a E_a d_{31}(t_a + t_b)V_a, \tag{4.2.12}$$

where f_a is the actuator calibration factor = 0.7, discussed in Section (4.1.1). If, for convention, the edge of the actuator nearest the cantilevered end of the beam is Station 1, and the end nearest the free end is Station 2, then the applied moment can be modeled spatially as

$$M(x) = a_1 V_a\,[\mathrm{h}(x - x_1) - \mathrm{h}(x - x_2)], \tag{4.2.13}$$

where $a_1 = f_a W_a E_a\, d_{31}(t_a + t_b)$, h(•) is the Heaviside step function. Substituting Eq. (4.2.13) into Eq. (4.2.10), we find that the equation of motion of the beam becomes

$$m(x)\frac{\partial^2 y}{\partial t^2} + \frac{\partial^2}{\partial x^2}\left(E(x)I(x)\frac{\partial^2 y}{\partial x^2}\right) = a_1 V_a \frac{\partial}{\partial x}[\delta(x - x_1) - \delta(x - x_2)], \quad (4.2.14)$$

where $\delta(\bullet)$ is the Dirac delta function. We make use of the usual modal expansion of y, namely:

$$y(x,t) = \xi_i(t)\,\phi_i(x). \qquad \text{(sum on } i\text{)} \qquad (4.2.15)$$

Substituting into Eq. (4.2.14) gives

$$m(x)\,\phi_i\,\ddot{\xi}_i(t) + \xi_i(t)\frac{\partial^2}{\partial x^2}\left[E(x)I(x)\frac{\partial^2 \phi_i(x)}{\partial x^2}\right] = a_1 V_a \frac{\partial}{\partial x}[\delta(x - x_1) - \delta(x - x_2)]. \quad (4.7.16)$$

We now multiply by $\phi_j(x)$ and integrate over the domain.

$$\ddot{\xi}_i(t)\underbrace{\int_0^L \phi_j(x) m(x) \phi_i(x)\, dx}_{\delta_{ij}} + \xi_i(t)\underbrace{\int_0^L \phi_j(x)\frac{\partial^2}{\partial x^2}\left[E(x)I(x)\frac{\partial^2 \phi_i(x)}{\partial x^2}\right] dx}_{\delta_{ij}\,\omega_j^2}$$
$$= a_1 V_a \int_0^L \phi_j(x)\frac{\partial}{\partial x}[\delta(x - x_1) - \delta(x - x_2)]\, dx \quad (4.2.17)$$

Integrating the third term by parts we have

$$\ddot{\xi}_i(t)\,\delta_{ij} + \xi_i(t)\,\delta_{ij}\,\omega_j^2 = a_1\, V_a\Big\{\left[\phi_j(x)[\delta(x - x_1) - \delta(x - x_2)]\right]_0^L - \int_0^L \frac{\partial \phi_j(x)}{\partial x}[\delta(x - x_1) - \delta(x - x_2)]\, dx\Big\}. \quad (4.2.18)$$

Since the actuators do not reach to the ends of the beam, the first term on the right-hand side is identically zero. Hence:

$$\ddot{\xi}_j(t) + \xi_j(t)\,\omega_j^2 = a_1\,V_a[\phi_j'(x_2) - \phi_j'(x_1)]. \qquad \text{(no sum)} \qquad (4.2.19)$$

We see that the actuators couple into the modes through the difference in the slopes of the mass-normalized mode shapes at the ends of the actuators. If we define

$$D_j \equiv [\phi_j'(x_2) - \phi_j'(x_1)], \qquad (4.2.20)$$

then the modal equations are simply

$$\ddot{\xi}_j(t) + \xi_j(t)\,\omega_j^2 = a_1\,D_j\,V_a. \qquad \text{(no sum)} \qquad (4.2.21)$$

This type of coupling into the modes is problematical in that it requires accurate knowledge of the D_j, which are *slopes* of the mode shapes at discontinuities in beam section properties.

4.3 Plant Transfer Function

The open loop plant transfer function that relates a voltage at the actuator to a voltage at the sensor is derived in this section. The equation relating bending moment to stress on the sensor was derived in Section (4.1.2) and is given in Eq. (4.1.22). Substituting for the term $(y - D)$ for the present geometry gives

$$\sigma_s = -\tfrac{1}{2}(t_s + t_b)\frac{M}{I}. \qquad (4.3.1)$$

Substituting into Eq. (4.1.21) gives the sensor voltage as

$$V_s = -\tfrac{1}{2} g_{31}\, t_s (t_s + t_b) \frac{M}{I}. \tag{4.3.2}$$

Assuming small strains, we can approximate the sensor voltage as

$$V_s \doteq \underbrace{\tfrac{1}{2} f_s\, g_{31}\, t_s (t_s + t_b) E_b}_{a_2} \frac{\partial^2 y}{\partial x^2}, \tag{4.3.3}$$

where f_s is the sensor calibration factor = 0.75, defined in Section (4.1.2), and the minus sign is incorporated in the sensor poling geometry. Equation (4.3.3) assumes that the curvature is constant along the length of the sensor. In general this is not the case, and the actual voltage will depend in an unknown way on the distribution of curvature along the length. We call this unknown functional $C(\bullet)$. Equation (4.3.3) then becomes

$$V_s = a_2\, C\left(\frac{\partial^2 y}{\partial x^2}\right), \tag{4.3.4}$$

where a_2 is defined in Eq. (4.3.3). Using the modal expansion of Eq. (4.2.15) yields

$$V_s = a_2\, C\left(\frac{\partial^2 (\xi_i(t)\phi_i(x))}{\partial x^2}\right). \tag{4.3.5}$$

Assuming that the functional $C(\bullet)$ is not a function of time, we have

$$V_s = a_2 \xi_i(t)\, C\left(\frac{\partial^2 \phi_i(x)}{\partial x^2}\right) = a_2 \xi_i(t) C_i. \tag{4.3.6}$$

Augmenting Eq. (4.2.21) to include modal damping we have the following pair of equations

$$\ddot{\xi}_j(t) + 2\varsigma_j\omega_j\dot{\xi}_j(t) + \omega_j^2\xi_j(t) = a_1\, D_j\, V_a(t), \quad \text{(no sum)} \tag{4.3.7a}$$

$$V_s(t) = a_2 \sum_i \xi_i(t) C_i. \tag{4.3.7b}$$

Taking the Laplace transform and assuming zero initial conditions gives

$$(s^2 + 2\varsigma_j\omega_j s + \omega_j^2)\hat{\xi}_j(s) = a_1\, D_j\, \hat{V}_a(s), \tag{4.3.8a}$$

$$\hat{V}_s(s) = a_2 \sum_i \hat{\xi}_i(s) C_i. \tag{4.3.8b}$$

The circumflex indicates a transformed quantity. The ratio of $\hat{V}_s(s)$ to $\hat{V}_a(s)$ is the desired transfer function $P(s)$

$$P(s) = \frac{\hat{V}_s(s)}{\hat{V}_a(s)} = \frac{a_1 a_2\, D_1 C_1}{s^2 + 2\varsigma_1\omega_1 s + \omega_1^2} + \frac{a_1 a_2\, D_2 C_2}{s^2 + 2\varsigma_2\omega_2 s + \omega_2^2} + \cdots. \tag{4.3.9}$$

Each term on the right-hand side of Eq. (4.3.9) represents a structural mode. In theory, there are an infinite number of terms in the series, that converges quickly or slowly depending on the type of modal coupling. In practice, the frequency range of interest is bounded, and all the modes above that range act as real scalar constants. Thus, the modeling approach taken is to keep the modal transfer functions up to the highest mode of interest, and lump the higher modes into an additive real scalar constant A. The resulting transfer function, keeping n modes $P_n(s)$, is given by:

$$P_n(s) = \frac{a_1 a_2 D_1 C_1}{s^2 + 2\zeta_1\omega_1 s + \omega_1^2} + \frac{a_1 a_2 D_2 C_2}{s^2 + 2\zeta_2\omega_2 s + \omega_2^2} + \cdots \qquad (4.3.10a)$$
$$+ \frac{a_1 a_2 D_n C_n}{s^2 + 2\zeta_n\omega_n s + \omega_n^2} + A,$$

$$A = \sum_{i=n+1}^{\infty} \frac{a_1 a_2 D_i C_i}{\omega_i^2}. \qquad (4.3.10b)$$

The series in Eq. (4.3.9) converges very slowly in the present case because the modal coupling is *curvature* coupling, and curvature increases rapidly with mass-normalized mode shape. This has two implications: First, many modes need to be retained in a state-space model in order to maintain good accuracy. Second, because curvature increases with mode shape, the transmission zeros occur very close to the structural poles. The effect is shown in Figure (4.4). As more modes are included in the series of Eq. (4.3.9), the zeros occur closer to the poles. This near pole-zero cancellation motivates the Positive Position Feedback performance recovery approach discussed in Section (2.2.4).

The curvatures of the mode shapes were calculated by first solving for the mode shape displacements using a refined mesh on the NASTRAN finite element model. The mode shape displacements were then curve-fit with a cubic spline,* which gave the curvatures at the grid points directly. The functional $C(\bullet)$ was assumed to be a uniform average of the grid point curvatures. Table (4.3.1) compares the calculated values of $a_1 a_2 C_j D_j$ with the values derived from transfer function measurements for the first five modes of the MIMO piezobeam. The details of how the coefficients are calculated from transfer function measurements are given in Chapter 5. As can be seen from the table, the calculated values do

* The program used for computing the curvatures from the spline fit is listed in Appendix F.

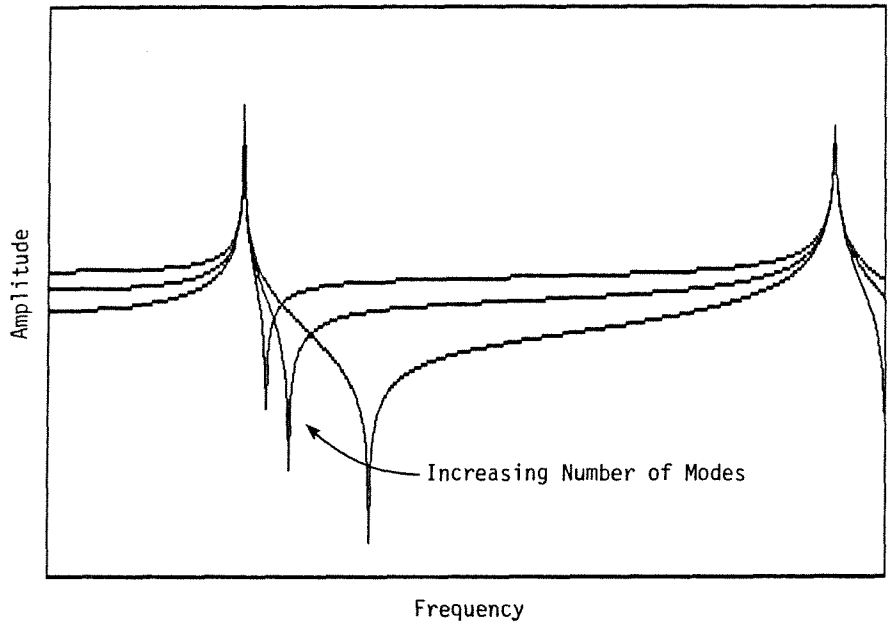

Figure 4.4 Transfer function as more modes are retained.

not match the measured values for all modes. In particular, the higher modes do not show good agreement. There are at least two reasons for this: First, the aluminum beam is so thin that the addition of the ceramics increases the bending stiffness EI by an order of magnitude. Thus, the section properties of the composite beam are strongly discontinuous at the endpoints of the ceramics, exactly where accurate slopes of the mode shapes are required for the calculation of the D_j. Secondly, because EI is discontinuous, the curvature of the piezobeam varies greatly over the length of the ceramics. The functional dependence of the sensor voltage on a non-uniform curvature field is not well understood. These shortcomings are due to the particular way the actuators and sensors couple into the structure. In particular, the sensors do not experience a uniform strain as they would in an active member of a space-truss. For this reason, *measured* coupling coefficients are incorporated in the structural plant models used for compensator synthesis.

Table 4.3.1 Calculated and Measured Coupling Coefficients $a_1 a_2 C_j D_j$ for MIMO Piezobeam

Mode	Sensor/Actuator 1			Sensor/Actuator 2		
Number	Calculated	Measured	Δ%	Calculated	Measured	Δ%
1	6.24	7.83	−20.3	3.53	4.49	−21.4
2	206	214	− 3.7	0.197	NM	—
3	1,080	1,130	− 4.4	439	650	−32.5
4	3,620	2,650	+36.6	3,010	2,763	+ 8.9
5	10,070	5,160	+95.2	2,530	1,350	+87.6

NM Not Measurable

An important result of this analysis is that the actuators couple into the modal equations through the difference of the slopes of the mode shapes at the ends of the actuator ceramic, while the sensors couple into the modal equations through an unknown function of the bending strain, which is related to the curvature of the mode shapes along the length of the sensor ceramic. Thus, the sensors and actuators are not strictly compatible. In addition, the coupling coefficients for the actuators and sensors are inherently difficult to calculate accurately, especially for the higher modes.

Incompatibility of the sensors and actuators in the present case means that the D_j and C_j are not proportional to each other. However, they are roughly proportional for the lower modes. For collocated sensors and actuators which form an active-element of a space-truss, the coupling coefficients are proportional because the strain in the element is uniform and uniaxial. For the present experiment, we use measured coupling coefficients and cast the structural equations in modal form. The next section derives the coupled system equations for PPF control.

4.4 Derivation of System Equations

The following example will help define the coupled system equations for *local control* Positive Position Feedback, which is the form implemented in this work. In this example, two filters are used to control two modes using two actuator/sensor pairs located at different locations on the structure. Local control assumes that the sensor signal at a given location drives PPF filters which generate a control voltage applied to the collocated actuator only. In this example, one filter is associated with each actuator/sensor pair. Under these conditions, we have the following four equations

$$\ddot{\xi}_1 + 2\,\varsigma_1\,\omega_1\dot{\xi}_1 + \omega_1^2\xi_1 = a_1 C_{11}\,g_1\,\eta_1 + a_1 C_{12}\,g_2\,\eta_2, \tag{4.4.1a}$$

$$\ddot{\xi}_2 + 2\,\varsigma_2\,\omega_2\dot{\xi}_2 + \omega_2^2\xi_2 = a_1 C_{11}\,g_1\,\eta_1 + a_1 C_{12}\,g_2\,\eta_2, \tag{4.4.1b}$$

$$\ddot{\eta}_1 + 2\,\varsigma_{f1}\,\omega_{f1}\dot{\eta}_1 + \omega_{f1}^2\eta_1 = a_2\,\omega_{f1}^2\,C_{11}\,\xi_1 + a_2\,\omega_{f1}^2\,C_{21}\,\xi_2, \tag{4.4.1c}$$

$$\ddot{\eta}_2 + 2\,\varsigma_{f2}\,\omega_{f2}\dot{\eta}_2 + \omega_{f2}^2\eta_2 = a_2\,\omega_{f2}^2\,C_{12}\,\xi_1 + a_2\,\omega_{f2}^2\,C_{22}\,\xi_2. \tag{4.4.1d}$$

The ξ_i and η_i are the mode and filter coordinates, respectively. The scalar gain of the i^{th} filter is g_i. The above system assumes that the actuators and sensors couple into the modal equations through coefficients that are proportional. In this case the C_{ij} appear on the right hand side of both the modal and filter equations. The first subscript refers to the mode number, and the second subscript refers to the actuator/sensor pair that the C_{ij} corresponds to. Defining the modal and filter vectors

$$\boldsymbol{\xi} = \begin{Bmatrix} \xi_1 \\ \xi_2 \end{Bmatrix}; \qquad \boldsymbol{\eta} = \begin{Bmatrix} \eta_1 \\ \eta_2 \end{Bmatrix}, \tag{4.4.2}$$

and the following matrices

$$\Omega = \begin{bmatrix} \omega_1^2 & 0 \\ 0 & \omega_2^2 \end{bmatrix}; \qquad \Omega_f = \begin{bmatrix} \omega_{f1}^2 & 0 \\ 0 & \omega_{f2}^2 \end{bmatrix},$$
$$D = \begin{bmatrix} 2\zeta_1\omega_1 & 0 \\ 0 & 2\zeta_2\omega_2 \end{bmatrix}; \qquad D_f = \begin{bmatrix} 2\zeta_{f1}\omega_{f1} & 0 \\ 0 & 2\zeta_{f2}\omega_{f2} \end{bmatrix}, \tag{4.4.3}$$
$$C = \begin{bmatrix} C_{11} & C_{21} \\ C_{12} & C_{22} \end{bmatrix}; \qquad G = \begin{bmatrix} g_1 & 0 \\ 0 & g_2 \end{bmatrix},$$

we have the following system of equations:

$$\begin{aligned} \ddot{\boldsymbol{\xi}} + D\,\dot{\boldsymbol{\xi}} + \Omega\,\boldsymbol{\xi} &= a_1\,C^T G\,\boldsymbol{\eta}, \\ \ddot{\boldsymbol{\eta}} + D_f\,\dot{\boldsymbol{\eta}} + \Omega_f\,\boldsymbol{\eta} &= a_2\,\Omega_f\,C\,\boldsymbol{\xi}. \end{aligned} \tag{4.4.4}$$

The structure of Eq. (4.4.4) is the same no matter how many modes, filters, or actuator/sensor pairs are included. This work implements Positive Position Feedback using internal force producing actuators and strain sensors; therefore, Eq. (4.4.4) is complete without including the rigid-body modes. The stability of this system of equations will be examined in the next section.

4.5 Positive Position Stability Theorem

Consider the following system of equations which models the general MIMO Positive Position Feedback case

$$\begin{aligned} \ddot{\boldsymbol{\xi}} + D\,\dot{\boldsymbol{\xi}} + \Omega\,\boldsymbol{\xi} &= a_1\,C^T G\,\boldsymbol{\eta}, \\ \ddot{\boldsymbol{\eta}} + D_f\,\dot{\boldsymbol{\eta}} + \Omega_f\,\boldsymbol{\eta} &= a_2\,\Omega_f\,C\,\boldsymbol{\xi}, \end{aligned} \tag{4.5.1}$$

where the vectors and matrices are defined as follows:

$\boldsymbol{\xi} \equiv$ modal state vector of length N_m,

$\boldsymbol{\eta} \equiv$ filter state vector of length N_f,

$$G \equiv \text{gain matrix – diag. } N_f = \begin{bmatrix} g_1 & & & \mathbf{0} \\ & g_2 & & \\ & & \ddots & \\ \mathbf{0} & & & g_{N_f} \end{bmatrix} > 0,$$

$$C \equiv \text{participation matrix – } N_f \times N_m = \begin{bmatrix} \cdots & \cdots & \cdots \\ \cdots & \text{Full} & \cdots \\ \cdots & \cdots & \cdots \end{bmatrix},$$

$$\Omega \equiv \text{modal frequency matrix – diag. } N_m = \begin{bmatrix} \omega_1^2 & & & \mathbf{0} \\ & \omega_2^2 & & \\ & & \ddots & \\ \mathbf{0} & & & \omega_{N_m}^2 \end{bmatrix} > 0,$$

$$\Omega_f \equiv \text{filter frequency matrix – diag. } N_f = \begin{bmatrix} \omega_{f1}^2 & & & \mathbf{0} \\ & \omega_{f2}^2 & & \\ & & \ddots & \\ \mathbf{0} & & & \omega_{fN_f}^2 \end{bmatrix} > 0,$$

$$D \equiv \text{modal damping matrix – diag. } N_m = \begin{bmatrix} 2\varsigma_1\omega_1^2 & & & \mathbf{0} \\ & 2\varsigma_2\omega_2^2 & & \\ & & \ddots & \\ \mathbf{0} & & & 2\varsigma_{N_m}\omega_{N_m}^2 \end{bmatrix} > 0,$$

$$D_f \equiv \text{filter damping matrix – diag. } N_f = \begin{bmatrix} 2\varsigma_{f1}\omega_{f1}^2 & & & \mathbf{0} \\ & 2\varsigma_{f2}\omega_{f2}^2 & & \\ & & \ddots & \\ \mathbf{0} & & & 2\varsigma_{fN_f}\omega_{fN_f}^2 \end{bmatrix} > 0.$$

Theorem 4.5.1: *System (4.5.1) is Lyapunov Asymptotically Stable iff:*

$$\Omega - a_1 a_2\, C^T G\, C > 0, \text{ i.e., positive definite.}$$

Proof:

The Lyapunov Direct Method will be used to prove sufficiency, and the definition of positive definiteness of a matrix in terms of its principal minors will be used to prove necessity. The necessity proof can also be argued in reverse as an alternate proof of sufficiency.

In order that the equations may be symmetrized, it is useful to make the following substitution:

$$\boldsymbol{\psi} \equiv \sqrt{\frac{a_1}{a_2}}\, \Omega_f^{-1/2}\, G^{1/2}\, \boldsymbol{\eta}, \quad \text{or} \quad \boldsymbol{\eta} = \sqrt{\frac{a_2}{a_1}}\, G^{-1/2}\, \Omega_f^{1/2}\, \boldsymbol{\psi}. \tag{4.5.2}$$

Upon substituting Eq. (4.5.2), and premultiplying the second equation by $\sqrt{a_1/a_2}\, \Omega_f^{-T/2} G^{T/2}$, we have the following pair of equations

$$\begin{aligned} \ddot{\boldsymbol{\xi}} + D\dot{\boldsymbol{\xi}} + \Omega\boldsymbol{\xi} &= \sqrt{a_1 a_2}\, C^T G^{1/2} \Omega_f^{1/2}\, \boldsymbol{\psi}, \\ \ddot{\boldsymbol{\psi}} + D_f\, \dot{\boldsymbol{\psi}} + \Omega_f\, \boldsymbol{\psi} &= \sqrt{a_1 a_2}\, \Omega_f^{1/2} G^{1/2} C\, \boldsymbol{\xi}. \end{aligned} \tag{4.5.3}$$

If we define $E^{1/2} \equiv \sqrt{a_1 a_2}\, G^{1/2} C$, we have the system equation in matrix form as

$$\begin{bmatrix} \ddot{\boldsymbol{\xi}} \\ \ddot{\boldsymbol{\psi}} \end{bmatrix} + \underbrace{\begin{bmatrix} D & \mathbf{0} \\ \mathbf{0} & D_f \end{bmatrix}}_{L} \begin{bmatrix} \dot{\boldsymbol{\xi}} \\ \dot{\boldsymbol{\psi}} \end{bmatrix} + \underbrace{\begin{bmatrix} \Omega & -E^{T/2}\, \Omega_f^{T/2} \\ -\Omega_f^{1/2}\, E^{1/2} & \Omega_f \end{bmatrix}}_{N} \begin{bmatrix} \boldsymbol{\xi} \\ \boldsymbol{\psi} \end{bmatrix} = \mathbf{0}. \tag{4.5.4}$$

Sufficiency

Define the Lyapunov Function V as

$$V = \tfrac{1}{2} \begin{bmatrix} \dot{\boldsymbol{\xi}}^T & \dot{\boldsymbol{\psi}}^T \end{bmatrix} \begin{bmatrix} \dot{\boldsymbol{\xi}} \\ \dot{\boldsymbol{\psi}} \end{bmatrix} + \tfrac{1}{2} \begin{bmatrix} \boldsymbol{\xi}^T & \boldsymbol{\psi}^T \end{bmatrix} \begin{bmatrix} \Omega & -E^{T/2}\, \Omega_f^{T/2} \\ -\Omega_f^{1/2}\, E^{1/2} & \Omega_f \end{bmatrix} \begin{bmatrix} \boldsymbol{\xi} \\ \boldsymbol{\psi} \end{bmatrix}. \tag{4.5.5}$$

Then

$$V = \tfrac{1}{2}\left[\dot{\boldsymbol{\xi}}^T\dot{\boldsymbol{\xi}} + \dot{\boldsymbol{\psi}}^T\dot{\boldsymbol{\psi}}\right] + \tfrac{1}{2}\boldsymbol{\xi}^T\Omega\,\boldsymbol{\xi} + \tfrac{1}{2}\boldsymbol{\psi}^T\Omega_f\,\boldsymbol{\psi} - \boldsymbol{\xi}^T E^{T/2}\Omega_f^{T/2}\,\boldsymbol{\psi}. \tag{4.5.6}$$

Taking the absolute value of the last term

$$V \geq \tfrac{1}{2}\left[\dot{\boldsymbol{\xi}}^T\dot{\boldsymbol{\xi}} + \dot{\boldsymbol{\psi}}^T\dot{\boldsymbol{\psi}}\right] + \tfrac{1}{2}\boldsymbol{\xi}^T\Omega\,\boldsymbol{\xi} + \tfrac{1}{2}\boldsymbol{\psi}^T\Omega_f\,\boldsymbol{\psi} - |\,\boldsymbol{\xi}^T E^{T/2}\Omega_f^{T/2}\,\boldsymbol{\psi}\,|\,. \tag{4.5.7}$$

Making use of the Cauchy-Schwartz inequality on the last term gives

$$V \geq \tfrac{1}{2}\left[\dot{\boldsymbol{\xi}}^T\dot{\boldsymbol{\xi}} + \dot{\boldsymbol{\psi}}^T\dot{\boldsymbol{\psi}}\right] + \tfrac{1}{2}\boldsymbol{\xi}^T\Omega\,\boldsymbol{\xi} + \tfrac{1}{2}\boldsymbol{\psi}^T\Omega_f\,\boldsymbol{\psi} - \tfrac{1}{2}\boldsymbol{\xi}^T\underbrace{E^{T/2}E^{1/2}}_{E}\,\boldsymbol{\xi} - \tfrac{1}{2}\boldsymbol{\psi}^T\,\Omega_f\,\boldsymbol{\psi}; \tag{4.5.8}$$

$$V \geq \tfrac{1}{2}\dot{\boldsymbol{\xi}}^T\dot{\boldsymbol{\xi}} + \tfrac{1}{2}\dot{\boldsymbol{\psi}}^T\dot{\boldsymbol{\psi}} + \tfrac{1}{2}\boldsymbol{\xi}^T(\Omega - E)\boldsymbol{\xi}. \tag{4.5.9}$$

Thus, if $(\Omega - E)$ is positive definite, then $V > 0$ for all nontrivial $\boldsymbol{\xi}, \boldsymbol{\psi}, \dot{\boldsymbol{\xi}}, \dot{\boldsymbol{\psi}}$. Taking the time derivative of the Lyapunov function V, we have

$$\dot{V} = \begin{bmatrix}\dot{\boldsymbol{\xi}}^T & \dot{\boldsymbol{\psi}}^T\end{bmatrix}\begin{bmatrix}\ddot{\boldsymbol{\xi}} \\ \ddot{\boldsymbol{\psi}}\end{bmatrix} + \begin{bmatrix}\boldsymbol{\xi}^T & \boldsymbol{\psi}^T\end{bmatrix}\begin{bmatrix}\Omega & -E^{T/2}\,\Omega_f^{T/2} \\ -\Omega_f^{1/2}\,E^{1/2} & \Omega_f\end{bmatrix}\begin{bmatrix}\dot{\boldsymbol{\xi}} \\ \dot{\boldsymbol{\psi}}\end{bmatrix}. \tag{4.5.10}$$

Substituting Eq. (4.5.4) we have that

$$\dot{V} = -\dot{\boldsymbol{\xi}}^T D\dot{\boldsymbol{\xi}} - \dot{\boldsymbol{\psi}}^T D_f\dot{\boldsymbol{\psi}} \leq 0. \tag{4.5.11}$$

The function V can be zero only on a set of measure zero in time; hence $\dot{V}$ is actually negative definite

$$\dot{V} < 0. \tag{4.5.12}$$

Therefore, if $\Omega - E > 0$, then system (4.5.1) is LAS by the well-known Lyapunov Theorem. The sufficient condition for stability is:

$$\Omega - a_1 a_2 C^T G C > 0. \tag{4.5.13}$$

Necessity

It is a known result that for $L > 0$, Eq. (4.5.4) is LAS iff $N > 0$ [2]. A matrix is positive definite iff all of its principal minors are positive [70]. It is useful to rewrite matrix N in the partitioned form

$$N = \left[\begin{array}{c|c} \Omega & B \\ \hline B^T & \Omega_f \end{array}\right]. \tag{4.5.14}$$

For system (4.5.1) to be stable, it is necessary that all the principal minors of N be positive. If we start at the lower right element of N, then the first N_f principal minors are the principal minors of Ω_f, which are positive since Ω_f is positive definite. If we wish to evaluate an arbitrary minor of N of order $> N_f$, we partition the matrix further as shown below:

$$N = \left[\begin{array}{c|c|c} \Omega_{11} & \mathbf{0} & B_1 \\ \hline \mathbf{0} & \Omega_{22} & B_2 \\ \hline B_1^T & B_2^T & \Omega_f \end{array}\right], \tag{4.5.15}$$

where Ω_{22} is dimension $0 \leq k \leq N_m$. The $N_f + k^{th}$ principal minor P_k of N is then

$$P_k = \begin{vmatrix} \Omega_{22} & B_2 \\ B_2^T & \Omega_f \end{vmatrix} = |\Omega_f| \left|\Omega_{22} - B_2 \Omega_f^{-1} B_2^T\right|. \tag{4.5.16}$$

Since Ω_f is positive definite, the necessary condition for the minor P_k to be positive is

$$\left|\Omega_{22} - B_2\Omega_f^{-1}B_2^T\right| > 0. \tag{4.5.17}$$

Next, we show that the determinant in (4.5.17) is the k^{th} principal minor of $\Omega - B\Omega_f^{-1}B^T$. Using the same partitions defined in (4.5.15) we have:

$$\Omega - B\Omega_f^{-1}B^T = \left[\begin{array}{c|c} \Omega_{11} & \mathbf{0} \\ \hline \mathbf{0} & \Omega_{22} \end{array}\right] - \left[\begin{array}{c} B_1 \\ \hline B_2 \end{array}\right] \Omega_f^{-1} \left[B_1^T \mid B_2^T\right], \tag{4.5.18}$$

$$= \left[\begin{array}{c|c} \Omega_{11} - B_1\Omega_f^{-1}B_1^T & -B_1\Omega_f^{-1}B_2^T \\ \hline -B_2\Omega_f^{-1}B_1^T & \Omega_{22} - B_2\Omega_f^{-1}B_2^T \end{array}\right]. \tag{4.5.19}$$

It can be seen that the k^{th} principal minor of (4.5.19) is given in (4.5.17). Since it is necessary that all the minors P_k $(0 \leq k \leq N_m)$ be positive, it is necessary that $\Omega - B\Omega_f^{-1}B^T > 0$. Recasting the necessary condition in terms of the original matrices of (4.5.10) we have that $\Omega - E > 0$, or

$$\Omega - a_1 a_2\, C^T G C > 0, \tag{4.5.20}$$

and the proof is complete.

4.6 Structural Dynamic Response

This section identifies the quantities that will be used in Chapter 5 as measures of closed loop performance of the vibration suppression system. Many significant aspects of structural dynamic response of LSS pertaining to vibration suppression can be understood from a study of the single degree-of-freedom

(SDOF) damped linear oscillator. The forced SDOF damped linear oscillator is given by

$$m\ddot{x}(t) + c\dot{x}(t) + kx(t) = F(t), \tag{4.6.1}$$

where m is mass, c is a damping coefficient, k is stiffness, and $F(t)$ is an arbitrary excitation force. If we make the usual substitutions

$$\omega_n^2 \equiv \frac{k}{m} \quad \text{and} \quad \varsigma \equiv \frac{c}{2\sqrt{km}}, \tag{4.6.2}$$

we obtain the equation in canonical form given by

$$\ddot{x}(t) + 2\varsigma\omega_n\dot{x}(t) + \omega_n^2 x(t) = \frac{1}{m}F(t) = \frac{\omega_n^2}{k}F(t). \tag{4.6.3}$$

The damping ratio ς is the damping coefficient divided by the critical damping coefficient, and ω_n is the natural frequency of the oscillator. For a distributed parameter system such as an LSS, the equation describing each modal coordinate would take the form of Eq. (4.6.3), the only modification being that the right-hand side coefficient would be a modal participation factor. It should be noted, however, that the physical displacements are then also functions of the mode shapes.

The two types of dynamic response of interest in this analysis are the steady-state response under sinusoidal excitation and the free response.

Forced Response

The SDOF damped linear oscillator under steady sinusoidal excitation is given by

$$\ddot{x}(t) + 2\varsigma\omega_n\dot{x}(t) + \omega_n^2 x(t) = \frac{\omega_n^2}{k}P\cos\omega t. \tag{4.6.4}$$

If $\varsigma < 0.707$, the response reaches a maximum amplitude of

$$|x(t)|_{\max} = \frac{P/k}{2\varsigma\sqrt{1-\varsigma^2}} \qquad \text{at} \quad \omega = \omega_n\sqrt{1-2\varsigma^2}. \tag{4.6.5}$$

For ς small (< 0.20) the maximum amplitude can be approximated by

$$|x(t)|_{\max} \approx \frac{P}{2\varsigma k} = \frac{P}{2m\varsigma\omega_n^2}. \tag{4.6.6}$$

If the amplitude of excitation is given and the mass is fixed, then the quantity of interest in reducing the steady-state response amplitude is ςk, or equivalently $\varsigma\omega_n^2$. If $\varsigma\omega_n^2$ is increased, the maximum response amplitude will be reduced proportionately.

Free Response

The free response of the SDOF damped linear oscillator is given by the solution to the homogeneous equation

$$\ddot{x}(t) + 2\varsigma\omega_n\dot{x}(t) + \omega_n^2 x(t) = 0, \tag{4.6.7}$$

which can be written explicitly as

$$x(t) \;=\; e^{-\varsigma\omega_n t}(A\cos\omega_d t \;+\; B\sin\omega_d t), \tag{4.6.8}$$

where $\omega_d \equiv \omega_n\sqrt{1-\varsigma^2}$, and A and B depend on the initial conditions. The free response is an oscillation at the damped natural frequency enveloped by an exponential decay. The settling time is the time the oscillation takes to damp out to a specified percentage of its initial steady-state value. In four e-folding time constants the response has decayed to two percent of its initial value. The

quantity of interest, then, is $\varsigma\omega_n$. If $\varsigma\omega_n$ is increased, the settling time will be decreased proportionately.

There are other measures of dynamic response: peak overshoot, rise time, delay time, etc., but these are of lesser significance in vibration suppression and will not be analyzed here. The interested reader is referred to Saucedo and Schiring [71]. It is interesting to note that the peak overshoot, which is the amount by which the response of an underdamped oscillator, under unit step excitation, exceeds the steady-state value,* can be shown to be a function of damping ratio ς:

$$\text{peak overshoot} = \exp\left(-\frac{\varsigma\pi}{\sqrt{(1-\varsigma^2)}}\right). \tag{4.6.9}$$

For small ς, the quantity of interest in reducing overshoot is $e^{-\varsigma\pi}$. The damping ratio ς must exceed about 0.20 before significant reductions in overshoot are achieved. As mentioned before, the actual motions at any point of a structure are functions of the mode shapes. This is particularly important for step response. Additionally, the steady-state value is a function of the static stiffness of the structure.

In summary, the quantities related to response amplitude and settling time are $\varsigma\omega_n^2$ and $\varsigma\omega_n$, respectively. These are different criteria. If we wish to minimize both response amplitude and settling time, two different quantities must be maximized simultaneously.

---

* The response is normalized such that the steady-state value = 1.

Chapter 5

SISO EXPERIMENTS AND RESULTS

This chapter and the following describe the control experiments performed, and their results. The single-input-single-output (SISO) experiments are described in the present chapter. The SISO experiments make use of one actuator/sensor pair located at the root of the beam as shown in Figure (3.1). This location was chosen because most of the bending strain of the lower vibratory modes of a cantilever beam occurs at the root.

It was found that the piezoelectric sensors develop stray voltages if they are not electrically shunted to ground. It is shown that shunting the sensor creates a high-pass filter which must be taken into consideration in the control system design. Ultimately, the first three modes of the beam were controlled by means of one actuator and one sensor, with dramatic reduction in dynamic response.

5.1 Plant Characterization

The block diagram of the control system* is shown in Figure (5.1). Each block represents the frequency domain transfer function between the outputs and inputs of the corresponding component of the system. The block labeled $B(s)$ represents the piezobeam structure. The response of the beam, indicated by the vector of modal coordinates $\boldsymbol{\xi}$, produces a voltage V_s on the sensor depending on the C_i of Eq. (4.3.6), which form the matrix C. The sensor voltage is then input to the control compensator $K(s)$, which consists of PPF filters with transfer functions given by Eq. (3.5.1). The output of the filters, multiplied by the gain matrix G, forms the control voltage V_a. The control voltage is applied to the

* See Sections (3.2) and (3.3) for a more detailed description of the experiment hardware.

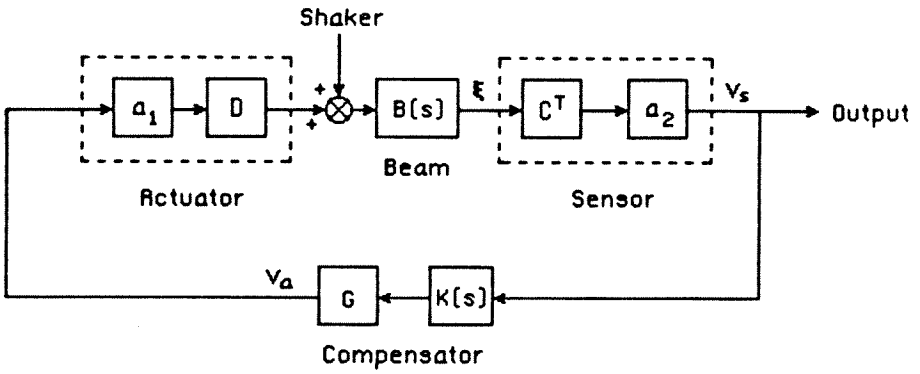

Figure 5.1 Block diagram of control system.

actuators, which in turn produce modal control forces depending on the D_j of Eq. (4.2.20) that form the matrix D. The constants a_1 and a_2 are defined in Eqs. (4.2.13) and (4.3.3). Since the sensors and actuators are part of the composite structure, we use the term *plant* to refer to the cascaded actuator-beam-sensor blocks. The transfer function from the actuator voltage to the sensor voltage is given by Eq. (4.3.9). The shaker excites the beam by base excitation, which couples into the modal equations in a different manner than the actuators.

5.1.1 Plant Transfer Function Measurements

The transfer function of the plant was measured by injecting a signal at the actuator and measuring the response at the sensor while the loop was broken, as shown in Figure (5.2). The SWIFT program was used in order to obtain very high signal-to-noise ratio measurements, and the results are shown in Figures (5.3a–d). An error in the VAMP software was uncovered during these identification tests. The result of the software error was to send random numbers through the Digital-to-Analog-Conversion system during portions of the sine

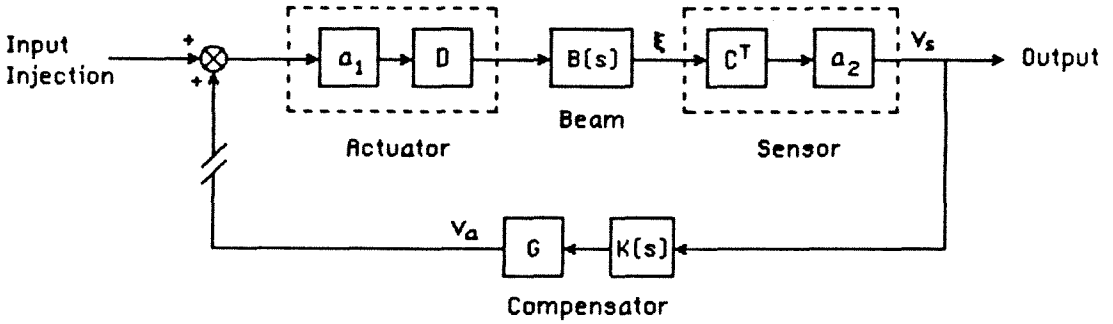

Figure 5.2 Plant transfer function measurement technique.

sweep. The problem was most serious at higher frequencies and caused some noise in the plots of the transfer function near Modes 4 and 5 in Figure (5.3d). The results, however, showed good accuracy for the first three modes, which were the object of the SISO control experiments. The software error was eventually corrected, enabling testing at the higher modes for the MIMO experiment described in Chapter 6.

Figures (5.3a–d) present the raw transfer function data as four pairs of plots showing the amplitude and phase vs. frequency in Hz. The amplitude is the ratio of the sensor voltage to the actuator voltage, and the phase measures how far the sensor voltage lags behind the actuator voltage. The phase starts at zero, passes through 90 degrees at resonance, and proceeds to nearly 180 degrees, at which point the response of the mode drops off and is cancelled by the quasi-static response of all the higher modes. This is the region near the transmission zero, after which the phase quickly returns to zero. This behavior is typical of structural plants; there is always a phase lag between 0 and 180 degrees. No phase leads are ever encountered. Notice how close the zeros are

to the poles, especially for the lower modes. The *very* close poles and zeros are unusual and are due to the curvature coupling explained in Section (4.3).

5.1.2 Modal Residual Calculation

In order to accurately predict closed loop pole locations for a plant with close pole-zero pairs, the plant transfer function model must correctly predict the plant zero locations. An error in the zero locations strongly affects the root locus as shown in Figure (2.7b,c). Correct zero locations require that the numerators of the modal transfer function terms of Eq. (4.3.10a), the so-called residuals, must be accurate. These residuals involve the D_j and C_j, which are difficult to calculate accurately due to the nature of the modal coupling. The values of the numerators can, however, be inferred from the transfer function measurements. The approach is outlined below.

In the vicinity of a particular mode, the transfer function is dominated by the dynamics of that mode and the quasi-static response of all the higher modes. Thus, the plant transfer function $J_i(s)$ in the vicinity of the i^{th} mode can be described by

$$J_i(s) = \frac{a}{s^2 + 2\,\zeta_i\,\omega_i s + \omega_i^2} + b, \tag{5.1.1}$$

where s is the Laplace transform variable; ω_i and ζ_i are the frequency and damping ratio of the i^{th} mode, respectively; a is the residual of the i^{th} mode; and b is the real scalar constant representing the quasi-static response of the higher modes as defined in Eq. (4.3.10b). For sinusoidal signals, the frequency function is given by

$$J_i(j\omega) = \left[\frac{a}{(\omega_i^2 - \omega^2)} + b\right] - j\left[\frac{2a\zeta_i\omega_i\omega}{(\omega_i^2 - \omega^2)^2}\right], \tag{5.1.2}$$

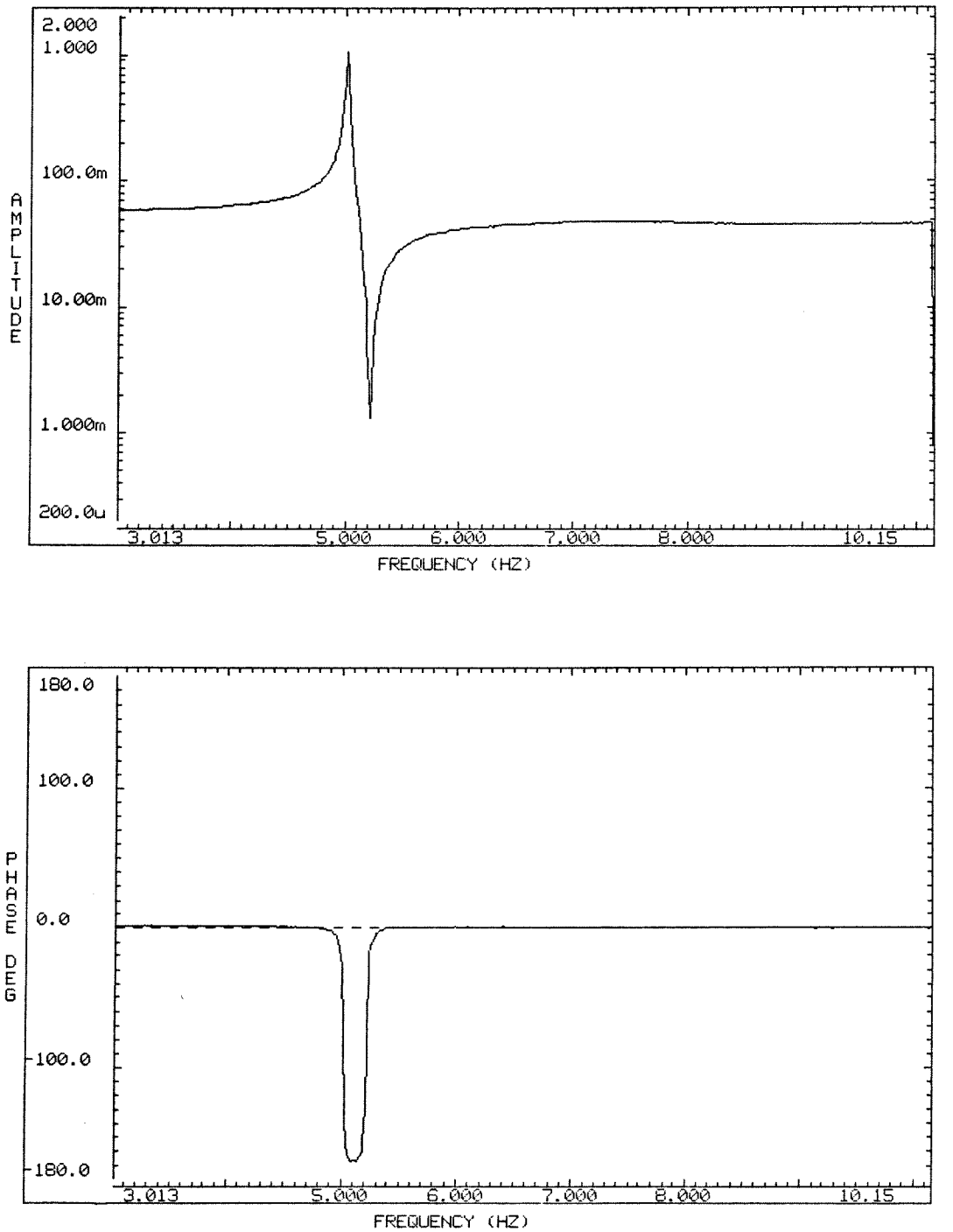

Figure 5.3a Plant frequency function. Mode 1. The "m" and "u" represent $\times 10^{-3}$ and $\times 10^{-6}$, respectively.

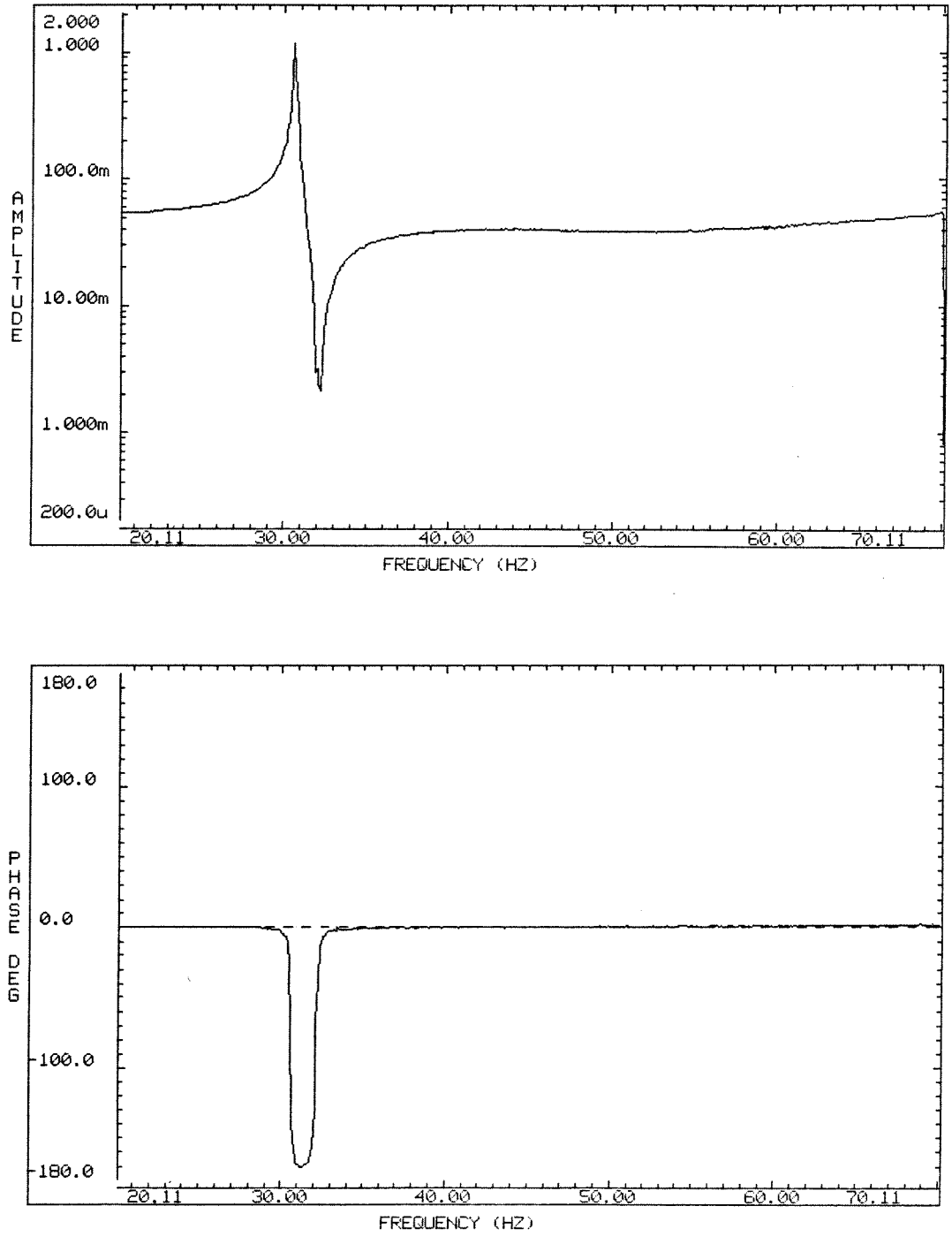

Figure 5.3b Plant frequency function. Mode 2.

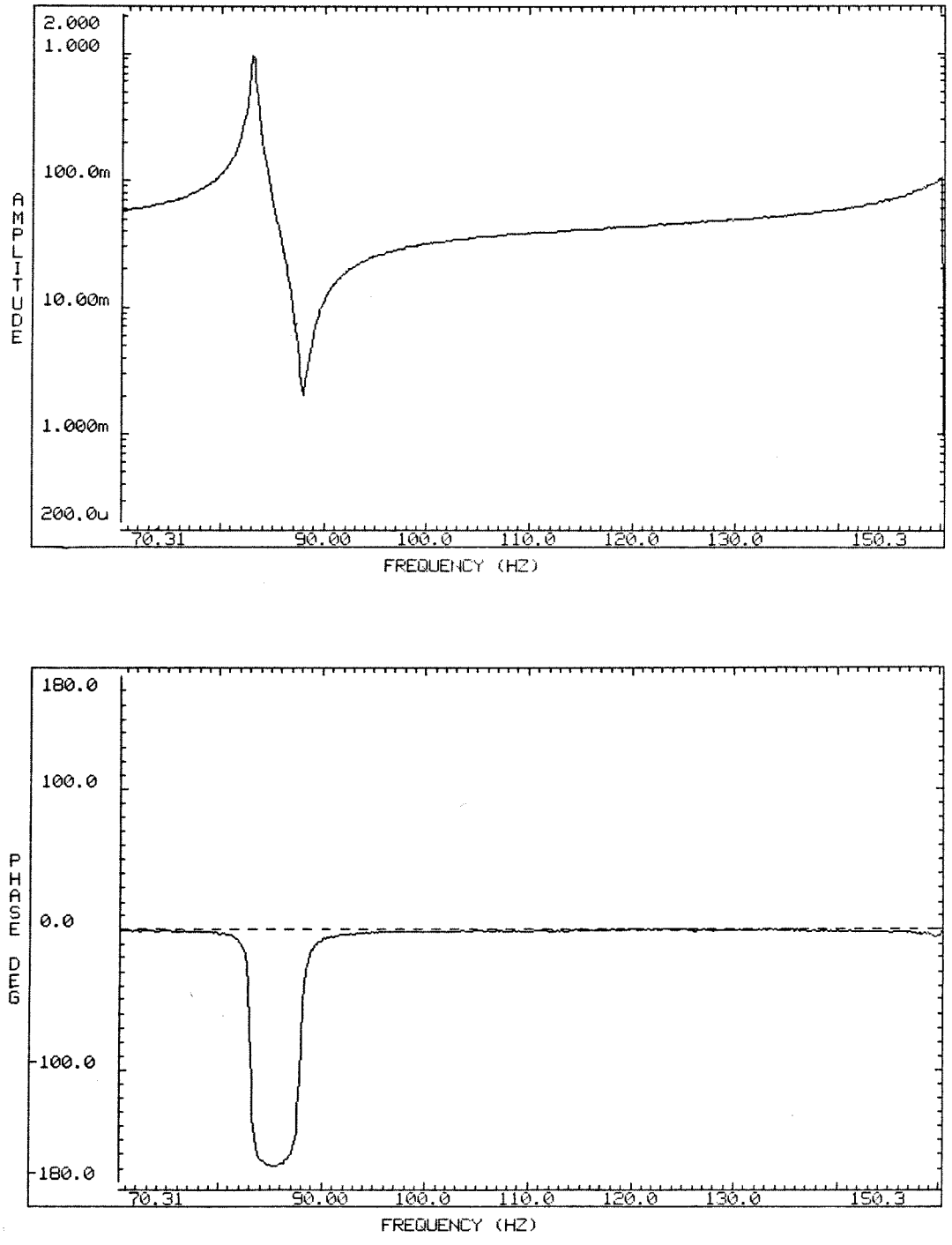

Figure 5.3c Plant frequency function. Mode 3.

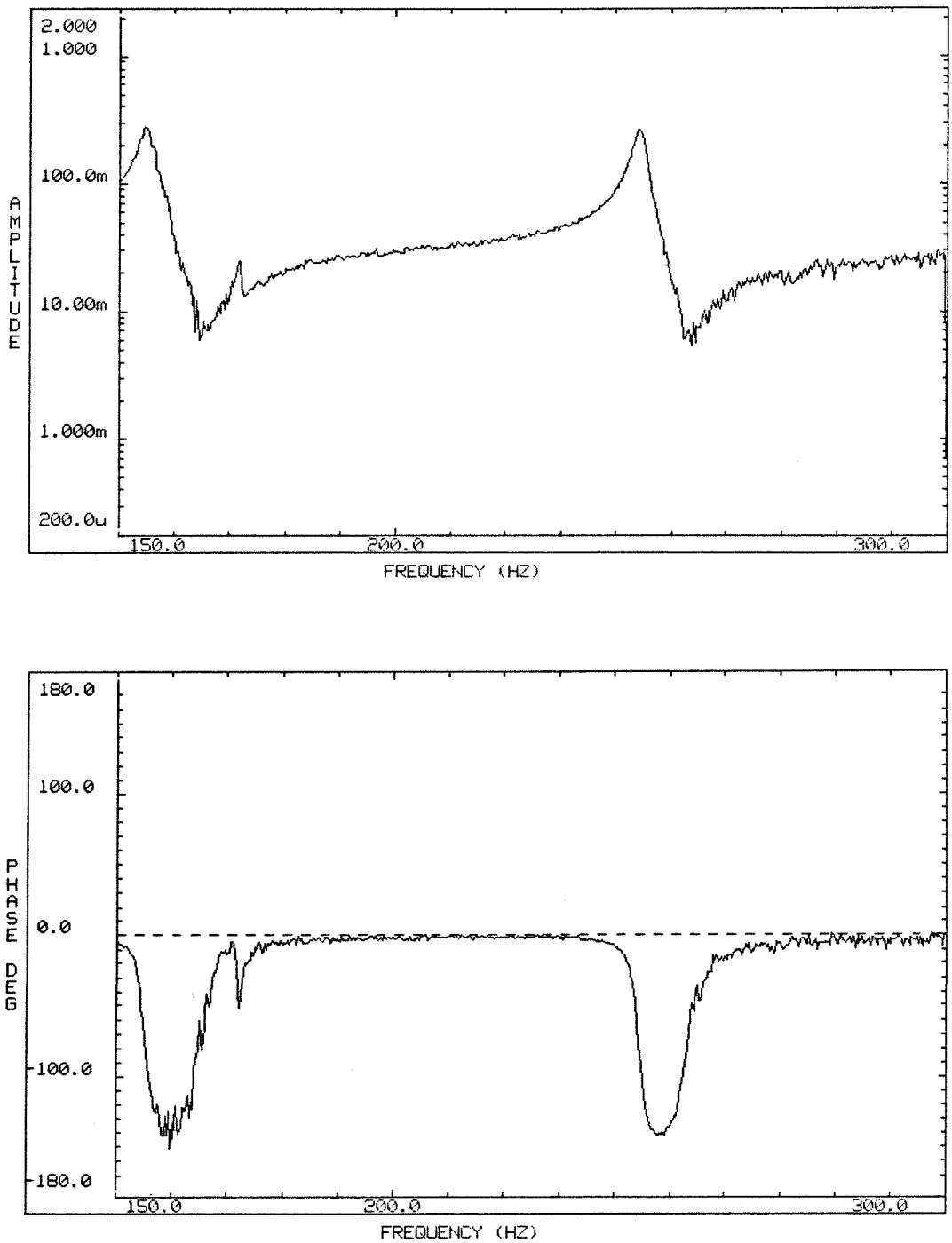

Figure 5.3d Plant frequency function. Modes 4 and 5.

where $j = \sqrt{-1}$. The damping ratios of our plant modes are very small; hence Eq. (5.1.2) can be simplified by assuming the ζ_i are zero. In this case, the ω_i are the open loop pole locations ω_{pi}. The magnitude of the transfer function is then

$$\left|J_i(j\omega)\right| \doteq \frac{a}{\omega_{pi}^2 - \omega^2} + b. \tag{5.1.3}$$

If the damping ratio ζ_i is zero, then the transmission zero occurs at the frequency ω_{zi}, where the magnitude of the transfer function vanishes.

$$\left|J_i(j\omega_{zi})\right| = \frac{a}{\omega_{pi}^2 - \omega_{zi}^2} + b = 0, \tag{5.1.4a}$$

and

$$\frac{a}{b} = \omega_{zi}^2 - \omega_{pi}^2. \tag{5.1.4b}$$

The pole and zero frequencies are known from the system identification tests, and the starting value of b is obtained by measuring the inter-mode value of the transfer function between the i^{th} mode and the $i+1^{th}$ mode. This gives good initial values for the numerators. They can then be adjusted to give correct zero locations including the damping ratios in the modal transfer functions. The two mode model determined in this fashion and used for the SISO control synthesis is:

$$P_2(s) = \frac{4.5}{s^2 + 2\,\zeta_1\,\omega_1^2 + \omega_1^2} + \frac{248}{s^2 + 2\,\zeta_2\,\omega_2^2 + \omega_2^2} + 0.045, \tag{5.1.5}$$

where $\omega_1 = 31.5$ rad/sec, $\zeta_1 = 0.0023$, $\omega_2 = 192.4$ rad/sec , and $\zeta_2 = 0.0015$.

5.1.3 Non-Ideal Sensor Behavior

In Section (4.1.2) we analyzed the sensor, assuming that it was a non-dynamic component; the relation between applied stress and sensor voltage, given in Eq. (4.1.21), contains no dynamic terms. In practice, we found that if the sensor electrode was connected to a high input-impedance buffer consisting of a 741 operational amplifier, a spurious voltage of about 1 volt developed spontaneously. The stray voltage was reduced to a few millivolts by means of a shunt resistance as shown in Figure (5.4). This essentially AC-couples the sensor to the control circuit, for the shunt resistor combines with the capacitance of the nickel-plated ceramic sheet to produce a high-pass filter.

This low frequency behavior changes the nature of the instability encountered with PPF as the gain is increased beyond the stability boundary. Instead of a static instability, as shown in Figure (2.7), instability occurs at a finite frequency. The effect of the high-pass dynamics is to introduce a differentiator into the loop, with its corresponding phase lead, which reduces the gain margin. In order to include this parasitic effect in the plant model, the sensor transfer function is derived. Figure (5.4) shows the circuit designed to reduce the stray voltage on the sensor. The voltage V_{PZT}, produced by the ceramic material itself, is applied to the electrode surface which is modeled as a separate capacitor. The voltage measured to be the sensor voltage is V_s. The differential equation that describes this circuit is

$$C_{PZT}\frac{d}{dt}(V_{PZT} - V_s) = \frac{V_s}{R}, \tag{5.1.6}$$

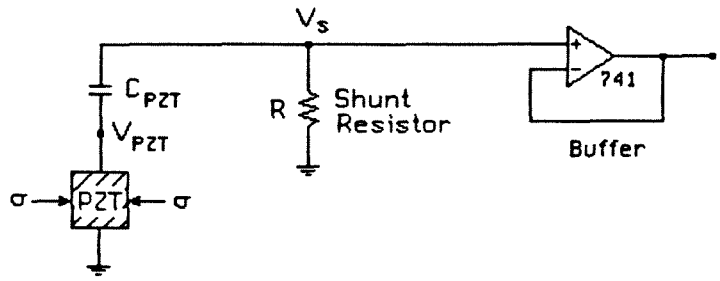

Figure 5.4 Sensor shunt circuit.

where C_{PZT} is the capacitance of the sensor, and R is the resistance of the shunt resistor. Taking the Laplace Transform gives the transfer function as

$$\frac{\hat{V}_s(s)}{\hat{V}_{PZT}(s)} = \frac{s}{s + \frac{1}{RC_{PZT}}}. \tag{5.1.7}$$

We see that there is a zero located at the origin, and a pole located on the negative real axis at $-1/RC_{PZT}$. In Chapter 6, a compensator circuit is derived which nearly cancels the pole and zero to remove the sensor dynamics from the problem. The value of $1/RC_{PZT}$ for the SISO experiments is 0.832 sec^{-1}.

5.2 Single Mode Control

The first step in developing a control system to suppress the dynamic response of the test beam is to control single modes with one actuator/sensor pair and one PPF filter tuned to the controlled mode. Mode 1 and Mode 2 are controlled individually. The stabilizing spillover effects on the uncontrolled modes are observed and compared with the theoretical predictions.

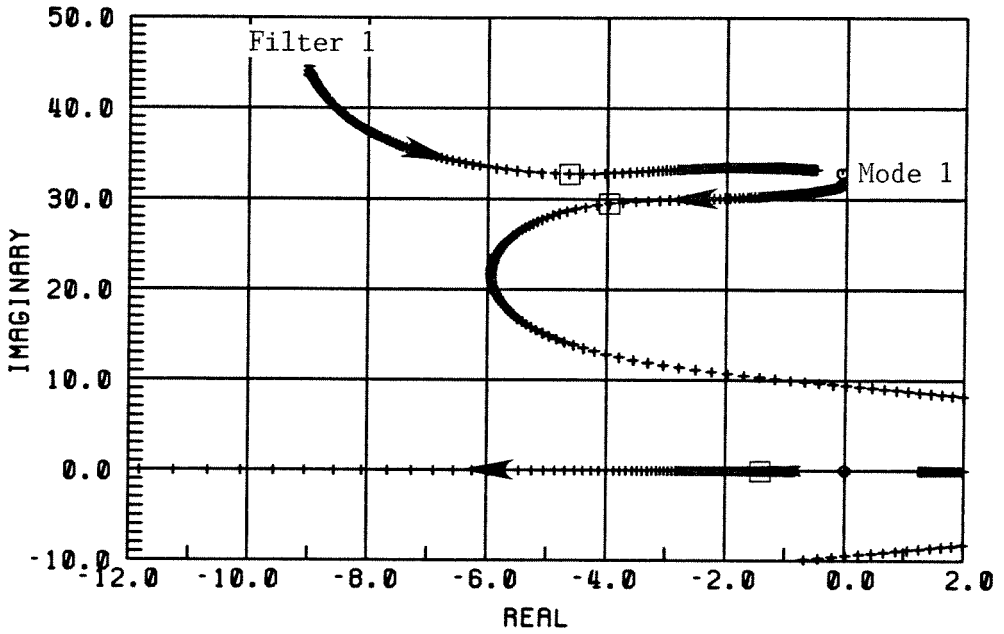

Figure 5.5 Root locus for Mode 1 control showing movement of Mode 1 pole. Tics plotted for $0 \leq g \leq 30$. Boxes indicate poles at $g = 9.0$.

5.2.1 Control Synthesis for Mode 1

The approach to the design of the control circuit is based on the performance recovery technique for close pole-zero pairs described in Section (2.2.4). Basically, this involves placing the PPF filter pole at a higher damped natural frequency than the pole of the controlled mode. For the Mode 1 control case, a filter frequency of 45 rad/sec and damping ratio of 0.20 produced pole coalescence at a gain of approximately 9.0. Figure (5.5) shows the root locus plot in the region of Mode 1 for gain ranging from 0 to 30. The tic marks show the closed loop pole locations at gain intervals of 0.1. The effect of the non-ideal sensor dynamics on stability can be seen in the branches of the locus that cross into the right half-plane at a non-zero frequency. The stability margin occurs at a gain of 17.0.

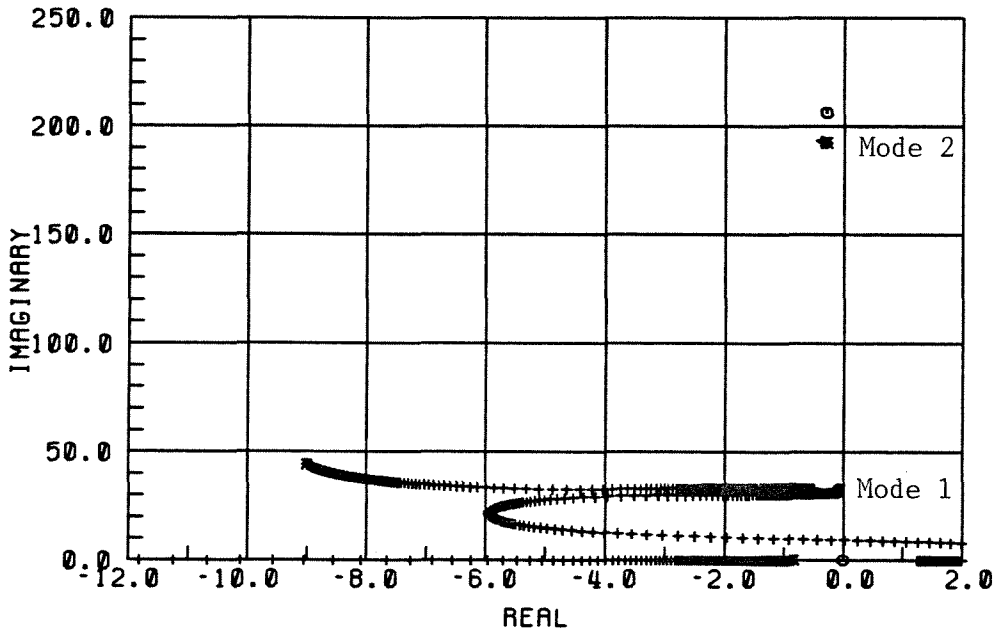

Figure 5.6 Root locus for Mode 1 control showing movement of both Mode 1 and Mode 2 poles. Tics plotted for $0 \leq g \leq 30$.

Figure (5.6) shows the root locus including the Mode 2 pole. There is very little movement of the Mode 2 pole because the PPF filters have a two pole rolloff, and the second mode is far enough away in frequency that the coupling is small. Nevertheless, the upward spillover into Mode 2 causes the pole to move farther into the left half-plane, which is stabilizing.

5.2.2 Mode 1 Control Results

Figure (5.7) shows both the open loop and closed loop frequency response functions for the region of Modes 1 and 2. As can be seen, the response of Mode 1 is greatly attenuated, and the response of Mode 2 is essentially unchanged. The shape of the closed loop response near Mode 1 is a single hump, which is due to the close proximity of the highly damped filter and structural poles. The process of identifying the frequency and damping values of the closed loop poles

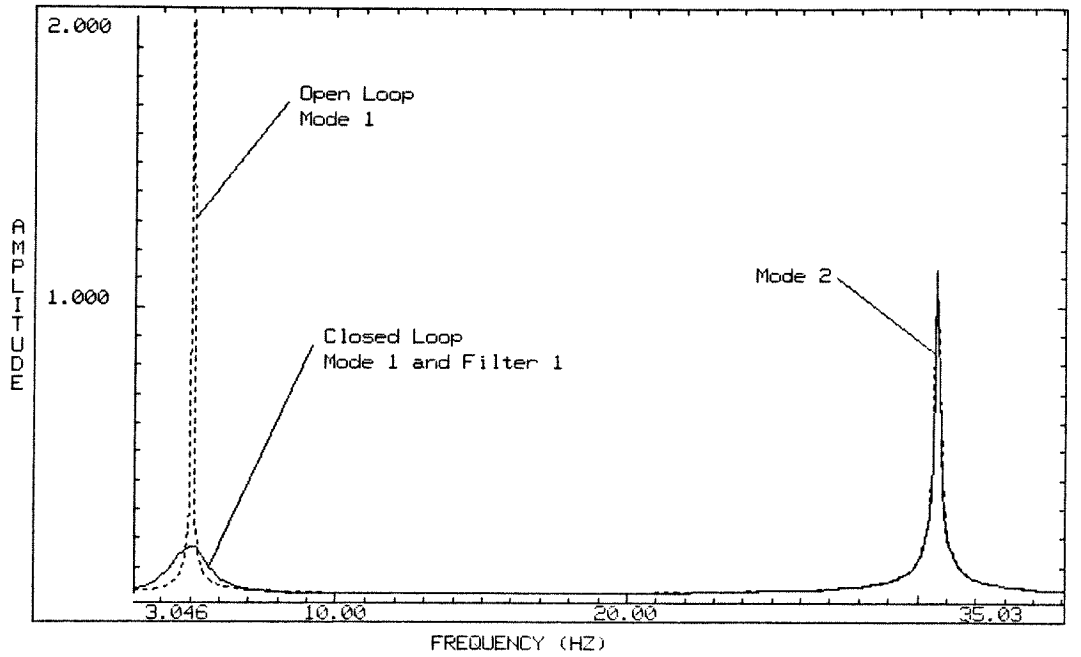

Figure 5.7 Open loop and closed loop frequency response functions for Mode 1 control. Dashed line – open loop. Solid line – closed loop.

by means of a complex curve-fit becomes ill-conditioned when they are so close together. Nevertheless, these closed loop values can usually be extracted by the FITTER software.

Figure (5.8) shows open loop and closed loop free decay response for Mode 1. The settling time for Mode 1 is greatly reduced. Figure (5.9) shows a comparison of the sensor and actuator voltages during the closed loop free decay. Table (5.2.1) summarizes the closed loop performance results.

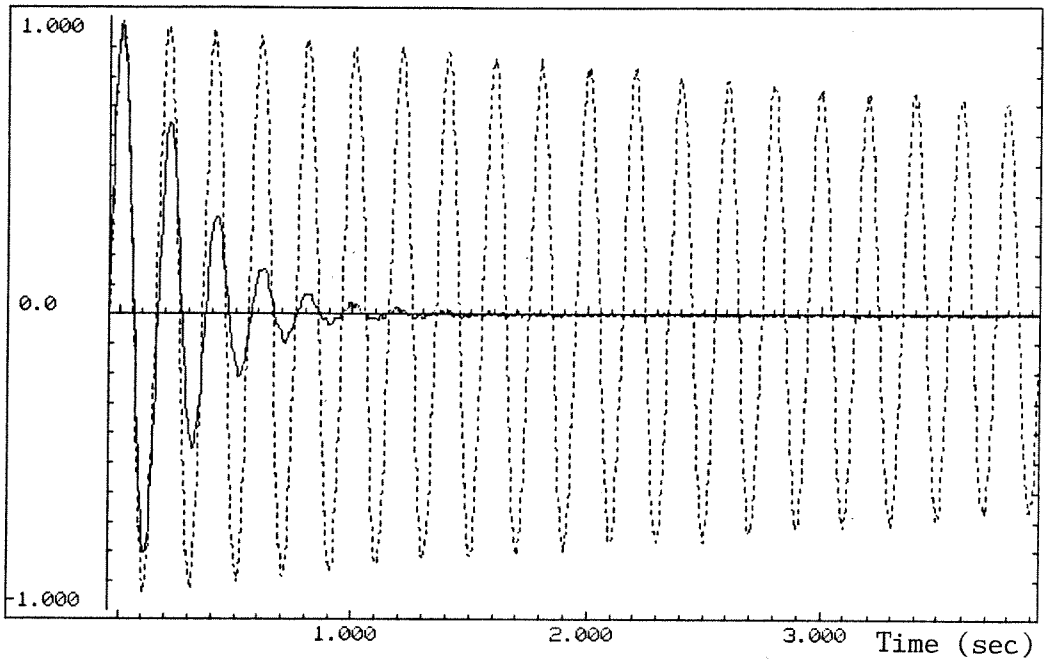

Figure 5.8 Open loop and closed loop free decay response for Mode 1 control. Dashed line – open loop. Solid line – closed loop.

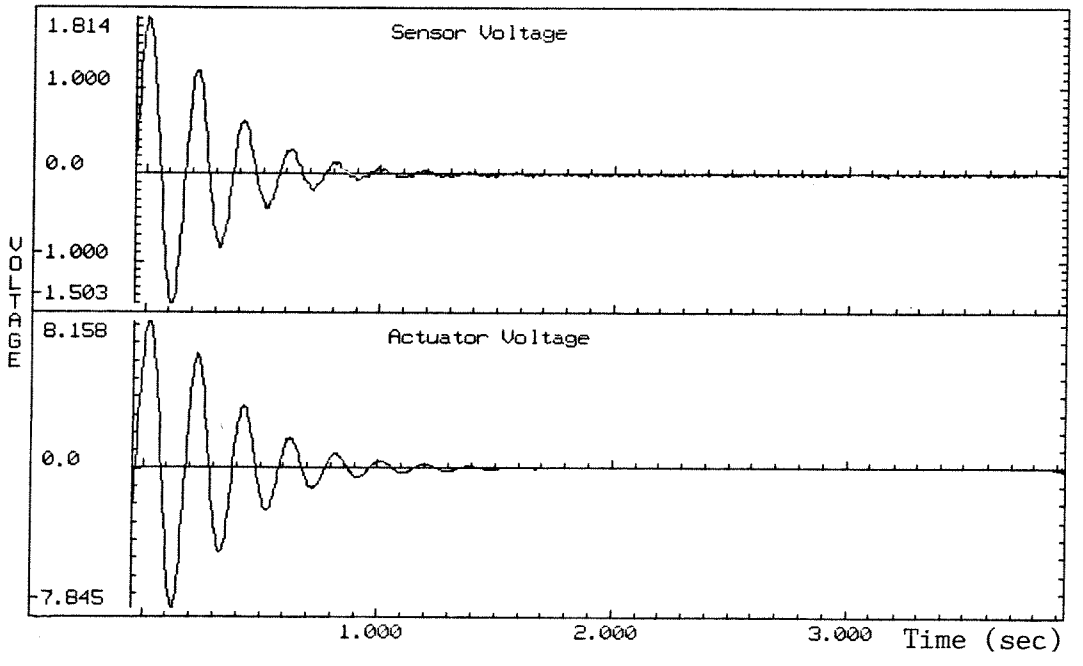

Figure 5.9 Sensor and actuator voltages during free decay.

Table 5.2.1 Effect of Mode 1 Control on Modes 1 & 2

	Mode 1			Filter 1		
	$\varsigma_1(\%)$	$\varsigma_1\omega_1$	$\varsigma_1\omega_1^2$	$\varsigma_{f1}(\%)$	$\varsigma_{f1}\omega_{f1}$	$\varsigma_{f1}\omega_{f1}^2$
Open Loop	0.23	0.0721	2.27	20.0	9.00	405.
Closed Loop	16.3	4.68	135.	10.4	3.41	112.
*Percent Change**	*7,000*	*6,400*	*5,800*	—	—	—
Predicted†	13.3	3.96	118.	14.0	4.63	154.
	Mode 2			Filter 2		
	$\varsigma_2(\%)$	$\varsigma_2\omega_2$	$\varsigma_2\omega_2^2$	$\varsigma_{f2}(\%)$	$\varsigma_{f2}\omega_{f2}$	$\varsigma_{f2}\omega_{f2}^2$
Open Loop	0.15	0.289	55.5	—	—	—
Closed Loop	0.19	0.366	70.3	—	—	—
*Percent Change**	*26.7*	*26.6*	*26.7*	—	—	—
Predicted†	0.17	0.320	61.7	—	—	—

* Percent Change Between Measured Values † Predicted Closed Loop Values

5.2.3 Control Synthesis for Mode 2

For the Mode 2 control case, a single filter was tuned to Mode 2. A filter frequency of 250 rad/sec and damping ratio of 0.20 produced good performance at a gain of approximately 8.0. Figure (5.10) shows the root locus plot in the region of Mode 2 for the gain g ranging from 0 to 30. The gain is chosen to place the poles slightly beyond the point of closest approach. We will see in the two mode control case that the effect of the Mode 1 filter is to back the Mode 2 poles up on the locus slightly. Figure (5.11) shows the effect of the downward control spillover on Mode 1. The Mode 1 pole at first moves back into the left half-plane, and moves downward. Eventually, Mode 1 will go unstable. It is characteristic of PPF that the lowest mode is the mode that will eventually go unstable. The lowering of the frequency of Mode 1 results in a penalty on the performance quantity $\varsigma\omega^2$, since the frequency is squared.

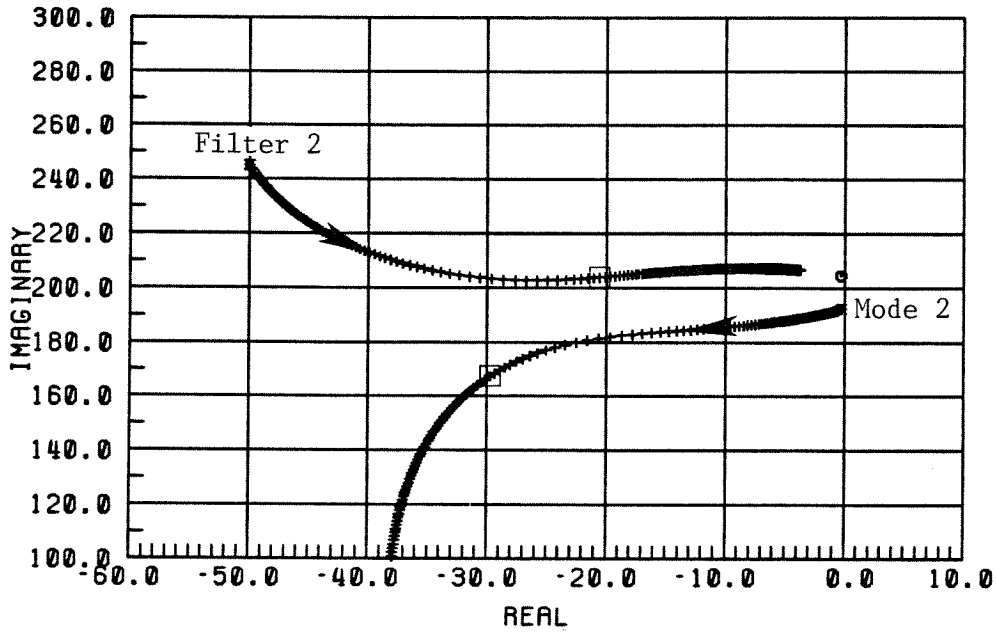

Figure 5.10 Root locus for Mode 2 control showing movement of Mode 2 pole. Tics plotted for $0 \leq g \leq 30$. Boxes indicate poles at $g = 8.0$.

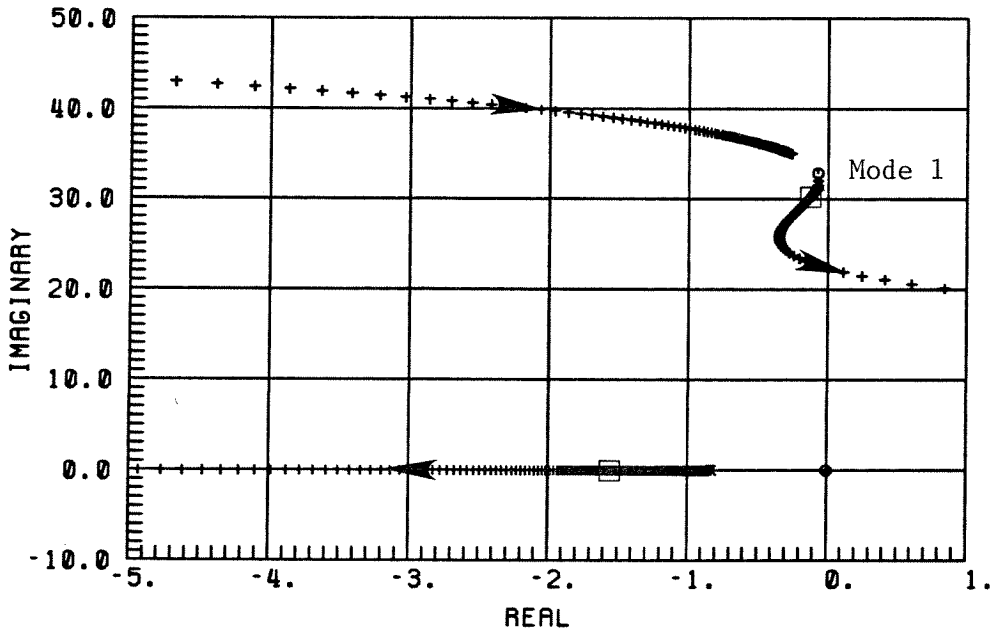

Figure 5.11 Root locus for Mode 2 control showing movement of Mode 1 pole. Boxes indicate poles at $g = 8.0$.

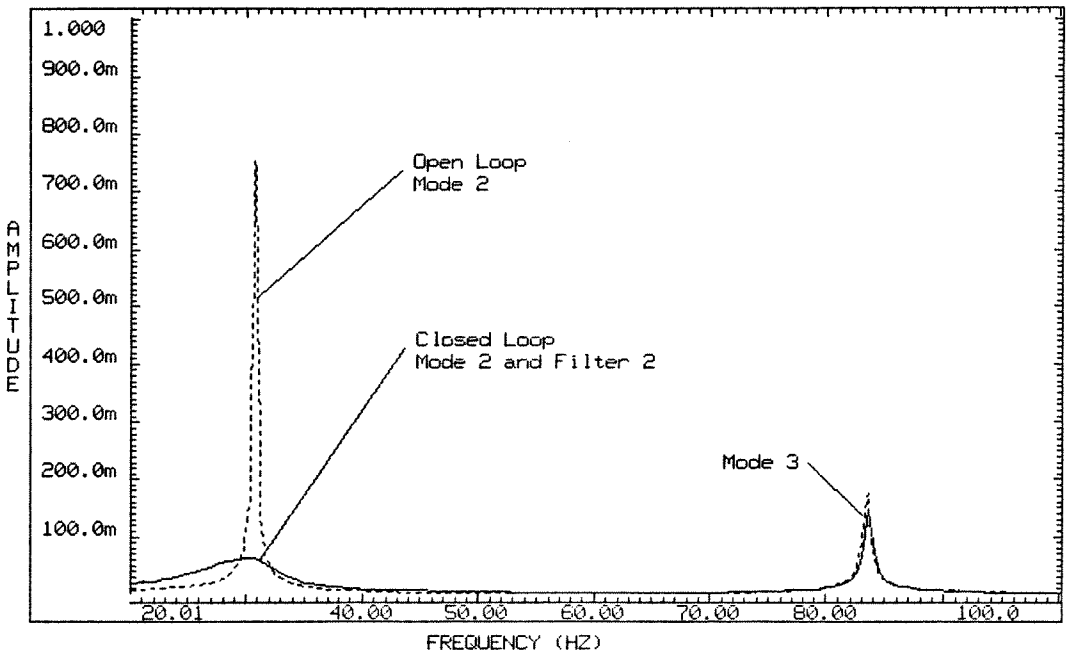

Figure 5.12 Open loop and closed loop frequency response functions for Mode 2 control. Dashed line – open loop. Solid line – closed loop.

5.2.4 Mode 2 Control Results

Figure (5.12) shows the open loop and closed loop frequency response functions for the region of Modes 2 and 3. The response of Mode 2 is greatly reduced, and the response of Mode 3 is slightly reduced. Figure (5.13) shows the downward spillover into Mode 1. As can be seen, the frequency of Mode 1 is lowered and the damping ratio is increased as predicted. The closed loop performance is summarized in Table (5.2.2).

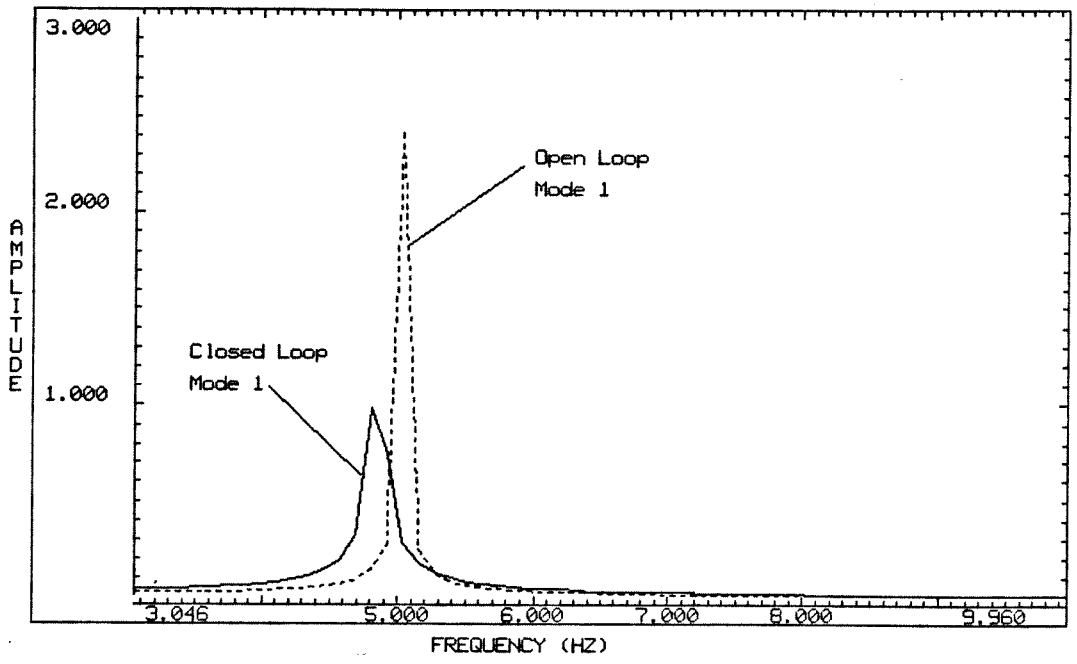

Figure 5.13 Open and closed loop frequency response for Mode 2 control showing downward spillover into Mode 1.

Table 5.2.2 Effect of Mode 2 Control on Modes 1 & 2

	Mode 1			Filter 1		
	$\varsigma_1(\%)$	$\varsigma_1\omega_1$	$\varsigma_1\omega_1^2$	$\varsigma_{f1}(\%)$	$\varsigma_{f1}\omega_{f1}$	$\varsigma_{f1}\omega_{f1}^2$
Open Loop	0.23	0.0721	2.27	—	—	—
Closed Loop	0.43	0.131	4.00	—	—	—
*Percent Change**	*87*	*80*	*76*	—	—	—
Predicted†	0.37	0.112	3.40	—	—	—
	Mode 2			Filter 2		
	$\varsigma_2(\%)$	$\varsigma_2\omega_2$	$\varsigma_2\omega_2^2$	$\varsigma_{f2}(\%)$	$\varsigma_{f2}\omega_{f2}$	$\varsigma_{f2}\omega_{f2}^2$
Open Loop	0.15	0.289	55.5	20.0	50.0	1.25×10^4
Closed Loop	12.7	22.4	3.95×10^3	6.73	13.3	2.62×10^3
*Percent Change**	*8,400*	*7,700*	*7,000*	—	—	—
Predicted†	13.3	23.5	4.18×10^3	12.6	26.2	5.47×10^3

* Percent Change Between Measured Values † Predicted Closed Loop Values

5.3 Two Mode Control

In this experiment, the first two modes are controlled simultaneously using two PPF filters, one tuned to each mode. A technique for synthesizing a multi-filter compensator using the root locus is derived. The two mode control results are compared with the predicted closed loop performance.

5.3.1 Control Synthesis for Modes 1 and 2

The single mode control compensators were designed using the root locus technique. This works well when there is only one gain to be varied. In the two mode control case there are two filters and therefore two independent gains which must be varied in the design process. The *root contour* technique provides a means of analyzing the effect of varying one gain while the other remains fixed. The details are discussed below.

If we call the plant transfer function $P(s)$, and the two filter transfer functions $k_1(s)$ and $k_2(s)$, then the closed loop transfer function $T(s)$ is given by

$$T(s) = \frac{P(s)}{1 - P(s)[g_1\, k_1(s) + g_2\, k_2(s)]}, \tag{5.3.1}$$

where g_1 and g_2 are the two scalar gains associated with the PPF filters. Root locus calculation programs require the unity gain loop transfer function as an input, and then compute the root locus as a function of a single gain multiplying that loop transfer function. If the unity gain loop transfer function of Eq. (5.3.1) were used, both filters would be multiplied by the same gain, which is not satisfactory. Suppose instead that we calculate the effect on the closed loop poles of varying g_2, assuming that g_1 is set to a fixed value γ. We first assume a

form for the closed loop transfer function that involves an undetermined function $A(s)$ as follows:

$$T(s) = \frac{\left(\frac{P(s)}{A(s)}\right)}{1 - g_2\left(\frac{k_2(s)P(s)}{A(s)}\right)}, \tag{5.3.2a}$$

or

$$T(s) = \frac{P(s)}{A(s) - g_2\, k_2(s)\, P(s)}. \tag{5.3.2b}$$

The closed loop poles are the zeros of the denominator of the transfer function $T(s)$. The function $A(s)$ is determined by setting $g_1 = \gamma$ in Eq. (5.3.1) and equating the denominators of Eqs. (5.3.1) and (5.3.2b).

$$1 - P(s)[\gamma k_1(s) + g_2\, k_2(s)] = A(s) - g_2\, k_2(s)\, P(s), \tag{5.3.3a}$$

$$A(s) = 1 - \gamma k_1(s)\, P(s) \tag{5.3.3b}$$

Thus, the new "loop transfer function" is given by

$$\text{loop transfer function} = \frac{k_2(s)\, P(s)}{1 - \gamma k_1(s)\, P(s)}. \tag{5.3.4}$$

The method is illustrated in Figures (5.14) and (5.15). Figure (5.14) shows the effect on Mode 1 of the Mode 2 control filter. The Mode 1 filter is the same as that used for the Mode 1 control described in Section (5.2.1). The gain is set to the value chosen for the Mode 1 control case: $g_1 = 9.0$. When the gain of the Mode 2 filter is zero, we have the single Mode 1 control case, which is why the starting positions of the manifolds in Figure (5.14) correspond to the design pole locations in Figure (5.5). The Mode 2 filter is the same as that used for the Mode 2 control case of Section (5.2.3). Figure (5.14) traces the movement of the

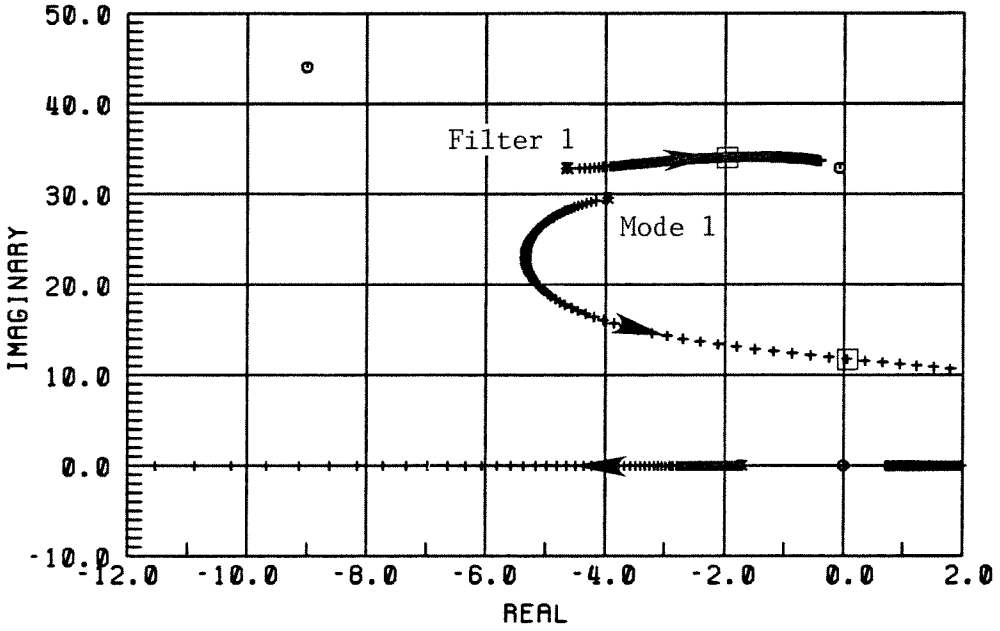

Figure 5.14 Root contour showing effect of Mode 2 control on Mode 1 and Filter 1 poles. $g_1 = 9.0$. $0 \leq g_2 \leq 30$. Boxes indicate $g_2 = 8.0$.

closed loop poles as the Mode 2 filter gain is increased from 0 to 30. When the gain reaches a value of 8.0, the design gain of Section (5.2.3), Mode 1 has gone unstable, as indicated by the boxed pole location in the right half-plane. We see that the effect of the Mode 2 control is to move the Mode 1 poles farther along the single mode control case manifolds. The effect of the higher mode control on the lower modes is strong because the PPF filter transfer functions have magnitude one at zero frequency. It is also seen that the multi-filter compensator cannot be designed using the single mode control values for filter gains.

Figure (5.15) shows the effect on Mode 2 of the Mode 1 control filter, again using the values for filter parameters and gain from the single mode control cases. The starting points of the manifolds in Figure (5.15) correspond to the design pole positions of Figure (5.10). There is very little movement of the

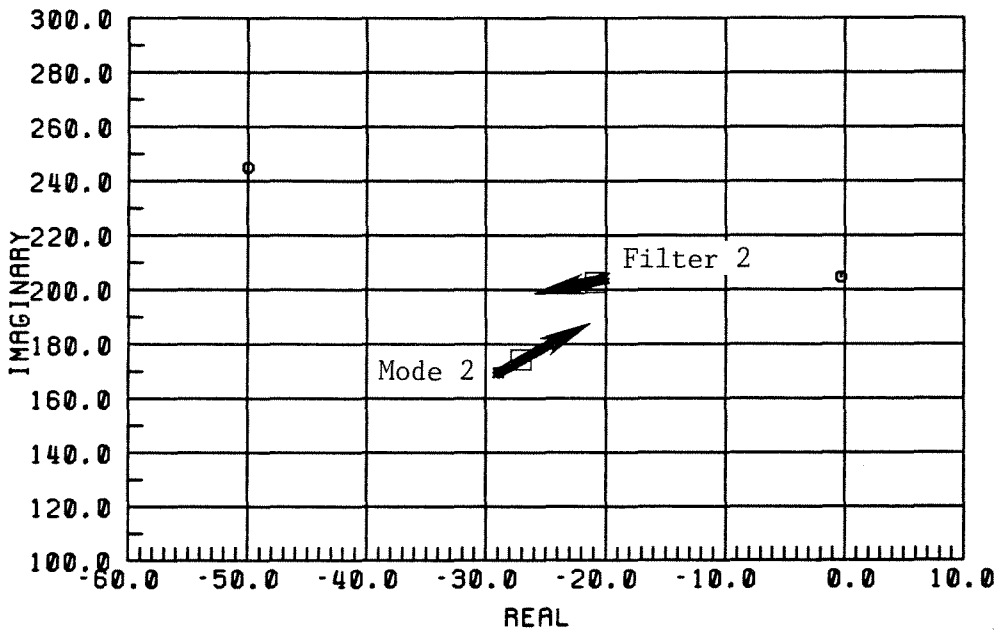

Figure 5.15 Root contour showing effect of Mode 1 control on Mode 2 and Filter 2 poles. $g_2 = 8.0$. $0 \leq g_1 \leq 30$. Boxes indicate $g_1 = 9.0$.

Mode 2 poles even for a Mode 1 filter gain of 30. This is because the filter transfer functions have a two pole rolloff, and the two modes are far apart in frequency. The small amount of movement tends to back the Mode 2 poles up in the direction that they came in the single mode control root locus.

The synthesis strategy is then to design the highest mode control filter parameters and gain based on a single mode control root locus. The same is done for the next lower mode. Then, keeping the lower mode control gain fixed, we observe the effect on the closed loop positions of varying the high mode control gain to the nominal value used initially. By iteration, we reduce the lower mode gain until the nominal gain of the higher filter produces good performance in the lower mode. The process is repeated for as many modes as are to be controlled. This procedure is somewhat ad hoc, but in the absence of

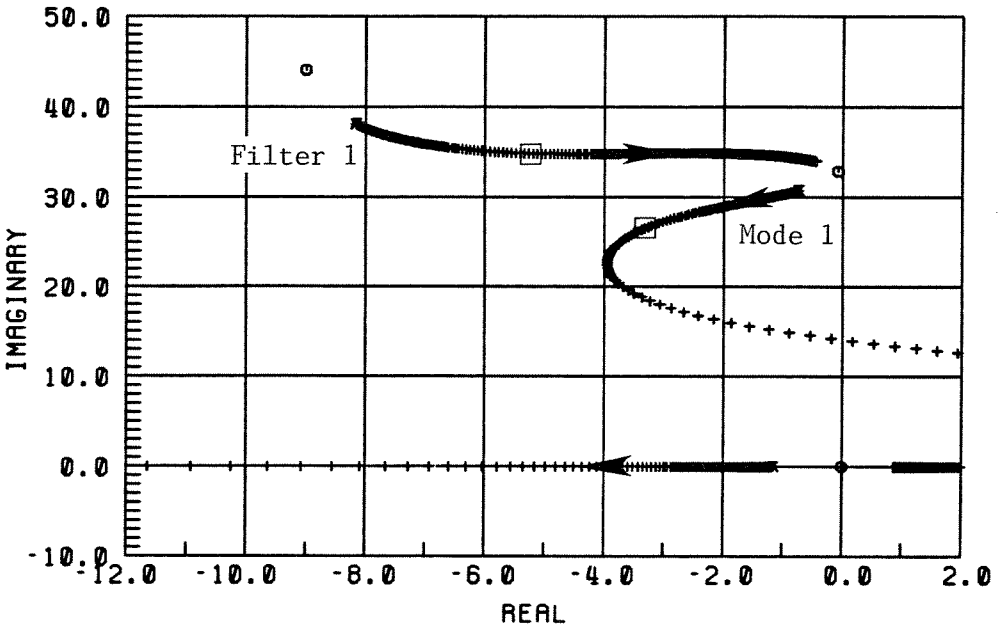

Figure 5.16 Root contour showing effect of Mode 2 control on Mode 1 and Filter 1 poles. $g_1 = 5.0$. $0 \leq g_2 \leq 30$. Boxes indicate $g_2 = 8.0$.

a synthesis theory for close pole-zero pairs, it is the best available and produces satisfactory results.

Figure (5.16) shows the root contour for the Mode 1 control gain set to 5.0, and the Mode 2 gain set to 8.0. These values are used in the two mode control experiment and the results are discussed below.

5.3.2 Two Mode Control Results

Figure (5.17) shows the open and closed loop frequency response functions for the region of Modes 1 and 2; Figure (5.18) shows the frequency response functions for the region of Modes 2 and 3. The spillover into Mode 3 is seen to be stabilizing, as expected. Table (5.3.1) summarizes the two mode control results.

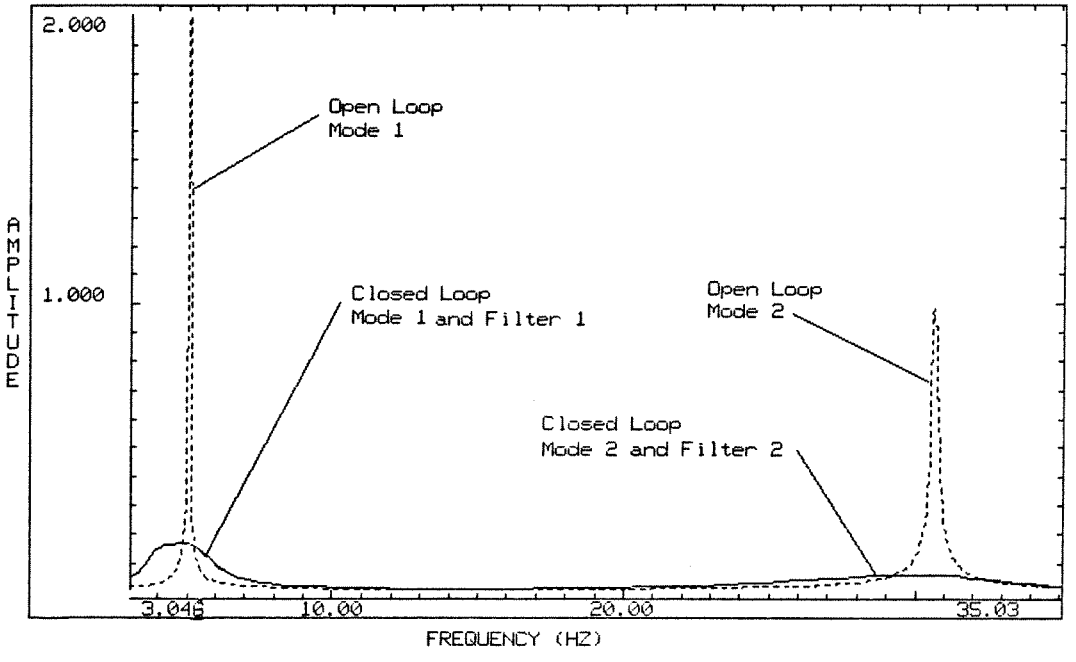

Figure 5.17 Open loop and closed loop frequency response functions for two mode control. Dashed line – open loop. Solid line – closed loop.

Table 5.3.1 Effect of Two Mode Control on Modes 1 & 2

	Mode 1			Filter 1		
	$\varsigma_1(\%)$	$\varsigma_1\omega_1$	$\varsigma_1\omega_1^2$	$\varsigma_{f1}(\%)$	$\varsigma_{f1}\omega_{f1}$	$\varsigma_{f1}\omega_{f1}^2$
Open Loop	0.23	0.0721	2.27	20.0	9.00	405.
Closed Loop	15.3	3.81	94.7	13.6	4.61	156.
*Percent Change**	*6,600*	*5,200*	*4,100*	—	—	—
Predicted†	12.7	3.38	89.9	14.9	5.27	185.
	Mode 2			Filter 2		
	$\varsigma_2(\%)$	$\varsigma_2\omega_2$	$\varsigma_2\omega_2^2$	$\varsigma_{f2}(\%)$	$\varsigma_{f2}\omega_{f2}$	$\varsigma_{f2}\omega_{f2}^2$
Open Loop	0.15	0.289	55.5	20.0	50.0	1.25×10^4
Closed Loop	13.8	23.7	4.05×10^3	7.70	15.0	2.93×10^3
*Percent Change**	*9,100*	*8,100*	*7,200*	—	—	—
Predicted†	12.7	22.8	4.07×10^3	12.9	26.8	5.56×10^3

* Percent Change Between Measured Values † Predicted Closed Loop Values

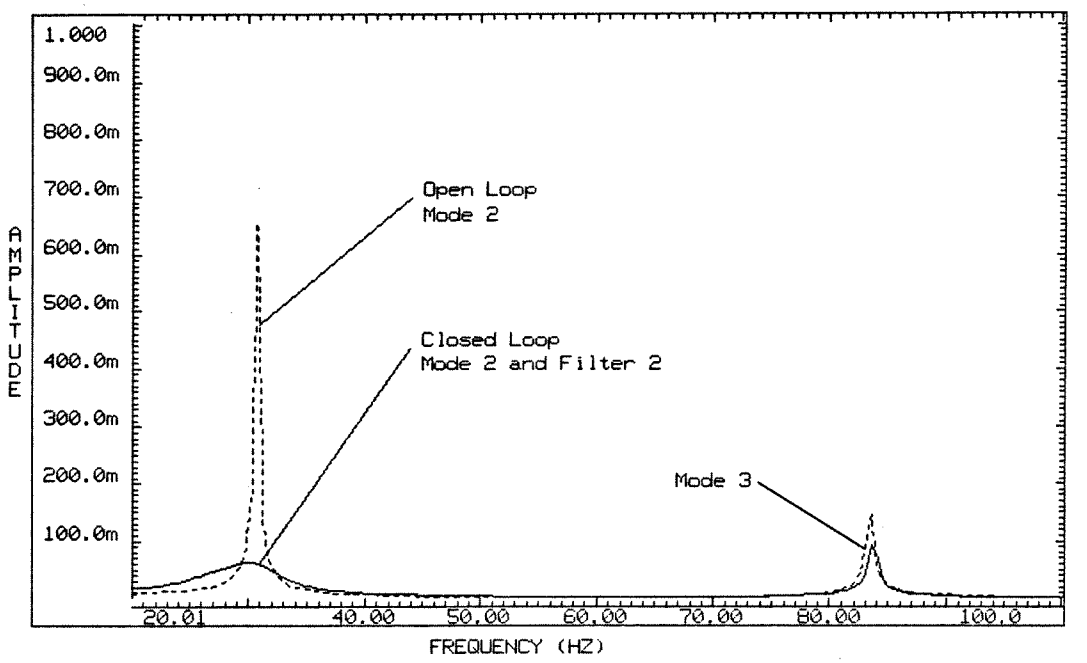

Figure 5.18 Open and closed loop frequency response functions for two mode control showing upward spillover into Mode 3.

5.4 Three Mode Control

This experiment controls the first three modes of the piezobeam using three PPF filters. The results of the single mode and two mode control experiments are used to select the Mode 3 filter parameters.

5.4.1 Control Synthesis for Modes 1, 2 and 3

The synthesis for the single mode and two mode control experiments made use of the root contour technique. For the three mode control case, a three mode plant model must be used. It was found that the computer program CC, which was used for the previous syntheses, could not accommodate the increased order of the loop transfer function and would not compute the correct root loci. We

then turned to the mainframe controls software package $MATRIX_X$* in order to make the computations. Unfortunately, $MATRIX_X$ could not accommodate the close pole-zero pairs of the plant transfer function. ISI, the writers of $MATRIX_X$, determined that the problem could be solved with a change to the source code (which was planned for an upcoming version of the program). Since the source code was unavailable, we wrote our own program to compute the root locus by solving for the roots of the characteristic equation. The program listing is contained in Appendix G.

Having no timely analysis tool readily available, we could not perform the three mode control synthesis. Instead, the results from the previous experiments were used to suggest suitable values for the Mode 3 filter and the three control filter gains. The gains were then fine-tuned in the laboratory to produce optimal performance, and the measurements were made.

For the two single mode control experiments, the ratio of the filter frequency to the mode frequency was 1.4 for Mode 1, and 1.2 for Mode 2. This suggests a Mode 3 filter frequency equal to 1.4 times the frequency of Mode 3, or 748 rad/sec. The filters for Mode 1 and 2 had damping ratios equal to 0.20. The Mode 3 filter was constructed and measured to have a damping ratio of 0.22. Since none of the parameters for the three mode case are designed to specific values, the damping ratio was not fine-tuned to 0.20.

The two mode control experiment demonstrates that a filter at a higher mode necessitates a reduction in the optimal gain of the lower filter. Specifically, the Mode 1 gain was reduced from 9.0 to 5.0. The effect a filter at Mode 3 must

* $MATRIX_X$ is a control design and analysis program marketed by Integrated Systems Inc., (ISI).

be to require a reduction in the gains of the Mode 1 and Mode 2 filters. We set these gains equal to 3.0 initially. The control circuit, shown in Figure (5.19), was built and implemented, and proved to be stable and to perform well. The gains were adjusted in the laboratory to give the best performance with the following results:

$$g_1 = 3.5,$$
$$g_2 = 3.6, \tag{5.4.1}$$
$$g_3 = 4.7.$$

The resulting closed loop performance is discussed in the next section.

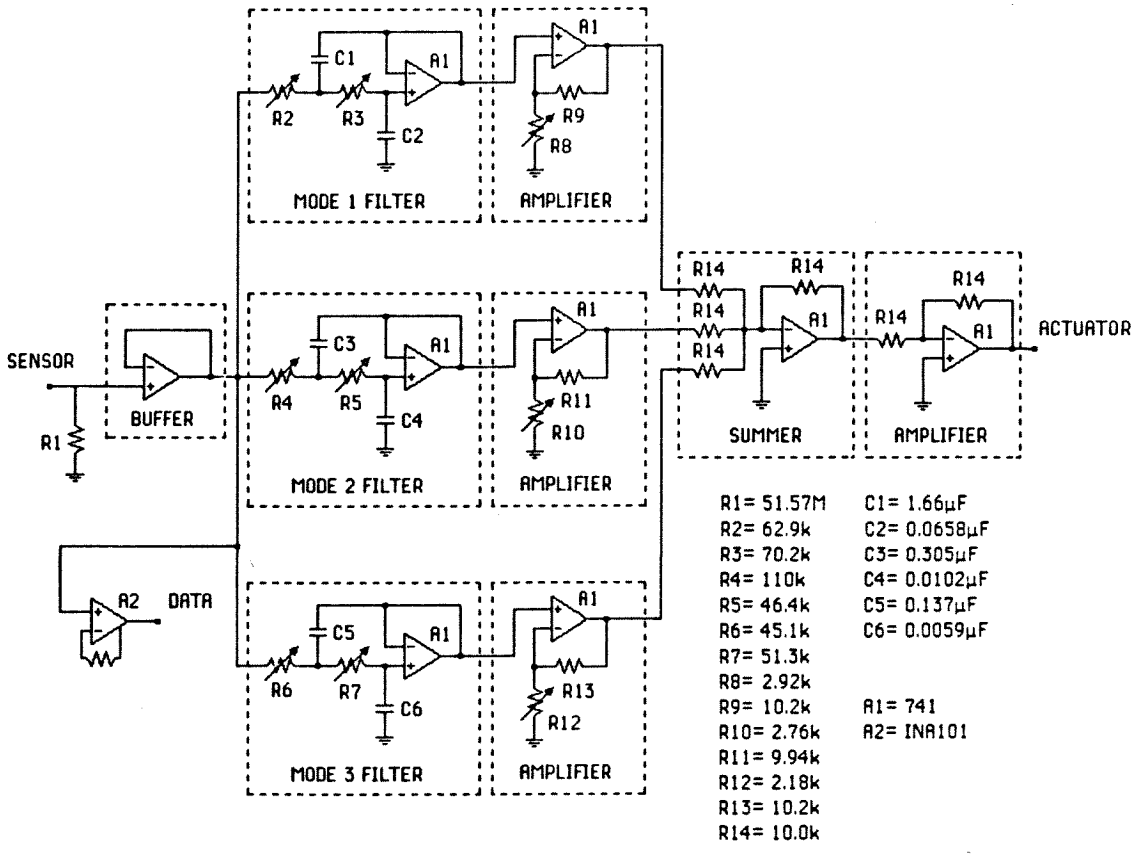

Figure 5.19 Three mode control circuit.

5.4.2 Three Mode Control Results

Figure (5.20) shows the frequency response functions for the region of Modes 1 and 2. Both modes exhibit substantially reduced dynamic response. Figure (5.21) shows the frequency response functions for the region of Modes 2 and 3. The dynamic response of Mode 3 is also significantly reduced.

Figures (5.22a,b) show the Mode 1 open loop and closed loop free decay. These photographs were made directly from the oscilloscope and show the free decay response for 50 sec and for 9 sec. They demonstrate the greatly reduced settling time of Mode 1. Table (5.4.1) summarizes the closed loop performance. The frequency and damping ratio for the Mode 3 filter could not be identified by FITTER. This is probably due to the filter pole being too far into the left half plane to be detected.

Extensive measurements were made of the loop frequency function, the compensator frequency function, and the closed loop frequency function, which are contained in Appendix H.

It is interesting to look at the Nyquist plot of the loop frequency function shown in Figure (5.23). The plot is fairly complicated because it includes the three PPF control filters and the first five structural modes. Since PPF is arranged as a positive feedback loop (see Figure (5.2)), the critical point in the Nyquist plane is $(+1,0)$, not the usual $(-1,0)$. The curve begins at the end near the critical point corresponding to a frequency of 0.48 Hz. The curve moves off the lower right hand side as the amplitude grows, and the phase shifts, passing through Mode 1. Past Mode 1 the curve re-enters on the left just above the real axis and proceeds toward the origin. The curve then loops around in a tight circle corresponding to the highly damped Mode 1 filter. Approaching

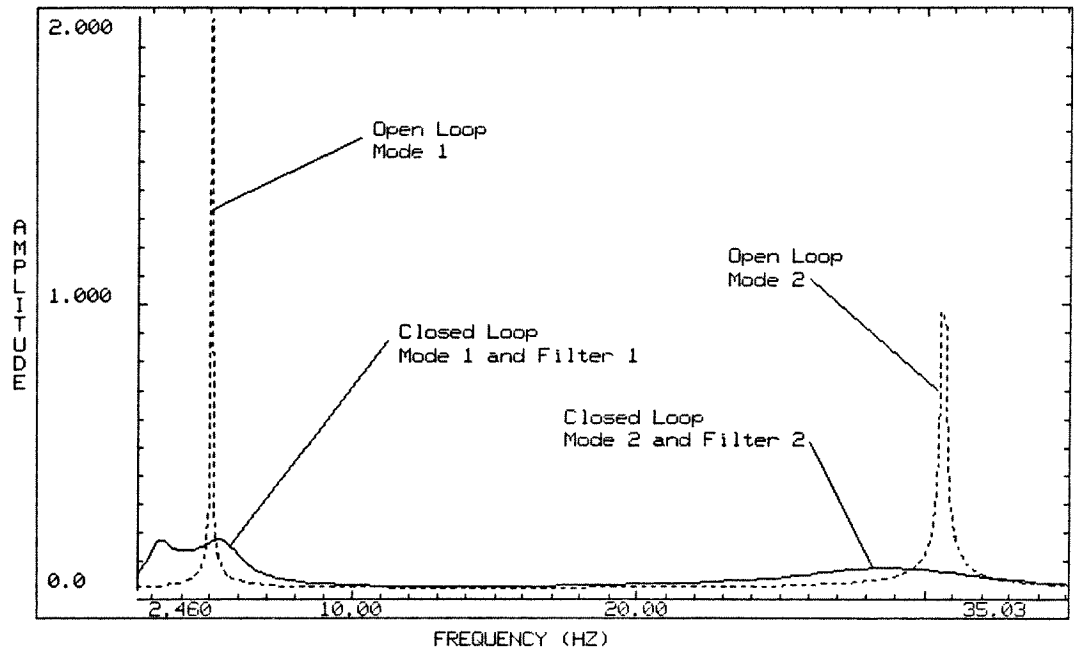

Figure 5.20 Open loop and closed loop frequency response functions for three mode control. Dashed line – open loop. Solid line – closed loop.

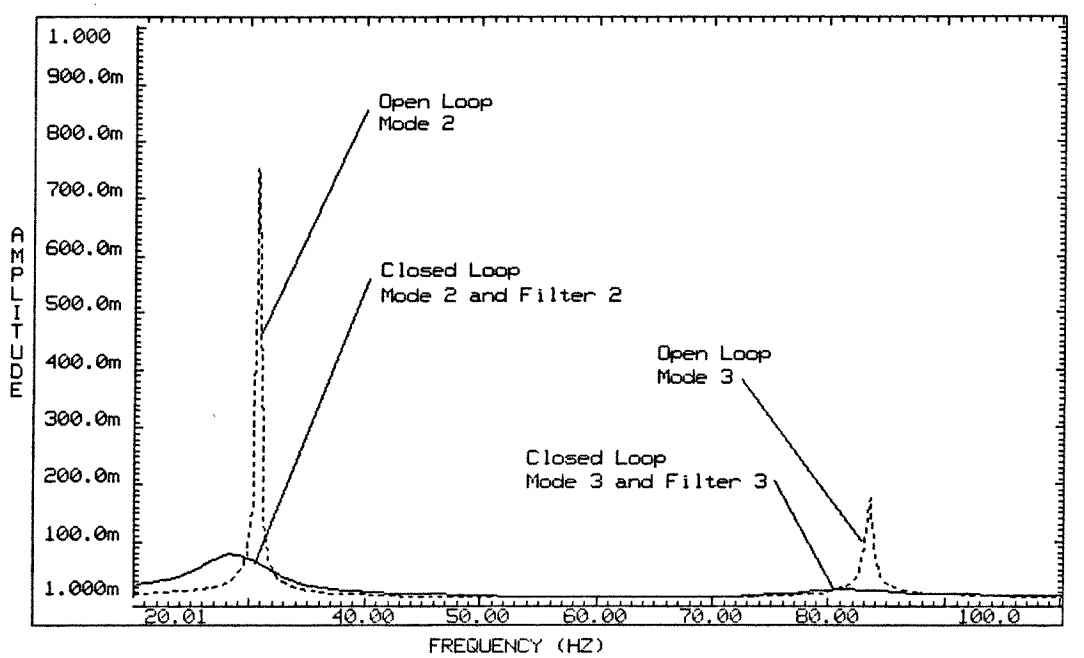

Figure 5.21 Open loop and closed loop frequency response functions for three mode control in region of Modes 2 and 3.

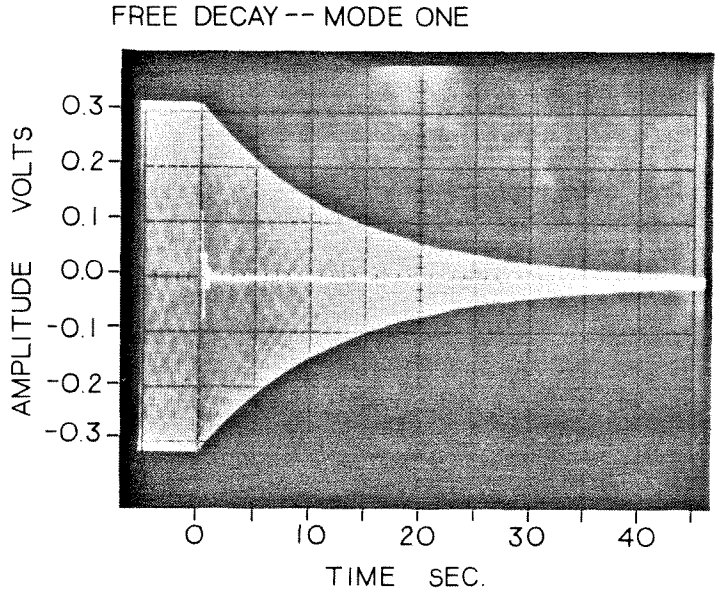

Figure 5.22a Open loop and closed loop free decay of Mode 1 for three mode control.

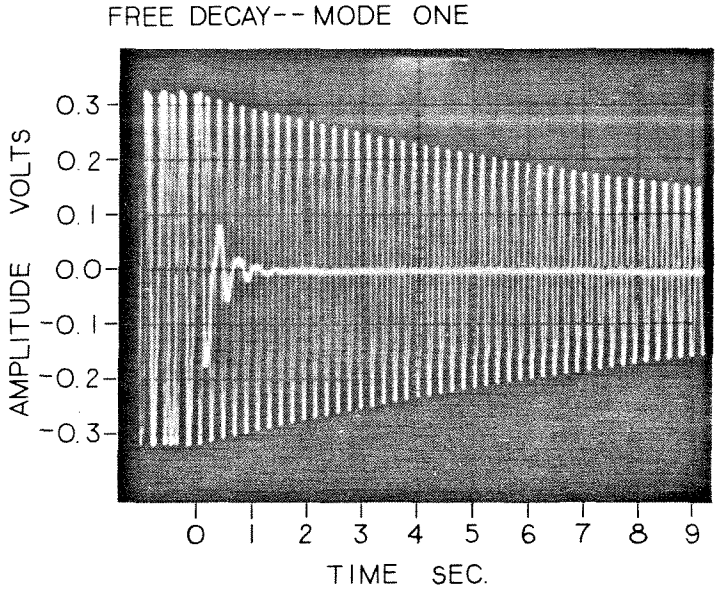

Figure 5.22b Open loop and closed loop free decay of Mode 1 for three mode control.

Table 5.4.1 Effect of Three Mode Control on Modes 1, 2 & 3

	Mode 1			Filter 1		
	$\varsigma_1(\%)$	$\varsigma_1\omega_1$	$\varsigma_1\omega_1^2$	$\varsigma_{f1}(\%)$	$\varsigma_{f1}\omega_{f1}$	$\varsigma_{f1}\omega_{f1}^2$
Open Loop	0.23	0.0721	2.27	20.0	9.00	405.
Closed Loop	13.4	2.63	51.5	12.6	4.36	151.
*Percent Change**	*5,700*	*3,500*	*2,200*	—	—	—
Predicted†	—	—	—	—	—	—
	Mode 2			Filter 2		
	$\varsigma_2(\%)$	$\varsigma_2\omega_2$	$\varsigma_2\omega_2^2$	$\varsigma_{f2}(\%)$	$\varsigma_{f2}\omega_{f2}$	$\varsigma_{f2}\omega_{f2}^2$
Open Loop	0.15	0.289	55.5	20.0	50.0	1.25×10^4
Closed Loop	8.85	15.7	2.78×10^3	8.09	15.9	3.10×10^3
*Percent Change**	*5,800*	*5,300*	*4,900*	—	—	—
Predicted†	—	—	—	—	—	—
	Mode 3			Filter 3		
	$\varsigma_3(\%)$	$\varsigma_3\omega_3$	$\varsigma_3\omega_3^2$	$\varsigma_{f3}(\%)$	$\varsigma_{f3}\omega_{f3}$	$\varsigma_{f3}\omega_{f3}^2$
Open Loop	0.27	1.41	738.	0.22	162.	1.21×10^5
Closed Loop	3.99	20.4	1.04×10^4	NM	NM	NM
*Percent Change**	*1,400*	*1,300*	*1,300*	—	—	—
Predicted†	—	—	—	—	—	—

* Percent Change Between Measured Values † Closed Loop Performance Not Predicted
NM Not Measurable

Mode 2, the curve again exits at the lower right. There is another tight loop corresponding to the Mode 2 filter and another corresponding to the Mode 3 filter. Since the Mode 3 filter is the last one, the curve does not exit at the right but continues directly around the Mode 4 loop. The size of the Mode 4 loop is much smaller than for the first three modes because the loop transfer function is attenuated by the two pole rolloff of the compensator. Finally, the small circular loop of Mode 5 lies close to the origin where the loop gain is attenuated below unity.

Several interesting insights into Positive Position Feedback can be gleaned from this plot. First, the part of the curve nearest the critical point is the *low*

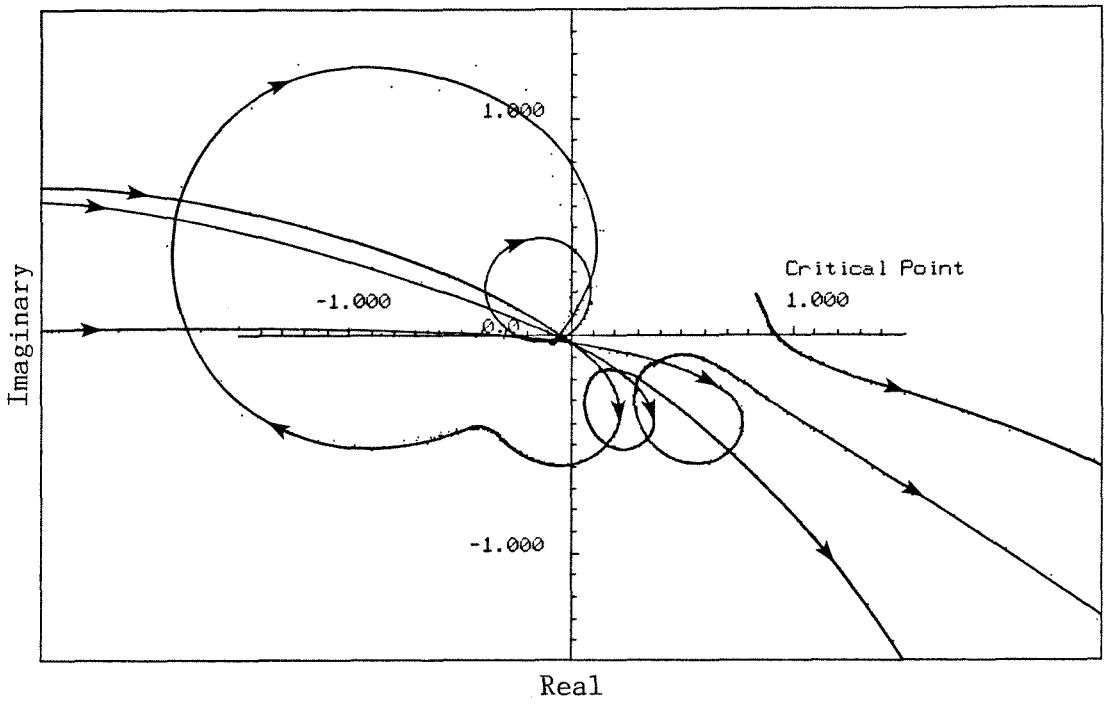

Figure 5.23 Nyquist plot of three mode control loop frequency function from 0.48 Hz. to 300 Hz.

frequency portion. This explains why instabilities in PPF occur at the lowest mode. The dog-eared bend in the curve at low frequency is due to the non-ideal sensor behavior which introduces a phase lead. Under ideal sensor conditions, the curve would become straight at low frequency and would remain below the real axis until, at zero frequency, the curve would intersect the real axis. Thus, the non-ideal sensor behavior lowers the stability margin. Secondly, the superior stability of PPF through the crossover region can be understood by looking at the position of the Mode 4 and 5 loops. These loops are rotated such that they occur in the left half-plane, away from the critical point. This is due to the asymptotic 180 degree phase shift of the compensator at rolloff. It is also very interesting that phase lag perturbations (clockwise rotations) move the portion of the curve nearest the critical point *away* from instability. Thus, a small time

delay in the three mode control loop would actually improve the stability margin somewhat.

In practice, no unintentional instabilties were ever encountered in any of the experiments performed, even though on one occasion completely wrong filter gains were inadvertently set.

Chapter 6

MIMO EXPERIMENT AND RESULTS

This chapter describes the multi-input-multi-output (MIMO) experiment and results. The MIMO experiment makes use of two actuator/sensor pairs located at two different locations on the beam. The first location is the same as that used in the SISO experiments; the selection of the second location is described in Section (6.1.1). A circuit to compensate for the non-ideal sensor behavior is derived and implemented, removing the sensor dynamics from consideration in the synthesis of the control filters.

The MIMO experiment uses six PPF filters to control the first six modes of the piezobeam. Modes 4, 5 and 6 are controlled from the second actuator/sensor location, and Modes 1, 2 and 3 are controlled from the actuator/sensor at the root of the beam. Root contour methods described in Chapter 5 are used to synthesize the two sets of filters, and the stability condition of Chapter 4 is used to confirm MIMO stability.

Good performance was achieved in the first four modes. The performance of Modes 5 and 6 was below design, indicating too much sensitivity to error in the plant models. Spillover into Modes 7 and 8 increased their damping. In general, the damping ratios of all modes were increased and no instability was observed. Some softening, however, was observed due to the stiffness perturbing effects of the higher mode PPF filters.

6.1 Plant Characterization

The location of the second actuator/sensor pair was determined using NASTRAN generated mode shape estimates of the modal coupling factors for

four candidate locations. Once the best location was determined and the ceramics were adhered to the beam, two open loop plant models, one for each actuator/sensor pair, were calculated from frequency function measurements using the method described in Section (5.1.2). Additionally, a plant model for the first three modes under the influence of the Mode 4, 5 and 6 controller was calculated. This model was used for synthesizing the lower mode filters.

6.1.1 Selection of Second Actuator/Sensor Location

The location of the second actuator/sensor pair, which is used to control Modes 4, 5 and 6 was selected to provide as high participation factors for these modes as possible at a single location. Candidate locations were selected based on mode shapes of the SISO piezobeam given in Appendix B. Four locations were analyzed at distances of 0.75 in., 1.0 in., 1.25 in., and 1.5 in. down from the first pair. The relative participation factors $(D_i C_i/\omega_i^2)$ for the four cases are shown in the bar charts of Figures (6.1a–d). The participation coefficients for the first pair at the root of the beam are labeled "set at nodes 2–7."

The location at 1.25 in. down from the first pair gives the best overall participation for Modes 4, 5 and 6 and was chosen for use in the MIMO experiment. The schematic for the two actuator/sensor locations is shown in Figure (6.2).

6.1.2 Open Loop Plant Models

Two open loop plant models were formulated following the method of Section (5.1.2), one for each actuator/sensor location. They retain the first six modes. The second subscript on the transfer function name pertains to the

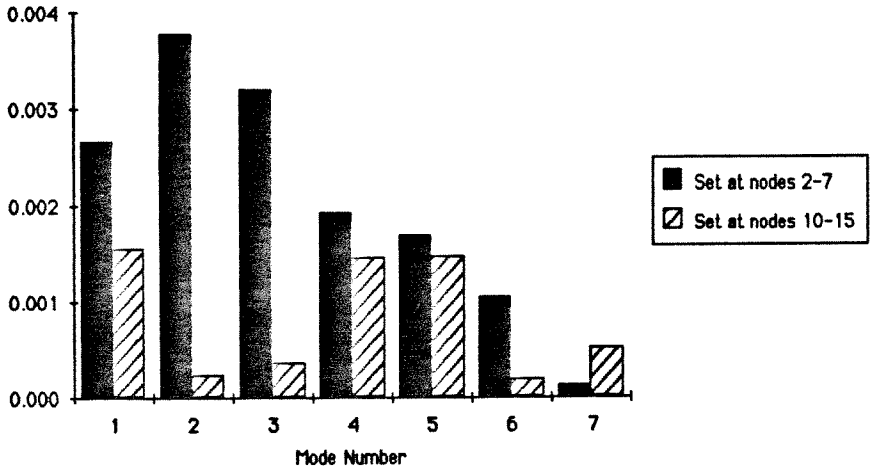

Figure 6.1a Modal participation factors for two actuator locations. Second pair at 0.75 in. down from the first pair.

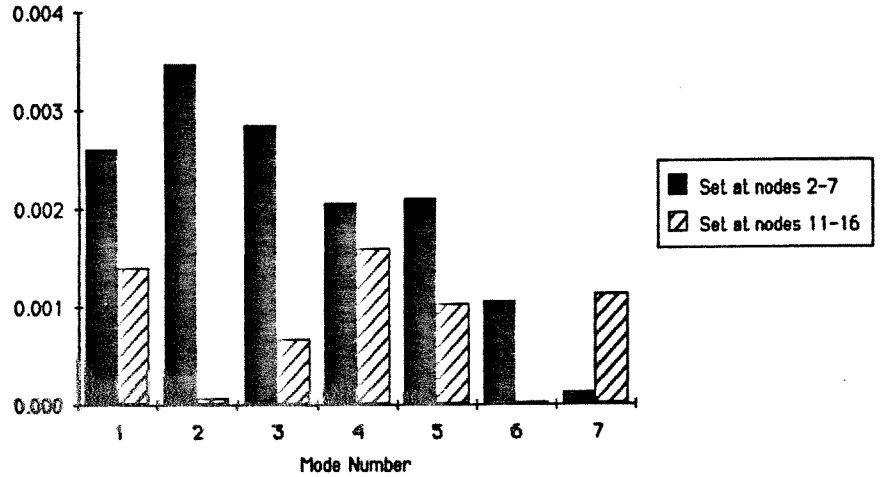

Figure 6.1b Modal participation factors for second pair at 1.0 in. down from the first pair.

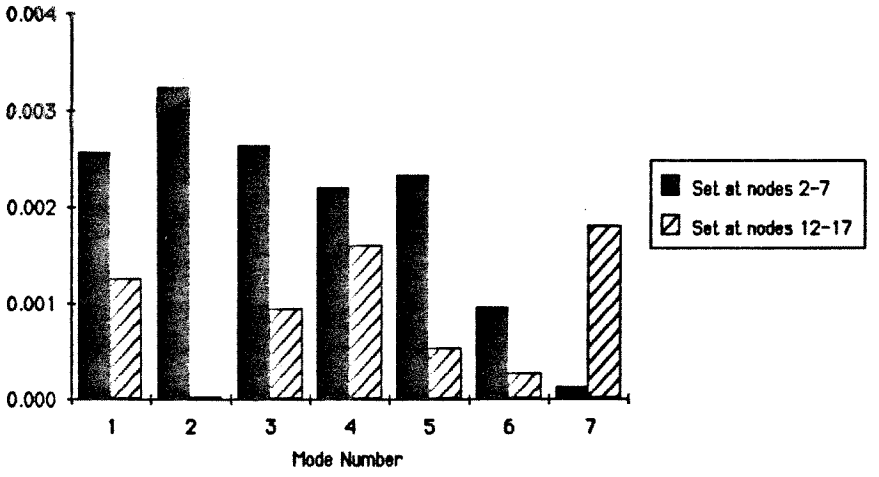

Figure 6.1c Modal participation factors for second pair at 1.25 in. down from the first pair.

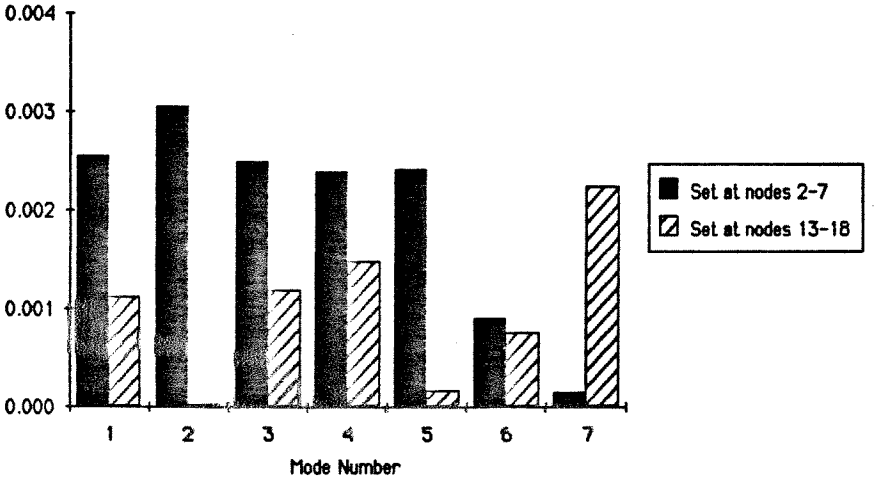

Figure 6.1d Modal participation factors for second pair at 1.5 in. down from the first pair.

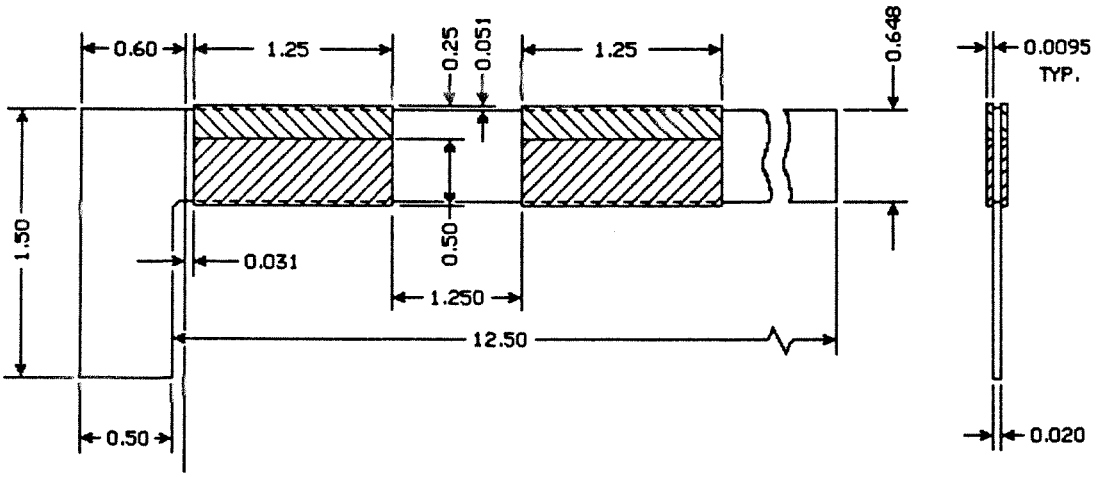

Figure 6.2 Actuator/Sensor locations for MIMO piezobeam. All dimensions in inches.

actuator/sensor pair number.

$$P_{61}(s) = \frac{7.83}{s^2 + 2\zeta_1\omega_1 s + \omega_1^2} + \frac{214}{s^2 + 2\zeta_2\omega_2 s + \omega_2^2} + \frac{1{,}129}{s^2 + 2\zeta_3\omega_3 s + \omega_3^2} + \frac{2{,}650}{s^2 + 2\zeta_4\omega_4 s + \omega_4^2} + \frac{5{,}162}{s^2 + 2\zeta_5\omega_5 s + \omega_5^2} + \frac{5{,}414}{s^2 + 2\zeta_6\omega_6 s + \omega_6^2} + 0.0354, \tag{6.1.1}$$

$$P_{62}(s) = \frac{4.49}{s^2 + 2\zeta_1\omega_1 s + \omega_1^2} + \frac{0.17}{s^2 + 2\zeta_2\omega_2 s + \omega_2^2} + \frac{650}{s^2 + 2\zeta_3\omega_3 s + \omega_3^2} + \frac{2{,}763}{s^2 + 2\zeta_4\omega_4 s + \omega_4^2} + \frac{1{,}350}{s^2 + 2\zeta_5\omega_5 s + \omega_5^2} + \frac{8{,}500}{s^2 + 2\zeta_6\omega_6 s + \omega_6^2} + 0.0430. \tag{6.1.2}$$

6.1.3 Compensation of Non-Ideal Sensor Behavior by Pole-Zero Cancellation

It was found in Chapter 5 that the non-ideal sensor dynamics reduces the stability margin of the closed loop system. A circuit that nearly cancels the

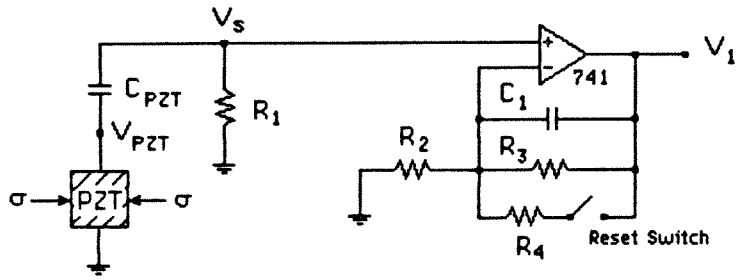

Figure 6.3 Sensor shunt and compensator circuit.

sensor dynamics is shown in Figure (6.3). The sensor buffer amplifier of the SISO experiments is replaced by a dynamic filter with one pole and one zero, which can be adjusted to nearly cancel the pole and zero of the shunt-induced high-pass filter. The differential equation describing the compensator portion of the circuit is

$$C_1 \frac{d}{dt}(V_1 - V_s) + \frac{V_1 - V_s}{R_3} = \frac{V_s}{R_2}. \tag{6.1.3}$$

Taking the Laplace transform gives the transfer function as

$$\frac{\hat{V}_1(s)}{\hat{V}_s(s)} = \frac{s + (\frac{1}{R_3 C_1} + \frac{1}{R_2 C_1})}{s + \frac{1}{R_3 C_1}}. \tag{6.1.4}$$

The zero, which is located on the negative real axis at: $-(1/R_3C_1 + 1/R_2C_1)$, can be placed at the pole location of the shunt high-pass filter; and the pole, located on the real axis at: $-1/R_3C_1$, can be placed very near the high-pass zero at the origin. What had been a widely spaced pole-zero pair can be converted into a nearly cancelled pole-zero pair at the origin. The small residual dynamics occurs at such a low frequency that it can be ignored in the present case.

6.2 MIMO Control Synthesis

The strategy for the MIMO experiment is to design a local PPF control system, where the first three modes are controlled from the actuator near the root of the beam, and the next three modes are controlled from the actuator nearer to the free end. The approach to synthesis takes advantage of the fact that PPF filters produce very weak upward control spillover due to their two pole rolloff.

The first step is to design the Mode 4, 5 and 6 control system by means of the root contour techniques, using the open loop plant transfer function $P_{62}(s)$. There will be downward control spillover into Modes 1 and 3, which will change their pole locations. There is no spillover into Mode 2 because there is virtually no participation in that mode from actuator/sensor location 2 as shown in Figure (6.1c). With the system operating closed loop at the second actuator/sensor pair, another identification test is performed to identify the new "open loop" plant at the first actuator/sensor pair. The Mode 1, 2 and 3 control compensator is then designed based on this new plant model. Since there is very little upward spillover, the lower mode control filters will not affect the design at Modes 4, 5 and 6. Finally, the stability condition of Theorem (4.5.1) is evaluated for a six mode model to check MIMO closed loop stability.

6.2.1 Synthesis for Modes 4, 5 and 6

The modal participation factors for Modes 4, 5 and 6 at the location of the second actuator are significantly lower than those for Modes 1, 2 and 3 at the actuator near the root of the beam. This can be seen from the chart of Figure (6.1c). As a consequence, if PPF filters with damping ratios in the range of 0.2 are used, the gains required for pole coalescence are higher than

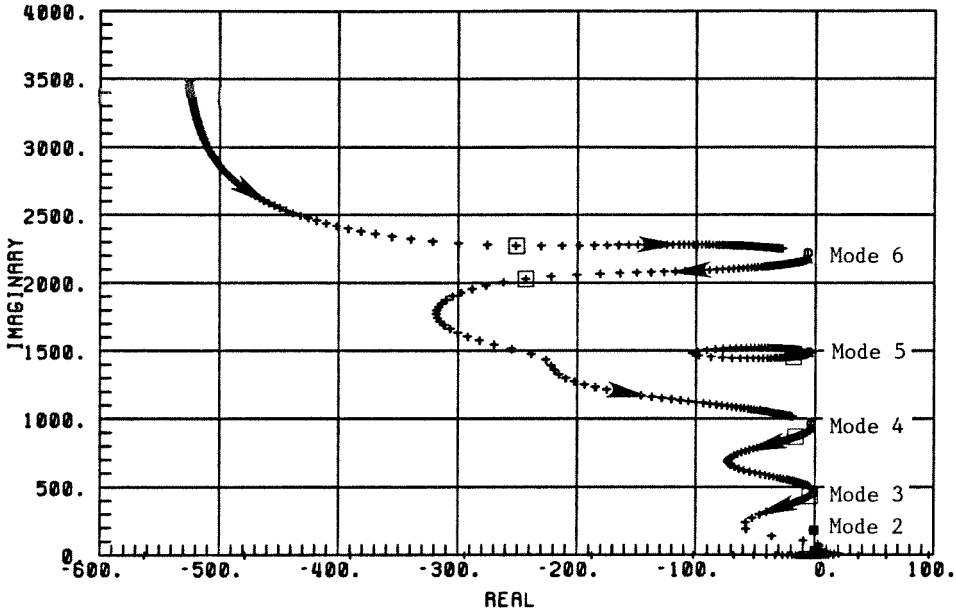

Figure 6.4 Mode 6 PPF filter with $\omega_{f6} = 3{,}500$ rad/sec and $\zeta_{f6} = 0.15$. Boxes indicate pole locations at $g_6 = 14.2$.

for the SISO experiments, as is shown in Figure (6.4). Here, a filter with a damping ratio of 0.15 is used to control Mode 6. The optimal gain for Mode 6 control is 14.2, as indicated by the boxes in the figure. This is too large a gain for a single filter. Moreover, the filter frequency is sufficiently high that it will begin to encroach on the frequency region of Mode 7. The modes are becoming more densly spaced at these frequencies, resulting in increased coupling between adjacent structural poles and highly damped control filters.

The solution to this problem is either to decrease the damping ratios of the PPF filters, or to use fewer filters than modes. We choose to decrease the filter damping ratios. The filter values summarized in Table (6.2.1) result in the

Table 6.2.1 Filter Parameters for Modes 4, 5 and 6

Filter No.	ω (rad/sec)	ς	Gain
6	2,450	0.05	7.0
5	1,800	0.05	5.0
4	1,150	0.07	2.9

root locus of Figure (6.5). This root locus plot shows the effect of simultaneously increasing all the filter gains at rates proportional to their design values. Figure (6.6) shows the movement of the Mode 1, 2 and 3 poles.

6.2.2 Synthesis for Modes 1, 2 and 3

With the Mode 4, 5 and 6 control system operating closed loop, a system identification test was performed at the actuator location near the root of the beam and a plant model calculated for the first three modes. The resulting plant model P_{31}, which is used for the design of the Mode 1, 2 and 3 filters, is given by

$$P_{31}(s) = \frac{6.0}{s^2 + 2\varsigma_1\omega_1 s + \omega_1^2} + \frac{315}{s^2 + 2\varsigma_2\omega_2 s + \omega_2^2} + \frac{1{,}580}{s^2 + 2\varsigma_3\omega_3 s + \omega_3^2} + 0.0354. \tag{6.2.1}$$

The filter values summarized in Table (6.2.2) result in the root locus of Figures (6.7a,b).

Table 6.2.2 Filter Parameters for Modes 1, 2 and 3

Filter No.	ω (rad/sec)	ς	Gain
3	480	0.20	5.7
2	230	0.25	4.3
1	45	0.35	2.9

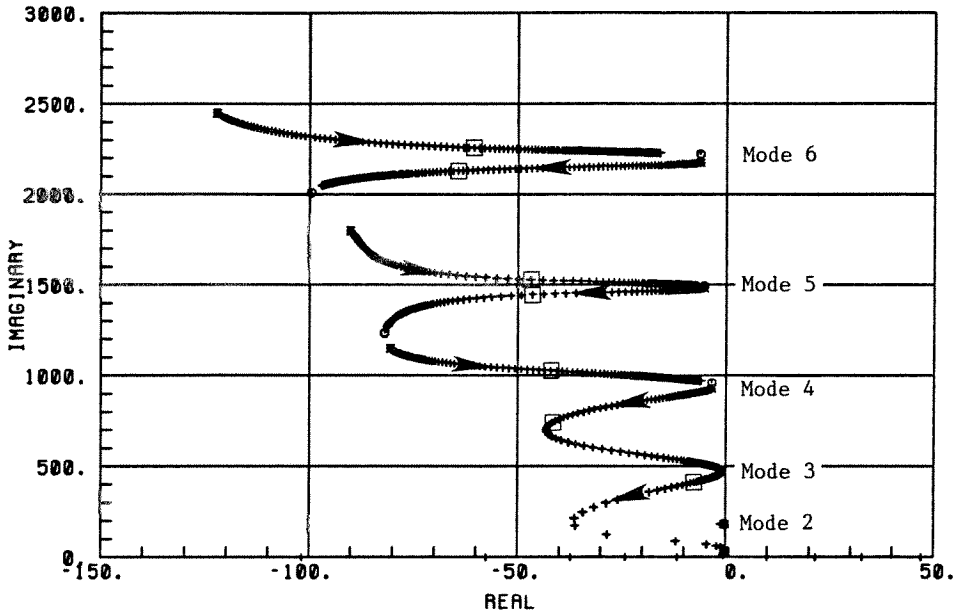

Figure 6.5 Root locus showing effect of Mode 4, 5 and 6 control on Modes 1 through 6.

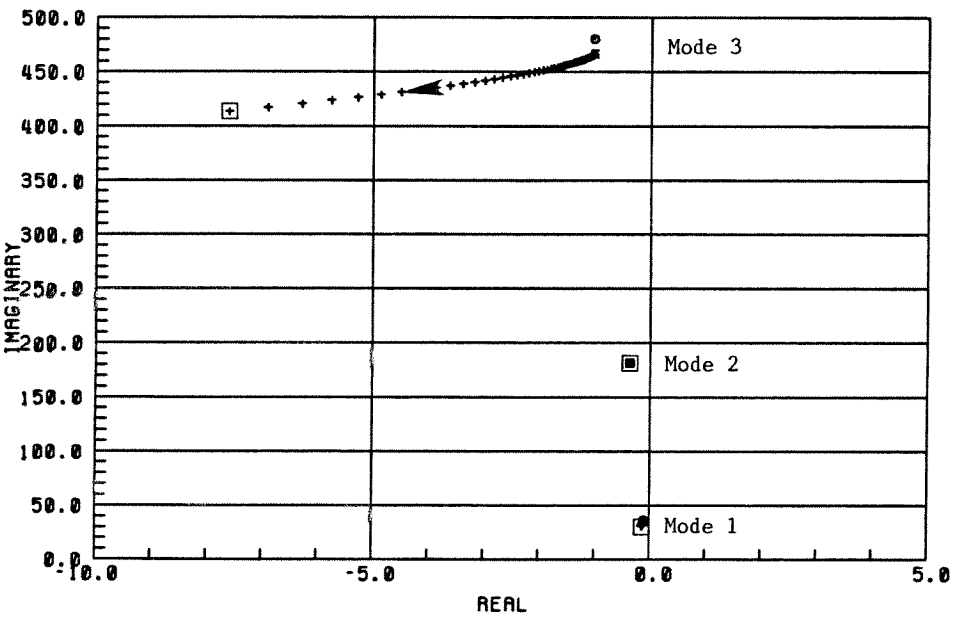

Figure 6.6 Root locus showing effect of Mode 4, 5 and 6 control on Modes 1, 2 and 3.

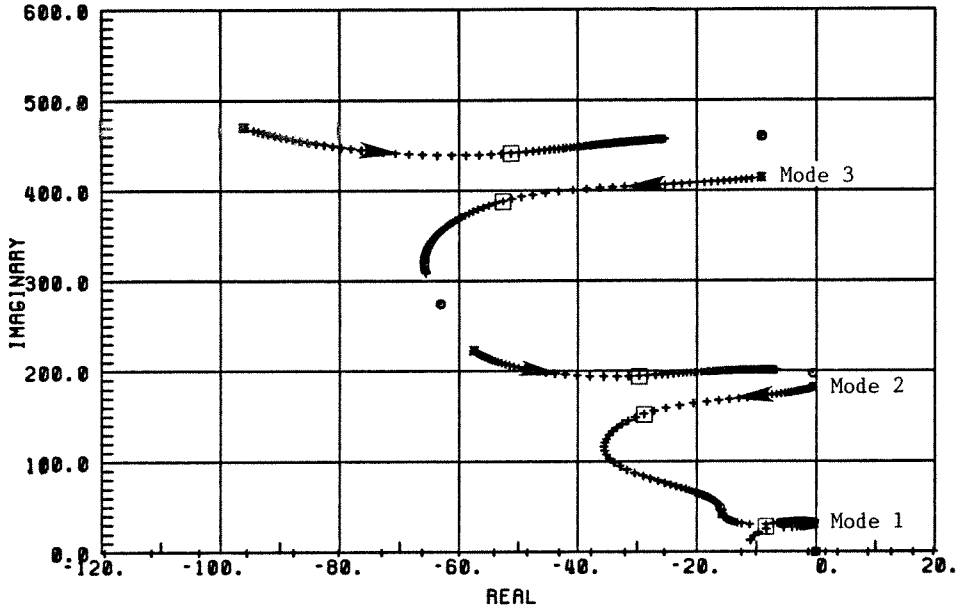

Figure 6.7a Root locus showing effect of Mode 1, 2 and 3 control on perturbed Modes 1, 2 and 3. Boxes indicate design gain pole locations.

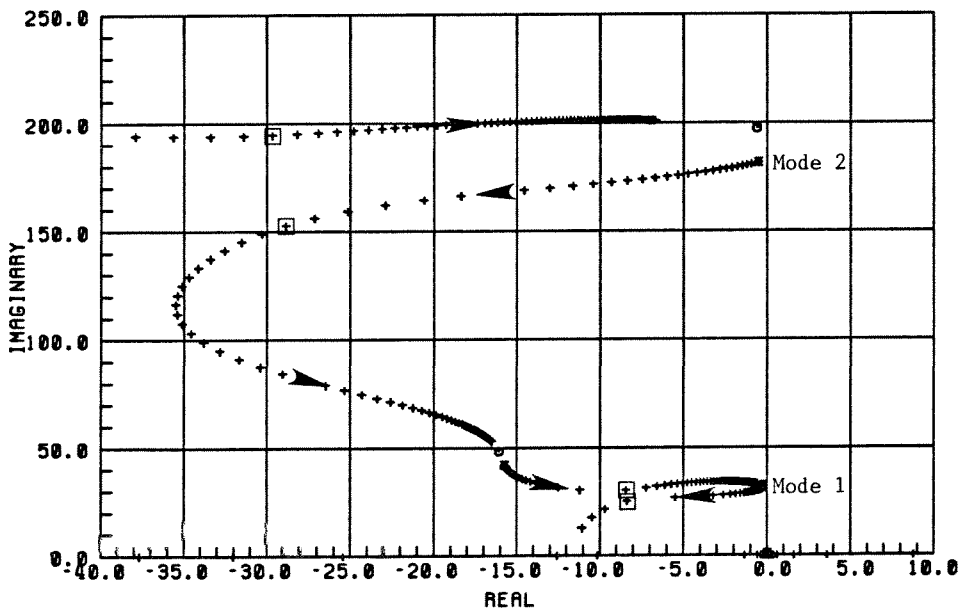

Figure 6.7b Root locus showing increased resolution on Modes 1, 2 and 3.

As a check of stability with both sets of filters closed loop, we will evaluate the eigenvalues of the matrix $\Omega - a_1 a_2 C^T G C$, which is a necessary and sufficient condition for stability from Theorem (4.5.1). The theorem applies to systems with compatible sensors and actuators. Our sensors and actuators are not strictly compatible but are nearly so for the lower modes. We shall apply the theorem assuming that they are compatible for all modes.

The numerator of the i^{th} term of the plant transfer function given in Eq. (4.3.9) is

$$n_i = a_1 a_2 \, D_i C_i. \tag{6.2.2}$$

Assuming the the D_i and C_i are equal (in fact they are nearly equal for the lower modes), we can derive estimates of the C_i from the numerators of Eqs. (6.1.1) and (6.1.2) as

$$C_{ij} = \sqrt{\frac{n_{ij}}{a_1 a_2}}, \tag{6.2.3}$$

where the second subscript refers to the actuator/sensor location. The constant $a_1 a_2 = 1.47$, and the matrices are listed below.

$$\Omega = 10^3 \begin{bmatrix} 1.26 & 0 & 0 & 0 & 0 & 0 \\ 0 & 33.7 & 0 & 0 & 0 & 0 \\ 0 & 0 & 218. & 0 & 0 & 0 \\ 0 & 0 & 0 & 8.60 \times 10^2 & 0 & 0 \\ 0 & 0 & 0 & 0 & 2.20 \times 10^3 & 0 \\ 0 & 0 & 0 & 0 & 0 & 4.71 \times 10^3 \end{bmatrix} \tag{6.2.4a}$$

$$C = \begin{bmatrix} 2.31 & 12.1 & 27.7 & 42.5 & 59.3 & 60.7 \\ 2.31 & 12.1 & 27.7 & 42.5 & 59.3 & 60.7 \\ 2.31 & 12.1 & 27.7 & 42.5 & 59.3 & 60.7 \\ 1.75 & 0.34 & 21.0 & 43.4 & 30.3 & 76.0 \\ 1.75 & 0.34 & 21.0 & 43.4 & 30.3 & 76.0 \\ 1.75 & 0.34 & 21.0 & 43.4 & 30.3 & 76.0 \end{bmatrix} \tag{6.2.4b}$$

$$G = \begin{bmatrix} 2.9 & 0 & 0 & 0 & 0 & 0 \\ 0 & 4.3 & 0 & 0 & 0 & 0 \\ 0 & 0 & 5.7 & 0 & 0 & 0 \\ 0 & 0 & 0 & 2.9 & 0 & 0 \\ 0 & 0 & 0 & 0 & 5.0 & 0 \\ 0 & 0 & 0 & 0 & 0 & 7.0 \end{bmatrix} \tag{6.2.4c}$$

The matrix $\Omega - a_1 a_2 C^T G C$ is symmetric and hence its eigenvalues are real. The six eigenvalues are listed below and all are positive, indicating that the system is LAS.

$$\begin{aligned} \lambda_1 &= 4.53 \times 10^6 \\ \lambda_2 &= 2.11 \times 10^6 \\ \lambda_3 &= 7.80 \times 10^5 \\ \lambda_4 &= 1.89 \times 10^5 \\ \lambda_5 &= 3.02 \times 10^4 \\ \lambda_6 &= 1.01 \times 10^3 \end{aligned} \tag{6.2.5}$$

The six mode control was found in practice to be stable.

6.3 MIMO Control Results

The steady-state response is shown in Figures (6.8a,b) through (6.11a,b). Each set of figures show the same measurements taken at each sensor location. Figures (6.8a,b) and (6.9a,b) show three measurements in each frame. The dashed line indicates the open loop response. The dash–dot–dash line shows the frequency response when only the Mode 4, 5 and 6 controller is closed loop.

The solid line is the six mode MIMO closed loop response. Because there is insignificant upward spillover from the lower mode filters, Figures (6.10a,b) and (6.11a,b) show only the open loop and MIMO closed loop response.

Figure (6.8a) shows the response in the region of Modes 1 and 2 for the sensor at the root of the beam. The curve for "high mode control," i.e., the Mode 4, 5 and 6 control closed loop, shows a reduction in amplitude for Mode 1 and no change at all for Mode 2. This is consistent with the stabilizing downward spillover into Mode 1 and the very small participation for Mode 2 at the location that the high mode control is implemented. The amplitude for both modes is greatly reduced in the MIMO case.

The response for the second sensor location, shown in Figure (6.8b), indicates a somewhat different situation. The high mode control curve for Mode 1 indicates that the damping has been increased, which can be seen from the increased half-power bandwidth of the spike, but the peak amplitude of response is *greater* than for the open loop response. This is due to the *softening* effect of the Positive Position Feedback filters. Below the dynamic region of the filters (which is below Mode 4 for the high mode control case), the stiffness of the structure is perturbed toward singularity. This means that it is *softened* in this region. In effect, the mode shape has been changed to allow more bending at the second actuator location. The softening occurs at the second actuator location, since that is where the high mode control filters are effected. The MIMO response indicates that the softening effects are counteracted by the lower mode control filters implemented at a different location.

A similar but more pronounced softening effect is seen in the region of Mode 3 in Figure (6.9b). In this case, even under MIMO control, the Mode 3

response at the second sensor location is reduced by only about half. It appears that it is best not to control higher modes only, or softening may become substantial. Figure (6.9b) also shows that the Mode 4 and Filter 4 poles are fairly widely spaced and appear as two distinct humps on either side of the open loop peak. This is consistant with the pole locations of Figure (6.5).

Figure (6.10b) indicates that the closed loop poles for Mode 5 are not near the design values. The structural pole, indicated by the sharp closed loop spike, is only moderately more damped than for open loop. The Mode 5 filter pole can be seen as a highly damped hump at slightly higher frequency. Evidently, the Mode 5 filter design placed the poles too close together which made them too sensitive to modeling errors. The Mode 5 pole pair shown in Figure (6.5) is the closest pair in the design. Since the response is the sum of the individual modal responses, the Mode 5 spike rides on top of the highly damped filter hump and so appears to be a higher amplitude response than for open loop. The Mode 6 response is significantly reduced.

Figures (6.11a,b) show the spillover into Modes 7 and 8. Their frequencies and damping ratios are increased slightly, as expected. Figure (6.12) shows a combined plot of the open and closed loop response for the region of 2 to 800 Hz, including Modes 1 through 8. These data are for the sensor at the root of the beam.

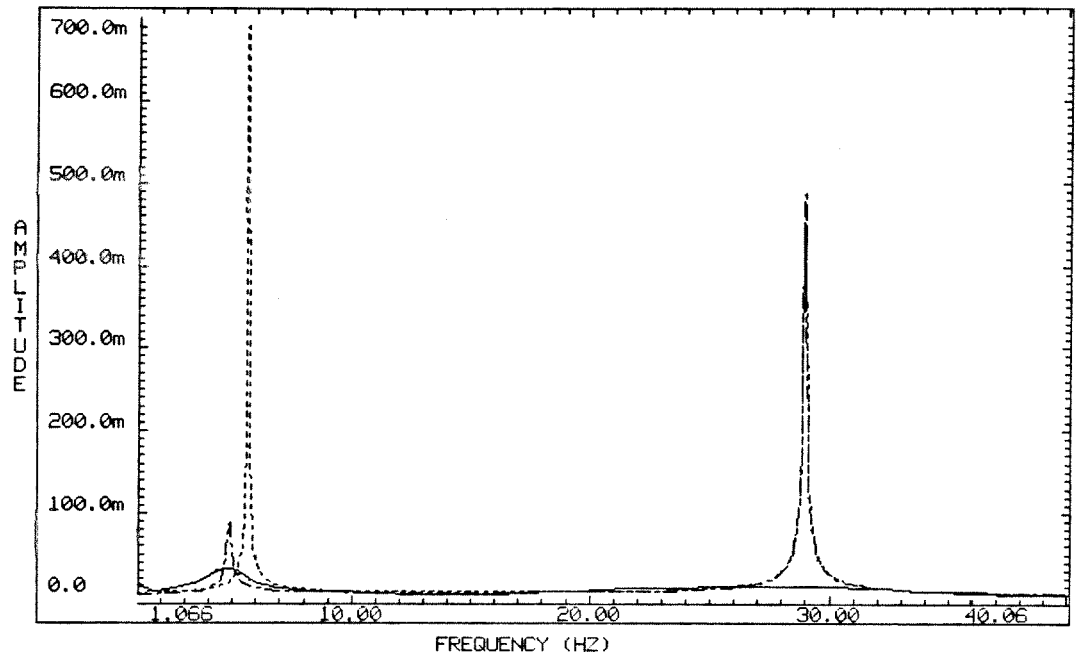

Figure 6.8a Sensor 1 response functions for the region of Modes 1 and 2. Dashed: open loop, dash–dot–dash: high mode, solid: MIMO closed loop.

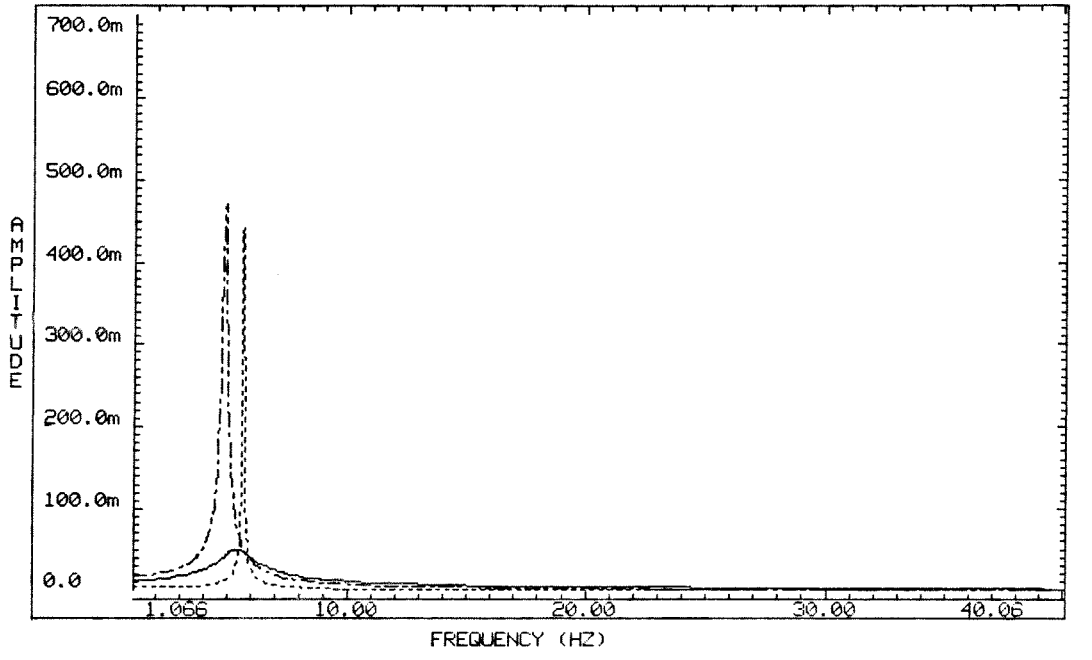

Figure 6.8b Sensor 2 response functions for the region of Modes 1 and 2. Dashed: open loop, dash–dot–dash: high mode, solid: MIMO closed loop.

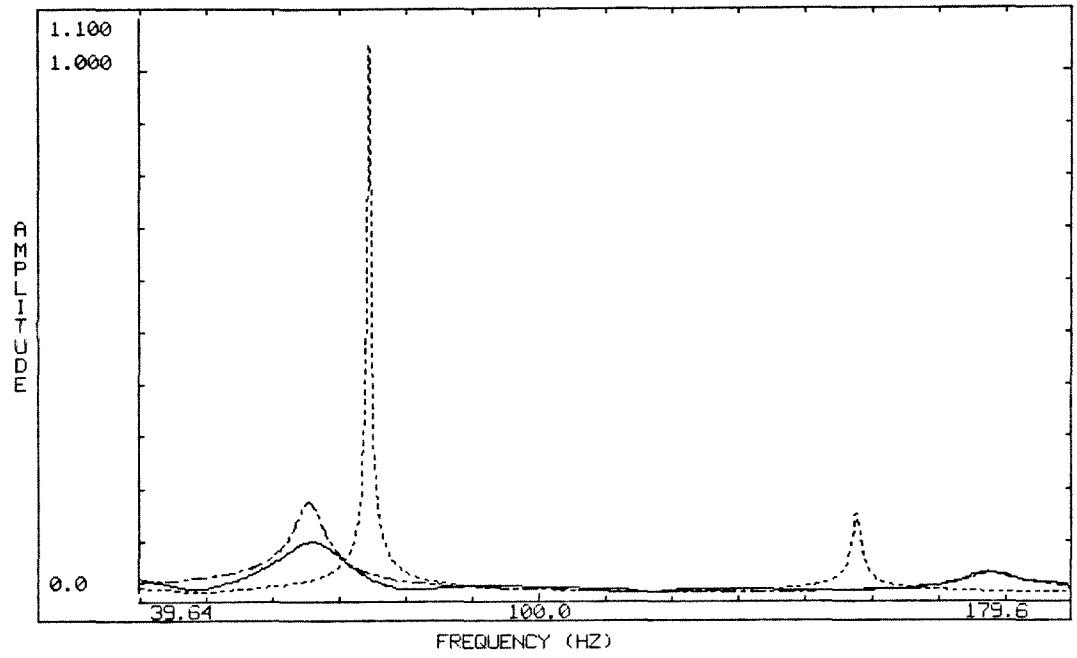

Figure 6.9a Sensor 1 response functions for the region of Modes 3 and 4. Dashed: open loop, dash–dot–dash: high mode, solid: MIMO closed loop.

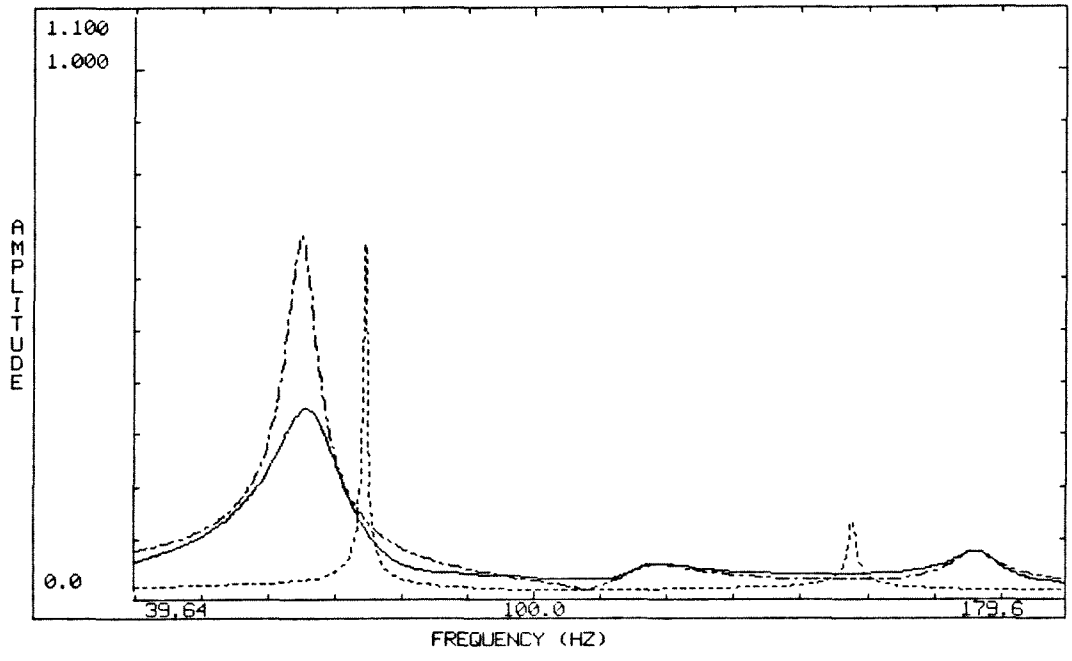

Figure 6.9b Sensor 2 response functions for the region of Modes 3 and 4. Dashed: open loop, dash–dot–dash: high mode, solid: MIMO closed loop.

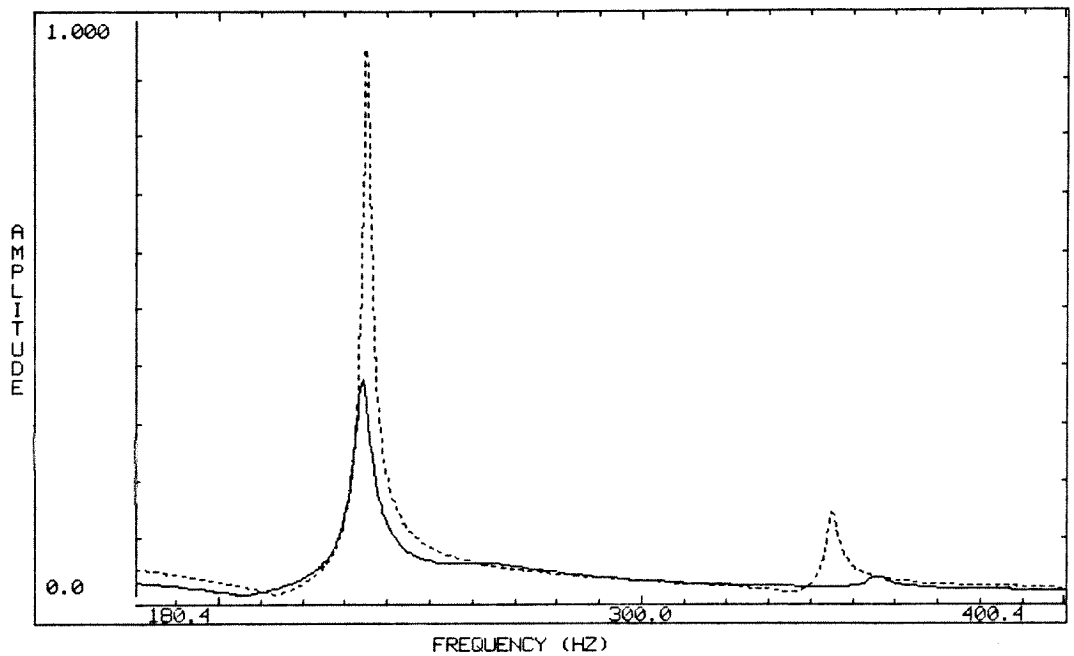

Figure 6.10a Sensor 1 response functions for the region of Modes 5 and 6. Dashed line – open loop. Solid line – MIMO closed loop.

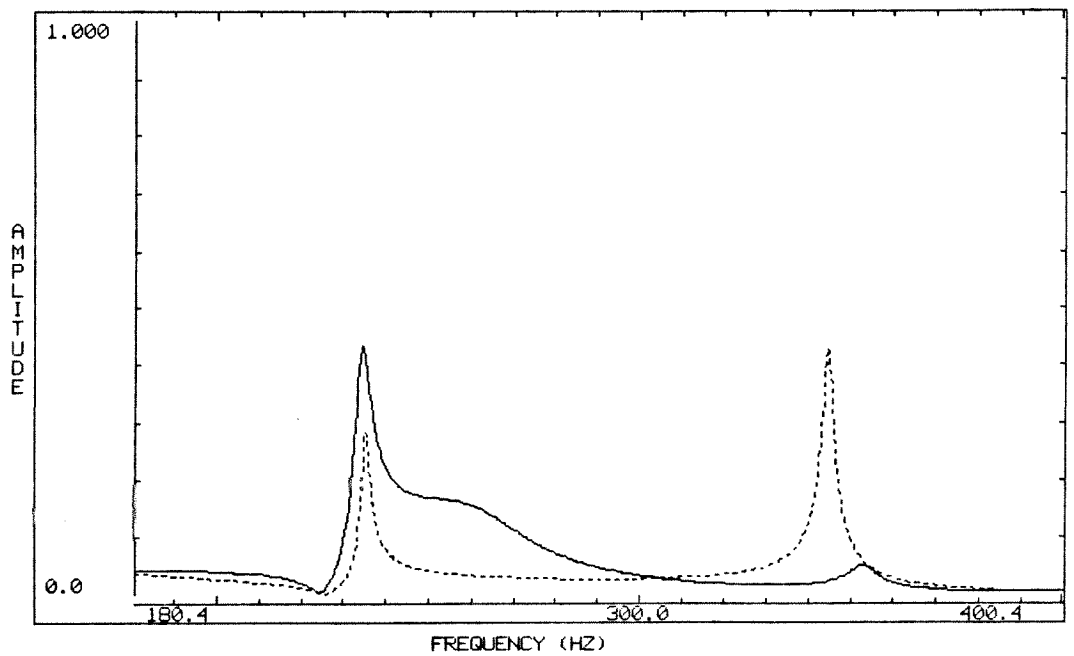

Figure 6.10b Sensor 2 response functions for the region of Modes 5 and 6. Dashed line – open loop. Solid line – MIMO closed loop.

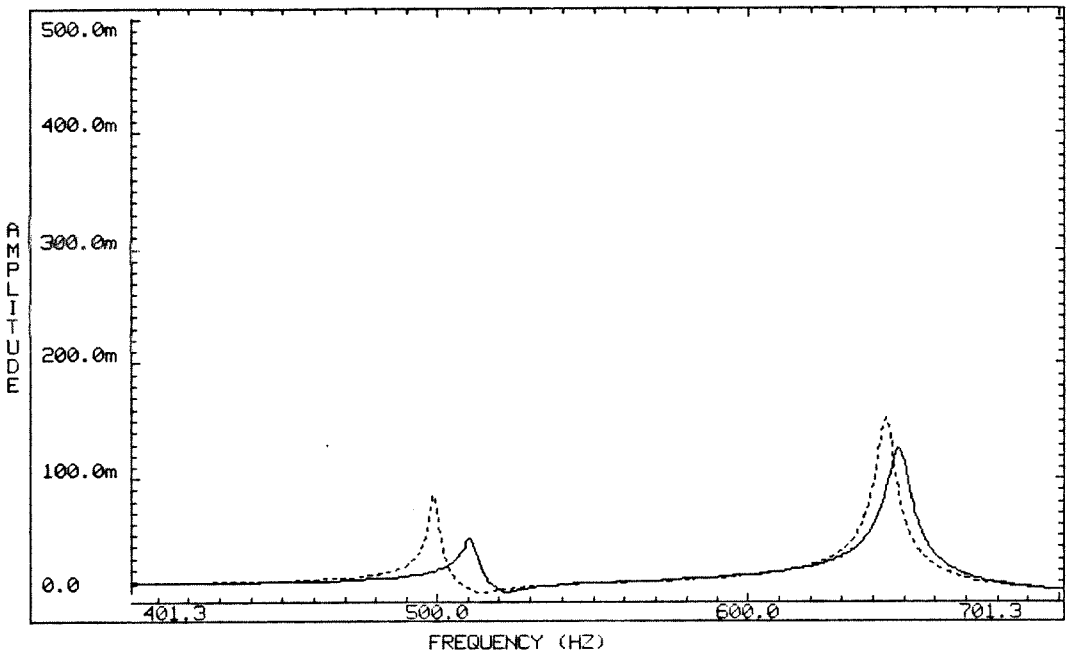

Figure 6.11a Sensor 1 response functions for the region of Modes 7 and 8. Dashed line – open loop. Solid line – MIMO closed loop.

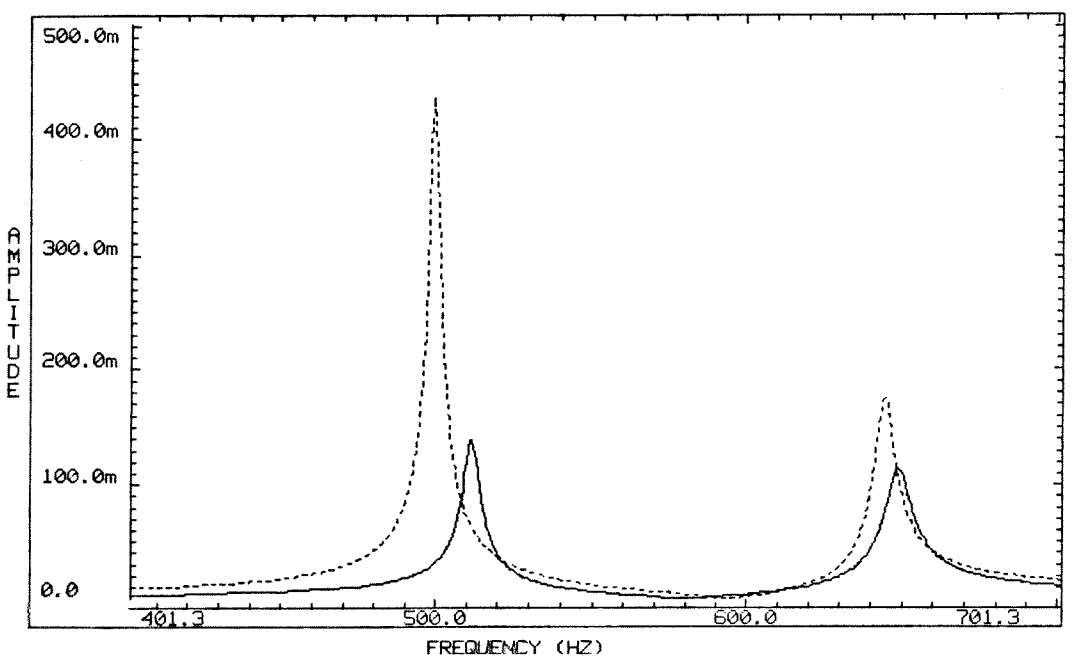

Figure 6.11b Sensor 2 response functions for the region of Modes 7 and 8. Dashed line – open loop. Solid line – MIMO closed loop.

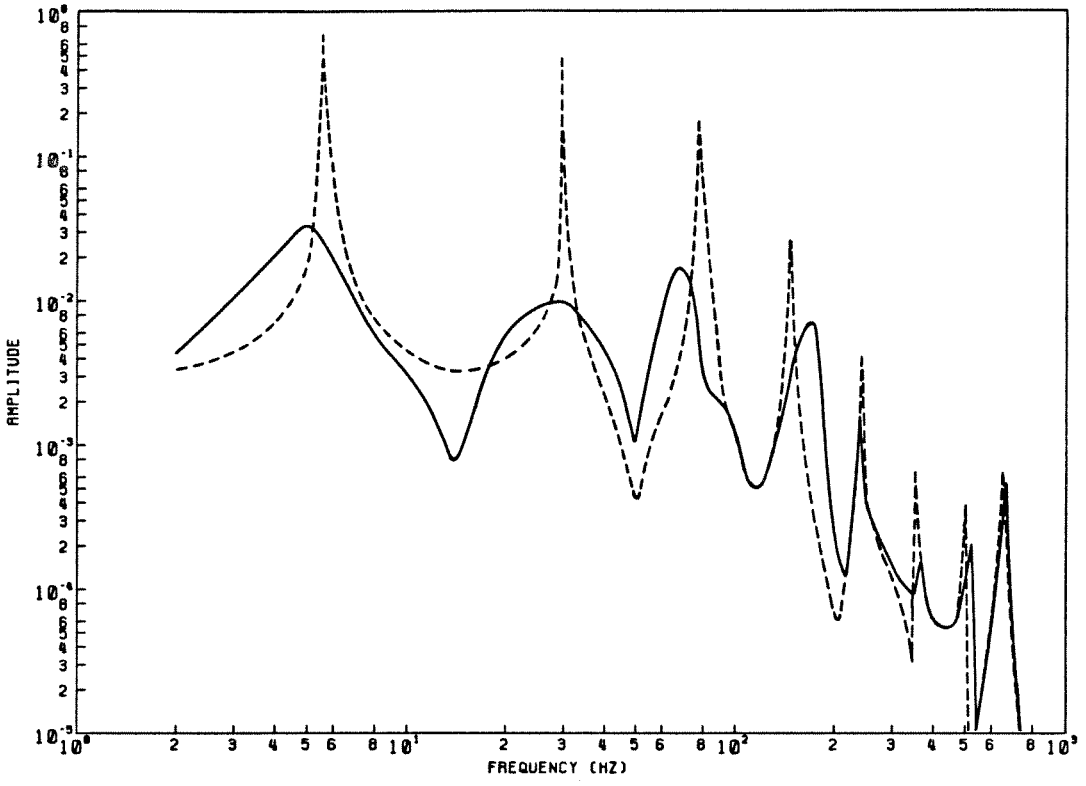

Figure 6.12 Open loop and MIMO closed loop frequency response functions for Sensor 1.

Figures (6.13a–f) show the open loop and MIMO closed loop free decay responses for Modes 1 through 6. As can be seen, there is very dramatic reduction of the settling times for Modes 1 through 4; Modes 5 and 6 are somewhat reduced. The superimposed low frequency oscillation seen in Figures (6.13b–f) is the 10 Hz fixture mode and is an artifact of the test apparatus.

A summary of the MIMO performance results is given in Tables (6.3.1) and (6.3.2). Table (6.3.1) contains the results for the six controlled modes, and Table (6.3.2) shows the upward spillover into Modes 7 and 8. The results for Modes 1 through 4 are very dramatic. The Mode 5 control performance is poor indicating that the poles were designed too close together. Mode 6 performance is significantly below design, which may indicate reduced performance robustness

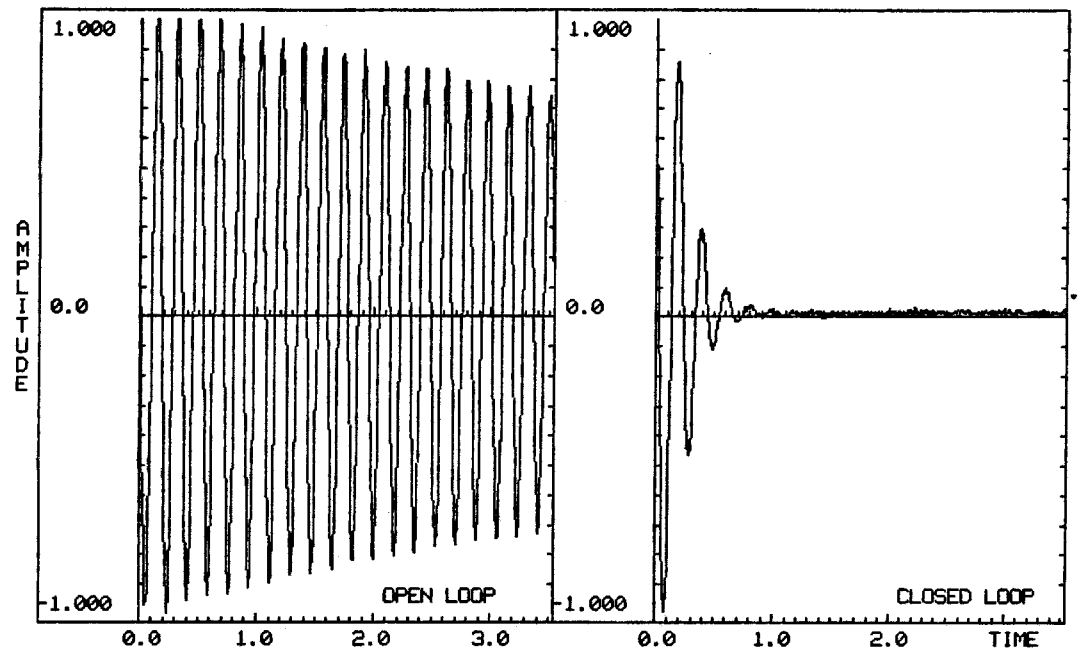

Figure 6.13a MIMO open loop and closed loop free decay for Mode 1.

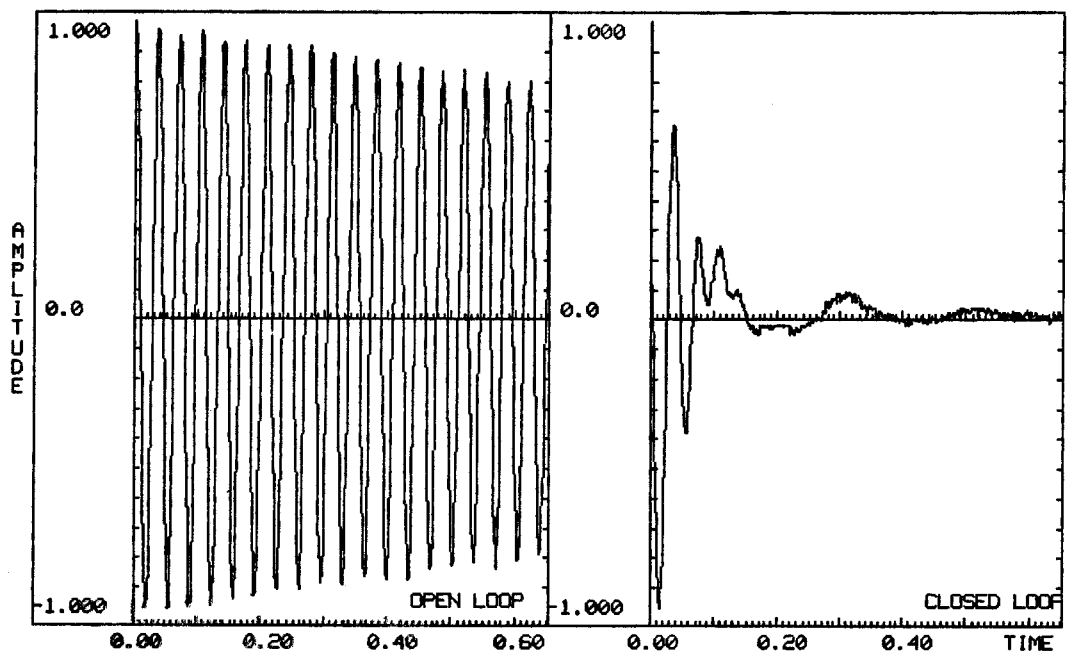

Figure 6.13b MIMO open loop and closed loop free decay for Mode 2.

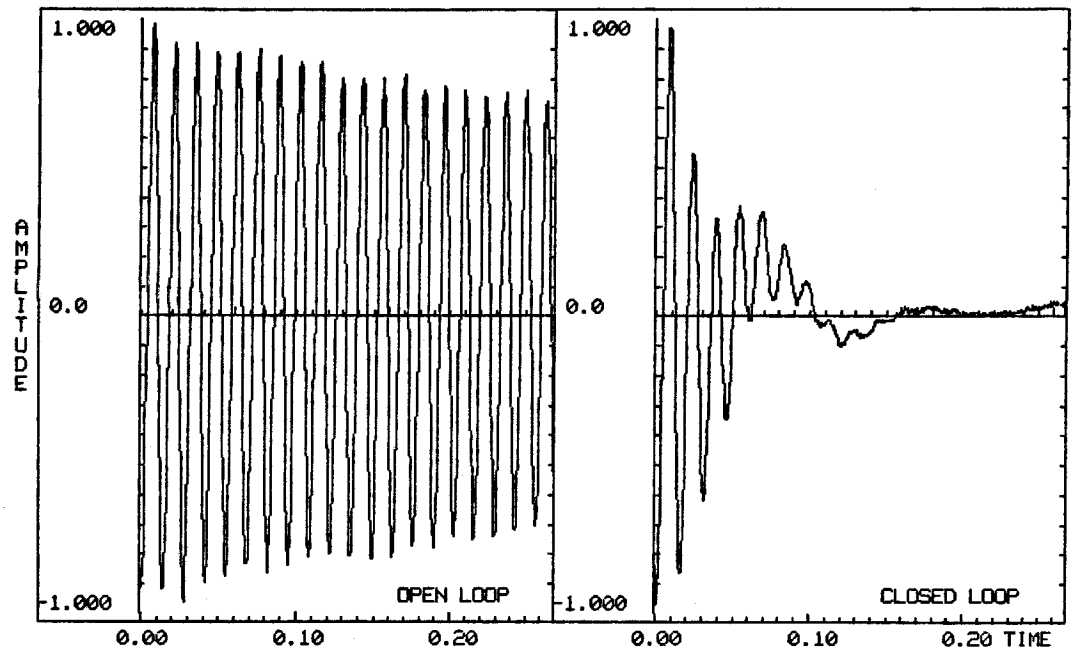

Figure 6.13c MIMO open loop and closed loop free decay for Mode 3.

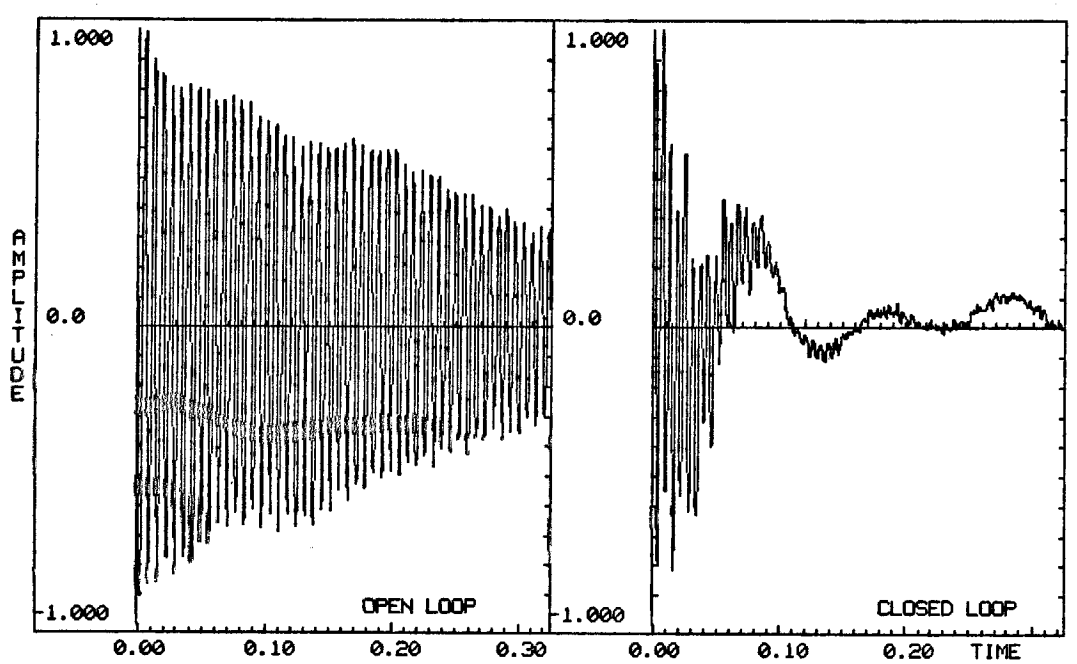

Figure 6.13d MIMO open loop and closed loop free decay for Mode 4.

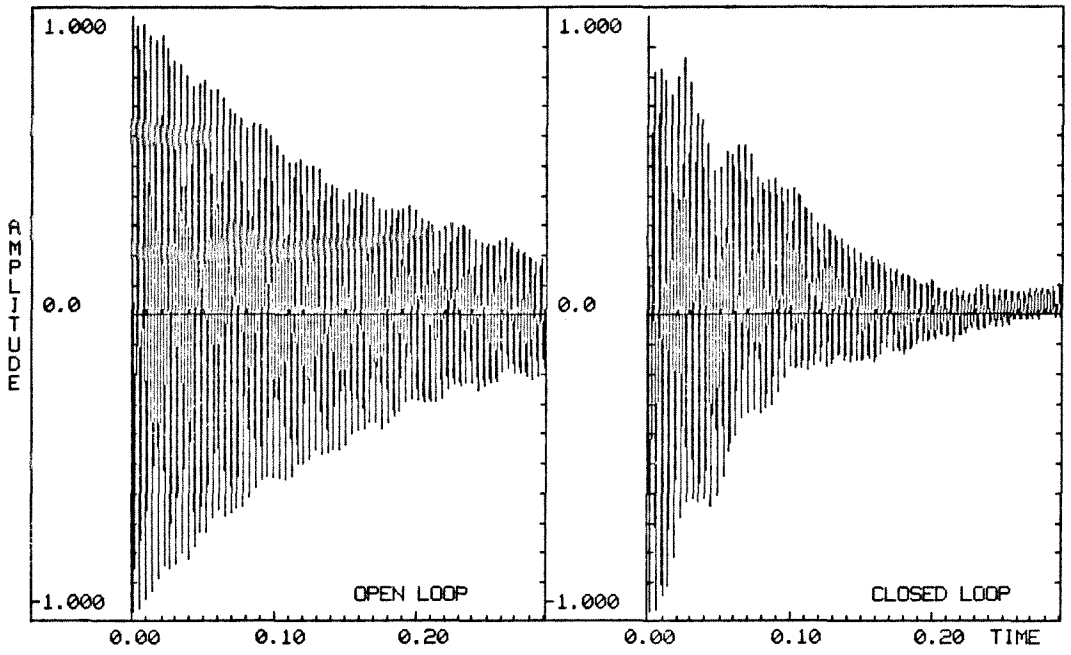

Figure 6.13e MIMO open loop and closed loop free decay for Mode 5.

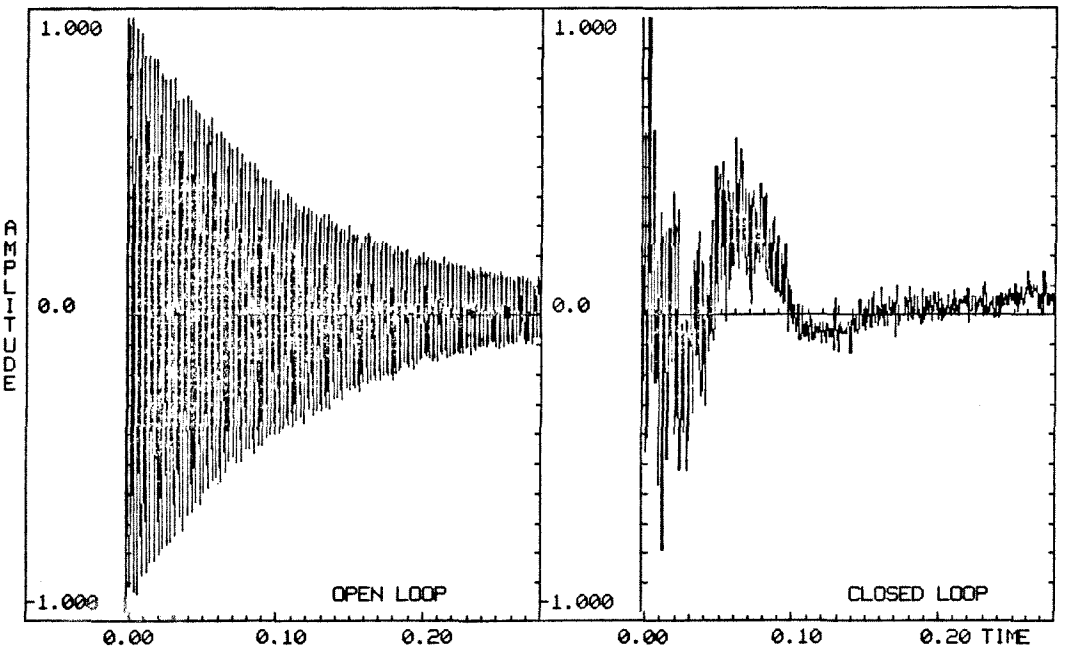

Figure 6.13f MIMO open loop and closed loop free decay for Mode 6.

Table 6.3.1 Effect of MIMO Control on Modes 1 through 6

Sensor 1	Mode 1			Filter 1		
	$\varsigma_1(\%)$	$\varsigma_1\omega_1$	$\varsigma_1\omega_1^2$	$\varsigma_{f1}(\%)$	$\varsigma_{f1}\omega_{f1}$	$\varsigma_{f1}\omega_{f1}^2$
Open Loop	0.33	0.116	4.11	35.0	15.8	709.
Closed Loop‡	20.0	5.93	176.	15.0	4.96	164.
*Percent Change**	*6,000*	*5,000*	*4,200*	—	—	—
Predicted†	31.5	8.37	200.	26.9	8.42	245.
Sensor 1	Mode 2			Filter 2		
	$\varsigma_2(\%)$	$\varsigma_2\omega_2$	$\varsigma_2\omega_2^2$	$\varsigma_{f2}(\%)$	$\varsigma_{f2}\omega_{f2}$	$\varsigma_{f2}\omega_{f2}^2$
Open Loop	0.19	0.352	64.1	25.0	57.5	1.32×10^4
Closed Loop‡	24.8	34.0	4.65×10^3	12.0	24.0	4.79×10^3
*Percent Change**	*13,000*	*9,600*	*7,200*	—	—	—
Predicted†	18.6	28.8	4.44×10^3	15.1	29.7	5.84×10^3
Sensor 1	Mode 3			Filter 3		
	$\varsigma_3(\%)$	$\varsigma_3\omega_3$	$\varsigma_3\omega_3^2$	$\varsigma_{f3}(\%)$	$\varsigma_{f3}\omega_{f3}$	$\varsigma_{f3}\omega_{f3}^2$
Open Loop	0.23	1.05	489.	20.0	96.0	4.61×10^4
Closed Loop‡	8.00	33.2	1.38×10^4	15.0	68.3	3.11×10^4
*Percent Change**	*3,400*	*3,100*	*2,700*	—	—	—
Predicted†	13.4	52.5	2.06×10^4	11.5	51.1	2.27×10^4
Sensor 2	Mode 4			Filter 4		
	$\varsigma_4(\%)$	$\varsigma_4\omega_4$	$\varsigma_4\omega_4^2$	$\varsigma_{f4}(\%)$	$\varsigma_{f4}\omega_{f4}$	$\varsigma_{f4}\omega_{f4}^2$
Open Loop	0.38	3.54	3.30×10^3	7.00	80.5	9.26×10^4
Closed Loop	4.05	29.8	2.19×10^4	2.23	23.4	2.46×10^4
*Percent Change**	*970*	*740*	*560*	—	—	—
Predicted†	5.44	41.0	3.08×10^4	4.10	42.1	4.32×10^4
Sensor 2	Mode 5			Filter 5		
	$\varsigma_5(\%)$	$\varsigma_5\omega_5$	$\varsigma_5\omega_5^2$	$\varsigma_{f5}(\%)$	$\varsigma_{f5}\omega_{f5}$	$\varsigma_{f5}\omega_{f5}^2$
Open Loop	0.39	5.73	8.42×10^3	5.00	90.0	1.62×10^5
Closed Loop	0.78	11.4	1.68×10^4	4.97	82.1	1.36×10^5
*Percent Change**	*100*	*100*	*100*	—	—	—
Predicted†	3.24	46.9	6.81×10^4	3.04	46.4	7.08×10^4
Sensor 2	Mode 6			Filter 6		
	$\varsigma_6(\%)$	$\varsigma_6\omega_6$	$\varsigma_6\omega_6^2$	$\varsigma_{f6}(\%)$	$\varsigma_{f6}\omega_{f6}$	$\varsigma_{f6}\omega_{f6}^2$
Open Loop	0.37	7.98	1.73×10^4	5.00	123.	3.00×10^6
Closed Loop‡	0.62	14.1	3.14×10^4	NM	NM	NM
*Percent Change**	*70*	*80*	*80*	—	—	—
Predicted†	3.03	64.7	1.38×10^5	2.67	60.2	1.36×10^5

* Percent Change Between Measured Values † Predicted Closed Loop Values

‡ May Contain Significant Error from FITTER NM Not Measurable

Table 6.3.2 MIMO Control Spillover into Modes 7 and 8

Sensor 2	Mode 7			Filter 7		
	$\varsigma_7(\%)$	$\varsigma_7\omega_7$	$\varsigma_7\omega_7^2$	$\varsigma_{f7}(\%)$	$\varsigma_{f7}\omega_{f7}$	$\varsigma_{f7}\omega_{f7}^2$
Open Loop	0.34	10.6	3.32×10^4	—	—	—
Closed Loop	0.45	15.9	5.09×10^4	—	—	—
*Percent Change**	*46*	*50*	*53*	—	—	—
Predicted†	—	—	—	—	—	—
Sensor 2	Mode 8			Filter 8		
	$\varsigma_8(\%)$	$\varsigma_8\omega_8$	$\varsigma_8\omega_8^2$	$\varsigma_{f8}(\%)$	$\varsigma_{f8}\omega_{f8}$	$\varsigma_{f8}\omega_{f8}^2$
Open Loop	0.36	11.3	3.55×10^4	—	—	—
Closed Loop	0.50	16.2	5.20×10^4	—	—	—
*Percent Change**	*40*	*43*	*46*	—	—	—
Predicted†	—	—	—	—	—	—

* Percent Change Between Measured Values † Closed Loop Values not Predicted

to modeling errors. It is difficult to determine if the resulting performance reduction is due to the PPF control strategy itself or to the difficulty in modeling and testing the structure at these very high frequencies. A more realistic test is needed to resolve this question.

Chapter 7

CONCLUSIONS

7.1 Concluding Remarks

This thesis has investigated the feasibility of using piezoelectric materials as dual structural elements/actuators for vibration suppression in Large Space Structures, and the use of *Positive Position Feedback* (PPF) as a vibration suppression control strategy. A flexible cantilever beam test structure was designed to incorporate many of the characteristics of Large Space Structures. Piezoelectric ceramic material was adhered to the beam and used to simulate an *active-member* on a space-truss type structure. Multi-mode vibration suppression was achieved with dramatic reduction in dynamic response.

Piezoelectric material was also used as a strain sensor. Strain was chosen as the only measurement quantity, since it is the quantity most intimately related to the elastic motion that is to be suppressed, and because it can be measured accurately at very low frequencies and g-levels. The actuators exert forces *internal* to the structure to effect the control which, together with strain measurement, completely decouples the rigid-body motion from the elastic vibratory motion. The actuation and sensing implementation consitutes a *space-realizable* control technique. The concept of a piezoelectric active-member appears to be a feasible approach to the actuation problem for the vibration suppression control objective.

The method of Positive Position Feedback, originally proposed by Caughey and Goh, has been demonstrated to be a promising technique for vibration suppression in Large Space Structures. A necessary and sufficient condition for

stability using Positive Position Feedback has been developed, involving a simple non-dynamic stability criterion which is in general easily satisfied. The experiments have provided new insight into the superior robust stability properties of Positive Position Feedback in relation to Large Space Structure control. In addition to being simple to implement, Positive Position Feedback appears to be immune from the destabilizing effects of observation and control spillover, as well as the destabilizing effects of finite actuator dynamics. No unintentional instability ever occurred in the course of the experiments. The phenomenon of softening was observed, which is a result of the perturbing effects on stiffness of PPF. Softening appears to be the price paid for increased robust stability.

The cantilever beam test structure was chosen because it is *structurally* the simplest structure that can exhibit the characteristics of Large Space Structures. From a controls point of view, however, this particular structure, together with the piezoelectric ceramic actuators and sensors, was somewhat pathological. The modal coupling of the sensors and actuators was found to be different, making them incompatible. The sensors and actuators are curvature coupled to the structure, resulting in a plant with unusually close pole-zero pairs. And, because the structural bending stiffness is discontinuous, the calculation of accurate participation coefficients for the higher modes was difficult. In retrospect, a different test specimen, perhaps structurally more complex, might have been easier to control.

It was found that the existing synthesis theory for Positive Position Feedback produced sub-optimal closed loop performance, due to the very close pole-zero pairs of the plant transfer function. A new approach was implemented for recovering performance in the presence of close pole-zero pairs. It was found

that good performance can be obtained if the closed loop structural pole and PPF control filter pole are not designed too close together.

Four single-input-single-output (SISO), and one multi-input-multi-output (MIMO) experiments were performed. The control in all the experiments was realized as an analog circuit. The SISO experiments made use of one actuator/sensor pair near the root of the beam. The first two structural modes were controlled individually and then together using two PPF filters. Three PPF filters were used to control the first three modes. The damping ratios of the first three modes were increased by factors of 58, 59 and 15, respectively, over their open loop values.

The MIMO experiment used six PPF filters and two actuator/sensor pairs in a local control arrangement to control the first six modes. The damping ratios of the lower modes were increased by factors ranging from 11 to 130 times the open loop values. The performance of the other two modes was below the design level, because the damping ratios of the filters were too large for the smaller participation factors and increased density of these modes. In the case of Mode 5, the closed loop poles were also designed too close together, resulting in reduced performance robustness to plant modeling errors.

In general, the damping ratios of all modes, controlled or uncontrolled, were increased over their open loop values, demonstrating the stabilizing effects of spillover with Positive Position Feedback.

7.2 Directions for Further Research

These experimental investigations have brought to light several areas where further research is necessary. In relation to Positive Position Feedback, a synthesis theory for plants with close pole-zero pairs and with dense modes is necessary.

This should give procedures for the selection of gains where strong coupling exists between adjacent structural poles and control filters. Additionally, a synthesis theory for fewer filters than controlled modes is necessary for high authority control on plants with densly spaced modes. Further investigations into the phenomenon of *softening* are necessary along with techniques for reducing its effects. A method for identifying frequency and damping parameters for closely spaced highly damped modes is needed.

In relation to the piezoelectric active-member concept, a true active-member needs to be developed. These experiments have simulated the use of active members, but further tests with actual flight-like hardware are necessary. Experiments on more realistic structures are needed, with emphasis on incorporating active members and including the one important feature of Large Space Structures not simulated in these experiments — dense modes. In particular, dense controlled modes, and dense modes in the region of rolloff are required. This could be achieved using a three-dimensional space-truss beam or frame, with appropriate concentrated mass distributions.

The most important requirement for the development of realistic Large Space Structure control technologies at this point is access to zero-gravity testing environments. The upcoming NASA Control of Flexible Structures (COFS) program will make the Space Shuttle available for such tests. These and other flight opportunities promise a future of interesting research ahead.

Appendix A

NASTRAN Input File for SISO Piezobeam

The following NASTRAN data file was used for the eigen-analysis of the SISO piezobeam referred to in Chapter 3.

```
ID JLF,PIEZOBEAM
SOL 3
TIME 5
READ 9
CEND
TITLE=NORMAL MODES FOR PIEZOBEAM
METHOD=100
DISPLACEMENT=ALL
SPC=200
BEGIN BULK
$ASET1,345,2,THRU,52
CBAR,1,1,1,2,53
CBAR,2,2,2,3,53
=,*1,=,*1,*1,=
=3
CBAR,7,1,7,8,53
=,*1,=,*1,*1,=
=43
EIGR,100,MGIV,0.01,2500.
GRID,1
GRID,2,,0.0413
=,*1,,*0.25
=48
GRID,52,,12.40
GRID,53,,,10.0
MAT1,1,1.0+7,,0.3,2.590-4
MAT1,2,1.0+7,,0.3,4.927-4
PARAM,COUPMASS,+1
PBAR,1,1,1.32-2,1.0,4.584-7,4.63-4
PBAR,2,2,2.747-2,1.0,3.333-6,1.13-3
SPC1,200,123456,1,53
SPC1,200,126,2,THRU,52
ENDDATA
```

Appendix B

Mode Shapes of SISO Piezobeam

The following plots are the first eight mode shapes of the SISO piezobeam, which were generated from the NASTRAN run of Appendix A.

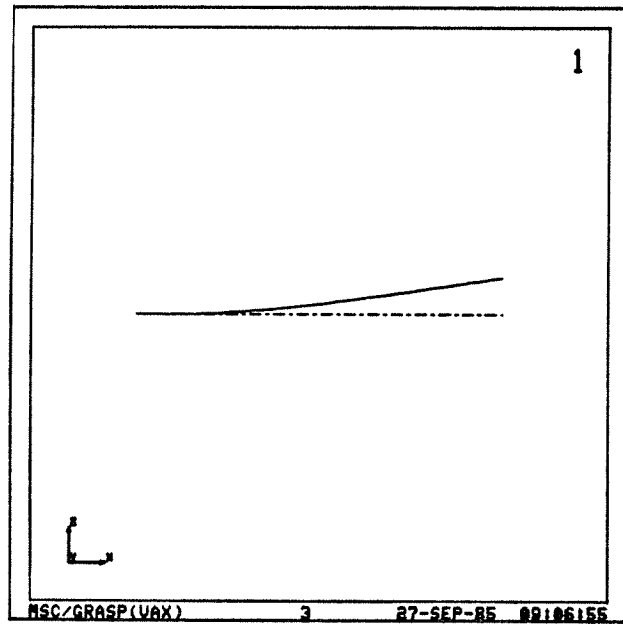

Figure B.1a Mode 1 of SISO Piezobeam.

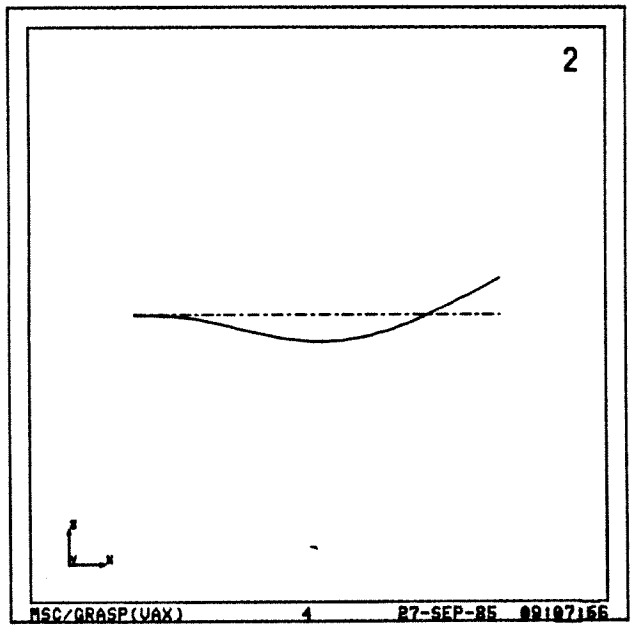

Figure B.1b Mode 2 of SISO Piezobeam.

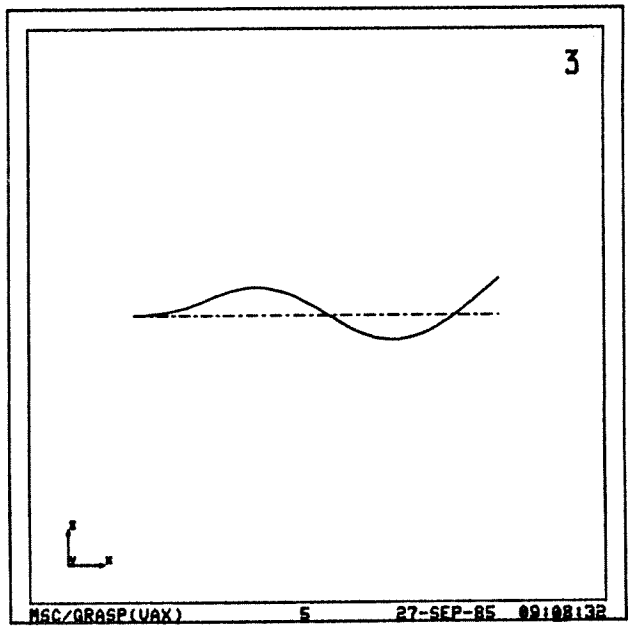

Figure B.1c Mode 3 of SISO Piezobeam.

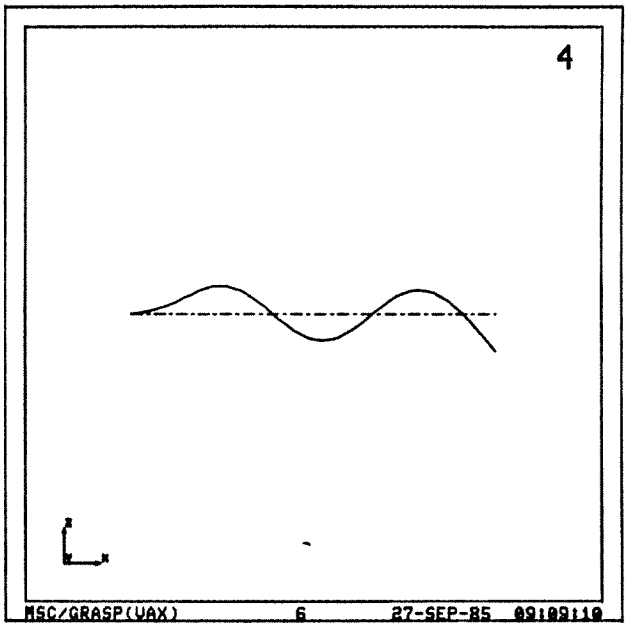

Figure B.1d Mode 4 of SISO Piezobeam.

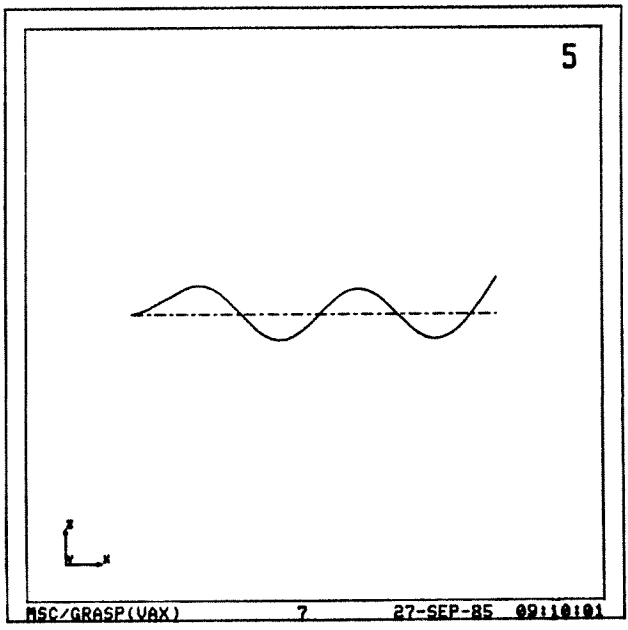

Figure B.1e Mode 5 of SISO Piezobeam.

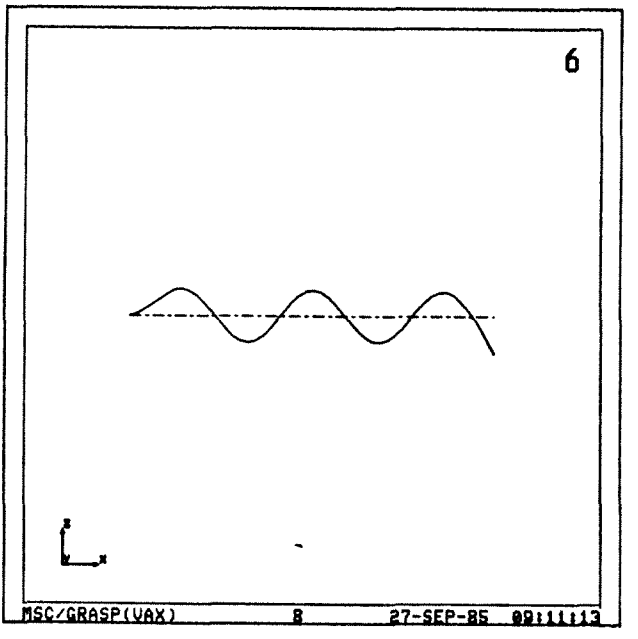

Figure B.1f Mode 6 of SISO Piezobeam.

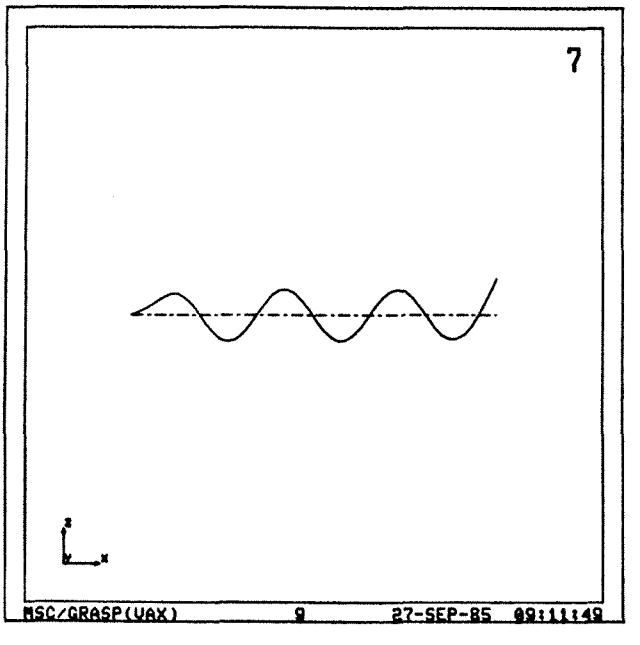

Figure B.1g Mode 7 of SISO Piezobeam.

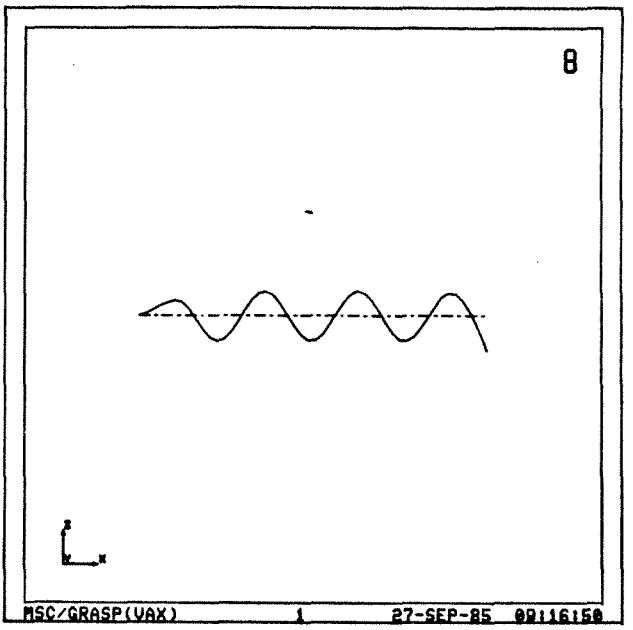

Figure B.1h Mode 8 of SISO Piezobeam.

Appendix C

Bonding Procedure for Piezoelectric Ceramics

The following procedure was used to bond the ceramics to the aluminum cantilever beam.

Step 1: The aluminum of the beam and the nickel electrode of the ceramic is thoroughly degreased with Chlorothene NU* aerosol solvent.

Step 2: The degreased aluminum surface is wetted with M-Prep Conditioner A.* While the surface is wet, it is abraded with 400-grit silicon-carbide paper and then wiped dry with a gauze sponge.

Step 3: M-Prep Neutralizer 5* is then applied with a cotton-tipped applicator and the surface carefully dried with a single wiping motion of a gauze sponge.

Step 4: The ceramic is then positioned in the exact location where it is to be bonded on the beam. PCT-2* cellophane tape is applied over the ceramic and onto the beam such that the ceramic is hinged on the tape.

Step 5: M-Bond 200* catalyst is then applied to the nickel electrode of the ceramic in a thin, uniform coat. The catalyst is allowed to dry at least one minute.

Step 6: Locktite® cyanoacrylate adhesive is then applied to the beam in a thin, uniform coat, making sure that none of the adhesive comes in contact with the copper strip.

---

* Materials identified with the asterisk are manufactured by Micro-Measurements Division of Measurements Group, Inc.

Step 7: Immediately after step 6, the ceramic is rotated into position slowly and firm contact is made with the beam. Pressure is applied to the ceramic with the thumb for at least one minute. The "thumb heat" helps to speed adhesive polymerization.

Step 8: After at least two minutes, the tape is removed by slowly pulling it back over itself, peeling it off the surface. The bond is now made.

Appendix D

Shaker Specifications and Vibration Fixture Drawings

The specifications for the Brüel & Kjær type 4810 Mini-Shaker are given below. Detail drawings for the test beam and test fixture follow.

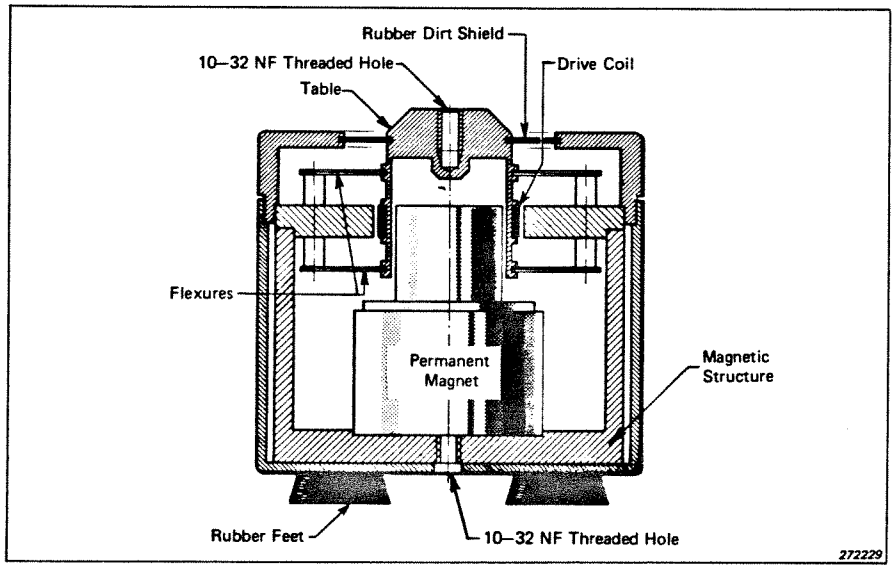

Figure D.1 Sectional drawing of the Mini-Shaker type 4810.

Specifications 4810

Frequency Range:
DC to 18 kHz

First Major Armature Resonance:
Above 18 kHz

Force Rating (Peak):
10 Newton (2,25 lbf). 65 Hz to 4 kHz
7 Newton (1,5 lbf). 65 Hz to 18 kHz

Max. Bare Table Acceleration (Peak):
550 ms^{-2} (65 Hz to 4 kHz)
383 ms^{-2} (4 kHz to 18 kHz)
(1 ms^{-2} = 0,102 g)

Max. Displacement (Peak-to-Peak):
6 mm (0,236 in)

Dynamic Flexure Stiffness:
2 Newton/mm (11,5 lbs/in)

Dynamic Weight of the Moving System.
18 grams

Magnetic Field:
Permanent magnet

Max. Input Current:
1,8 A. RMS

Coil Impedance:
3,5 Ω at 500 Hz

Connection:
Microsocket NF 10 — 32

Table Size:
14 mm (0,55 in) diameter

Fastening Thread:
NF 10 — 32

Weight:
1,1 kg (2,4 lb)

Dimensions:
Diameter: 76 mm (3 in)
Height: 75 mm (2,9 in)

Accessories Available:
Cable for connection of Mini-Shaker to Power Amplifier AO 0069

Mounting Accessories (includes isolated studs YP 0150 and non-isolated studs YQ 2960) UA 0125

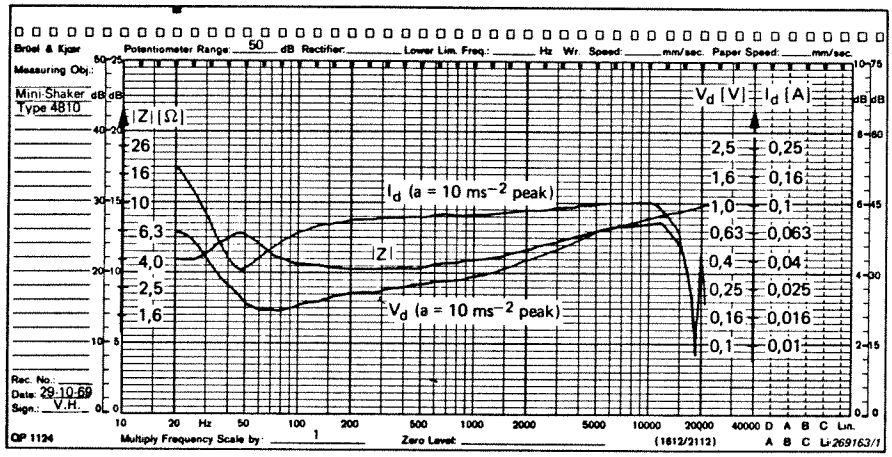

Figure D.2 Frequency response of the 4810 shaker for impedance (Z), current (I), and voltage (V).

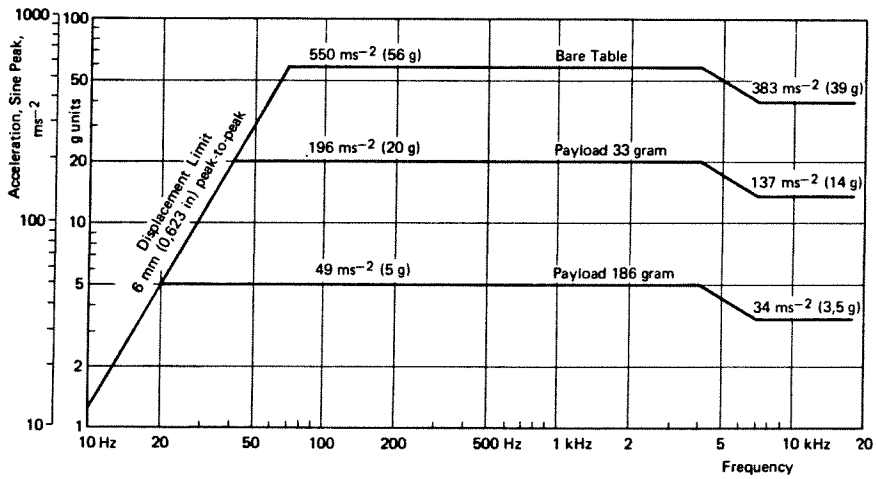

Figure D.3 Sine performance curves for the 4810 shaker.

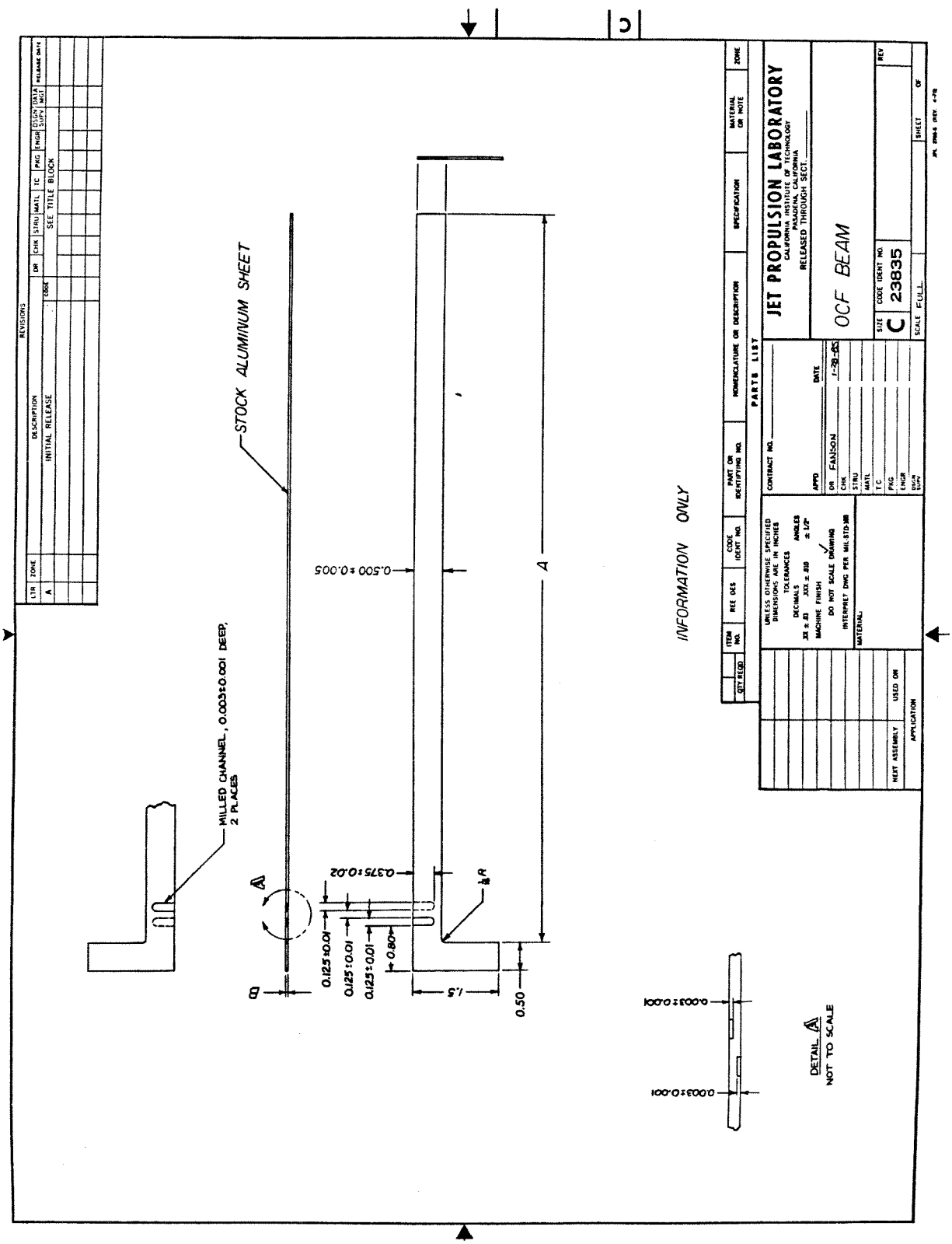
STOCK ALUMINUM SHEET
MILLED CHANNEL, 0.003±0.001 DEEP, 2 PLACES
0.500±0.005
A
0.375±0.02
0.125±0.01
0.125±0.01
0.125±0.01
0.80
1.5
0.50
B
DETAIL A
NOT TO SCALE
0.003±0.001
0.003±0.001
INFORMATION ONLY
JET PROPULSION LABORATORY
CALIFORNIA INSTITUTE OF TECHNOLOGY
PASADENA, CALIFORNIA
RELEASED THROUGH SECT.
OCF BEAM
CODE IDENT NO. 23835
SIZE C
SCALE FULL
SHEET OF
REVISIONS
DESCRIPTION
INITIAL RELEASE
SEE TITLE BLOCK
PARTS LIST
UNLESS OTHERWISE SPECIFIED DIMENSIONS ARE IN INCHES
TOLERANCES
DECIMALS
ANGLES ± 1/2°
MACHINE FINISH
DO NOT SCALE DRAWING
INTERPRET DWG PER MIL-STD-100
MATERIAL
NEXT ASSEMBLY
USED ON
APPLICATION
DR FANSON 1-28-65
CHK
STRU
MATL
T C
PKG
ENGR
DSGN DATA RELEASE DATE

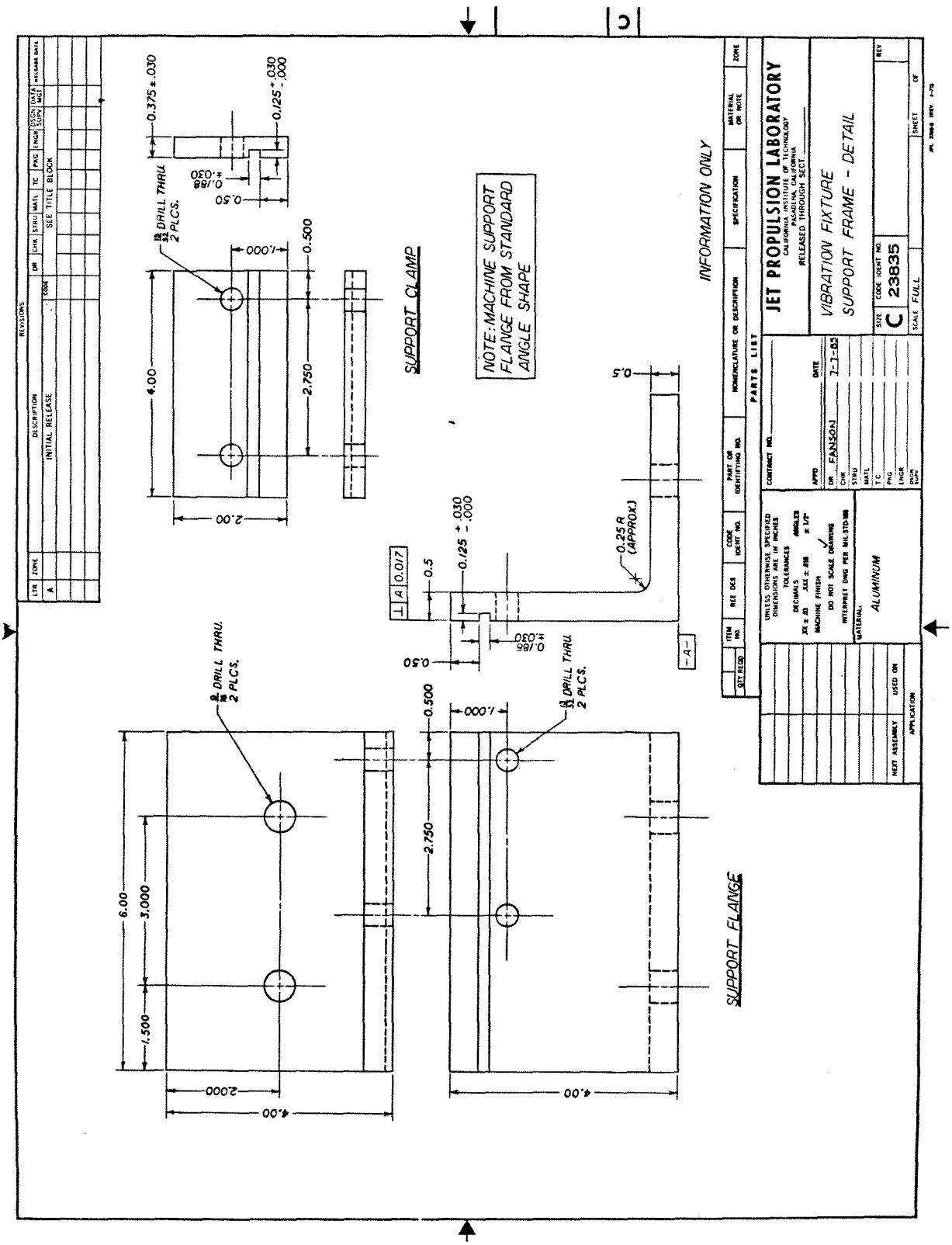
SUPPORT CLAMP
NOTE: MACHINE SUPPORT FLANGE FROM STANDARD ANGLE SHAPE
INFORMATION ONLY
SUPPORT FLANGE
JET PROPULSION LABORATORY
CALIFORNIA INSTITUTE OF TECHNOLOGY
PASADENA, CALIFORNIA
RELEASED THROUGH SECT.
VIBRATION FIXTURE
SUPPORT FRAME - DETAIL
ALUMINUM
C 23835
PARTS LIST
REVISIONS
INITIAL RELEASE
SEE TITLE BLOCK
DRILL THRU 2 PLCS.
0.375 ± .030
0.125 +.030 -.000
0.50
0.88 ±.030
1.000
0.500
4.00
2.00
2.750
0.5
0.25 R (APPROX.)
5.0
0.017 A
-A-
6.00
3.000
1.500

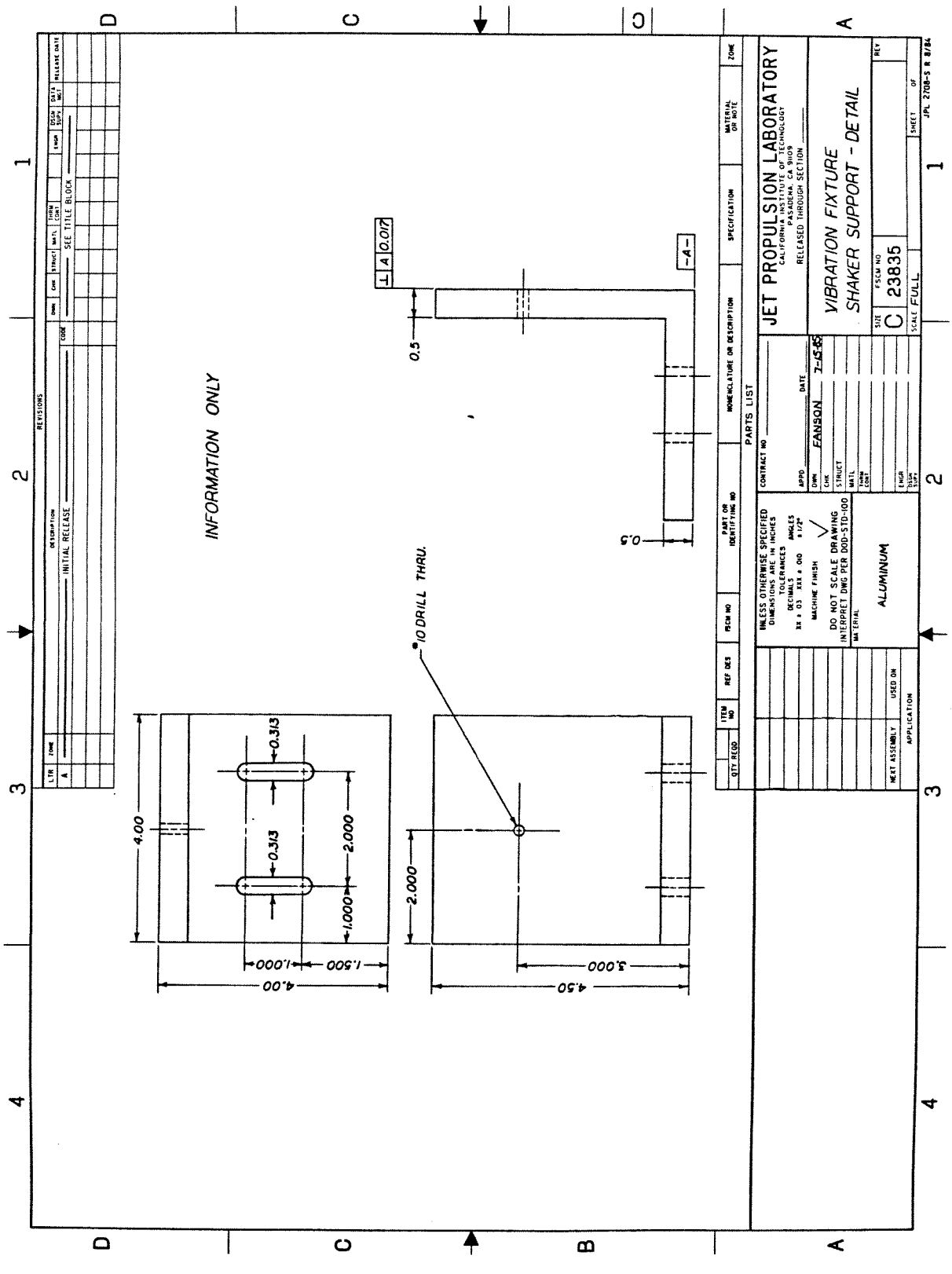
INFORMATION ONLY
⊥ A 0.01
0.5
-A-
0.5
*.10 DRILL THRU.
4.00
0.313
0.313
2.000
1.000
1.500
1.000
4.00
2.000
3.000
4.50
REVISIONS
LTR
ZONE
DESCRIPTION
A
INITIAL RELEASE
SEE TITLE BLOCK
PARTS LIST
QTY REQD
ITEM NO
REF DES
FSCM NO
PART OR IDENTIFYING NO
NOMENCLATURE OR DESCRIPTION
SPECIFICATION
MATERIAL OR NOTE
ZONE
NEXT ASSEMBLY
USED ON
APPLICATION
UNLESS OTHERWISE SPECIFIED
DIMENSIONS ARE IN INCHES
TOLERANCES
DECIMALS
ANGLES
MACHINE FINISH
DO NOT SCALE DRAWING
INTERPRET DWG PER DOD-STD-100
MATERIAL
ALUMINUM
CONTRACT NO
APPD
DWN
FANSON
CHK
STRUCT
MATL
THRM CONT
ENGR
DESN DATA
DATE
7-15-85
JET PROPULSION LABORATORY
CALIFORNIA INSTITUTE OF TECHNOLOGY
PASADENA, CA 91109
RELEASED THROUGH SECTION
VIBRATION FIXTURE
SHAKER SUPPORT - DETAIL
SIZE
C
FSCM NO
23835
REV
SCALE FULL
SHEET
OF
JPL 2708-5 R 8/84

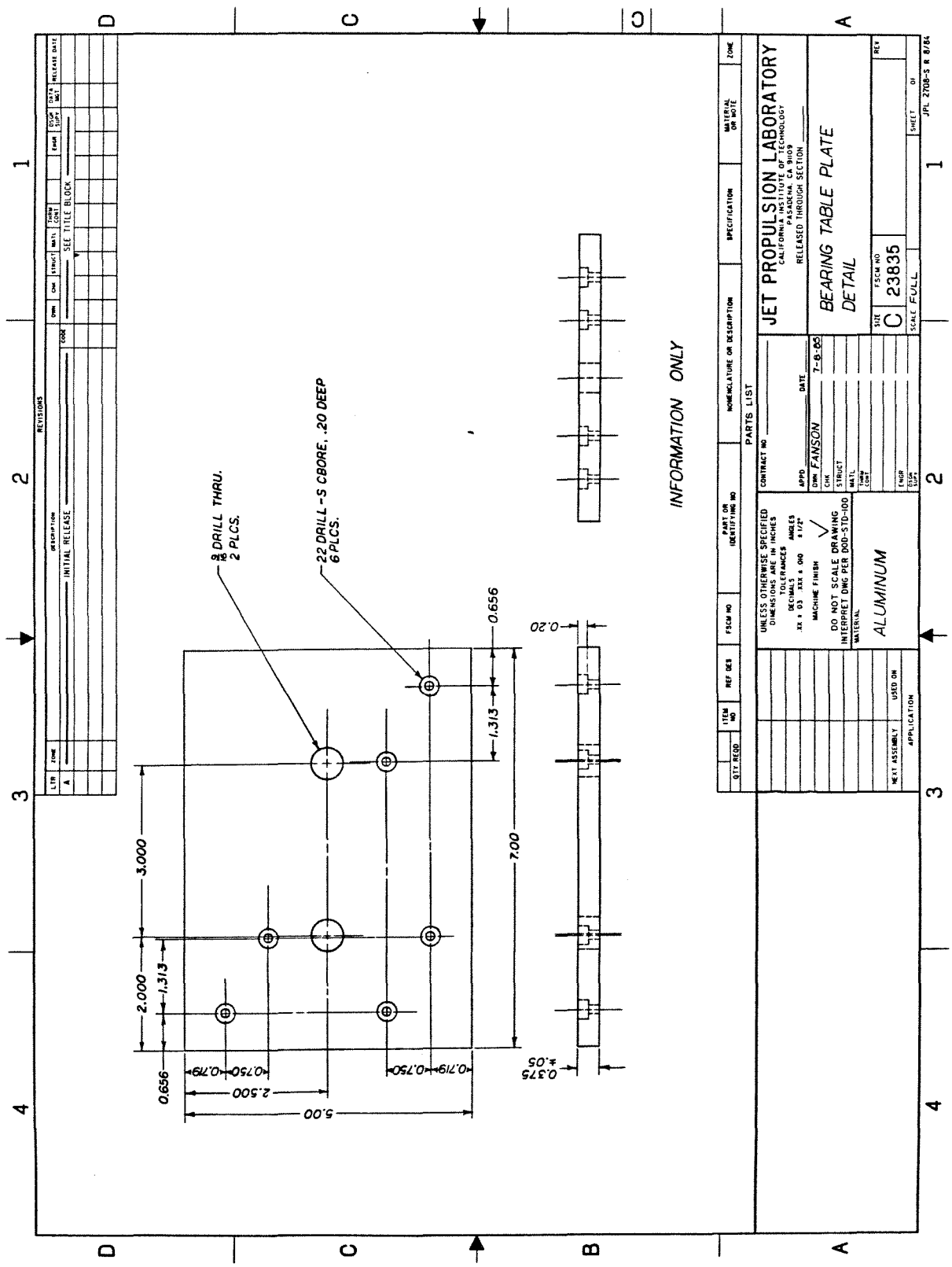
INFORMATION ONLY
2 DRILL THRU. 2 PLCS.
22 DRILL -S CBORE, .20 DEEP 6 PLCS.
3.000
2.000
1.313
0.656
0.750
0.719
2.500
5.00
7.00
0.375 ±.05
0.20
JET PROPULSION LABORATORY
CALIFORNIA INSTITUTE OF TECHNOLOGY
PASADENA, CA 91109
RELEASED THROUGH SECTION
BEARING TABLE PLATE
DETAIL
FSCM NO 23835
SIZE C
SCALE FULL
SHEET 01
REV
ALUMINUM
DO NOT SCALE DRAWING
INTERPRET DWG PER DOD-STD-100
UNLESS OTHERWISE SPECIFIED DIMENSIONS ARE IN INCHES
TOLERANCES
DECIMALS
ANGLES ±1/2°
MACHINE FINISH
PARTS LIST
ITEM NO
QTY REQD
REF DES
FSCM NO
PART OR IDENTIFYING NO
NOMENCLATURE OR DESCRIPTION
SPECIFICATION
MATERIAL OR NOTE
ZONE
NEXT ASSEMBLY
USED ON
APPLICATION
DWN FANSON 7-6-65
CHK
APPD
STRUCT
MATL
THERM CONT
ENGR
DSGN
QUAL
PROJ
CONTRACT NO
REVISIONS
LTR
ZONE
DESCRIPTION
DWN
CHK
STRUCT
MATL
THERM CONT
ENGR
DSGN QUAL
DATE RELEASED
A
INITIAL RELEASE
SEE TITLE BLOCK
JPL 2708-5 R 8/64

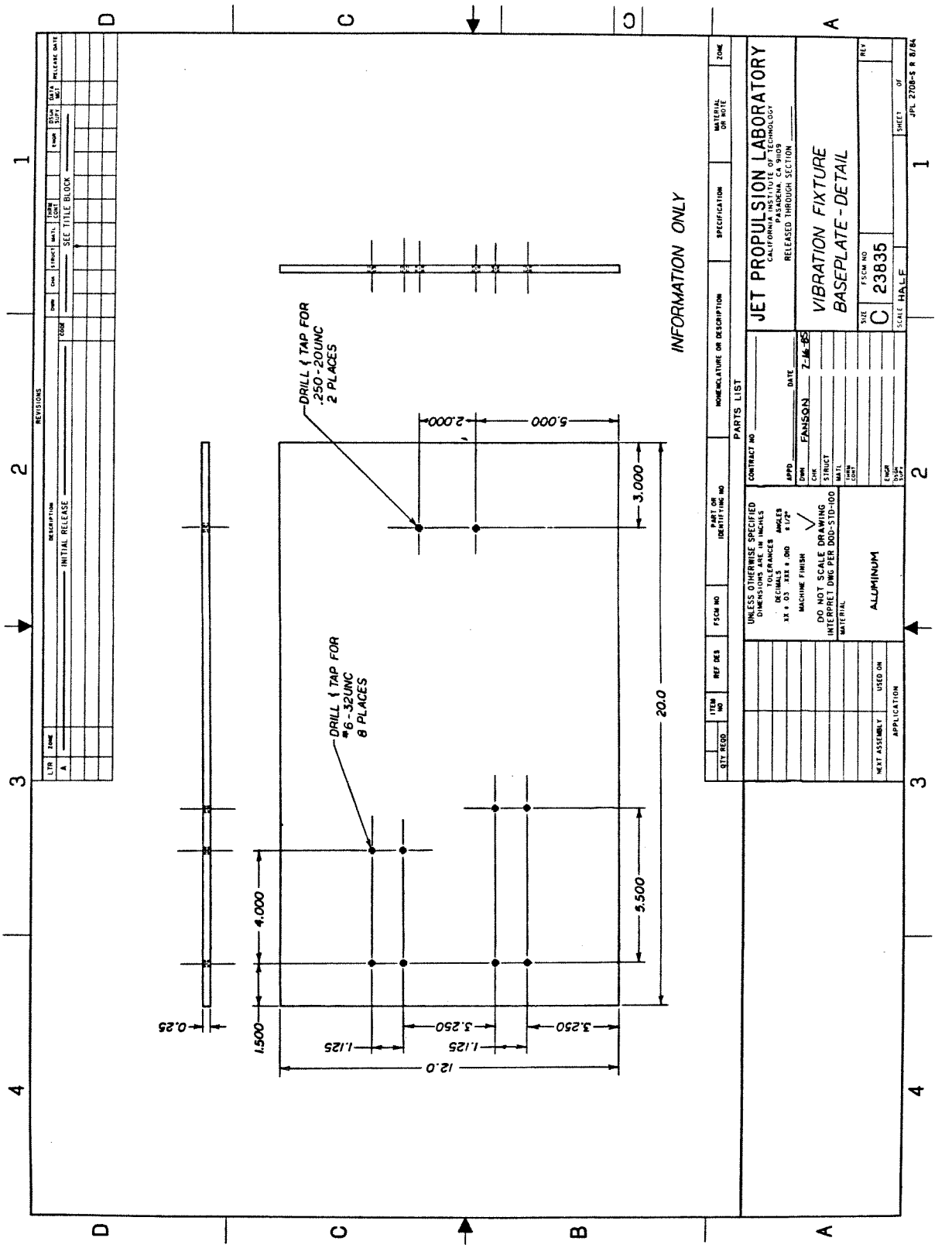
INFORMATION ONLY
DRILL & TAP FOR .250-20UNC 2 PLACES
DRILL & TAP FOR #6-32UNC 8 PLACES
2.000
5.000
3.000
20.0
4.000
5.500
1.500
0.25
1.125
5.250
1.125
3.250
12.0
JET PROPULSION LABORATORY
CALIFORNIA INSTITUTE OF TECHNOLOGY
PASADENA, CA 91109
RELEASED THROUGH SECTION
VIBRATION FIXTURE
BASEPLATE - DETAIL
SIZE C
FSCM NO 23835
SCALE HALF
SHEET OF
REV
DO NOT SCALE DRAWING
INTERPRET DWG PER DOD-STD-100
MATERIAL
ALUMINUM
UNLESS OTHERWISE SPECIFIED
DIMENSIONS ARE IN INCHES
TOLERANCES
DECIMALS
XX ± .03 XXX ± .010
ANGLES ± 1/2°
MACHINE FINISH
PARTS LIST
QTY REQD
ITEM NO
REF DES
FSCM NO
PART OR IDENTIFYING NO
NOMENCLATURE OR DESCRIPTION
SPECIFICATION
MATERIAL OR NOTE
ZONE
CONTRACT NO
APPD FANSON 7-16-85
DWN
CHK
STRUCT
MATL
ELECT
COMP
ENGR
DSGN
SUPV
NEXT ASSEMBLY
USED ON
APPLICATION
REVISIONS
LTR
ZONE
DESCRIPTION
DWN
CHK
STRUCT
MATL
CHRG CONT
ENGR
DSGN SUPV
DATA MGT
RELEASE DATE
A
INITIAL RELEASE
SEE TITLE BLOCK
JPL 2708-5 R 8/84

Appendix E

Parameter Values and Dimensions for Hardware

The following are the values for material properties and dimensions for the beam, sensor and actuator components.

$$t_a = 0.0095 \text{ in}$$

$$t_b = 0.0204 \text{ in}$$

$$t_s = 0.0095 \text{ in}$$

$$E_a = 9.1 \times 10^6 \text{ psi}$$

$$E_b = 10 \times 10^6 \text{ psi}$$

$$E_s = 8 \times 10^6 \text{ psi}$$

$$W_a = 0.50 \text{ in}$$

$$W_b = 0.648 \text{ in}$$

$$W_s = 0.25 \text{ in}$$

$$d_{31} = 7.48 \times 10^{-9} \frac{\text{in}}{\text{volt}}$$

$$g_{31} = 1.926 \frac{\text{volt} \cdot \text{in}}{\text{lb}_\text{f}}$$

Appendix F

Spline-Fit Program Listing

The following program was used to determine the mode shape curvatures at the finite element model grid points using NASTRAN generated displacements.

```
C     This program will calculate the curvatures at the grid points of
C     a NASTRAN mode shape.
C
      PARAMETER NMAX=100
C
      CHARACTER ST*3
      DIMENSION X(NMAX),Y(NMAX),S(NMAX),A(NMAX,4)
      LOGICAL EX
C     Read in the mode number, the size of the mode shape,
C     and the end condition.
      READ (7,*) M,N,IEND
      WRITE (6,100) M,N,IEND
100   FORMAT(' Mode Number: ',I2,' Size: ',I2,' End Condition: ',I2)
      IF (N.GT.NMAX) STOP 'Reset NMAX to a larger value.'
C     Read in the grid locations.
      DO I=1,N
        READ (7,*) X(I)
        WRITE (6,101) I,X(I)
101     FORMAT (' X(',I2,')=',G10.4)
      END DO
C     Read in the mode shape values.
      DO I=1,N
        READ (7,*) Y(I)
        WRITE (6,102) I,Y(I)
102     FORMAT (' Y(',I2,')=',G10.4)
      END DO
C     Now do the Spline Fit
      CALL SPLINE(X,Y,S,N,NMAX,IEND,A)
C     Now print out the curvatures into file: CURVE.DAT.
      INQUIRE(FILE='CURVE.DAT',EXIST=EX)
      IF (EX) THEN
         ST='OLD'
      ELSE
         ST='NEW'
      END IF
      OPEN(10,FILE='CURVE.DAT',ACCESS='SEQUENTIAL',FORM='FORMATTED',
     1STATUS=ST,CARRIAGECONTROL='LIST')
      WRITE (10,1000) M
1000  FORMAT(' Curvatures for Mode No. ',I2,//)
      DO I=1,N
       WRITE (10,1001) I,S(I)
1001  FORMAT(' S(',I2,') = ',G10.4)
      END DO
      STOP
      END
      SUBROUTINE SPLINE(X,Y,S,N,NMAX,IEND,A)
C
C     This program for spline fits is taken from "Applied Numerical
C     Analysis", 2nd edition, by Curtis F. Gerald, Addison Wesley,
C     1978, pp 508-509.  The adaptation to FORTRAN 77 was done by
C     Bob Norton, Dec 1, 1983.
C
```

```
      DIMENSION X(N),Y(N),S(NMAX),A(NMAX,4)
C
C     This subroutine computes the matrix for finding the coefficients
C     of a cubic spline through a set of data points.  The system is
C     then solved to obtain the second derivative values.
C     Parameters are:
C        X,Y  arrays of x and y values to be fitted
C        S    array of second derivative values at the data points
C        N    number of data points
C        IEND type of end condition to be used
C                IEND=1  linear ends, S(1)=S(N)=0 "natural" spline
C                IEND=2  parabolic ends, S(1)=S(2), S(N)=S(N-1)
C                IEND=3  cubic ends, S(1) & S(N) are extrapolated
C        A    augmented matrix of coefficients and right-hand side
C
C     compute for the N-2 rows:
C
      NM2=N-2
      NM1=N-1
      DX1=X(2)-X(1)
      DY1=(Y(2)-Y(1))/DX1*6.0
      DO I=1,NM2
         DX2=X(I+2)-X(I+1)
         DY2=(Y(I+2)-Y(I+1))/DX2*6.0
         A(I,1)=DX1
         A(I,2)=2.0*(DX1+DX2)
         A(I,3)=DX2
         A(I,4)=DY2-DY1
         DX1=DX2
         DY1=DY2
      END DO
C
C     Adjust the first and last rows for the designated end condition
C
C     for IEND=1 no chXkS%s needed
C
      IF (IEND .EQ. 2) THEN
C
C     for IEND=2 S(1)=S(2), S(N)=S(N-1) (parabolic ends)
C
         A(1,2)=A(1,2)+X(2)-X(1)
         A(NM2,2)=A(NM2,2)+X(N)-X(NM1)
      ELSE IF (IEND .EQ. 3) THEN
C
C     for IEND=3 S(1) and S(N) are extrapolated (cubic ends)
C
         DX1=X(2)-X(1)
         DX2=X(3)-X(2)
         A(1,2)=(DX1+DX2)*(DX1+2.0*DX2)/DX2
         A(1,3)=(DX2*DX2-DX1*DX1)/DX2
         DXN2=X(NM1)-X(NM2)
         DXN1=X(N)-X(NM1)
         A(NM2,1)=(DXN2*DXN2-DXN1*DXN1)/DXN2
         A(NM2,2)=(DXN1+DXN2)*(DXN1+2.0*DXN2)/DXN2
      ENDIF
C
C     now solve the tridiagonal system, first reduce
C
      DO I=2,NM2
         A(I,2)=A(I,2)-A(I,1)/A(I-1,2)*A(I-1,3)
         A(I,4)=A(I,4)-A(I,1)/A(I-1,2)*A(I-1,4)
      END DO
C
C     now back substitute
C
      A(NM2,4)=A(NM2,4)/A(NM2,2)
      DO I=2,NM2
         J=NM1-I
```

```
         A(J,4)=(A(J,4)-A(J,3)*A(J+1,4))/A(J,2)
      END DO
C
C     now put the values into the S vector
C
      DO I=1,NM2
         S(I+1)=A(I,4)
      END DO
C
C     get S(1) and S(N) using the various end conditions
C
      IF (IEND .EQ. 1) THEN
C
C     for linear ends S(1)=0, S(N)=0
C
         S(1)=0.0
         S(N)=0.0
      ELSE IF (IEND .EQ. 2) THEN
C
C     for parabolic ends, S(1)=S(2), S(N)=S(N-1)
         S(1)=S(2)
         S(N)=S(N-1)
      ELSE IF (IEND .EQ. 3) THEN
C
C     for cubic ends, extrapolate to get S(1) and S(N)
C
         S(1)=((DX1 +DX2) *S(2)  +DX1* S(3))  /DX2
         S(N)=((DXN2+DXN1)*S(NM1)-DXN1*S(NM2))/DXN2
      ENDIF
      RETURN
      END
      SUBROUTINE INTERP(XX,YY,X,Y,S,N,NMAX)
      DIMENSION X(N),Y(N),S(NMAX)
C
C     This subroutine uses the results of a spline fit analysis to
C     interpolate intermediate values.
C
      IF (XX .LT. X(1)  .OR.  XX .GT. X(N)) THEN
         WRITE (6,2000) XX
         STOP
      ENDIF
      I=1
      DO WHILE (XX .GT. X(I+1))
         IF (I+1 .GT. N) STOP 'x out of range'
         I=I+1
      END DO
C
C     compute the coefficients for the interpolation
C
      HI=X(I+1)-X(I)
      AI=(S(I+1)-S(I))/(6.0*HI)
      BI=S(I)/2.0
      CI=(Y(I+1)-Y(I))/HI - HI*(2.0*S(I)+S(I+1))/6.0
      DX=XX-X(I)
      YY=AI*DX**3 + BI*DX*DX + CI*DX +Y(I)
      RETURN
2000  FORMAT ('0***Fatal error***, requested x value is out of range',
     >1G15.5)
      END
```

Appendix G

Root Locus Program Listing

The following program was used to solve for the roots of the characteristic equation as a function of loop gain and produced the root locus plots of Chapters 5 and 6. The subroutine POLYRT is taken from the COSMIC SAMSAN library.

```
C       PROGRAM TO BRUTE FORCE THE ROOT LOCUS OF A TRANSFER FUNCTION
C       VERSION 2
C
      PARAMETER NP=10000
      IMPLICIT REAL*8(A-H,O-Z)
      REAL*8 N,D
      REAL*4 AR,AI,SR,SI,G,OPENPR,OPENPI,OPENZR,OPENZI
      CHARACTER ST*3
      DIMENSION AD(NP),AR(NP),AI(NP),N(NP),D(NP),SR(2),SI(2),
     1ZEROR(NP),ZEROI(NP),G(NP),OPENPR(NP),OPENPI(NP),OPENZR(NP),
     2OPENZI(NP),TEMP(NP)
      LOGICAL EX
C
C       READ IN THE SIZES OF THE NUMERATOR AND DENOMINATOR AND SCALE FACTOR
      READ (7,*) N1,ND1,SCALE
      WRITE (6,1000) N1,ND1
1000  FORMAT(' The numerator is order: ',I2,'  The denominator is
     1order:',I2)
      WRITE (6,1010) SCALE
1010  FORMAT(' The scale factor is: ',G10.4)
C
C       READ IN THE RANGE OF GAIN AND THE NUMBER OF POINTS
      READ (7,*) GAINL,GAINU,NPTS
      N2=ND1*NPTS
      IF(N2.GT.NP) STOP 'Reset NP to a larger value'
      WRITE (6,1001) GAINL,GAINU,NPTS
1001  FORMAT(/' The gain range is ',G10.4,' to ',G10.4,'   The number
     1of points is ',I4)
C
C       READ IN THE NUMERATOR AND DENOMINATOR
      READ (7,*) (N(I), I=1,N1+1)
      READ (7,*) (D(I), I=1,ND1+1)
C
      WRITE (6,1002)
1002  FORMAT(/' Numerator Coefficients')
      DO I=1,N1+1
         WRITE (6,1003) I,N(I)
1003     FORMAT(' N(',I2,') = ',G10.4)
      END DO
      WRITE (6,1004)
1004  FORMAT(/' Denominator Coefficients')
      DO I=1,ND1+1
         WRITE (6,1005) I,D(I)
1005     FORMAT(' D(',I2,') = ',G10.4)
      END DO
C
C       READ IN THE PLOTTING INFORMATION
C       READ THE MAX AND MIN VALUES FOR THE REAL AND IMAGINARY AXES
      READ (7,*) SR(1),SR(2),SI(1),SI(2)
      WRITE (6,1007) SR(1),SR(2)
1007  FORMAT(/' The Real axis range is from ',G10.4' to ',g10.4)
```

```
      WRITE (6,1008) SI(1),SI(2)
1008  FORMAT(/' The Imaginary axis range is from ',g10.4,
     1' to ',g10.4)
      WRITE (6,1009)
1009  FORMAT(//)
C
C       COMPUTE THE OPEN LOOP POLES AND ZEROS
      DO I=1,N1
         N3=N1-I+1
         TEMP(N3)= N(I+1)/(N(1)*SCALE**I)
      END DO
C       COMPUTE THE OPEN LOOP ZEROS
      CALL POLYRT(TEMP,N1,ZEROR,ZEROI,IFAIL)
      DO I=1,N1
         OPENZR(I)= ZEROR(I)*SCALE
         OPENZI(I)= ZEROI(I)*SCALE
      END DO
C       COMPUTE THE OPEN LOOP POLES
      DO I= 1,ND1
         N3=ND1-I+1
         TEMP(N3)=D(I+1)/(D(1)*SCALE**I)
      END DO
      CALL POLYRT(TEMP,ND1,ZEROR,ZEROI,IFAIL)
      DO I=1,ND1
         OPENPR(I)= ZEROR(I)*SCALE
         OPENPI(I)= ZEROI(I)*SCALE
      END DO
C
C       CONSTRUCT CURRENT POLYNOMIAL
      GAIN=GAINL
      NCOUNT1=0
      NCOUNT2=1
C
C       CONSTRUCTION OF POLYNOMIAL COEFFICIENTS
50    N4=1
      DO 70 I= ND1,1,-1
         N3= ND1-I+1
         IF(I.GT.N1+1) GOTO 60
         AD(I) = (D(N3+1) +GAIN*N(N4))/(D(1)*SCALE**N3)
         N4=N4+1
         GOTO 70
60       AD(I) = D(N3+1)/(D(1)*SCALE**N3)
70    CONTINUE
C
C       COMPUTE CLOSED LOOP EIGENVALUES
      CALL POLYRT(AD,ND1,ZEROR,ZEROI,IFAIL)
C
      WRITE(6,1006) NCOUNT2,IFAIL,GAIN
1006  FORMAT('+Point No. ',I4,'  IFAIL = ',I4,'   GAIN = ',G10.4)
C
C       CHECK ON RESULTS OF ROOT CRUNCH
      IF (IFAIL.EQ.0) GOTO 300
      IF (IFAIL.EQ.1) GOTO 100
      IF (IFAIL.EQ.-1) GOTO 200
      STOP 'Should not have reached this line'
100   WRITE (6,2000) ND1,GAIN
2000  FORMAT(' Fewer than ',I3,' roots were found. The gain
     1was: ',G10.4)
      STOP
200   WRITE (6,2001) GAIN
2001  FORMAT(//' All the roots were found but accuracy is poor.
     1The gain was: ',G10.4)
C
C       STORE ROOTS FOR LATER PLOTTING
300   DO I=1,ND1
         I2= NCOUNT1 +I
         AR(I2) = ZEROR(I)*SCALE
         AI(I2) = ZEROI(I)*SCALE
         G(I2)= GAIN
```

```
      END DO
C
C       SET UP FOR THE NEXT ITERATION
      NCOUNT2=NCOUNT2 +1
      NCOUNT1=NCOUNT1 +ND1
C
C       ARE WE FINISHED?
      IF(NCOUNT2.GT.NPTS) GOTO 400
      GAIN= GAINL +NCOUNT2*(GAINU-GAINL)/NPTS
      GOTO 50
C
C       WRITE OUT THE EIGENVALUES TO FILE RLPOLES.DAT
400   INQUIRE(FILE='RLPOLES.DAT',EXIST=EX)
      IF (EX) THEN
         ST='OLD'
      ELSE
         ST='NEW'
      END IF
      OPEN(10,FILE='RLPOLES.DAT',ACCESS='SEQUENTIAL',FORM='FORMATTED',
     1 STATUS=ST,CARRIAGECONTROL='LIST')
C       WRITE OUT THE OPEN LOOP ZEROS
      WRITE(10,2004)
2004  FORMAT(' OPEN LOOP ZEROS')
      WRITE(10,2005)
2005  FORMAT(' REAL',10X,'IMAGINARY')
      DO I=1,N1
         WRITE(10,2006) OPENZR(I),OPENZI(I)
2006     FORMAT(' ',G10.4,5X,G10.4)
      END DO
C       WRITE OUT THE OPEN LOOP POLES
      WRITE(10,2007)
2007  FORMAT(' OPEN LOOP POLES')
      WRITE(10,2008)
2008  FORMAT(' REAL',10X,'IMAGINARY')
      DO I=1,ND1
         WRITE(10,2009) OPENPR(I),OPENPI(I)
2009     FORMAT(' ',G10.4,5X,G10.4)
      END DO
C       WRITE OUT THE CLOSED LOOP POLES
      WRITE(10,2010)
2010  FORMAT(' CLOSED LOOP POLES')
      WRITE(10,2002)
2002  FORMAT(' REAL',10X,'IMAGINARY',10X,'GAIN')
      DO I=1,N2
         WRITE(10,2003) AR(I),AI(I),G(I)
2003     FORMAT(' ',G10.4,5X,G10.4,5X,G10.4)
      END DO
C       PLOTTING ROUTINE
      CALL BGNPLT('       ')
      CALL PLFORM('LINLIN',7.8,5.2)
      CALL PLABEL(' ',1,'REAL',4,'IMAGINARY',9)
      CALL LINCLR(1)
      CALL PLSCAL(SR,2,2,SI,2,2)
      CALL LINCLR(2)
C       PLOT OPEN LOOP POLES
      CALL PLCURV(OPENPR,OPENPI,ND1,-1,7)
      CALL LINCLR(7)
C       PLOT OPEN LOOP ZEROS
      CALL PLCURV(OPENZR,OPENZI,N1,-1,1)
      CALL LINCLR(3)
C       PLOT CLOSED LOOP POLES
      CALL PLCURV(AR,AI,N2,-1,3)
      CALL LINCLR(1)
      CALL ENDPLT
      STOP
      END
```

Appendix H

Three Mode Control Frequency Functions

Measurements of the open loop frequency function, compensator frequency function, and closed loop function for the three mode control case appear below. Block diagrams describe where the signals were injected and where the measurements were made for each test.

The compensator, open loop, and closed loop frequency functions were measured as indicated in Figures (H.1), (H.2) and (H.3), respectively.

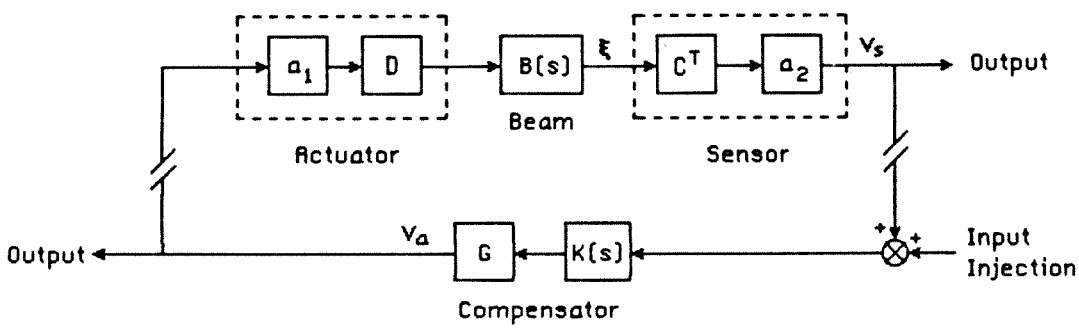

Figure H.1 Block diagram showing measurement method for the compensator frequency function.

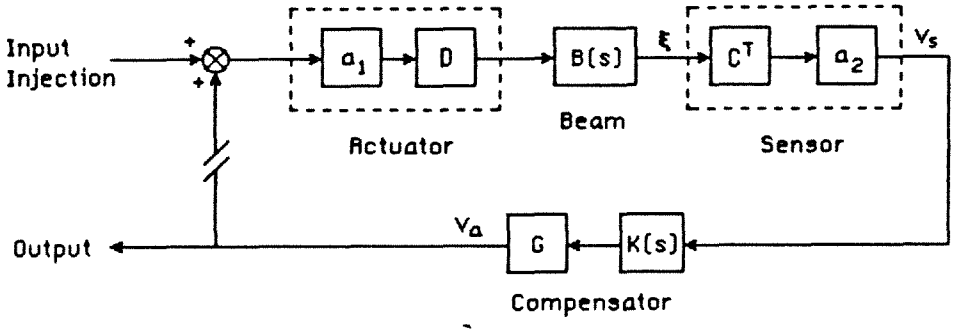

Figure H.2 Block diagram showing measurement method for the open loop frequency function.

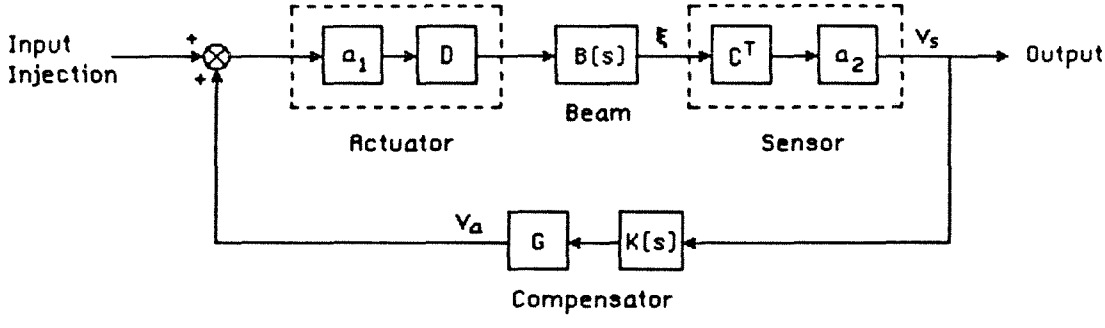

Figure H.3 Block diagram showing measurement method for the closed loop frequency function.

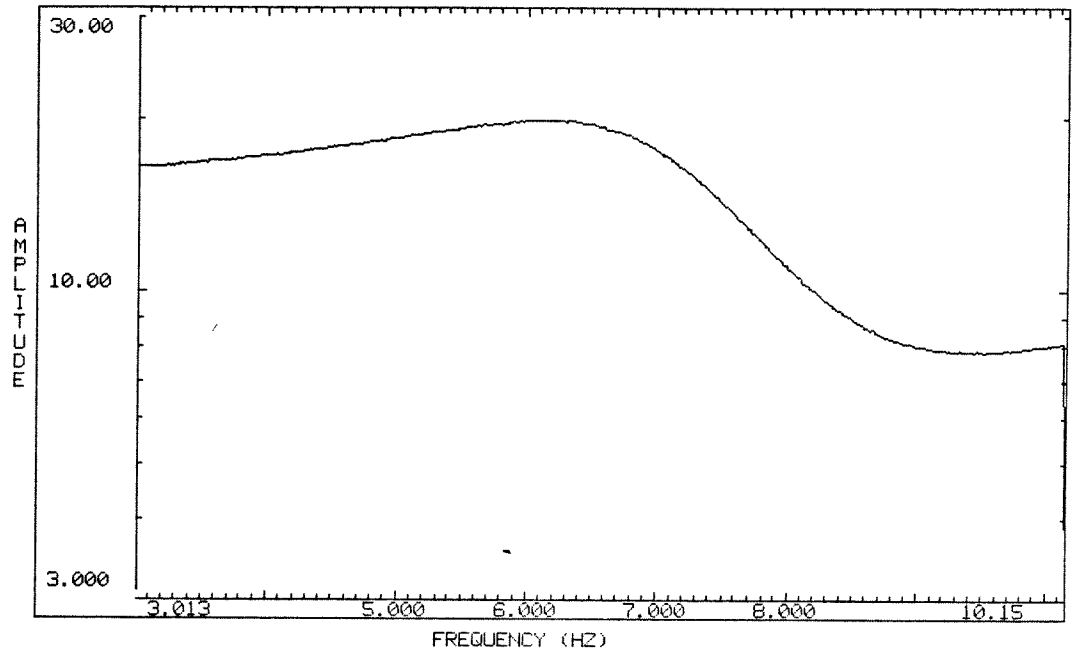

Figure H.4a Compensator frequency function amplitude plot for the Mode 1 PPF filter.

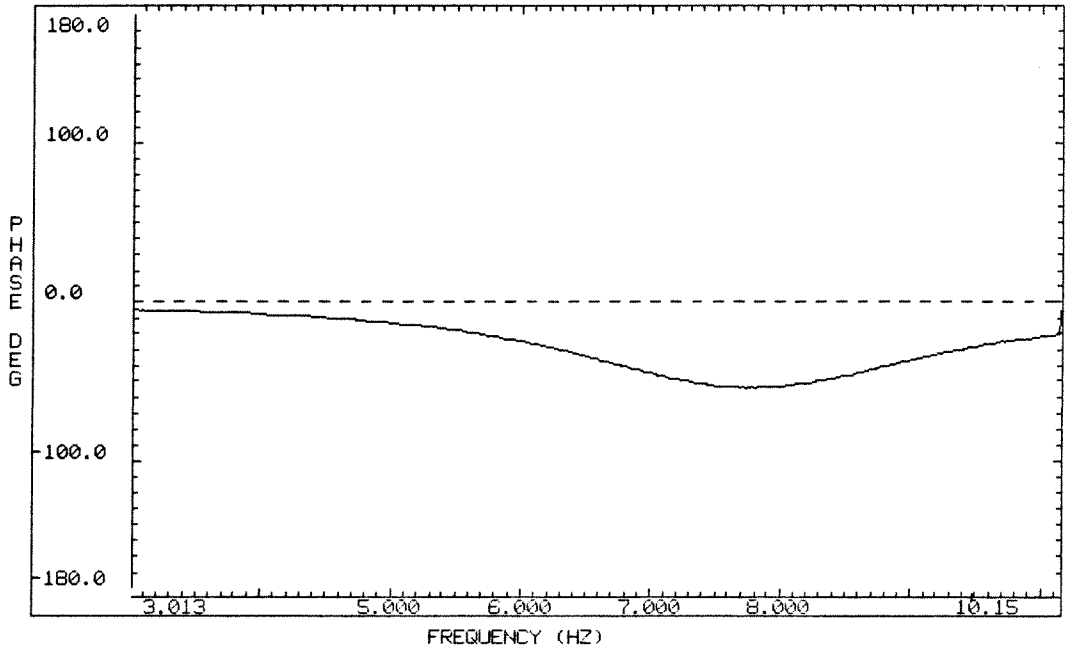

Figure H.4b Compensator frequency function phase plot for the Mode 1 PPF filter.

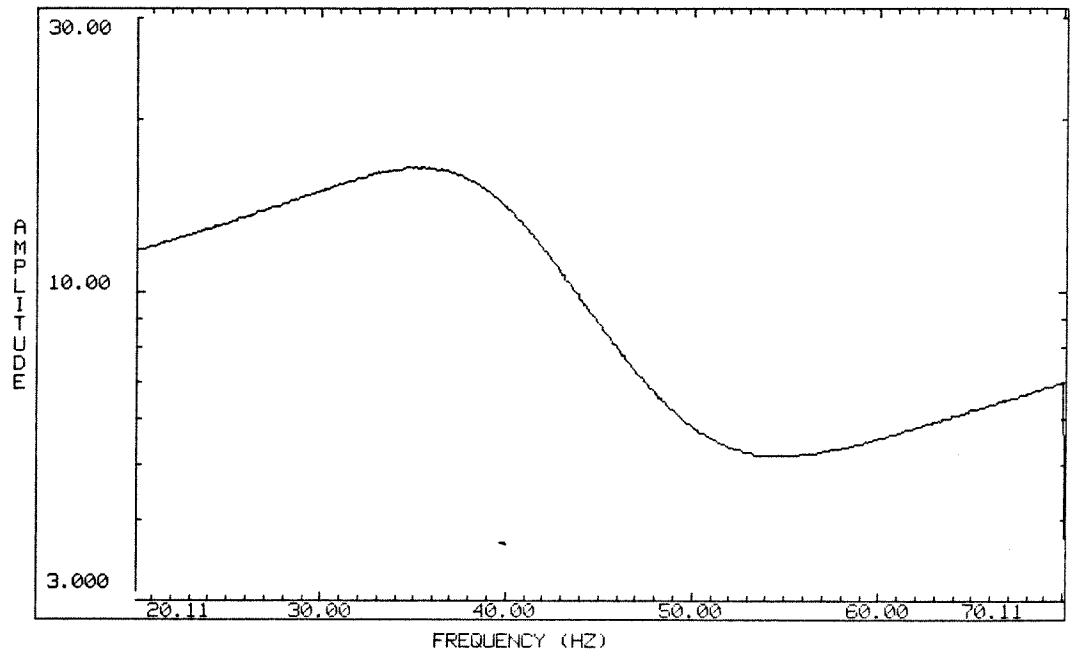

Figure H.4c Compensator frequency function amplitude plot for the Mode 2 PPF filter.

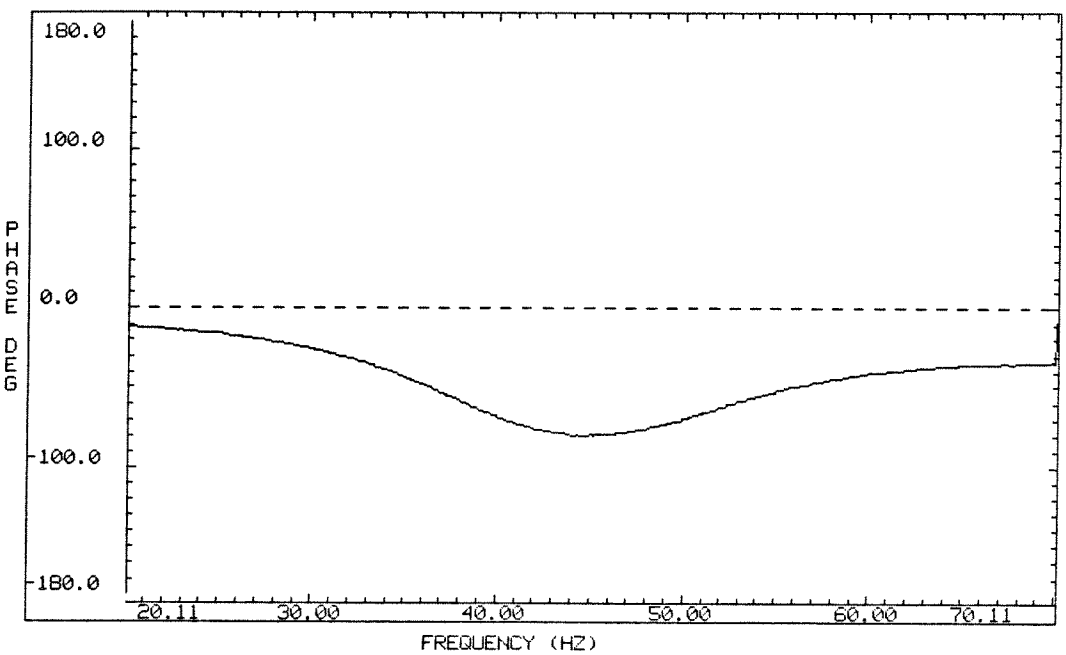

Figure H.4d Compensator frequency function phase plot for the Mode 2 PPF filter.

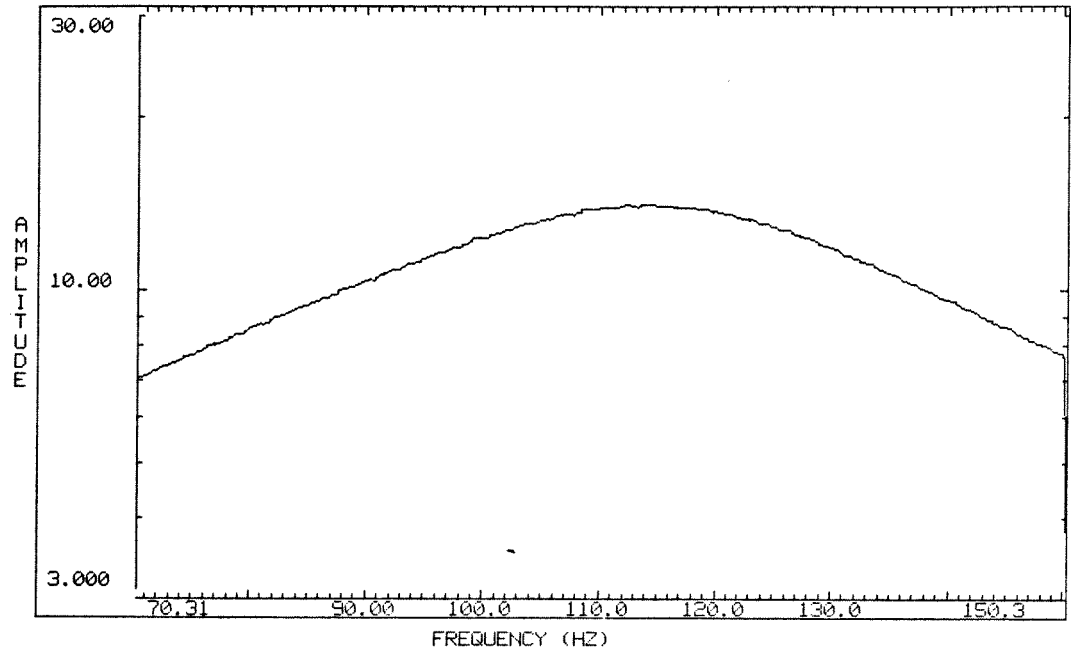

Figure H.4e Compensator frequency function amplitude plot for the Mode 3 PPF filter.

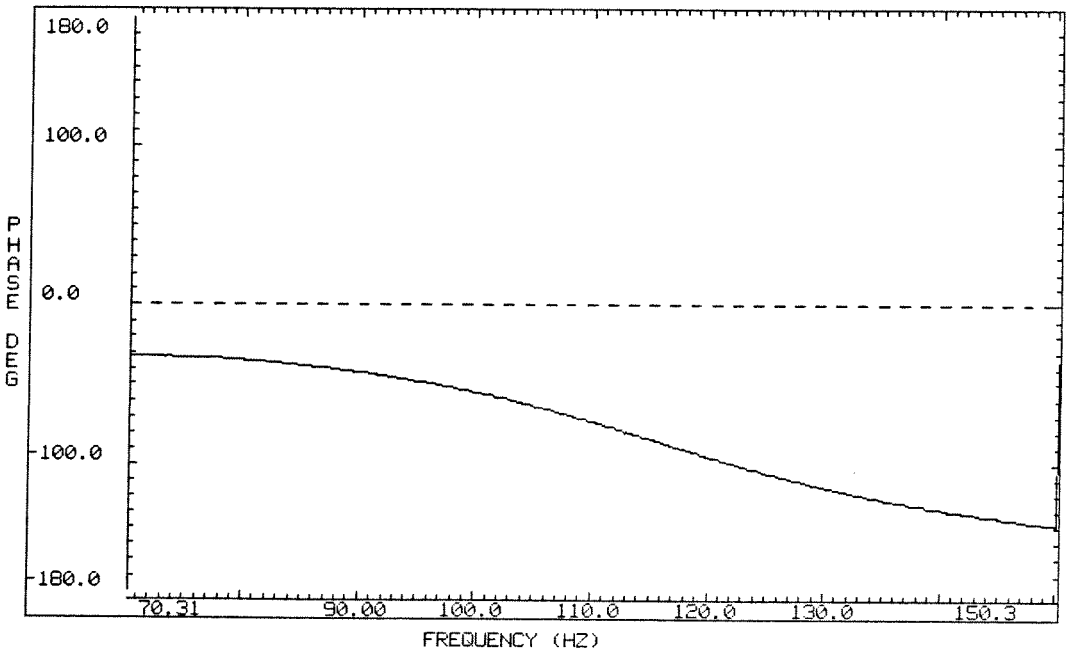

Figure H.4f Compensator frequency function phase plot for the Mode 3 PPF filter.

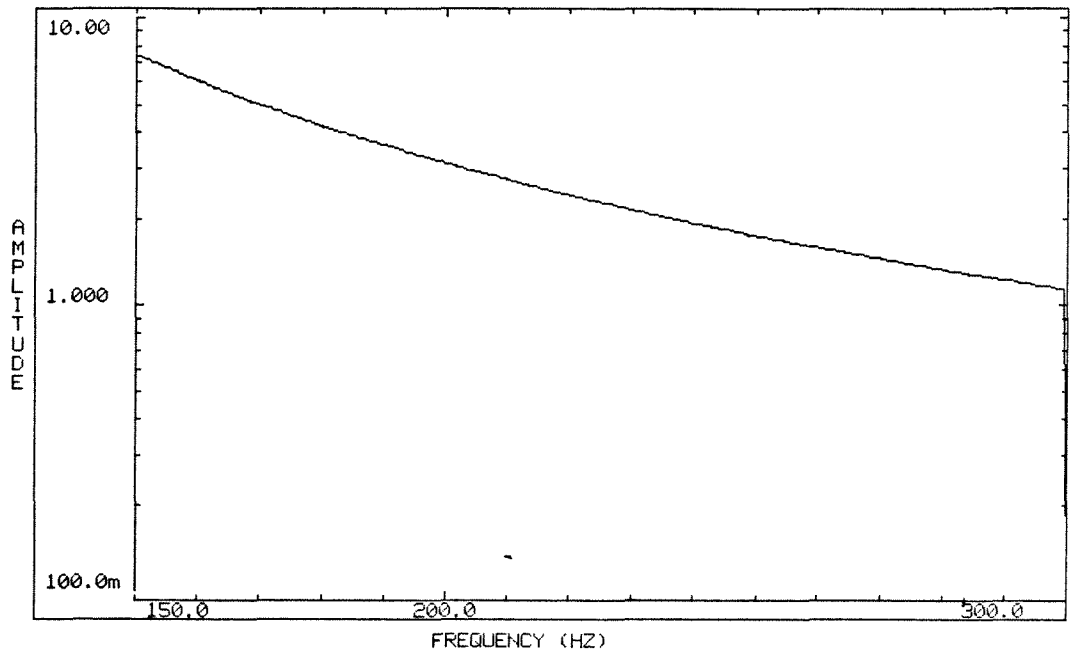

Figure H.4g Compensator frequency function amplitude plot past the Mode 3 PPF filter.

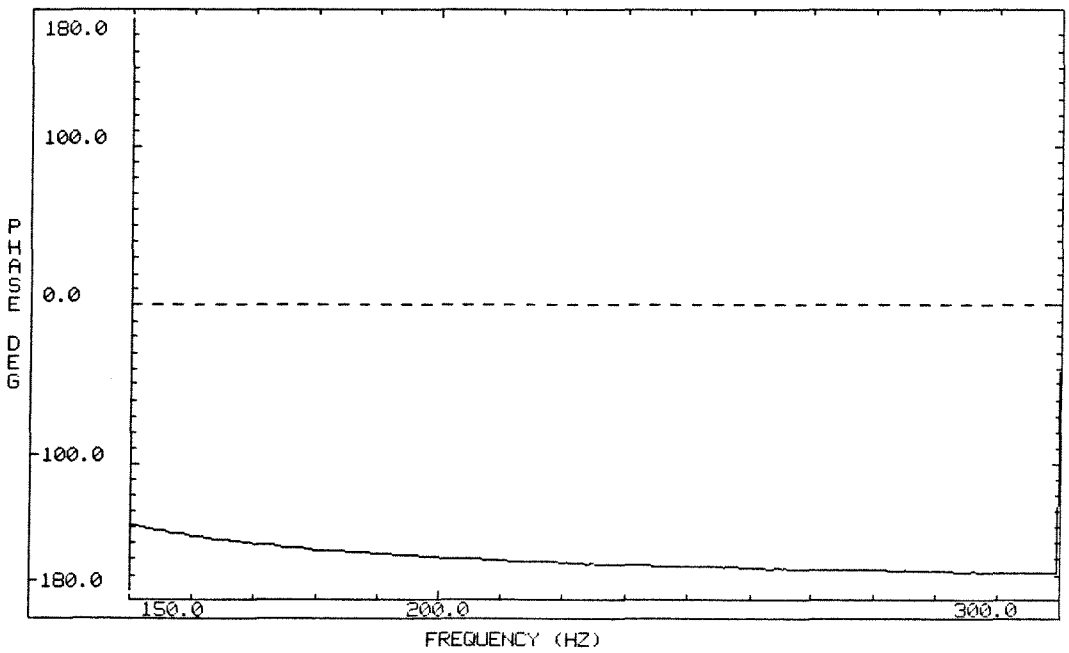

Figure H.4h Compensator frequency function phase plot past the Mode 3 PPF filter.

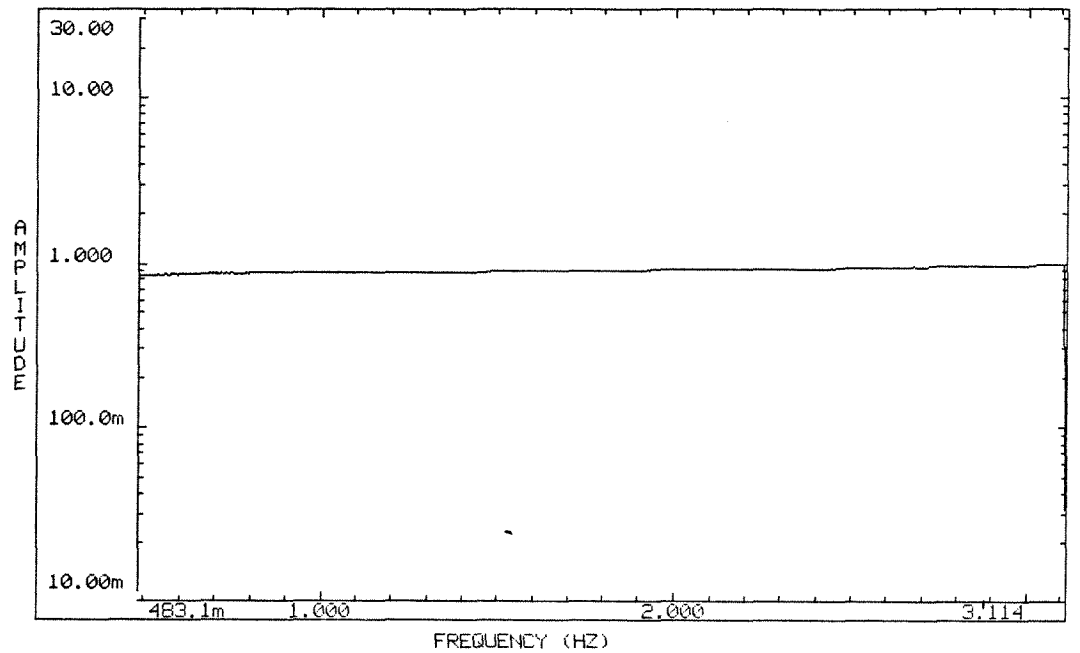

Figure H.5a Open Loop frequency function amplitude plot below Mode 1.

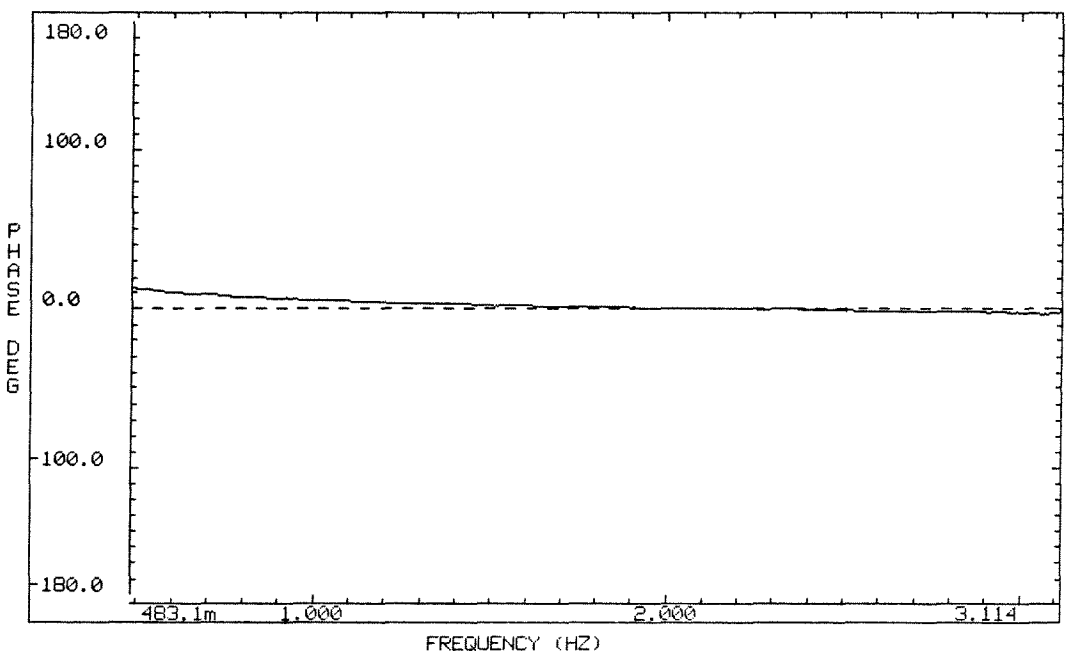

Figure H.5b Open Loop frequency function phase plot below Mode 1.

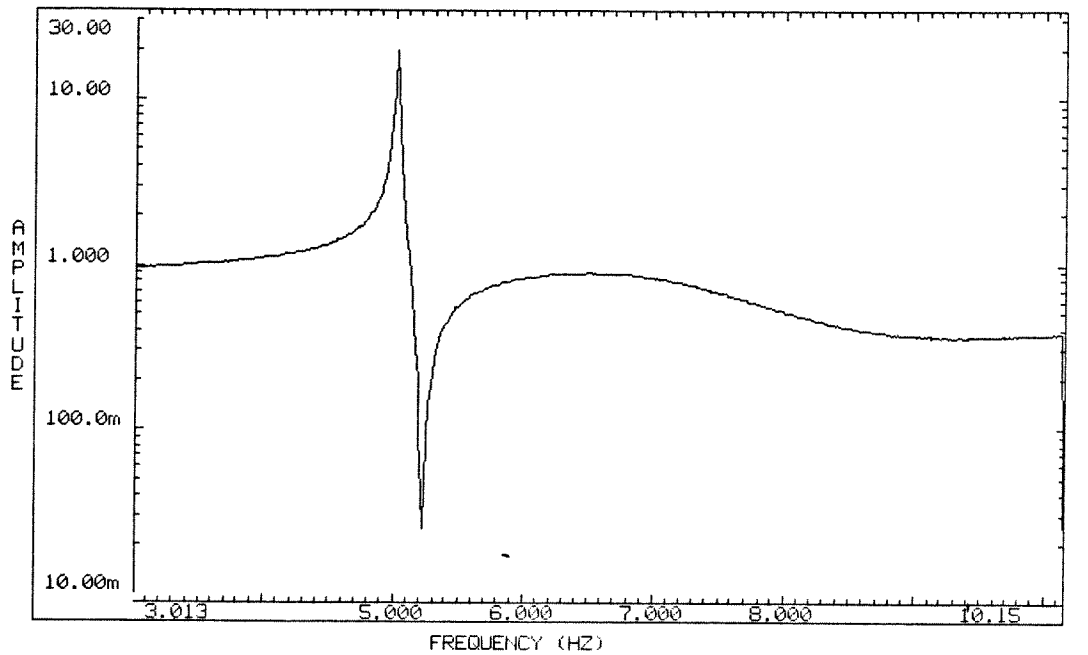

Figure H.5c Open Loop frequency function amplitude plot for Mode 1.

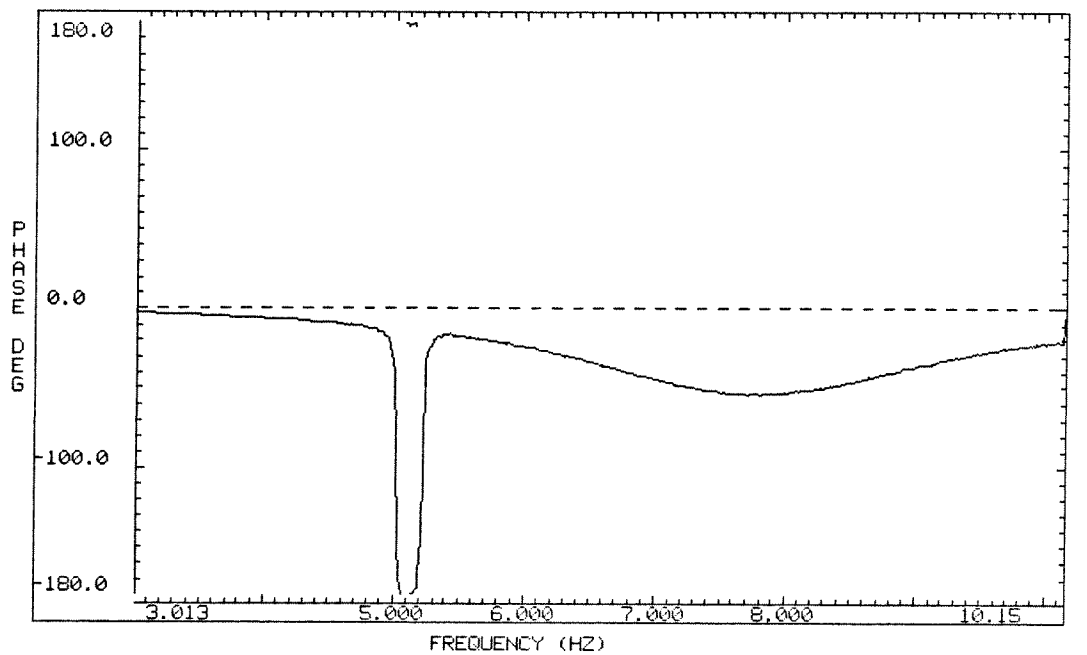

Figure H.5d Open Loop frequency function phase plot for Mode 1.

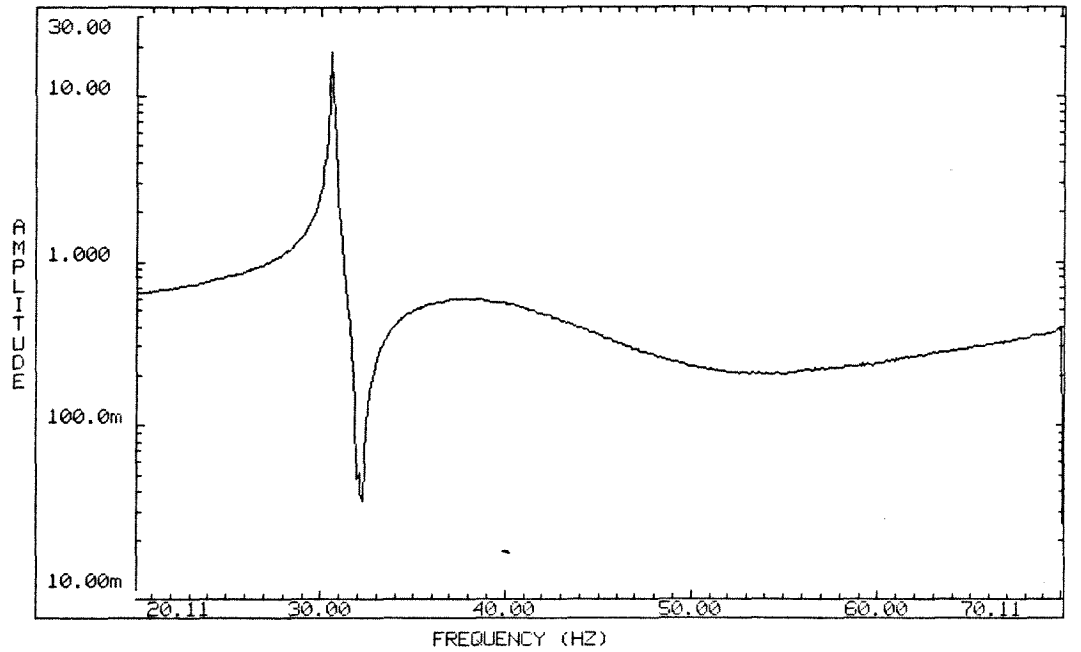

Figure H.5e Open Loop frequency function amplitude plot for Mode 2.

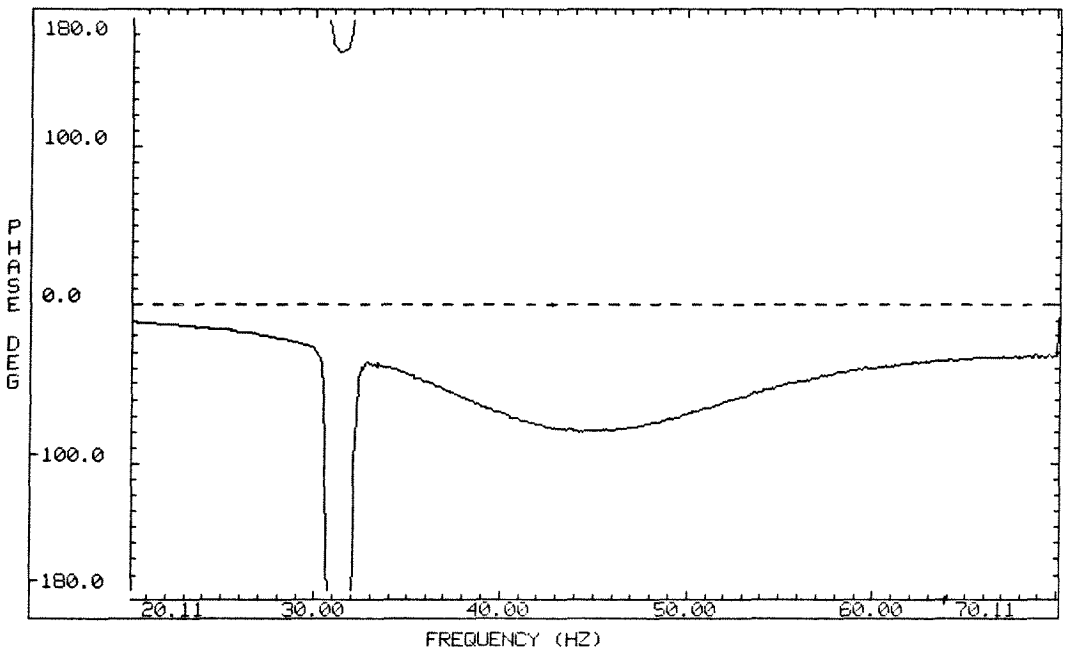

Figure H.5f Open Loop frequency function phase plot for Mode 2.

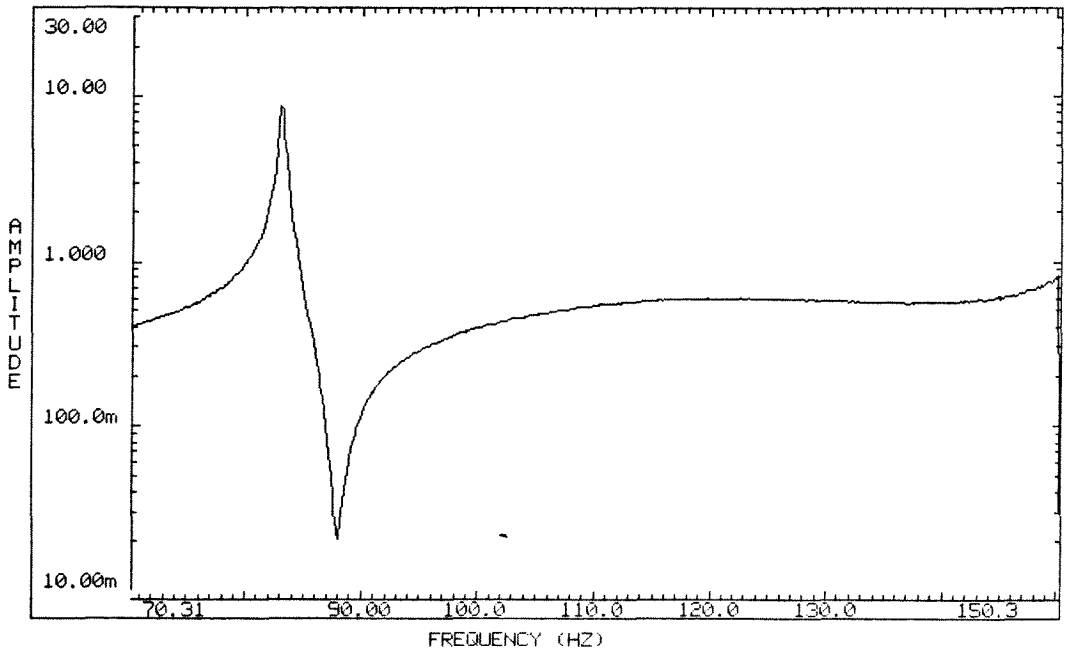

Figure H.5g Open Loop frequency function amplitude plot for Mode 3.

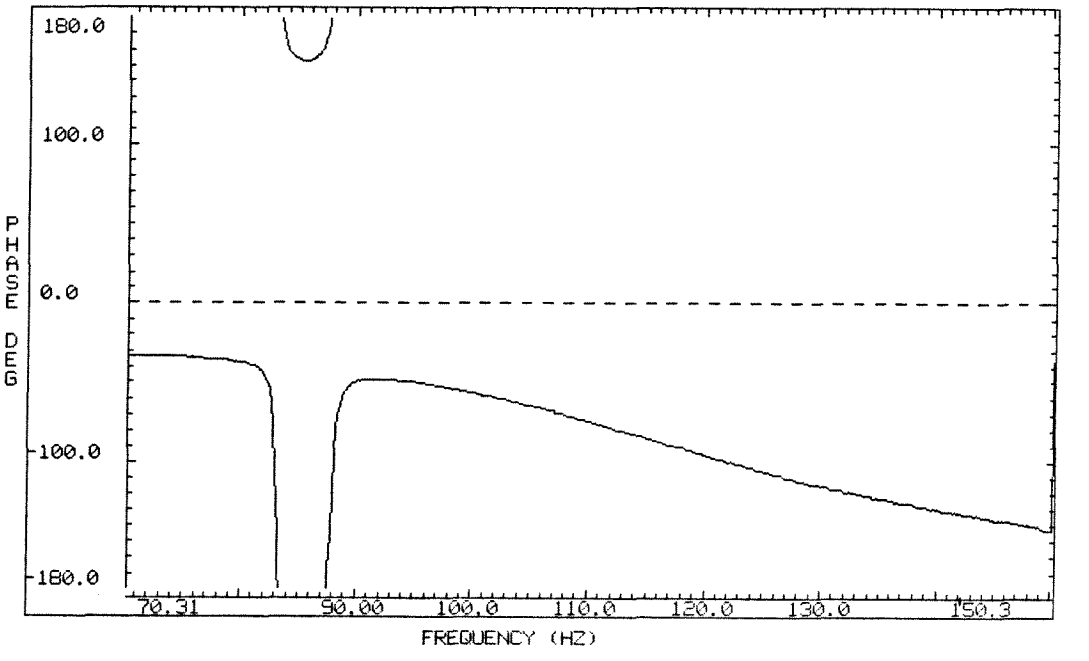

Figure H.5h Open Loop frequency function phase plot for Mode 3.

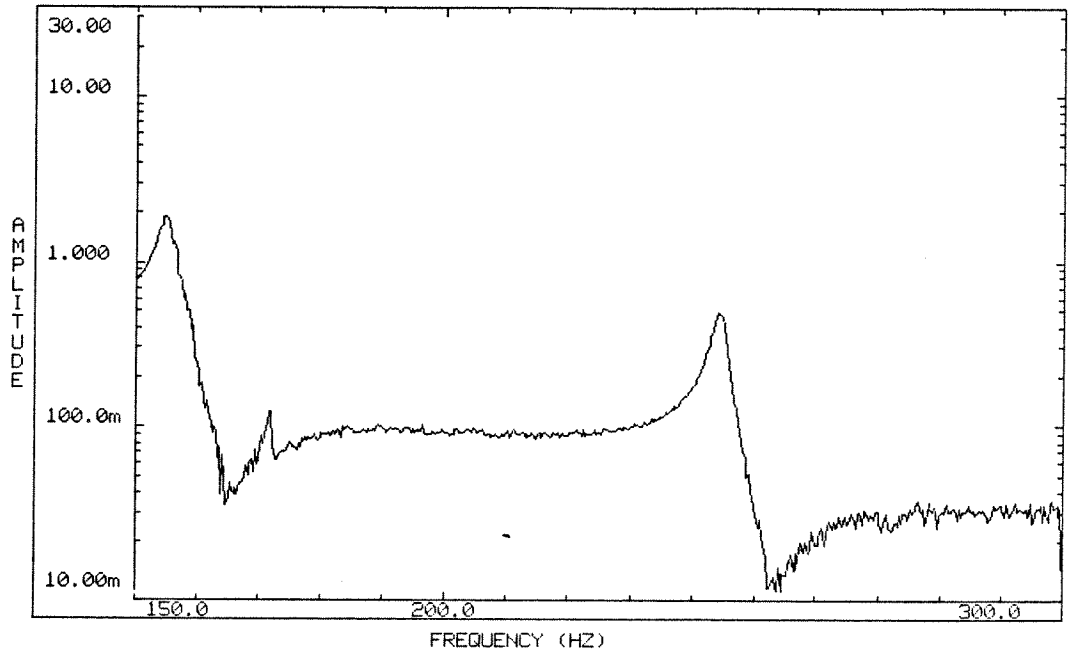

Figure H.5i Open Loop frequency function amplitude plot for Modes 4 and 5.

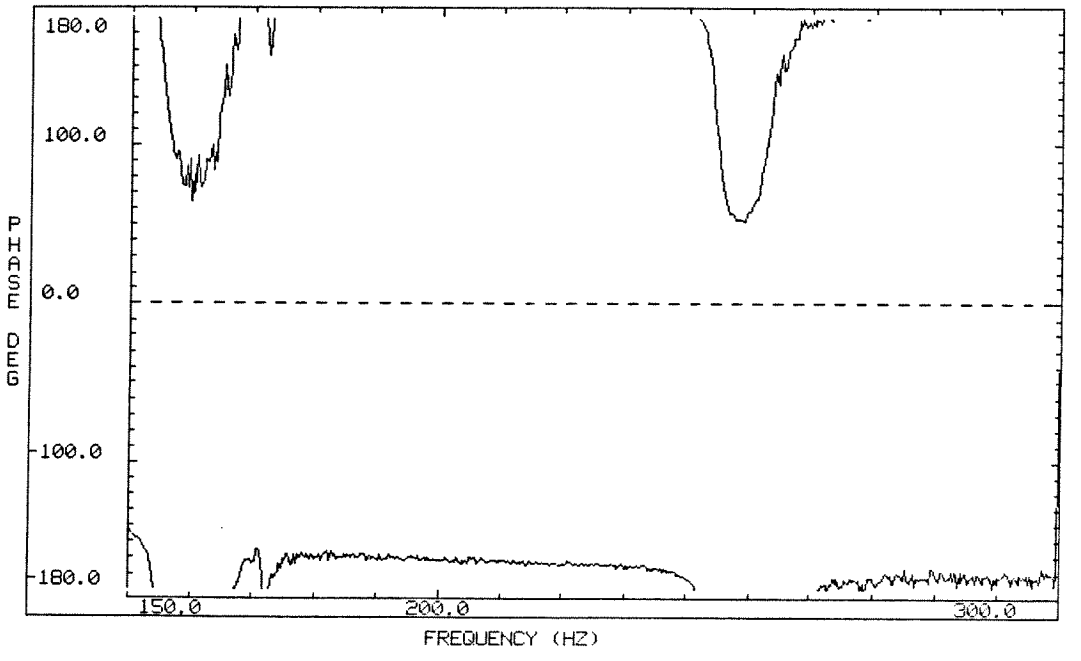

Figure H.5j Open Loop frequency function phase plot for Modes 4 and 5.

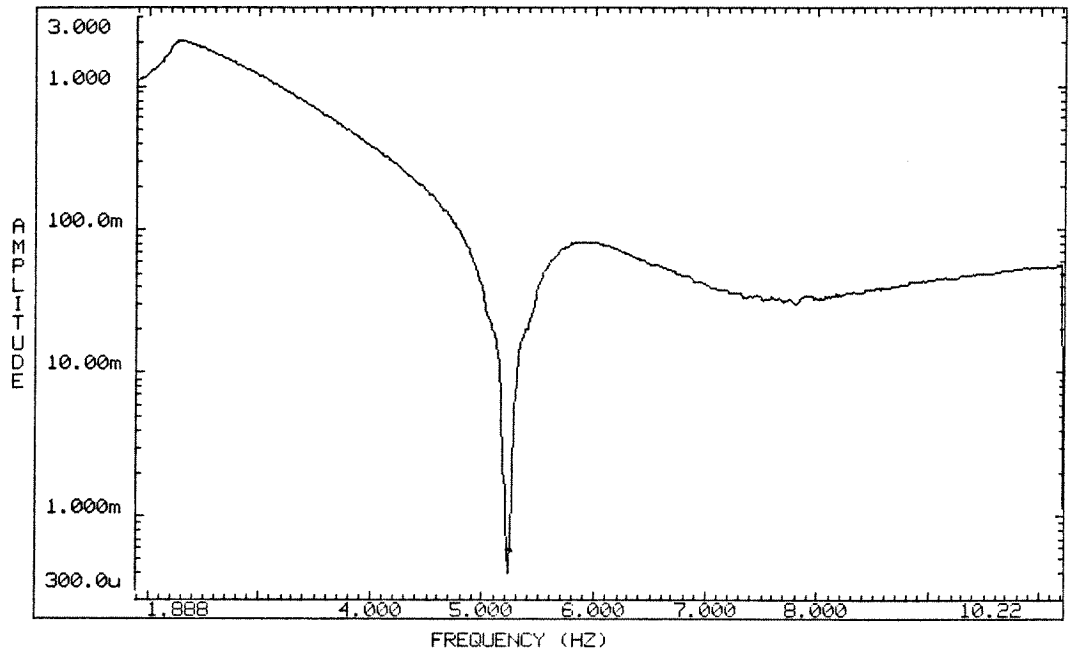

Figure H.6a Closed Loop frequency function amplitude plot for region near Mode 1.

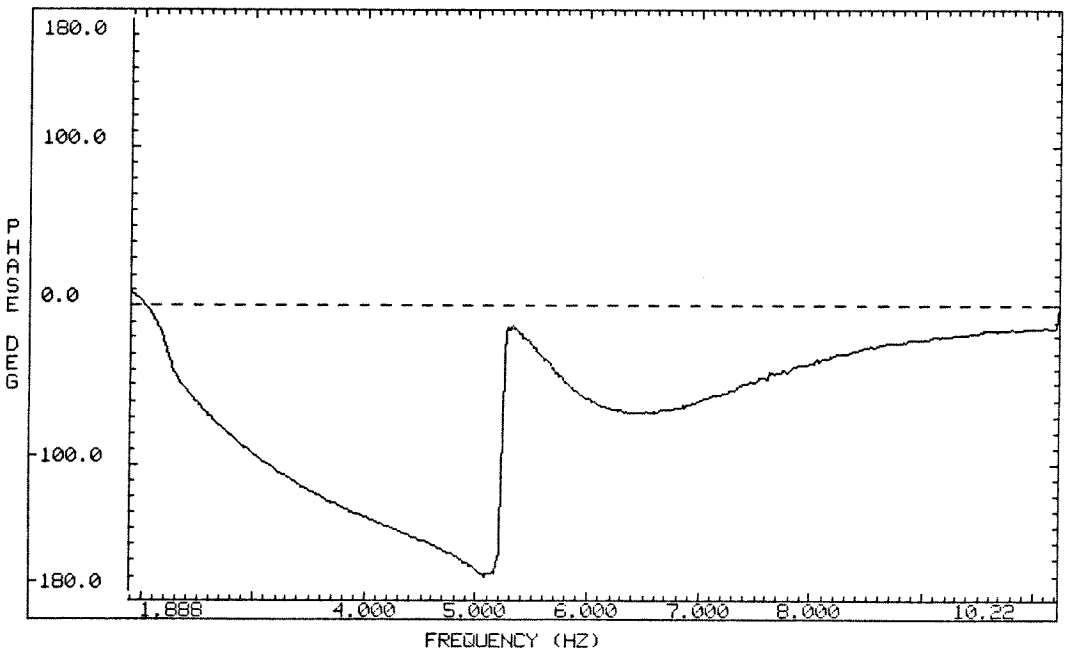

Figure H.6b Closed Loop frequency function phase plot for region near Mode 1.

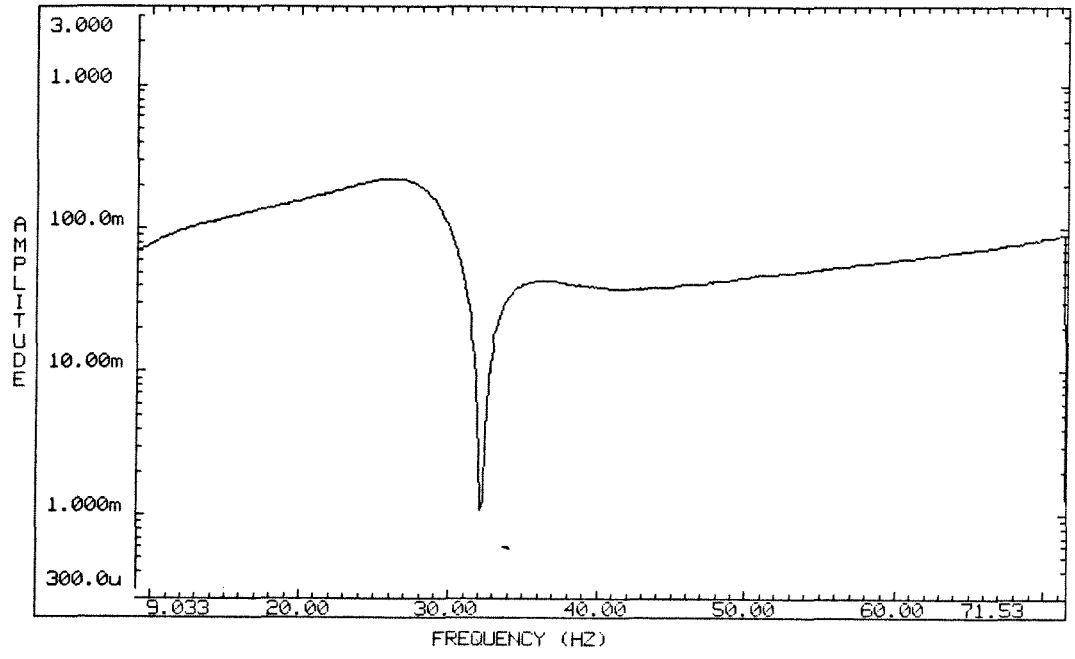

Figure H.6c Closed Loop frequency function amplitude plot for region near Mode 2.

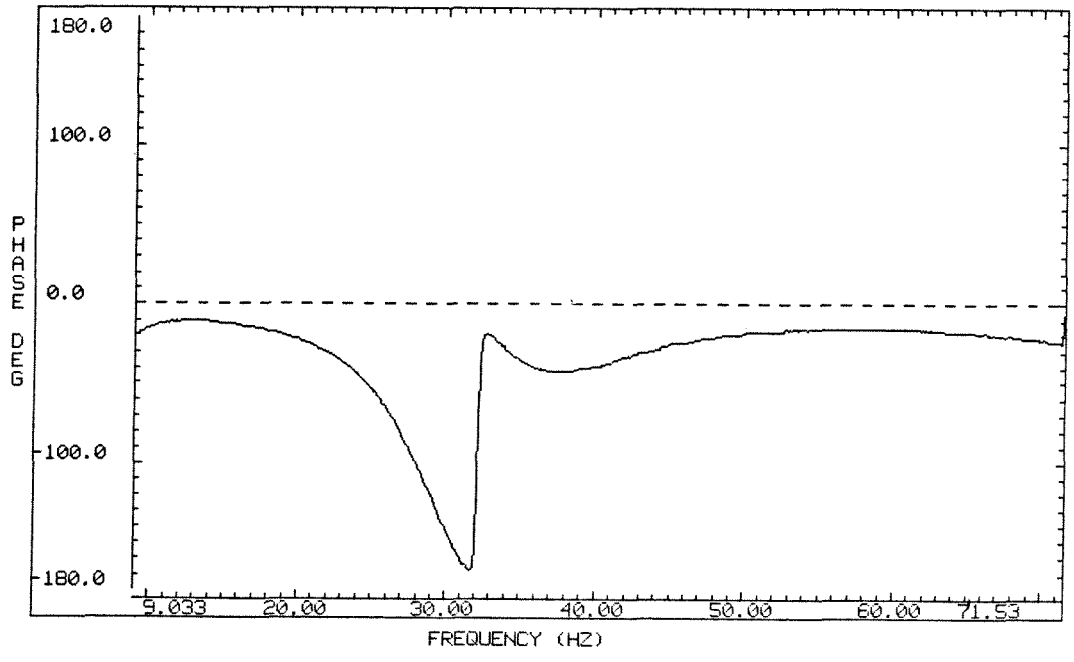

Figure H.6d Closed Loop frequency function phase plot for region near Mode 2.

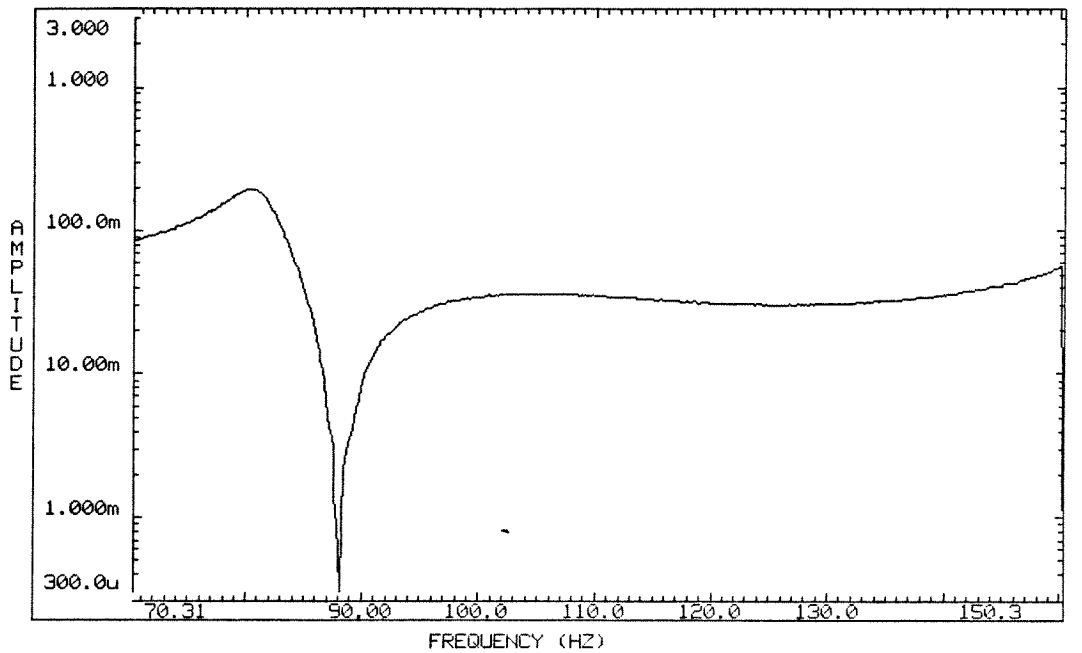

Figure H.6e Closed Loop frequency function amplitude plot for region near Mode 3.

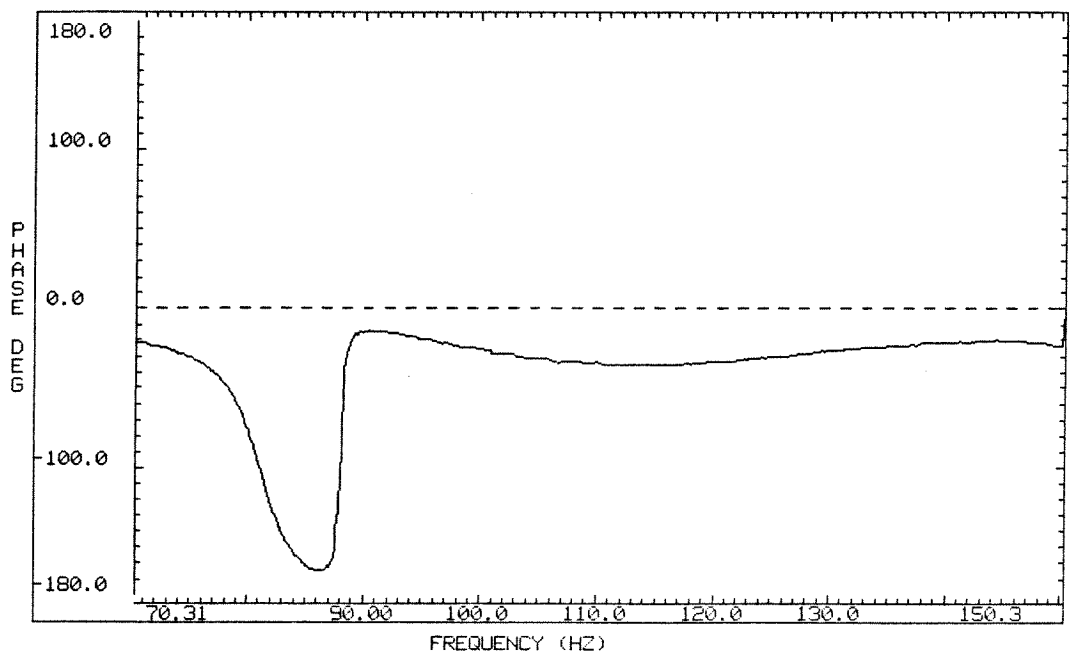

Figure H.6f Closed Loop frequency function phase plot for region near Mode 3.

REFERENCES

1. El-Raheb, M., and Wagner, P., "Static and Dynamic Characteristics of Large Deployable Space Reflectors," *AIAA 22nd Structures, Structural Dynamics and Materials Conference*, 1981.

2. Caughey, T. K., and Goh, C. J., "Analysis and Control of Quasi-Distributed Parameter Systems," *Caltech Dynamics Laboratory Report DYNL-82-3*, 1982.

3. Schaechter, D. B., "A Survey of Large Space Structure Control Approaches," JPL IOM 347-81-158, Jet Propulsion Laboratory, March 30, 1981.

4. Chen, J-C., "Evaluation of Modal Testing Methods," AIAA Paper No. 84-1071, *Proceedings of the AIAA Dynamics Specialist Conference*, 1984.

5. Kosut, R. L., "Robust Control of Flexible Spacecraft," *Journal of Guidance, Control, and Dynamics*, Vol. 6, No. 2, 1983, 104–111.

6. Gregory, C. Z., "Reduction of Large Flexible Spacecraft Models Using Internal Balancing Theory," *Journal of Guidance, Control, and Dynamics*, Vol. 7, 1984, 725–732.

7. Skelton, R. E., Hughes, P. C., and Hablani, H. B., "Order Reduction of Models of Space Structures Using Modal Cost Analysis," *Journal of Guidance, Control, and Dynamics*, July-August, 1982, 351–357.

8. Balas, M. J., "Active Control of Flexible Systems," *Journal of Optimization Theory and Applications*, Vol. 25, No. 3, 1978, 415–436.

9. Meirovitch, L., and Baruh, H., "Robustness of the Independent Modal-Space Control Method," *Journal of Guidance, Control, and Dynamics*, Vol. 6, No. 1, 1983, 20–25.

10. Meirovitch, L., "Modeling and Control of Distributed Structures," *Proceedings of the Workshop on Applications of Distributed System Theory to the Control of Large Space Structures*, 1983.

11. Goh, C. J., and Caughey, T. K., "On the Stability Problem Caused by Finite Actuator Dynamics in the Collocated Control of Large Space Structures," *International Journal of Control*, Vol. 41, No. 3, 1985, 787–802.

12. Hughes, P. C., "Space Structure Vibration Modes: How Many Exist? Which Ones are Important?," *Proceedings of the Workshop on Applications of Distributed System Theory to the Control of Large Space Structures*, 1983.

13. Balas, M. J., "Some Trends in Large Space Structure Control Theory: Fondest Hopes; Wildest Dreams," *Joint Automatic Control Conference*, 1979.

14. Balas, M. J., "Some Approaches to the Control of Large Space Structures," *AAS Guidance and Control Conference*, 1978.

15. Nurre, G. S., Ryan, R. S., Scofield, H. N., and Sims, J. L., "Dynamics and Control of Large Space Structures," *Journal of Guidance and Control*, Vol. 7, No. 5,1984, 514–526.

16. Meirovitch L., "A Comparison of Control Techniques for Large Flexible Systems," *AAS/AIAA Astrodynamics Specialist Conference*, 1981.

17. Athans, M., "The Role and Use of the Stochastic Linear-Quadratic-Gaussian Problem in Control System Design," *IEEE Transactions on Automatic Control*, Vol. AC-16, No. 6, 1971, 529–551.

18. Balas, M. J., "Direct Output Feedback Control of Large Space Structures," *Journal of the Astronautical Sciences*, Vol. 27, No. 2, 1979, 157–180.

19. Canavin, J. R., "The Control of Spacecraft Vibration Using Multivariable Output Feedback," *AIAA/AAS Astrodynamics Conference*, 1978.

20. Chen, C. L., "Direct Output Feedback Control of Large Flexible Spacecraft," *Caltech Dynamics Laboratory Report DYNL-82-1*, 1982.

21. Balas, M. J., "Reduced Order Control of Large Structures in Space," *17th Aerospace Sciences Meeting*, 1979.

22. Canavin, J. R., "Control Technology for Large Space Structures," *AIAA Conference on Large Space Platforms: Future Needs and Capabilities*, 1978.

23. Balas, M. J., "Direct Velocity Feedback Control of Large Space Structures," *Journal of Guidance and Control*, Vol. 2, No. 3, 1979, 252–253.

24. Kabamba, P. T., and Longman, R. W., "Exact Pole Assignment Using Direct or Dynamic Output Feedback," *The 3rd VPI & SU/AIAA Symposium on Dynamics and Control of Large Flexible Structures*, 1981.

25. Tseng, G. T., and Mahn, R. H., "Flexible Spacecraft Control Design Using Pole Allocation Techniques," *Journal of Guidance and Control*, Vol. 1, No. 4, 1978, 279–281.

26. Wu, Y. W., and Rice, R. B., "Control of Large Flexible Space Structures Using Pole Placement Design Techniques," *Journal of Guidance and Control*, Vol. 4, No. 3, 1981, 298–303.

27. Balas, M. J., "Modal Control of Certain Flexible Dynamics Systems," *SIAM Journal of Control and Optimizaton*, Vol. 16, No. 3, 1978, 450–462.

28. Balas, M. J., "Feedback Control of Flexible Systems," *IEEE Transactions on Automatic Control*, Vol. AC-23, No. 4, 1978, 673–679.

29. Sesak, J. R., Likins, P., and Coradetti, T., "Flexible Spacecraft Control by Model Error Sensitivity Suppression," *Journal of the Astronautical Sciences*, Vol. 27, No. 2, 1979, 131–156.

30. Skelton, R. E., and Likins, P. W., "An Approach to Model Error Compensation in the Control of Nonrigid Spacecraft," *Journal of Guidance and Control*, Vol. 1, No. 1, 1978, 41–49.

31. Premont, A., "Spillover Alleviation in Active Control of Flexible Structures," *Fourth IFAC Symposium on Control of Distributed Parameter Systems*, 1986.

32. Meirovitch, L., and Öz, H., "Modal-Space Control of Large Flexible Spacecraft Possessing Ignorable Coordinates," *Journal of Guidance and Control*, Vol. 3, No. 6, 1980, 569–577.

33. Meirovitch, L., and Baruh, H., "Control of Self-Adjoint Distributed Parameter Systems," *Journal of Guidance and Control*, Vol. 5, No. 1, 1982, 60–65.

34. Meirovitch, L., and Öz, H., "Computational Aspects of the Control of Large Flexible Structures," *IEEE Conference on Decision and Control*, 1979.

35. Aubrun, J. N., "Theory of the Control of Structures by Low-Authority Controllers," *Journal of Guidance and Control*, Vol. 3, No. 5, 1980, 444–451.

36. Schaechter, D., "Optimal Local Control of Flexible Structures," *Journal of Guidance and Control*, Vol. 4, No. 1, 1981, 22–26.

37. Kosut, R. L., "Robust Control of Flexible Spacecraft," *Journal of Guidance, Control, and Dynamics*, Vol. 6, No. 2, 1983, 104–111.

38. Johnson, C. D., "State-Variable Design Methods May Produce Unstable Feedback Controllers," *International Journal of Control*, Vol. 29, No. 4, 1979, 607–619.

39. Nesline, W. F., and Zarchan, P., "Why Modern Controllers Can Go Unstable in Practice," *Journal of Guidance, Control, and Dynamics*, Vol. 7, No. 4, 1984, 495–500.

40. Kabamba, P. T., and Longman, R. W., "An Integrated Approach to Optimal Reduced Order Control Theory," *The 3rd VPI & SU/AIAA Symposium on Dynamics and Control of Large Flexible Structures*, 1981.

41. Doyle, J. C., and Stein, G., "Multivariable Feedback Design: Concepts for a Classical/Modern Synthesis," *IEEE Transactions on Automatic Control*, Vol. AC-26, No. 1, 1981, 4–16.

42. Kosut, R. L., "Analysis of Performance Robustness for Uncertain Multivariable Systems," *Proceedings of IEEE Conference on Decision and Control*, 1982.

43. Gupta, N. K., "Frequency-Shaped Cost Functionals: Extension of Linear-Quadratic-Gaussian Design Methods," *Journal of Guidance and Control*, Vol. 3, No. 6, 1980, 529–535.

44. Anderson, B. D. O., and Mingori, D. L., "Use of Frequency Dependence in Linear Quadratic Control Problems to Frequency-Shape Robustness," *Journal of Guidance, Control, and Dynamics*, Vol. 8, No. 3, 1985, 397–401.

45. Hefner, R. D., and McKenzie, C. H., "Robust Controller Design Using Frequency Domain Constraints," *Proceedings of the Fourth VPI & SU/AIAA Symposium on Dynamics and Control of Large Flexible Structures*, 1983.

46. Banda, S. S., Ridgely, D. B., and Yeh, H-H., "Robustness of Reduced Order Control," *Proceedings of the Fourth VPI & SU/AIAA Symposium on Dynamics and Control of Large Flexible Structures*, 1983.

47. Benhabib, R. J., Iwens, R. P., and Jackson, R. L., "Stability of Large Space Structure Control Systems Using Positivity Concepts," *Journal of Guidance, Control and Dynamics*, Vol. 4, No. 5, 1981, 487–494.

48. Iwens, R. P., "Challenges in Stable and Robust Control System Design for Large Space Structures," *IEEE Conference on Decision and Control*, 1980.

49. Benhabib, R. J., Iwens, R. P., and Jackson, R. L., "Stability of Distributed Control for Large Flexible Structures Using Positivity Concepts," *AIAA Guidance and Control Conference*, 1979.

50. Iwens, R. P., Benhabib, R. J., and Jackson, R. L., "A Unified Approach to the Design of Large Space Structure Control Systems," *Joint Automatic Control Conference*, 1980.

51. Bailey, T., and Hubbard, J. E., "Distributed Piezoelectric-Polymer Active Vibration Control of a Cantilever Beam," *Journal of Guidance, Control, and Dynamics*, Vol. 8, No. 5, 1985, 605–611.

52. Aubrun, J-N., "Analytical and Experimental Research in Large Space Structures Control," *AIAA 23rd Aerospace Sciences Meeting*, 1985.

53. Dehghanyar, T. J., Masri, S. F., Miller, R. K., Bekey, G. A., and Caughey, T. K., "Sub-Optimal Control of Nonlinear Flexible Space Structures," *Proceedings of the Workshop on Identification and Control of Flexible Space Structures*, 1985.

54. Meirovitch, L., and Baruh, H., "Nonlinear Natural Control of an Experimental Beam," *Journal of Guidance, Control, and Dynamics*, Vol. 7, No. 4, 1984, 437–442.

55. Schäfer B. E., and Holzach, H., "Experimental Research on Flexible Beam Modal Control," *Journal of Guidance, Control, and Dynamics*, Vol. 8, No. 5, 1985, 597–604.

56. Schaechter, D. B., and Eldred, D. B., "Experimental Demonstration of the Control of Flexible Structures," *Journal of Guidance, Control, and Dynamics*, Vol. 7, No. 5, 1984, 527–534.

57. Hallauer, W. L., and Skidmore, G. R., "Modal-Space Active Damping of a Plane Grid: Experiment and Theory," *Journal of Guidance, Control and Dynamics*, Vol. 8, No. 3, 1985, 366–373.

58. Hanagud, S., Obal, M. W., and Meyyappa, "Electronic Damping Techniques and Active Vibration Control," *26th Structures, Structural Dynamics, and Materials Conference*, 1985.

59. Brennan, T. J., "Distributed Active Damping of Multiple Modes," *2nd Vibration Damping Workshop*, 1986.

60. Simonian, S. S., Major, C. S., and Gluck, R., "An Experimental Study of Passive Damping and Active Control of Large Space Structures," *Vibration Damping Workshop*, 1984.

61. Crawley, E. F., and de Luis, J., "Use of Piezo-Ceramics as Distributed Actuators in Large Space Structures," *26th Structures, Structural Dynamics, and Materials Conference*, 1985.

62. Crawley, E. F., and de Luis, J., "Experimental Verification of Distributed Piezoelectric Actuators for use in Precision Space Structures," *27th Structures, Structural Dynamics, and Materials Conference*, 1986.

63. Swigert., C. J., and Forward, R. L., "Electronic Damping of Orthogonal Bending Modes in a Cylindrical Mast – Theory," *Journal of Spacecraft and Rockets*, Vol. 18, No. 1, 1981, 5–10.

64. Forward, R. L., "Electronic Damping of Orthogonal Bending Modes in a Cylindrical Mast – Experiment," *Journal of Spacecraft and Rockets*, Vol. 18, No. 1, 1981, 11–17.

65. Caughey, T. K., Fanson, J. L., and Chen, J-C., "Stiffness Control of Large Space Structures," *Proceedings of the Workshop on Identification and Control of Flexible Space Structures*, 1985.

66. Chen, J-C., "Response of Large Space Structures with Stiffness Control," *AAS/AIAA Astrodynamics Specialist Conference*, 1983.

67. Jaffe, B.; Cook, W.; Jaffe, H. 1971. *Piezoelectric Ceramics*. Academic Press: New York, pp. 7–10.

68. Randall, R. B.; Tech, B. 1977. *Application of B&K Equipment to Frequency Analysis*. Nærum Offset: Denmark, pp. 197–200.

69. Williams, A. 1981. *Electronic Filter Design Handbook*. McGraw-Hill: New York, pp. 3-16.

70. Gantmacher, F. R. 1959. *The Theory of Matrices*. Chelsea: New York, pp. 304–305.

71. Saucedo, R.; Schiring, E. E. 1968. *Introduction to Continuous and Digital Control Systems*. MacMillan: New York, pp. 321–323.